METAL DECORATION OF EXFOLIATED GRAPHITE NANOPLATELETS (xGnP) FOR FUEL CELL APPLICATION

By

In-Hwan Do

A DISSERTATION

Submitted to
Michigan State University
in partial fulfillment of the requirements
for the degree of

DOCTOR OF PHILOSOPHY

Department of Chemical Engineering and Materials Science

2006

ABSTRACT

METAL DECORATION OF EXFOLIATED GRAPHITE NANOPLATELETS (xGnP) FOR FUEL CELL APPLICATION

By

In-Hwan Do

The synthesis and characterization of metal particles at nanometer length scale has been the object of much research in modern nanotechnology due to their great impact on new nanoscale scientific and technological applications. Nanoscale metal particles possess unique optical, thermal, electronic, magnetic properties and chemical reactivity since the size of the resulting materials is on the same order as the fundamental interaction distances that give rise to physical properties and thus shows the quantum size effect which is not observed in their bulky status. Therefore, an effective synthetic method is required to obtain uniform small metal powders with controlled size and a narrow size distribution and also to produce nanocomposites consisting of either metals or metal oxides supported on carbons or metals dispersed on metal oxides for a variety of applications in chemical industries, automobiles, energy and power generating devices, hydrogen economy as well as for sensors.

On the other hand, although their excellent mechanical, thermal and electrical conductivity, excellent corrosion and oxidation resistance, and low impurity levels which are required as a breakthrough material to increase performance of next generation energy devices, exfoliated graphite nanoplatelet (xGnP) has not been studied as deeply as recent new nanostructured carbon materials such as single wall carbon nanotubes (SWNT), multi-wall carbon nanotubes (MWNT), carbon nanohorn (CNH), graphite

nanofiber (GNF), and fullerenes. In addition, xGnP is much cost-effective compared to other carbon nanosturctures. Hence, it is interesting to evaluate the applicability of xGnP as a support material for fuel cell which is one of promising energy devices for the future.

In this research, a new simple, efficient and economic way is presented for the synthesis of noble metal nanoparticles such as Pt, Ru, Pd, etc and their deposition on various carbon supports and metal oxides via microwave heating in the presence of various types of room temperature ionic liquids (RTIL). The resulting metal nanocrystals were characterized by means of UV-vis spectroscopy, transmission electron microscopy (TEM), powder x-ray diffraction (XRD), X-ray photoelectron spectroscopy (XPS) and cyclic voltammetry measurement. Homogeneous metal nanocrystals with sizes of 0.9~3nm were synthesized and deposited on various carbon and metal oxide support materials through the reduction of the corresponding metal precursors. The size of metal nanocrystals could be easily and finely tuned by simply controlling experimental factors such as the concentration of RTIL.

xGnP-supported Pt based catalysts were prepared and tested for utilization in a direct methanol fuel cell. They showed much higher catalytic activity compared to commercial carbon black supported catalysts. Excellent activity of the xGnP-supported catalysts over the commercial catalysts originates from the morphology of xGnP facilitating contact between the reactant and catalytically active phase as well as the improved interaction between xGnP and metallic phases. This result proves the potential of xGnP as a support to replace carbon black. xGnP nanocomposites with metal nanocrystals may find potential applications as catalysts for other chemical reactions.

TO MY BEST FRIEND AND LOVELY WIFE

HEE YOUNG YOU

ACKNOWLEDGEMENT

I would like to thank my advisor Prof. Lawrence T. Drzal for his support throughout my graduate research. Without his support, this research has not been successfully accomplished. I also like to thank Prof. Andree Y. Lee, Prof. Krishnamurthy Jayaraman, Prof. Ilsoon Lee, Prof. Miller, and Prof. Swain for accepting to be my committee members and providing valuable comments on my research.

In addition, I would like to thank all members in Composite Materials and Structures Center for their help and guidance in learning and operating the equipments. My special thanks go to Dr. Per for his experimental and analytical support on X-ray Photoelectron Spectroscopes and UV-vis spectroscopy. I would also express my thanks to Dr. Xudong Fan for his good help in operating Transmission Electron Microscopy. Many thanks go to all other students for their friendship and help.

I thank my late parents who stay in my mind for their encouragement and support. This happy moment wouldn't have come true without their devotion throughout my life. Finally, I would like to express my deepest appreciation to my lovely wife, Heeyoung. She has devoted herself to support me with her tremendous patience and mental support and a full of humor during my graduate research. My research may not be successful without her presence and help in my life.

TABLE OF CONTENTS

TABLE OF CONTENTS

TABLE OF CONTENTS

TABLE OF CONTENTS

TABLE OF CONTENTS

LIST OF TABLES

CHAPTER 1

LIST OF FIGURES

CHAPTER 1

CHAPTER 2

CHAPTER 3

CHAPTER 4

LIST OF FIGURES

LIST OF FIGURES

CHAPTER 5

LIST OF FIGURES

CHAPTER 6

LIST OF FIGURES

CHAPTER 7

Fi

Fi

Fi

Fi

CHAPTER 1

BASICS AND RESEARCH CHALLENGE IN LOW TEMPERATURE FUEL CELLS

1.1 Introduction

Fuel cells are the electrochemical device continuously converting chemical energy into electrical energy [1]. Fuel cells are similar to batteries in that both of them generate electrical energy. However, fuel cells differ from batteries in that fuel cells need a continuous supply of fuels and the continuous removal of products and in that the fuel and oxidant are not contained within the fuel cell compartment. Hence, fuel cells do not store energy as batteries do, but must be refilled with fuel after use.

Fuel cells are considered as an ideal next generation energy conversion device that can meet the increasing concerns about green environment and energy security for the future and the tendency to increase the flexibility of electricity generation. Fuel cells are expected to reduce the dependence on fossil fuels and produce less greenhouse emissions into the atmosphere. The main advantages of fuel cells over conventional heat engines are high electrical efficiencies, zero or low emissions and less noise pollution [2, 3]. Some other favorable characteristics of fuel cells that make them considered as next generation energy conversion devices are good reliability, no need of moving parts in the energy converter and remote and unattended operation [4]. Thanks to these merits, fuel cells are being developed for numerous commercial and military applications, such as automobiles, portable electronic devices, and mobile and stationary power generation. Among the various types of fuel cell, the proton-exchange membrane fuel cell (PEMFC) and the direct methanol fuel cell (DMFC) are attractive because they are close to commercial applications.

PEMFC is the most promising candidate for power application ranging from micropower to large-scale stationary power for building due to their advantageous

features such as low-operating temperature, high current density, light weight, long operating life time, low cost, suitability for discontinuous operation, small volume, etc. [5~7]. On the other hand, DMFC can be potentially applied in clean and mobile power sources due to their high energy efficiency and quick cold starting and in an electric vehicle, elimination of the need for fuel reformation [8, 9].

In this chapter, a review on the general background of low temperature fuel cells, especially PEMFC and DMFC, is provided. The focus is placed on the current status of the technology and the important technological challenges in carbon-supported metal catalysts for PEMFC and DMFC. At the end of this chapter, general features of the direct ethanol fuel cell (DEFC) and the direct formic acid fuel cell (DFAFC) are also discussed briefly since they also possess excellent characteristics for portable power devices and use precious metal catalysts on carbon supports similar to in PEMFC and DMFC.

1.2 Fundamentals of Fuel Cells

1.2.1 Basic principles

The basic structure of all fuel cells consists of two electrodes on opposite sides of an electrolyte. The electrodes are exposed to fuel or oxidant (e.g. hydrogen or oxygen in the case of PEMFC) supplied in the form of gas or liquid. The electrodes must be gas or liquid permeable but the electrolyte should not be permeable to the gas or liquid. Depending on the types of fuel cells, hydrogen or methanol is oxidized at the anode liberating electrons and protons which travel through the electrolyte:

$$H_2 \longrightarrow 2H^+ + 2e^- \qquad (1.1)$$

The liberated electrons flow in the external circuit producing electrical energy and arrive at the cathode to participate in the reduction of oxygen:

$$O_2 + 4e^- \longrightarrow 2O^{2-} \qquad (1.2)$$

The oxygen ions recombine with protons to form water:

$$O^{2-} + 2H^+ \longrightarrow H_2O \text{ with } \Delta G = -237 \text{ kJ/mol} \qquad (1.3)$$

Water can be produced at the anode if an oxygen ion conducting electrolyte is used as in alkaline fuel cell (AFC), molten carbonate fuel cell (MCFC), and solid oxide fuel cell (SOFC). A schematic drawing of fuel cells and their simplified reactions are shown in **Figure 1.1**.

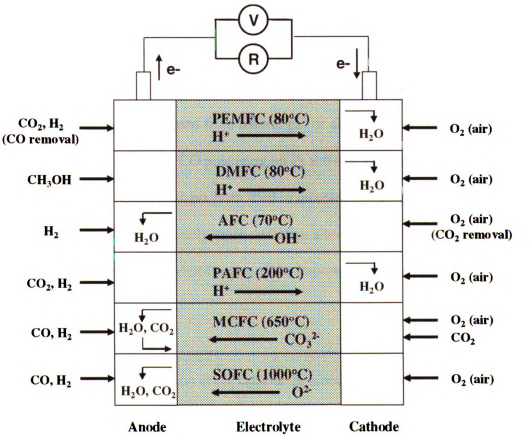

Figure 1.1. Summary of fuel cell types.

1.2.2 Important Reactions in Fuel Cells

1.2.2.1 Hydrogen oxidation

Pt-based catalysts are most widely used for the hydrogen oxidation at the anode in fuel cells. Hydrogen adsorbs on the surface of catalysts and then dissociates to two hydrogen ions as follows:

$$2Pt(s) + H_2 \longrightarrow Pt\text{-}H_{ads} + Pt\text{-}H_{ads} \qquad (1.4)$$

$$Pt\text{-}H_{ads} \longrightarrow Pt(s) + H^+ + e^- \qquad (1.5)$$

The overall reaction of hydrogen oxidation is:

$$H_2 \longrightarrow 2H^+ + 2e^- \quad E^O = 0V \qquad (1.6)$$

where E^O is the equilibrium cell voltage at standard condition.

This reaction is very fast with nearly no activation energy required when Pt is used as a catalyst or an electrode. Thus, very low loading of a Pt catalyst on the anode can be achieved [10]. However, the active sites of Pt surface can be poisoned by the adsorption of CO if impure hydrogen reformed from natural gas or alcohols is used as the fuel. To resolve the detrimental effect of CO poisoning on Pt activity, the application of air and an increased operating temperature have been tried to increase CO-tolerance. However, CO-tolerant catalysts are a fundamentally more attractive alternative and thus the development of CO-tolerant catalysts is one of the importance research issues [11].

1.2.2.2 Oxygen reduction

The oxygen reduction reaction at the cathode proceeds via a direct 4-electron reduction or an indirect 2-electron reduction shown in the following equations [12].

1) Direct four-electron reduction

a) in an alkaline electrolyte

$$Pt{-}O_2 + 2H_2O + 4e^- \longrightarrow 4OH^- \qquad (1.7)$$

b) or in an acidic electrolyte

$$Pt{-}O_2 + 4H_+ + 4e^- \longrightarrow 2H_2O \qquad (1.8)$$

2) Indirect two-electron reduction

a) in an alkaline electrolyte

$$Pt{-}O_2 + H_2O + 2e^- \longrightarrow HOO^- + OH^- \qquad (1.9)$$

followed by either

$$HOO^- + H_2O + 2e\text{-} \longrightarrow 3OH^- \qquad (1.10)$$

or

$$2HOO^- \longrightarrow 2OH^- \qquad (1.11)$$

b) or in an acid electrolyte

$$O_2 + 2H^+ + 2e^- \longrightarrow HOOH \qquad (1.12)$$

followed by either

$$HOO^- + 2H^+ + 2e^- \longrightarrow 2H_2O \qquad (1.13)$$

or

$$2HOOH \longrightarrow 2H_2O + O_2 \qquad (1.14)$$

The direct oxygen reduction in an acid electrolyte is preferable due to its high charge efficiency and no involvement of peroxide species.

The different reaction pathways result from the different adsorption sites on the surface of a catalyst, which is illustrated in **Figure 1.2** as an example in an acid electrolyte [13]. If only one side of oxygen adsorbs on the catalyst surface, pathway-II is favored without the change of O-O bonding. If adsorption takes place on both sides of

oxygen, the O_2 molecules are decomposed and four-electron reduction (pathway-I or III) is favored, resulting in no peroxide product. Carbon materials are suitable as support materials for carbon-supported noble metal catalysts for oxygen reduction reaction because they are inert in this acid environment [14].

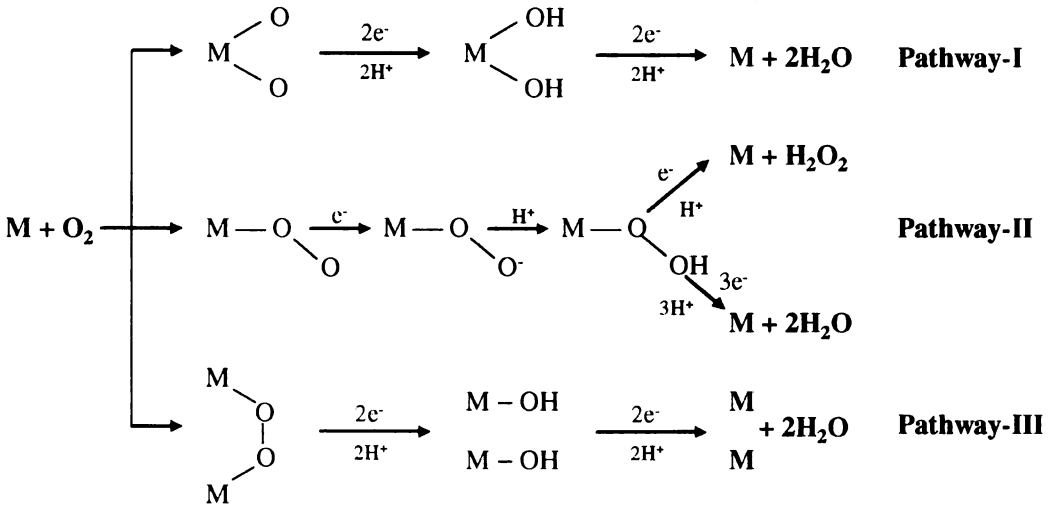

Figure 1.2. Pathways of oxygen reduction on catalyst surfaces in an acid electrolyte [15].

It has been known that many factors influence the kinetics of oxygen reduction reaction. The factors include particle size and crystal structure of catalysts, *d*-orbital vacancy of Pt-based catalysts, pretreatment and activation of electrode and distance between catalysts on the support surface [16~20]. Additionally, the oxygen reduction at cathode in fuel cells is very sensitive to the presence of every kind of impurity.

1.2.2.3 Methanol oxidation

Methanol oxidation in a DMFC takes place only at the anodes through a complicated process with many steps and many intermediates. Pt-based catalysts are most popular due

to their high stability and activity with methanol fuel. The methanol oxidation on Pt-based catalysts proceeds by a sequence of dehydrogenation steps giving rise to methanol molecules adsorbed on the catalyst surface, according to the following steps [21]:

i) $CH_3OH + Pt \longrightarrow Pt{-}CH_2OH + H^+ + 1e^-$ (1.15)

ii) $Pt{-}CH_2OH + Pt \longrightarrow Pt{-}CHOH + H^+ + 1e^-$ (1.16)

iii) $Pt{-}CHOH + Pt \longrightarrow Pt{-}CHO + H^+ + 1e^-$ (1.17)

iv) $Pt{-}CHO \longrightarrow Pt{-}C{\equiv}O + H^+ + 1e^-$ (1.18)

or $Pt{-}CHO + Pt \longrightarrow \overset{Pt}{\underset{Pt}{>}}C{=}O + H^+ + 1e^-$ (1.19)

CO is formed at the end of the methanol oxidation. This CO strongly adsorbs on the surface of the catalyst and poisons it, preventing further catalytic reaction. Hence, this CO must be removed by oxidizing the CO with oxygen generated from the dissociation of water supplied with methanol on the Pt surface or on a secondary metal (e.g. Ru) as shown below [22].

v) $Pt + H_2O \longrightarrow Pt{-}OH + H^+ + 1e^-$ (1.20)

vi) $Pt{-}OH + Pt{-}CO \longrightarrow 2Pt + CO_2 + H^+ + 1e^-$ (1.21)

or

vii) $Ru + H_2O \longrightarrow Ru{-}OH + H^+ + 1e^-$ (1.22)

viii) $Ru{-}OH + Pt{-}CO \longrightarrow Ru + Pt + CO_2 + H^+ + 1e^-$ (1.23)

The research challenge is to develop a catalyst which is not poisoned by CO. One of the most successful catalysts in DMFC is bimetallic PtRu catalyst supported on carbon.

Other promoters such as Sn, Co, Ni, W, Mo and other metals have been studied in the form of bimetallic or tertiary metallic alloys.

1.2.3 Types of Fuel Cells

Fuel cells can be categorized by either the electrolyte employed in the cell or the operating temperature for each of fuel cells. If the operating temperature is taken for the classification, the fuel cells can be divided into low temperature fuel cells and high temperature fuel cells. Low temperature fuel cells are the Alkaline Fuel Cell (AFC), PEMFC, DMFC and the Phosphoric Acid Fuel Cell (PAFC). The direct formic acid fuel cell (DFAFC) and the direct ethanol fuel cell (DAFC) which recently drew attention due to their merits over PEMFC and DMFC belong to low temperature fuel cells. High temperature fuel cells are the molten carbonate Fuel Cell (MCFC) and the solid oxide fuel cell (SOFC).

Typical characteristics and differences of various fuel cell systems are detailed in **Table 1.1** along with the advantages and disadvantages of each fuel cell. Pt-based catalysts or carbon-supported metal catalysts are commonly used in low temperature fuel cells. As shown in the last row, the development of new catalysts which is less expensive and more active than the present ones is an ongoing research issue requiring a solution to commercialize fuel cells. Among the fuel cells mentioned, DMFC and PEMFC are the target applications for the carbon-supported catalyst synthesized in this research. They are the most advanced low temperature fuel cells and are attracting much more attention for their potential as mobile power sources in the future.

Table 1.1. Typical characteristics and differences of various fuel cell systems

	PEMFC	DMFC	AFC	PAFC	MCFC	SOFC
Operating Temperature	25 - 90°C	60 - 120°C	< 100°C	160 - 220°C	550 - 660°C	800 - 1000°C
Reported Power Density	300 mW/cm^2	20 mW/cm^2	400 mW/cm^2	220 mW/cm^2	200 - 300 mW/cm^2	200 - 300 mW/cm^2
Fuel	H_2	CH_3OH	H_2	H_2	CH_4	CH_4, LPG
Electrolyte	Proton conducting membrane	Proton conducting membrane	30% KOH	Phosphoric acid	Molten alkali carbonate	Yttrium stabilized Zr support
Conducting Ion	H^+	H^+	OH^-	H^+	CO_3^{-2}	O^{-2}
Electrocatalyst	Pt, Pt/carbon	Pt, Pt/carbon	Pt/carbon, Ni/NiO_x	Pt, Pt/carbon	Porous Ni	Ni, Co, Yttria-zirconia
Efficiency	45%	25%	60%	42%	50~60%	50 - 60%
Advantages	Fast starting, high power density	Fast starting, management	Cheap materials, high performance	Tolerant to fuel impurities	High efficiency, cheap catalyst, fuel flexibility	High efficiency, cheap catalyst, fuel flexibility
Disadvantages	Expensive catalyst, sensitive to fuel impurities	Expensive catalyst	Expensive catalyst, corrosive electrolyte	Expensive catalyst, low lifetime	High temperature operating	High temperature operating
Applications	Transportation, portable applications	Transportation, portable applications	Transportation	Stationary power plants	Stationary power plants	Stationary power plants, transportation
Research Challenges	CO-tolerant catalyst, water management	Poisoning catalyst, CH_3OH permeability	Hydrogen catalyst, cathode corrosion	Oxygen catalyst, cathode corrosion	Better thermal cycling	Cheap fabrication process, rapid start up, robust thick film components

1.3. Proton Exchange Membrane Fuel Cell (PEMFC)

Owing to high power density and low operational temperature, PEMFC is considered as the fuel cell of choice for portable and transportation applications. The typical structure of a basic single cell in PEMFC stack is represented in **Figure 1.3**. The membrane electrode assembly (MEA) which is located between a pair of current collectors or flow field plates is the key component in a PEMFC. MEA consists of two electrodes separated by proton exchange membrane (PEM). Protons and electrons are generated by hydrogen oxidation at the anode and oxygen is reduced and then recombines with the protons to form water at cathode. Both PEMFC electrodes consist of Pt-based electrocatalysts bonded with Nafion ionomer and/or polytetrafluoroethylene (PTFE) on a gas diffusion layer.

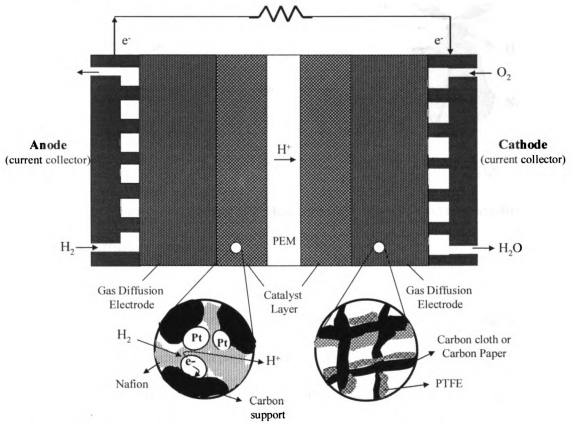

Figure 1.3. Typical structure of single cell in PEMFC (modified from [27]).

Nafion® as a trademark of DuPont for perfluorosulfonic acid ionomers is a perfluorinated polymer that contains small proportions of sulfonic functional groups. Its general chemical structure can be seen below in **Figure 1.4 (a)**. The SO_3^- groups is permanently attached to the chain, while the hydrogen ion is free to "hop" from one acid site to another. Electrons are blocked due to the fluorocarbon backbone being nonconductive. Hence, the Nafion is conductive for solvated hydrogen ions or protons but nonconductive for electrons because, which allow the Nafion to be qualified for ion-exchange membrane for applications such as Proton Exchange Membrane (PEM) fuel cells.

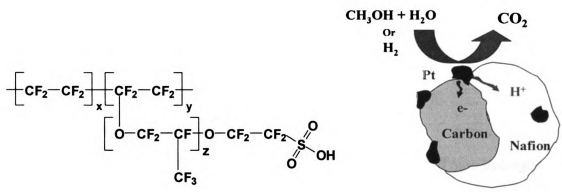

(a) (b)

Figure 1.4. (a) Chemical structure of Nafion ionomer and (b) three-phase boundary model at gas diffusion electrode.

The gas diffusion layer is normally carbon fiber paper or carbon cloth that acts as a current collector. The primary purpose of using Nafion is to provide a medium for the proton conducting pathway within the catalyst layer. The aim of PTFE is to bind together the electrode particles and to aid in water management.

The gas diffusion layer has to be porous to ensure the supply of the reactant to the active sites where Pt-based catalyst is in contact with ionic conductor (e.g. Nafion) and electronic conductor (carbon particles) to form "three-phase boundary" which is shown in **Figure 1.4 (b)**. The three-phase boundary is an important requirement for a good electrode. The catalyst, Nafion and/or PTFE are mixed together with water or alcohol to form an ink. This ink is deposited onto the diffusion layer by screen-printing, plating, brushing, filtering, or spraying techniques [23~26]. The ink can also be deposited onto PEM by the same techniques and then compressed with the diffusion layer.

In a normal PEMFC system, carbon-supported Pt catalysts and carbon supported Pt-based bimetallic alloy catalysts, especially PtRu, are applied at the cathode and anode, respectively. The general characteristics of electrodes in PEMFC are briefly presented in this section, followed by research challenges on the key materials for PEMFC.

1.3.1 Anode in PEMFC

The performance of a Pt catalyst in PEMFC anode is excellent if pure hydrogen is used. In reality, hydrogen reformed from other fuel sources such as methanol, propane, and natural gas is supplied but the reformed hydrogen has traces of CO. This CO strongly adsorbed on the surface of the Pt catalyst and blocks the active sites of the catalysts and consequently fewer sites are available for further the electro-oxidation of hydrogen, the so-called the poisoning effect [28]. The water-gas shift reaction or other gas processing methods are attached to the PEMFC system in order to resolve this problem but they make the system more complex and expensive [29, 30]. Hence, better catalysts which are tolerant to CO poisoning and can oxidize CO at low temperature are obviously desired.

Unsupported or supported Pt-Ru alloy is the most successful state-of-art catalyst resistant to CO poisoning. Two possible mechanisms on the positive effect of Ru were suggested: bifunctional mechanism [31~33] and ligand effect [34, 35]. The former involves the adsorption of an oxide species onto the Ru surface and then the production of Ru-OH. This Ru-OH is the source to oxidize CO on Pt to CO_2. The latter is related to the change of chemical properties of Pt atoms at the surface due to the presence of Ru in the catalyst. As a result, CO is bound more weakly to PtRu and thus the CO poisoning effect becomes weaker.

Other Pt-based alloys catalysts including Os, Mo, W, Co, Ir, and Pd have been studied by several groups for an improved CO-tolerance of anode catalysts [36~39]. Some of them were reported to show the CO-tolerance exceeding PtRu but still PtRu is most popular combination until they are firmly confirmed.

1.3.2 Cathode in PEMFC

The oxygen reduction reaction (ORR) on Pt occurs via dissociative adsorption of O_2 followed by protonation of the adsorbed species. The bridge model as shown in **Figure 1.5** [40] is widely accepted among several suggested and appears to describe this mechanism. Optimal Pt particle spacing and size are of critical importance [41]. The complex pathways of the ORR result in slow electrochemical kinetics. The rate of an electrochemical reaction for the ORR on Pt is 10^5 slower than that for hydrogen oxidation at Pt [42]. This explains why the activity at the cathode strongly influences the hydrogen fuel cell performance. Therefore, improving the cathode activity is a major focus for PEMFC electrode development.

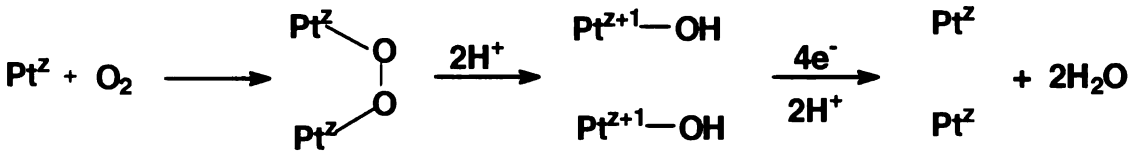

Fig. 1.5. The bridge model of oxygen reduction on Pt.

One successful way of increasing catalyst utilization is to employ carbon supported Pt catalysts. The ideal carbon support should have a suitable surface area, good electrical conductivity, high chemical/electrochemical stability, and pore size distribution, etc [43]. Vulcan XC-72 (Cabot Corp.) is the most common among a variety of grades of carbon black. Although carbon is an excellent electronic conductor, it is a very poor proton conductor due to its hydrophobicity. Increasing the hydrophilicity of the carbon support by creating carbon-oxygen complexes such as phenol, carbonyl, carboxylic, quinine, and lactone groups through oxidization has been shown to enhance proton conductivity of the catalyst layer. One serious issue with Pt/carbon catalysts is the sintering of the Pt particles [44]. Sintering occurs when Pt particles aggregate over their lifetime decreasing the Pt surface area, and ultimately leading to a decline in performance throughout the lifetime of operation.

Another approach is to improve the utilization of Pt catalyst. For successful catalyst utilization, it is important to enhance both the electrical and ionic conductivity of the carbon support at the same time. A proton conducting polymer like Nafion is added into the catalyst layer for that purpose. Pt catalyst near or directly in contact with Nafion provides the best performance. This increases the proton conductivity of the catalyst layer. It is also reported that carbon-supported Pt catalyst mixed with Nafion outperforms conventional Pt black electrodes having ten times the Pt loading [45]. When designing an

electrode with a carbon-supported catalyst and Nafion, they must be mixed in proper proportions to form a stable three-phase boundary where the gas, ion conductor, and catalytically active and electronically conductive phase are all present as mentioned previously. This requirement limits the amount of Nafion that can be added because the morphology, low gas permeability, and poor electronic conductivity of Nafion disrupt this boundary and adversely affects cell performance [46]. Hence, alternative methods for providing proton conductivity in the catalyst layer are of interest and importance.

1.3.3 Research Challenges on Catalysts in PEMFC

The key materials in a PEMFC are electrocatalyst, electrode, proton exchange membrane and bipolar plate. Further increases in the performance of PEMFC in use today is available from improvements of electrocatalytic activity especially at the cathode and from appropriate electrode design and from the enhancement of stability, proton conductivity, and operational temperature range in low cost proton exchange membrane. Non-noble metal based catalyst and low cost graphite bipolar plates are desired for the cost reduction of PEMFC system. Choice of hydrogen sources and optimization of thermal and water management also affect the performance of PEMFC.

The electrocatalyst should have high catalytic activity and high utilization. Pt-based catalysts are best in hydrogen oxidation at the anode and oxygen reduction at the cathode in PEMFC. Since hydrogen oxidation is not structurally sensitive, *smaller Pt particles* and *better their dispersion and utilization*, which will reduce the Pt loading and thus the cost of PEMFC.

There are two methods to overcome CO poisoning of Pt-based catalyst at the anode: One is to use CO-tolerant catalysts and the other is to introducing bilayer structure. CO-tolerant PtRu catalysts are commonly used for the case of the reformed hydrogen fuel as described previously. Metal loading of PtRu catalyst should be higher than that of Pt catalyst. This causes the agglomeration of catalytic phases, leading to the progressive loss of cell potential [47]. Hence, *new catalysts with higher CO-tolerance and aggregation-resistance* still need to be developed. Recently, PtSn/C, PtRuM/C (M = Mo, Nb, and Ta) and PtRu-HMO_3/C (M = Mo and W) have been investigated or this purpose [48~51]. For a bilayer anode, a carbon-supported Pt-based catalyst layer is inserted between the PtRu catalyst layer and the gas diffusion layer [52]. Using this bilayer anode construction resulted in extended anode lifetime and stable PEMFC performance.

In addition to resolving the CO poisoning of Pt-based catalysts, development of a Pt-free electrocatalyst is also of great importance to make it PEMFC economically competitive in market. PdAu-black alloys and PdAu/C catalysts were more resistant to CO poisoning and had higher catalytic activity at anode potential (0.5 – 0.1V) than PtRu/C [53]. This result was obtained only at a temperature below 60°C and thus optimization of PdAu/C is required for its catalytic improvement at relatively severe condition.

The oxygen reduction at the cathode is very sensitive to the structure of catalysts which is called as particle size effect [54]. According to the size effect, while a pure Pt electrocatalyst size should be around 4~5nm for high activity, PtM (M = Cr, Ni, Mo, Co, etc) is less affected by the size of active phases. Although some PtM catalysts have shown better activity than Pt catalyst, the increase of the electrical efficiency in PEMFC

is less than 2 % and their durability is unproven [55]. Hence, recent researches focus on *improving utilization of Pt catalyst* and more importantly developing much *more active oxygen reduction catalysts* than Pt catalysts.

1.4 Direct Methanol Fuel Cell (DMFC)

DMFC is very attractive fuel cell for commercialization. Since DMFC consumes liquid methanol fuel which is easily produced from natural gas or biomass, it has some system-related advantages over PEMFC, making it of interest to fuel cell manufacturer. The storage and transportation of methanol is less complicated and can be supplied through the existing gasoline infrastructure. The simplicity of design and cost-effectiveness are the main advantages of DMFC.

The principle of the DMFC is to directly oxidize methanol to carbon dioxide on the anode and to reduce oxygen to water on the cathode as shown from (1.24) to (1.26).

At anode:	$CH_3OH + H_2O \longrightarrow CO_2 + 6H^+ + 6e^-$	(1.24)
At cathode:	$3/2O_2 + 6H^+ + 6e^- \longrightarrow 3H_2O$	(1.25)
Overall:	$CH_3OH + O_2 \longrightarrow H_2O$ + Heat & Electricity	(1.26)

Although the thermodynamic characteristics of methanol oxidation at the anode are similar to hydrogen oxidation in PEMFC, the methanol oxidation is a slow process even on a high loading PtRu electrocatalysts. The thermodynamic cell potential in DMFC is about 1.185V, but in reality the cell potential is much lower [56]. Two slow reactions, i.e. methanol oxidation and oxygen reduction, the presence of a mixed potential at the

cathode caused by methanol crossover, and the CO-like poisoning of electrocatalysts are responsible for the reduction of the fuel consumption efficiency and the power density of DMFC.

Two important reactions occurring at the electrodes and a unique phenomenon (methanol crossover) happening only in DMFC will be described next . Research trends and challenges to resolve the problems of DMFC will also be briefly mentioned.

1.4.1. Anode in DMFC

Methanol oxidation at the anode in DMFC is a complicated process with many steps and many intermediates. The best catalyst to facilitate this oxidation process is Pt. However, CO intermediates strongly adsorb and poison the surface of Pt. The CO intermediates are removed when there are oxygenated species present on the Pt surface as represented in the following:

$$CH_3OH + Pt \longrightarrow Pt\text{–}CO_{ads} + 4H^+ + 4e^- \quad (1.27)$$

$$H_2O + Pt \longrightarrow Pt\text{–}OH_{ads} + H^+ + e^- \quad (1.28)$$

$$Pt\text{–}CO_{ads} + Pt\text{–}OH_{ads} \longrightarrow CO_2 + 2Pt + H^+ + e^- \quad (1.29)$$

Higher temperatures increase the rate of the oxidation and removal of CO intermediate, hence DMFC is operated at higher temperature (80 ~ 150°C) than PEMFC. To decrease the poisoning effect, bimetallic Pt catalysts can be used. Pt-Ru is the most effective bimetallic catalyst for methanol oxidation. The mechanism for methanol oxidation using PtRu is as follows:

$$CH_3OH + Pt \longrightarrow Pt\text{–}CO_{ads} + 4H^+ + 4e^- \quad (1.30)$$

$$H_2O + Ru \longrightarrow Ru\text{–}OH_{ads} + H^+ + e\text{-} \quad (1.31)$$

$$Pt - CO_{ads} + Ru\text{–}OH_{ads} \longrightarrow CO_2 + Pt + Ru + H^+ + e\text{-} \quad (1.32)$$

Oxygenated species form on Ru at lower potentials and Ru decreases the amount of CO intermediates formed on Pt [57, 58]. Additionally, Ru is much more stable than other promoters under the conditions of DMFC operation [59]. Pt-Ru catalysts can be prepared by numerous methods, such as chemical deposition [60], electrodeposition [61], sputter deposition [62], and organometallic routes [63]. Each method results in a catalyst with different properties due to different morphology, dispersion state, alloying state, particle size, structure, and composition that influence catalytic activity. Catalyst activation also influences fuel cell performance [64].

On the other hand, the oxidation state of Ru is in dispute. It is claimed that Pt^0Ru^0, pure metallic alloy, are much less active for methanol oxidation than a mixed phase alloy $PtRuO_xH_y$ [65] because the presence of hydrous oxides is expected to increase the rate of methanol oxidation by promoting the formation of $Ru\text{-}OH_{ads}$ species that assist the removal of CO species adsorbed on Pt. RuO_xH_y itself is a proton conductor. DMFC anodes containing RuO_xH_y have been shown to require smaller amount of Nafion in the catalyst layer [66]. The optimal atomic ratio of Pt to Ru is another issue. It is commonly held that a $Pt_{70}Ru_{30}$ composition is optimal for mixed alloys [67]. Although it is also claimed by catalyst manufacturer Johnson Matthey that $Pt_{50}Ru_{50}$ is the most active, it has been found by lattice parameter studies that the mixed phase catalysts with smaller Ru atom concentrations are desirable [68].

1.4.2. Cathodes in DMFC

The Nafion membrane used in DMFC is normally the same one used in PEMFC. The Nafion membrane was not optimized for DMFC but for PEMFC. Owing to the similar properties of methanol to water, methanol diffuses from the anode to the cathode. This is the so-called methanol crossover in DMFC. The transported methanol causes mixed potential due to the interference of methanol oxidation with oxygen reduction, resulting in a loss in cell performance [69]. As a result of methanol crossover, the cathode becomes water logged or flooded and thus is no longer an efficient structure for gas diffusion. This is another reason of potential loss in DMFC. Methanol crossover depends not only on the membrane permeability but also the concentration of methanol and the performance of the anode itself.

Most importantly, the membrane must be optimized for methanol blocking. This is possible by controlling the membrane thickness or modifying the membrane to be less permeable to methanol. For the latter, metal cations can be doped to alter the microstructure of the membrane [70]. Methanol crossover can be reduced by fueling an optimum concentration of methanol (1.5~2M) [71]. Another approach to cope with methanol crossover is to develop methanol-tolerant cathodes.

Poisoning of the Pt cathode catalyst by CO intermediates also occurs and in turn reduces the cathode activity. In order to circumvent some of these issues, one can optimize the electrode composition. High Pt loadings are employed to reduce the mixed potential loss. A large degree of hydrophobicity is incorporated into the cathode catalyst layer and backing to aid water removal.

1.4.3 Research challenges on Catalysts in DMFC

Carbon-supported metal based electrocatalysts are one of the most extensive research topics for fuel cell application. The properties of carbon supports play an important role in obtaining the maximum activity of the catalysts. However, this topic will be discussed in next chapter.

1.4.3.1 Electrocatalyst for the anode

Since PtRu binary alloy catalysts tolerant to CO-like intermediates at the DMFC anode was mentioned in section 1.4.2, other types of catalysts which have been studied to promote the performance of PtRu catalysts or to replace them is described in this section.

1) One approach to develop new electrocatalysts tolerant to CO-like species is to formulate PtRu with tungsten and molybdenum [72, 73]. Water is adsorbed on the oxide form of tungsten and molybdenum and interacts with CO adsorbed on Pt, thus facilitating CO oxidation to CO_2. Tungsten oxide and molybdenum oxides have the ability to easily exchange oxidation states by adsorbing hydroxyl ions from water and donate these species to methanol residues adsorbed on Pt. Ternary PtRuW or PtRuMo alloy catalysts also shows superior activity to methanol oxidation. Therefore, additional research with these electrocatalysts is required in combination with various carbon supports.

2) A novel route to increase methanol oxidation is to use heteropolyacids as an enhancer [74]. Heteropolyacids was proven to enhance the water discharging process and the oxidation of CO species strongly bonded to Pt due to a

number of factors such as redox behavior of heteropolyacids. They can be anchored on the surface of carbon supports. Heteropolyacids-anchored carbon supported PtRu catalysts or PtRu electrocatalysts promoted with heteropolyacids will be the excellent research topics for improving methanol electro-oxidation.

3) Non-noble metal catalysts are the most desirable alternative to Pt-based catalysts in that they can solve the high cost problem of materials employed in DMFC. Transition metal oxide catalysts are candidates. Mo/MoO_x and W/WO_x turn out to have better ability to coordinate water and to generate mobile hydroxyl species than Pt/PtO [75]. Hence it is worth exploring the possibility of tungsten oxide and molybdenum oxide as new electrocatalys for DMFC anodes.

1.4.3.2 Electrocatalyst for the cathode

Methanol oxidation and oxygen reduction should be considered at the same time to develop the best electrocatalysts for DMFC cathode [76]. Both reactions are affected by the particle size of electrocatalysts. If the particle size of the electrocatalysts is smaller than 3nm, the catalytic activity for oxygen reduction will be lower but the catalysts will be less poisonable, vice versa. Thus, the best compromise is to control the structure and the particle size in order to increase oxygen reduction and decrease methanol oxidation. Another is to use a promoter to enhance oxygen reduction and simultaneously hinder methanol chemisorption.

Non-noble metal based catalysts are always desirable for the same reason as in the anode. Transition metal sulfides [77] and organic transition metal complexes [78, 79] are proven to be good candidates.

1.5 Direct Ethanol Fuel Cells (DEFC)

DMFC has been actively investigated over many years and now it is regarded as a promising power source for mobile, stationary and portable application. However, although methanol is thought as a good fuel for low temperature fuel cells, it has some drawbacks. Methanol is relatively toxic and has a low boiling point. Therefore, other alcohols available from biomass resources are being considered as alternative fuels. In addition, it is still desirable to increase the number of liquid fuels for fuel cell systems in a bid to extend their practical applications and to facilitate their commercialization.

Low-weight molecular chemicals such as ethanol, propanol, and formic acid are good candidates for low temperature fuel cell [80, 81]. Ethylene glycol and glycerol are also considered for fuel cells [82]. Among them, ethanol is the most attractive. Ethanol is renewable, safe, convenient, and less toxic compared to methanol and it can be produced in large quantities from sugar-containing biomass sources. DEFC using ethanol as a fuel appears to be another promising low temperature fuel cell and thus this section is devoted to introduce the reaction mechanism and the role of electrocatalysts in DEFC.

1.5.1 Reaction Mechanism

The complete ethanol oxidation at anode, oxygen reduction on cathode, and overall reaction in DEFC can be described as follows [83]:

Anode: $CH_3CH_2OH + 3H_2O \longrightarrow 2CO_2 + 12H^+ + 12e^-$ (1.33)

Cathode: $3O_2 + 12H^+ + 12e^- \longrightarrow 6H_2O$ (1.34)

Overall: $CH_3CH_2OH + 3O_2 \longrightarrow 2CO_2 + 3H_2O$ (1.35)

Standard potential of overall reaction is 1.145V which is similar to DMFC's potential (1.185V). The complete anodic oxidation of ethanol involves 12 electrons per molecule and the cleavages of C-C bond [84]. The latter is an important factor of dominating the fuel efficiency and the yield of electrical energy. Many CO-like intermediates and products are also involved in anodic oxidation. This CO-like intermediates poisons the catalyst sites and thus need to be removed.

A detailed reaction mechanism of ethanol oxidation on Pt catalyst depending on electrode potential can be formulated as follows [85]:

$CH_3\text{-}CH_2OH \longrightarrow CH_3\text{-}CHO + 2H^+ + 2e^-$ (1.36)

$Pt + CH_3CHO \longrightarrow Pt\text{-}(CO\text{-}CH_3)_{ads} + H^+ + e^-$ (1.37)

$Pt + Pt\text{-}(CO\text{-}CH_3)_{ads} \longrightarrow Pt\text{-}(CO)_{ads} + Pt\text{-}(CH3)_{ads}$ (1.38)

$Pt + H_2O \longrightarrow Pt\text{-}H_{ads} + Pt\text{-}OH_{ads}$ (1.39)

$Pt\text{-}(CH_3)_{ads} + Pt\text{-}H_{ads} \longrightarrow CH_4$ (1.40)

$Pt\text{-}(CO)_{ads} + Pt\text{-}OH_{ads} \longrightarrow CO + H^+ + e^-$ (1.41)

Both poisoning species and some traces of methane are produced. Hence, the development of more active and selective electrocatalysts having the ability to break the C-C bond and to oxidize CO is required.

1.5.2. Electrocatalysts for DEFC

Pt is a good electrocatalyst for DEFC but not the best one. The addition of Ru to Pt results in the decrease of the electrocatalytic activity towards ethanol oxidation due to the inactivity of Ru toward ethanol. Other alloys such as PtRuSn and PtSn show very good efficiency for the anodic oxidation of ethanol. The presence of Sn not only promotes the cleavage of C-C bond but also oxidizes CO-like poisoning species to CO in DEFC [86]. This is true for other alcohol fuel cell using ethylene glycol, glycerol, and 2-propanol.

For DEFC, the effect of catalyst surface structure, metallic particle size, and other factors on the ethanol oxidation at anode must be systematically investigated. For practical application, carbon supported Pt-based catalysts containing Sn are used in order to stabilize the catalyst particles and to reduce the amount of precious metal. In this case, the interaction between metallic particles and supports are a critical parameter on the efficiency of the anodic oxidation of ethanol and thus is included in one of research topics.

The negative effect of ethanol crossover on cell performance in DEFC is smaller than methanol crossover in DMFC. Hence, highly active and effective anode catalysts will speed up the commercialization of DEFC.

1.6 Direct Formic Acid Fuel Cells (DFAFC)

Formic acid is not explosive and easy to store. Formic acid has high theoretical potential (1.45V) and shows negligible fuel crossover due to the repulsion between the partially dissociated formate anion (HCOOH) and sulfonic groups in the Nafion polymer membrane. Low contact resistance of formic acid as electrolyte is another significant

advantage over other liquid fuels [87-89]. Therefore, formic acid is a potential liquid fuel for fuel cell application.

Formic acid oxidation at anode based on traditional Pt-based catalysts proceeds via direct path way or indirect path way (CO path) in the following equations [90, 91]:

1) Direct oxidation

$$Pt + HCOOH \longrightarrow X \longrightarrow Pt + CO_2 + 2H^+ + 2e^- \quad (1.42)$$

2) Indirect oxidation (CO path)

$$Pt + HCOOH \longrightarrow X \longrightarrow Pt\text{-}CO + H_2O \quad (1.43)$$

$$Pt + H_2O \longrightarrow Pt\text{-}OH + H^+ + e^- \quad (1.44)$$

$$Pt\text{-}CO + Pt\text{-}OH \longrightarrow 2Pt + CO_2 + H^+ + e^- \quad (1.45)$$

In the direct path, HCOOH is directly oxidized to CO_2 via one or more active intermediates and generates two electrons. In the CO path, HCOOH is dehydrated to CO depending on the applied potential. CO remains on the surface of Pt particles and thus it must be removed by activating water. However, because the water activation reaction (1.44) is difficult, Pt catalysts become poisoned by CO and consequently overall activity is reduced.

Pt catalysts modified with Pd, Bi, and Sb have been studied to reduce CO poisoning and increase the catalytic activity [92~94]. Among them, PtPd catalysts showed the highest synergistic effect on both CO poisoning and the activity. Very recently, it turns out that Pd oxidizes HCOOH via a direct pathway, resulting in little or no CO poisoning effect on Pd particles and higher fuel cell performance than Pt-based catalysts [95]. However, a better synthetic method to prepare fine Pd nanoparticles black or supported on carbons will provide much potential of DFAFC in real commercialization.

1.7 Bibliography

1. M. Winter and R.J. Brodd, "What Are Batteries, Fuel Cells, and Supercapacitors?", Chem. Rev., 104, p4245~4270, 2004.

2. K.V. Kordesch and G.R. Simander, "Environmental Impact of Fuel Cell Technology ", Chem. Rev., 95, p191-207, 1995.

3. V. Plzak and B. Rohland, "Advanced Electrochemical Hydrogen Technologies, in Modern Aspects of Electrochemistry No. 26", Plenum Press, New York, p105, 1994.

4. L. Blomen and M.N. Mugerwa, "Fuel Cell Systems", Plenum, New York, 1993.

5. A.F. Ghenciu, "Review of fuel processing catalysts for hydrogen production in PEM fuel cell systems", Curr. Opin. Solid State Mater., 6, p389-399, 2002.

6. V. Mehta, J.S. Copper, "Review and analysis of PEM fuel cell design and manufacturing", J. Power Sources, 114, p32-53, 2003.

7. P. Costamagna, and S. Srinivasan, "Quantum jumps in the PEMFC science and technology from the 1960s to the year 2000: Part II. Engineering, technology development and application aspects", J. Power Sources, 102, p253-269, 2001.

8. X.M. Ren, P. Zelenay, A. Thomas, J. Davey, and S. Gottesfeld, "Recent advances in direct methanol fuel cells at Los Alamos National Laboratory", J. Power Sources, 86, p111-116, 2000.

9. S. Wasmus, and A. Kuver, "Investigation of direct methanol fuel cells based on unsupported Pt–Ru anode catalysts with different chemical properties", Electrochimica Acta, 45, p4319-4328, 2000.

10. M.S. Wilson, J.A. Valerio, and S. Gottesfeld, "Low platinum loading electrodes for polymer electrolyte fuel cells fabricated using thermoplastic ionomers", Electrochimica Acta, 40, p355-363, 1995.

11. B.N. Grgur and N.M. Markovic and P.N. Ross, "Electrooxidation of H_2, CO and H_2/CO mixtures on a well-characterized Pt–Re bulk alloy electrode and comparison with other Pt binary alloys", Electrochimica Acta, 43, p3631-3635, 1998.

12. L. Carrette, K.A. Friedrich, and U. Stimming, "Fuel cells: Principles, types, fuels, and applications", ChemPhysChem, 1, p162-193, 2000.

13. C.H. Hamann, A. Hamnett, and W. Vielstich, "Electrochemistry", 1st ed. Wieley-VCH, Weinheim, 1998.

14. E. Yeager, "Dioxygen electrocatalysis: mechanisms in relation to catalyst structure", J. of Mole. Catal., 38, p5-25, 1986.

15. E. Yeager, "Electrocatalysts for O_2 reduction", Electrochimica Acta, 29, p1527-1537, 1984.

16. Y. Takasu, N. Ohashi, X.G. Zhang, Y. Murakami, H. Minagawa, S. Sato and K. Yahikozawa, "Size effects of platinum particles on the electroreduction of oxygen", Electrochimica Acta, 41, p2595-2600, 1996.

17. M. Watanabe, H. Sei, and P. Stonehart, "The influence of platinum crystallite size on the electroreduction of oxygen", J. Electroanal. Chem., 261, p375-387, 1989.

18. S. Mukerjee, S. Srinivasan, M.P. Soriaga, and J. McBreen, "Effect of Preparation Conditions of Pt Alloys on Their Electronic, Structural, and Electrocatalytic Activities for Oxygen Reduction - XRD, XAS, and Electrochemical Studies", J. of Phys. Chem., 99, p4577-4589, 1995.

19. Y. Kiros, "Electrocatalytic properties of Co, Pt, and Pt-Co on carbon for the reduction of oxygen in alkaline fuel cells", J. of Electrochem. Soc., 143, p2152-2157, 1996.

20. E.K.W Lai, P.D. Beattie, E.P. Orfino, E. Simon and S. Holdcroft, "Electrochemical oxygen reduction at composite films of Nafion®, polyaniline and Pt", Electrochimica Acta, 44, p2559-2569, 1999.

21. A.S. Arico, S. Srinivasan, and V. Antonucci, "DMFCs: From Fundamental Aspects to Technology Development", Fuel Cells, 1, p133-161, 2001.

22. N. Giordano, E. Passalacqua, V. Alderucci, P. Staiti, L. Pino, H. Mirzaian, E.J. Taylor and G. Wilemski, "Morphological characteristics of PTFE bonded gas diffusion electrodes", Electrochim. Acta, 36, p1049-1055, 1991.

23. E.J. Taylor, E.B. Anderson and N.R.K. Vilambi, "Preparation of high platinum utilization gas diffusion electrodes for proton exchange membrane fuel cell", J. Electrochem. Soc., 139, L45, 1992.

24. V.A. Paganin, E.A. Ticianelli, and E.R. Gonzalez, "Development and electrochemical studies of gas diffusion electrodes for polymer electrolyte fuel cells", J. Appl. Electrochem., 26, p297-304, 1996.

25. G.S. Kumar, M. Raja and S. Parthasarathy, "High performance electrodes with very low Pt loading for polymer electrolyte fuel cell", Elecrochim. Acta, 40, p285-290, 1995.

26. J. Larminie and A. Dicks, "Fuel Cell Systems Explained", Wiley Publishing, New York, p200, 2000.

27. T. Thampan, S. Malhotra, J. Zhang, and R. Datta, "PEM fuel cell as a membrane reactor", Catal. Today, 67, 15-32, 2001.

28. H.F. Oetjen, V.M. Schmidt, U. Stimming, and F. Trilla, "Performance Data of a Proton Exchange Membrane Fuel Cell Using H_2/CO as Fuel Gas"J. Electrochem. Soc., 143, p3838-3842, 1996.

29. J.R. Rostrup-Neilson, "Production of synthesis gas", Catal. Today, 18, p305-324, 1993.

30. E. Yeager, "Electrocatalysts for O_2 reduction", Electrochim. Acta, 29, p1527, 1984.

31. H.A. Gasteiger, N.M. Markovic, P.N. Ross, "H2 and CO Electrooxidation on Well-Characterized Pt, Ru, and Pt-Ru. 1. Rotating Disk Electrode Studies of the Pure Gases Including Temperature Effects", J. Phys. Chem., 99, p8290-8301, 1995.

32. E. Herrero, K. Franaszczuk, and A. Wieckowski, "A voltammetric identification of the surface redox couple effective in methanol oxidation on a ruthenium-covered platinum (110) electrode", J. Electroanal. Chem., 361, p269-273, 1993.

33. K.A. Friedrich, K.P. Geyzers, U. Linke, U. Stimming, and J. Stumper, "CO adsorption and oxidation on a Pt(111) electrode modified by ruthenium deposition: an IR spectroscopic study", J. Electrocanal. Chem., 402, p123-128, 1996.

34. J. Davis, B.E. Hayden, and D.J. Pegg, "The electrooxidation of carbon monoxide on ruthenium modified Pt(110)", Electrochim. Acta, 44, p1181-1190, 1998.

35. H. Igarashi, T. Fujino, Y.M. Zhu, H. Uchida, and M. Watanabe, "CO Tolerance of Pt alloy electrocatalysts for polymer electrolyte fuel cells and the detoxification mechanism", Phys. Chem. Chem. Phys., 3, p306-314, 2001.

36. H. Yano, C. Ono, H. Shiroishi, and T. Okada, "New CO tolerant electro-catalysts exceeding Pt-Ru for the anode of fuel cells", Chem. Comm., p1212-1214, 2005.

37. C. Roth, M. Goetz and H. Fuses, "Synthesis and characterization of carbon-supported Pt–Ru–WO*x* catalysts by spectroscopic and diffraction methods", J. Appl. Electrochem., 31, p793-798, 2001.

38. E.I. Santiago, M.J. Giz, and E.A. Ticianelli, "Studies of carbon monoxide oxidation on carbon-supported platinum-osmium electrocatalysts", J. Solid State Electrochem., 7, p607-613, 2003.

39. B. Gurau, R. Viswanathan, R. Liu, T. Lafrenz, K.L. Ley, E.S. Smotkin, E. Reddington, A. Sapienza, B.C. Chan, T.E. Mallouk, and S. Sarangapani, "Structural and Electrochemical Characterization of Binary, Ternary, and Quaternary Platinum Alloy Catalysts for Methanol Electro-oxidation[1]", J. Chem. Phys. B, 102, p9997-10003, 1998.

40. K. Kinoshita, "Electrochemical Oxygen Technology", Wiley, New York, 1992.

41. A.J. Appleby, F.R. Foulkes, "A Fuel Cell Handbook", 2nd Ed., Kreiger Publishing, New York, 1993.

42. N.Y. Jia, R.B. Martin, Z. Qi, M.C. Lefebvre and P.G. Pickup, "Modification of carbon supported catalysts to improve performance in gas diffusion electrodes", Electrochim. Acta, 46, p2863-2869, 2001.

43. G.A. Gruver, R.F. Pascoe and H.R. Kunz, "Surface area loss of Pt supported on carbon in phosphoric acid electrolyte", J. Electrochem. Soc., 127, p1219-1224, 1980.

44. I.D. Raistri, Proceedings of the Symposium on Diaphragms, Separators, and Ion-Exchange Membranes, J.W. Van Zee, R.E. White, K. Kinoshita, and H.S. Burney, Eds.; The Electrochemical Society Inc.: Pennington, NJ, p172, 1986.

45. X.L. Cheng, B.L. Yi, M. Han, J.X. Zhang, Y.G. Qiao, and J.R. Yu, "Investigation of platinum utilization and morphology in catalyst layer of polymer electrolyte fuel cells", J. Power Sources, 79, p75, 1999.

46. R. Ianniello, V.M. Schmidt, U. Stimming, J. Stumper, and A. Wallau, "CO adsorption and oxidation on Pt and Pt---Ru alloys: dependence on substrate composition", Electrochim. Acta, 39, p1863, 1994.

47. T.R. Ralph and M.P. Hogarth, "Catalysts for low temperature fuel cells", Platinum Metal Rev., 46, p117-135, 2002.

48. E.M. Crabb, R. Marshall, and T. David, "Carbon Monoxide Electro-oxidation Properties of Carbon-Supported PtSn Catalysts Prepared Using Surface Organometallic Chemistry", J. Electrochem. Soc., 147, p4440-4447, 2000.

49. D.C. Papageorgopoulos, M. Keijzer, and F.A. de Bruijn, "The inclusion of Mo, Nb and Ta in Pt and PtRu carbon supported 3electrocatalysts in the quest for improved CO tolerant PEMFC anodes", Electrochim. Acta, 48, p197-204, 2002.

50. K.Y. Chen, Z. Sun, and A.C.C. Tseung, "Preparation and characterization of high-performance Pt-Ru/WO3/C anode catalysts for the oxidation of impure hydrogen", Electrochem. Solid-State Lett.,. 31, p10-12, 2000.

51. Z. Hou, B. Yi, H. Yu, Z. Lin, and H. Zhang, "CO tolerance electrocatalyst of PtRu-H_xMeO_3/C (Me = W, Mo) made by composite support method", J. Power Sources, 123, p116-125, 2003.

52. D.P. Wilkinson, H.H. Voss, K.B. Prater, G.A. Hards, T.R. Ralph and D. Thompsett, U.S. Patent 5795669, 1998.

53. T.J. Schmidt, M. Noeske, H.A. Gasteiger, R.J. Behm, P. Britz, and H. Boennemann, "On the CO tolerance of novel colloidal PdAu/carbon electrocatalysts", J. Electroanal. Chem. 501, p132-140, 2001.

54. H. Yu and B. Yi, "The Status and Prospects of Key Materials for the Proton Exchange Membrane Fuel Cell at the Dalian Institute of Chemical Physics", Fuel Cells, 4, p96-100, 2004.

55. T.R. Ralph and M.P. Hogarth, "Catalysis for Low Temperature Fuel Cells", Platinum Metal Rev., 46, p3-14, 2002.

56. J.OM. Bockris and S. Srinivasan, "Fuel Cells: Their Electrochemistry", McGraw-Hill Book Company, New York, 1969.

57. R. Parson and T. Vandernoot, "The oxidation of small organic molecules : A survey of recent fuel cell related research", J. Electroanal. Chem., 257, p9-45, 1989.

58. C. Lamy, J.M. Leger, and S. Srinivasan, DMFC: From a 20th Century Electrochmist's Dreams to a 21st Centruy Technology, in Modern Aspects of Electrochemistry, No. 34, B.E. Conway Eds., Kluwer Academic/Plenum Publishers, New York, p53, 2001.

59. S. Swathirajan and M. Mikhail, "Electrochemical oxidation of methanol at chemically prepared Pt-Ru alloy electrode", J. Electrochem. Soc., 138, p1321-1326, 1991.

60. M. Watanabe, Y. Genjima, and K. Turimi, "Direct Methanol Oxidation on Platinum Electrodes with Ruthenium Adatoms in Hot Phosphoric Acid", J. Electrochem. Soc., 144, p423, 1997.

61. C.K. Witham, W. Chun. T.I. Valdez, and S.R. Narayanan, "Performance of Direct Methanol Fuel Cells with Sputter-Deposited Anode Catalyst Layers", Electrochem. Solid-State Lett., 3, p497, 2000.

62. C.L. Lee and S.H. Bergens, "Deposition of Ru Adatoms on Pt Using Organometallic Chemistry: Catalysts for Electrooxidation of MeOH and Adsorbed Carbon Monoxide", J. Phys. Chem. B, 102, p193-199, 1998.

63. C. He, Z. Qi, M. Hollett, A. Kaufman, "An Electrochemical Method to Improve the Performance of Air Cathodes and Methanol Anodes", Electrochem. Solid-State Lett., 5, A181, 2002.

64. J.W. Long, R.M. Stroud, K.E. Swider-Lyons, and D.R. Rolison, "How To Make Electrocatalysts More Active for Direct Methanol Oxidation-Avoid PtRu Bimetallic Alloys!", J. Phys. Chem. B, 104, p9772-9776, 2000.

65. S.C. Thomsa, X. Ren, and S. Gottesfeld, "Influence of Ionomer Content in Catalyst Layers on Direct Methanol Fuel Cell Performance", J. Electrochem. Soc., 146, p4354-4359, 1999.

66. H.A. Gasteiger, M. Markovic, P.N. Ross, and E.J. Cairns, "Temperature dependent methanol electrooxidation on well characterized Pt-Ru alloys", J. Electrochem. Soc., 141, p1795-1803, 1994.

67. B. Gurau, R. Viswanathan, R.X. Liu, T.J. Lafrenz, K.L. Ley, E.S. Smotkin, E. Reddington, A. Sapienza, B.C. Chan, T.E. Mallouk, and S. Sarangapani, "Structural and Electrochemical Characterization of Binary, Ternary, and Quaternary Platinum Alloy Catalysts for Methanol Electro-oxidation[1]", J. Phys. Chem. B, 102, p9997, 1998.

68. H. Tributsch, M. Bron, M. Hilgendorff, H. Schulenburg, I. Dorbandt, V. Eyert, P. Bogdanoff, and S. Fiechter, "Methanol-resistant cathodic oxygen reduction catalysts for methanol fuel cells", J. Appl. Electrochem., 31, p739-748, 2001.

69. M.P. Hogarth and G.A. Hards, Platinum Metals. Rev., 40, p150, 1996.

70. V. Tricoli in Second Int. Symp. "Proton Conducting Membrane Fuel Cells II (Eds: S. Gottesfeld, T.F. Fuller)", Boston, MA, p358, 1998.

71. A. Kuver and W. Vielstich, "Investigation of methanol crossover and single electrode performance during PEMDMFC operation: A study using a solid polymer electrolyte membrane fuel cell system", J. Power Sources, 74, 211-218, 1998.

72. K.Y. Chen, Z. Sun, and A.C.C Tseung, "Preparation and characterization of high-performance Pt-Ru/WO3/C anode catalysts for the oxidation of impure hydrogen", Electrochem. Solid. State Lett., 3, p10-12, 2000.

73. P.Shen, K.Y. Chem, and A.C.C. Tseung, "Co-deposited Pt-WO3 electrodes .1. Methanol oxidation and in-situ FTIR studies", J. Chem. Soc., Faraday. Trans., 90, p3089-3096, 1994.

74. N. Giordano, S. Hocevar, P. Staiti, and A.S. Arico, "High performance fuel cell based on phosphotungstic acid as proton conducting electrolyte", Electrochim. Acta, 41, p397-403, 1996.

75. A.S. Arico, E. Modica, P. Creti, P.L. Antonucci, and V. Antonucci, "An electrode-kinetic investigation of CO and CO/H-2 oxidation in phosphotungstic acid ($H_3PW_{12}O_{40}$) electrolyte", J. New Mat. Electrochem, Systems, 3, p207-220, 2000.

76. Y. Takasu, T. Iwazaki, W. Sugimoto, and Y. Murakami, "Size effects of platinum particles on the electro-oxidation of methanol in an aqueous solution of HClO4", Electrochem. Comm., 2, p671-674, 2000.

77. N. Alonso Vante, H. Tributsch, "Energy conversion catalysis using semiconducting transition metal cluster compounds", Nature, 323, p431, 1986.

78. G.R. Sun, J.T. Wang, and R.F. Savinell, "Iron(III) tetramethoxyphenylporphyrin as methanol tolerant electrocatalyst for oxygen reduction in direct methanol fuel cells", J. Appl. Electrochem., 28, p1087-1093, 1998.

79. F. Franke, D. Ohms, and K. Wiesener, "Investigation of the influence of thermal treatment on the properties of carbon materials modified by N_4-chelates for the reduction of oxygen in acidic media", J. Electroanal. Chem., 260, p63-73, 1989.

80. C. Rice, S. Ha, R.I. Masel, and P. Waszczuk, "Direct formic acid fuel cells", J. Power Sources, 111, p83-89, 2002.

81. J.T. Wang, S. Wasmus, and R.F. Savinell, "Evaluation of ethanol, 1-propanol, and 5-propanol in a direct oxidation polymer-electrolyte fuel cell - A real-time mass spectrometry study", J. Electrochem. Soc., 142, p4218-4224, 1995.

82. H. Cnobloch, H. Nischik, and F. Vonstrum, "Determination of CO in air by reversible poisoning of electrocatalysts", J. Electroanal. Chem., 75, p747-761, 1977.

83. W.J. Zhou, S.Q. Song, W.Z. Li, Z.H. Zhou, G.Q. Sun, Q. Xin, S. Douvartzides, and P. Tsiakaras, "Direct ethanol fuel cells based on PtSn anodes: the effect of Sn content on the fuel cell performance", J. Power Sources, 140, p50-58, 2005.

84. F. Delime, J.M. Leger, and C. Lamy, "Enhancement of the electrooxidation of ethanol on a Pt–PEM electrode modified by tin. Part I: Half cell study", J. Appl. Electrochem., 29, p1249-1254, 1999.

85. C. Lamy, E.M. Belgsir and J.M. Leger, "Electrocatalytic oxidation of aliphatic alcohols: Application to the direct alcohol fuel cell (DAFC)", J. Appl. Electrochem., 31, p799-809, 2001.

86. R. Ianniello, V.M. Schmidt, J.L. Rodriguez, and E. Pastor, "Electrochemical surface reactions of intermediates formed in the oxidative ethanol adsorption on porous Pt and PtRu", J. Electroanal. Chem., 471, p167-179, 1999.

87. C. Rice, S. Ha, R.I. Masel, P. Waszczuk, A. Wieckowski, and T. Barnard, "Direct formic acid fuel cells", J. Power Sources, 111, p83-89, 2002.

88. X. Wang, J.M. Hu, and I.M. Hsing, "Electrochemical investigation of formic acid electro-oxidation and its crossover through a Nafion® membrane", J. Electroanal. Chem., 562, p73-80, 2004.

89. C. Rice, S. Ha, R.I. Masel, and A. Wieckowski, "Catalysts for direct formic acid fuel cells", J. Power Sources, 115, p229-235, 2003.

90. R. Parsons, and T. Vandernoot, "The oxidation of small organic molecules: A survey of recent fuel cell related research", J. Electroanal. Chem., 257, p9-45, 1998.

91. D. Capon and R. Parsons, "Oxidation of formic acid on noble metal electrode. 2. Comparison of behavior of pure electrodes", J. Electroanal. Chem., 44, p239-254, 1973.

92. M. Baldauf and D.M. Kolb, "Formic Acid Oxidation on Ultrathin Pd Films on Au(*hkl*) and Pt(*hkl*) Electrodes", J. Phys. Chem., 100, p11375-11381, 1996.

93. S.P.E. Smith, K.F. Ben-Dor, and H.D. Abruna, "Poison Formation upon the Dissociative Adsorption of Formic Acid on Bismuth-Modified Stepped Platinum Electrodes", Langmuir, 16, p787-794, 2000.

94. J.M. Feliu, A. Fernandez-Vega, A. Aldaz, and J. Clavilier, "New observations of a structure sensitive electrochemical behaviour of irreversibly adsorbed arsenic and antimony from acidic solutions on Pt (111) and Pt (100) orientations", J. Electroanal. Chem., 256, p149-163, 1998.

95. R. Larsen, S. Ha, J. Zakzeski, and R.I. Masel, "Unusually active palladium-based catalysts for the electrooxidation of formic acid", J. Power Sources, corrected online publish, 2005.

CHAPTER 2

BASICS ON MECHANISM OF NANOPARTICLE FORMATION, IONIC LIQUIDS, MICROWAVE AND POLYOL PROCESS

2.1. Introduction

In addition to the application for low temperature fuel cells, various synthesized carbon- or metal oxide-supported transition metal catalysts have a wide application window which includes energy generation/storage systems such as supercapacitors, rechargeable batteries and hydrogen generation and hydrogen storage. In this research, unsupported and carbon supported precious metal nanoparticles have been synthesized by microwave dielectric heating process of metal precursors in a polyol solution in the presence of a room temperature ionic liquid, which is a fast, simple, cost-effective, and consistent to produce very fine metal particles. Hence, a review of the formation mechanism of metal nanoparticles, the microwave heating process, the role of the polyol, and ionic liquids are necessary to understand the results of this research.

2.2. Formation Mechanisms of Nanostructured Metal Particles

All existing techniques for producing nanostructured metallic particles can be grouped into top-down methods [1, 2], phase transformation methods [3], or bottom-up methods [4, 5]. The top-down method consists of reducing the size of bulk metals to the desired dimensions of metal particles. Mechanical grinding of the solid metals and high vacuum sputtering are the representative techniques of the top-down methods. Although it is difficult to obtain monodispersed metal particles especially when high loading is needed and to achieve a uniform composition among different metal nanoparticles for specific applications, this method is convenient for rapid screening of mixed metal catalysts [6]. The phase transformation method is to convert finely divided metal compounds into metal through mostly thermolysis or pyrolysis. This process is useful to

obtain the uniform metal particles of different shapes. The bottom-up method is the wet chemical reduction of metal salts or the decomposition of metastable organometallic compounds. The metallic particles are constructed from the metal atoms. The nucleation, particle growth, and the interaction between particles in this process can be controlled in a liquid to generate monodispersed metal nanoparticles. Thus, this wet chemical, bottom-up process is the most versatile, economical, and easiest to perform procedure [7].

The general mechanism for the synthesis of nanosized metallic particles will be discussed in this section. Another objective of this section is to describe briefly how the mechanism can be manipulated to control the size, shape, composition, structure, and surface properties of metal nanoparticles as well as their dispersion.

2.2.1 General Mechanism

The successive process for the formation of metallic particles by wet chemical precipitation is illustrated in **Figure 2.1**.The formation of metallic particles begins with the electron transfer from a reducing agent (R) to the oxidized metallic species (M), which reduces the metal salt to give zero valent metal atoms. The driving force of the electron transfer is related to the standard redox potentials (E^0) of the metal species and the reducing agent associated with the reaction according to the following relation.

$$\Delta G^0 = -nF\Delta E^0 \qquad (2.1)$$

where G, n, and F have the usual meaning. The reduction reaction starts only if the redox potential difference (ΔE^0) of the reducing agent with reference to the metal species becomes positive. Thus, the reducing agent should have a more negative value than that

of metallic species for the reduction reaction and the difference must be larger than 0.3V to be practical. An increase of ΔE^0 results in a more rapid generation of metal atoms in the liquid phase, leading to higher supersaturation concentration and consequently faster nucleation.

The metal atoms formed by the reduction reaction are insoluble in solution and their lifetimes are very short in solution. The metal atoms tend to quickly collide with each other or with metal ions and coalesce into clusters which are called embryos [8]. As new metal atoms are generated in the system, embryos eventually reach a critical size and form the nuclei, which are the first stable entities of the metallic phase in the system. Nucleation can be very rarely the final stage of metal particles unless extremely special precautions are taken. The number of the nuclei and its size depend on many experimental parameters such as the concentration of metal salts or complexes, redox potential of the reduction reaction, reaction temperature, the properties and the concentration of protecting agents, and the properties of solvent such as viscosity. Nuclei with diameter less than 1nm depend on the difference between the redox potential of the metal salt and the reducing agent applied and the strength of the metal-metal bonds [9]. Once formed, the nuclei undergo rapid diffusional growth to unstable primary particles (PP) by further addition of the remaining metal atoms. As more metal atoms are provided in the system, the metal atoms continuously diffuse onto the primary particles by slow diffusion to submicrometer sized metal particles or already formed particles undergo fast aggregation to form larger particles up to several micrometers.

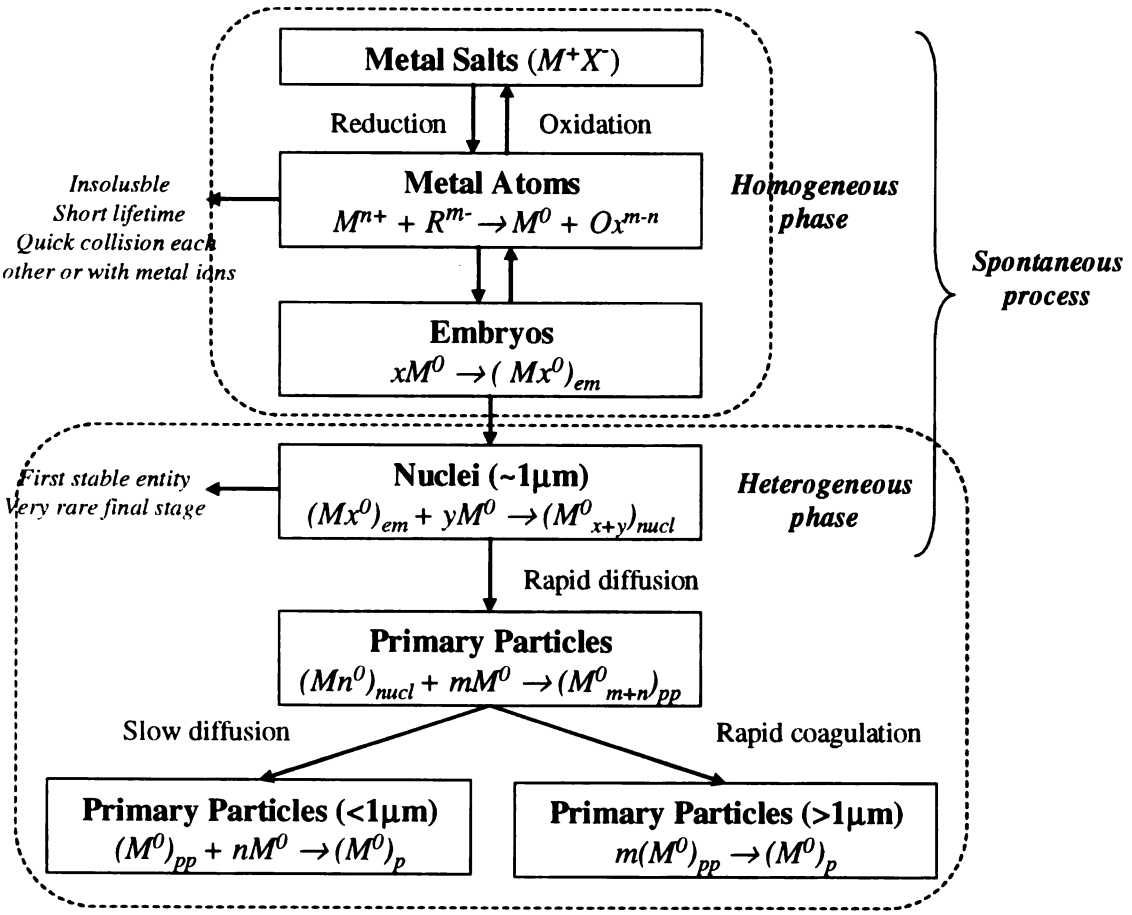

Figure 2.1. The successive process for the formation of metal particles by wet chemical reaction (modified from [10]).

It is normally expected that the monodispersed metal particles are formed by slow diffusional growth. However, it has been found that uniform metal particles are formed by the mechanism of rapid aggregation, not by slow diffusional growth which produces only amorphous metal particles [11-13]. The aggregation process must be captured in the early stage of particle formation in order to produce nanosized uniform metal particles. Capping materials such as ligands, polymers, and surfactants are frequently used to prevent agglomeration as well as stabilize nanosized metals [14-16]. Both mechanisms also have an effect on the crystallinity, internal structure, density and shape of the metal particles. The former favors the formation of metal crystal with few irregularities in their

lattice and internal grain boundary. The latter creates mostly spherical and polycrystalline metal crystals with large internal grain boundaries and low density.

2.2.2 How to Control Particle Size?

The ability of producing nanoparticles with a narrow size distribution is a key feature of modern synthetic methods. Although the kinetics of the particle nucleation from metal atoms and of the subsequent growth process can not be directly observed by physical methods, in practice, the size of metal particles can be manipulated by controlling the essential factors at the nucleation and particle growth stages for the separation of those two stages. The factors include the nature and concentration of metal salt and reducing agent [17-20], the presence of protecting agent [21], the reaction time [22], and the reaction temperature [23].

2.2.2.1 Metal salts and reducing agent

It was mentioned in previous section that there are two routes for particle growth: 1) by the attachment of metal atoms onto already formed particles and 2) aggregation of already formed particles [24]. Both mechanisms take place at the same time in a real system. The solute concentration in the nucleation stage can determine the final size of metal particles [25]. High supersaturation of metal atoms generates a large number of nuclei consuming a major fraction of the metal salts. If the aggregation is inhibited, the increase of particle size reflects diffusional growth by exhaustion of the remaining small fraction of metallic salts or complexes in solution and the final particles remain in the nanosize range. Thus, strong reducing agents are recommended to create a much large

number of nuclei if nanosized metal particles are desired. If a small number of nuclei is generated with the consumption of a small fraction of metal salts, the particle grows until the remaining large fraction of metal salts are used up and thus larger particles are produced.

The high value of ΔE affects the spontaneity of the reaction and thus the generation of nuclei. As ΔE of the reaction increase, more nuclei are generated, which lead to the smaller metallic particles. Strong agents are usually recommended. However, a large ΔE is not sufficient condition to achieve such uniform small metallic particles. Instead, other parameters which may affect the aggregation play a more important role in determining the final size of metal particles and their dispersion.

2.2.2.2. Temperature

The effect of temperature on the size of metallic particles was studied by synthesizing gold nanoparticles on carbon support and the steady-state size of the particle is related to the diffusion activation energy given by [23]:

$$R_{\max} = \frac{N_0 \sin\theta}{2\alpha\rho_s \nu} \exp\left(-\frac{E_o - Q}{RT}\right) \tag{2.2}$$

where θ is the angle that specified the degree of contact of the particle with the support, N_0 is the steady state concentration of the metal atoms on the surface, α represents the fraction of the exposed surface area, ρ_s the surface density of the particle, ν is the mean metal-metal vibration frequency ($\nu = kT_D/h$, T_D = Debye temperature), Q is the desorption activation energy. As expected in Equation (2.2), the size of metallic particles continued to increase as temperature increased until a certain range was achieved, above

which the particle size did not further increase. The nucleation of the small particles occurred at a specific temperature range which was independent of the supports and the density of the nucleation site did not increase with temperature.

2.2.2.3. Protecting agents

Ostwald ripening is the phenomenon by which larger particles attracts smaller particles during the growth process [26-28]. This agglomeration occurs at any stage during the synthesis of metal particles. To prevent the Ostwald ripening, the stabilization of metallic particles is required.

There are generally two approaches: 1) electrostatic repulsion resulting from the chemisorption of charged species (H^+ or OH^-) at the metal surface and 2) steric repulsion between particles caused by protecting agents such as surfactants, polymers, or other organics bound to the metal surface. The stabilization by steric repulsion is more common due to issues concerning the chemical stability of the metal particles at various pH values. Protecting agents play a role in stabilizing nanostructured metal particles and preventing their agglomeration [29]. In this way, protecting materials prevent aggregation and dictate the final size of metal particles.

2.3 Polyol Process

Because of its simplicity and advantage over most other wet chemical solution methods, the polyol mediated process becomes one of the most common processes to prepare nanoscaled metal and metal alloy particles. The polyols have mild reducing properties and act as solvent with a chelating effect which prevents agglomeration of

particles to some extent during their preparation. Materials obtained from this method show homogeneous phase composition and narrow size distribution. Owing to these features, the polyol process was selected as the main solvent for the synthesis of carbon-supported metal catalysts on which this research focuses. Hence, general aspects of polyol process will be briefly summarized in this section.

2.3.1. Characteristics of Polyol Process

Polyols such as ethylene glycol, diethylene glycol, triethylene glycol, or mixture of them) have the following characteristic features for synthesizing nanosized functional materials composed of noble metals (Au, Pt, Pd, Ru) [30-32], less noble metals (Fe, Co, Ni, Bi) [33-34], and other nanoscale elemental metals [35-36].

1) Metal salts and complexes are completely dissolved in the polyols due to the high polarity of the polyols (ε>30) [37].
2) Nucleation and growth of metal particles can be performed at high temperatures up to the boiling point of the polyols. Hence, well-crystallized metal particles can be synthesized [38].
3) The polyols are low weight molecules. Hence, they may act as weak stabilizers and can be removed from the surface of metal particles under mild experimental conditions [39].
4) The chelation of the solid nuclei by the polyols limits the particle growth as well as prevents agglomeration of particles [39].
5) The synthesis in the polyols is comparably easy to perform and suited for manufacturing large quantities of nanoscale materials.

Simply, the polyol-meditated process is a versatile and efficient strategy to produce nanoscale compounds and/or materials.

2.3.2 General Mechanism

At first, the polyols act as a solvent to dissolve the starting compound due to its high polarity. Subsequently, the polyols reduce the metal species and then act as the crystal growth medium for the metal particles.

The formation of metal particles in polyols has two steps [40]. In the first stage, metal hydroxide crystallizes followed by the precipitation of the intermediate phase by progressive dissolution of the starting hydroxide and evolution of water. In the second stage, the intermediate phase dissolves and then is reduced in solution, followed by homogeneous nucleation and growth of metal particles. The general mechanism of metal formation in ethylene glycol can be represented by the following reactions.

$$2CH_2OH - CH_2OH \rightarrow 2CH_3CHO + 2H_2O \quad (2.3)$$

$$2CH_3CHO + M(OH)_2 \rightarrow CH_3 - CO - CO - CH_3 + 2H_2O + M \quad (2.4)$$

The reducing action of the polyols can be different for different metal species and the intermediate solid phase is not a general feature. However, the mechanism of metal particles via nucleation and growth from the solution is general regardless of meal species in polyol process.

Recently, a modified mechanism was proposed to explain the stability of noble metal particles (Pt and Ru) in ethylene glycol in the presence of OH- as follows [41].

$$2CH_2OH - CH_2OH \rightarrow 2CH_3CHO + 2H_2O \quad (2.5)$$

$$2CH_3CHO + (PtCl_6)^{-2} + 6OH^- \rightarrow 2CH_3COO^- + Pt + 6Cl^- + 4H_2O \quad (2.6)$$

In this mechanism, hydroxide ions are necessary for the generation of acetate ions which have an effect on the stabilization of noble metal nanoparticles in ethylene glycol.

2.3.3 Control of Particle Size

2.2.3.1 Particle size in homogeneous nucleation.

If the nuclei in the nucleation stage form spontaneously without the promoting effect of impurities, the nucleation is called homogeneous. The formed nuclei grow into larger particles. This growth continues as long as the meal atoms are provided by the reduction. To obtain uniform size of metal particles, as described in section 2.1.2, nucleation and growth must be completely separated. In the polyol process, the polyol itself acts as an protecting agent for coagulation to some extent.

The final size of the metal particles in polyol process can be varied by mainly controlling temperature and the content of metal compounds or salts. The particle size usually decreases as the reaction temperature increases in polyol process. If the reaction temperature is increased, the number of nuclei formed during the short nucleation stage increase due to faster dissolution of the intermediate phase and faster reduction in solution. Consequently the average particle size decreases for a given amount of precipitated metal.

When the metal compound/polyol ratio increases, the particle size significantly increases. At a given temperature, the number of nuclei generated in the short and spontaneous nucleation stage is independent of the quantity of metal compounds added to the system. When the amount of metal compounds is increased, the number of particles grown from the same number of nuclei remains constant and their size increases.

2.3.3.2 Particle size in heterogeneous nucleation

In order to separate the nucleation step from the growth step more effectively and to control the number of nuclei in a better way, two modifications have been made in the polyol process: (1) addition of external foreign particles and (2) formation heterogeneous nuclei in situ [42, 43]. An example of the former is to introduce 3nm Pd nanoparticles before the spontaneous nucleation of cobalt in an ethylene glycol-diethylene glycol mixture. Reduction of a mixture containing a metal precursor of interest with a small amount of silver nitrate is the example of latter. Because silver nitrate is easily reduced in polyols, tiny particles of silver metal form more rapidly and then act as nuclei for the subsequent growth of the metal particles.

2.4. Microwave Process

Recently, microwave dielectric heating process has been applied to organic chemistry in the presence of catalysts [44-47] and for the preparation of metallic nanostructures [48-55]. Microwave application is desired for rapid and reliable production of new organic and inorganic entities as well as for homogeneous and heterogeneous catalysis. Hence, the principle of microwave heating, the general effects created in microwaves, and the advantages of microwave heating in the synthetic process will be described in this section.

2.4.1 Fundamental Theory of Microwave

Microwaves are electromagnetic waves consisting of electric and magnetic field components. The electric field forces charged particles or materials with molecular

dipoles to start to migrate or rotate, which causes their polarization. The combined forces of electric and magnetic components in microwaves result in rapid rotation of the molecular dipoles. Since the assembly of molecules cannot respond instantaneously to the changing direction of the electric field, energy in the form of heat is generated. Heat generated from materials with the dipoles is a result from internal resistance to the rotation under microwave irradiation. The principle of microwave heating of a medium, H_2O as an example, is shown in **Figure 2.2** [56].

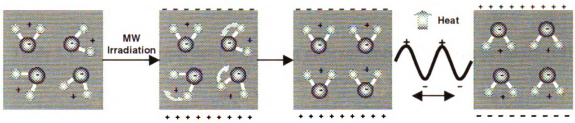

Figure 2.2. Microwave dielectric heating mechanism of H_2O [57].

The frequency of microwave for microwave dielectric heating is in the range of 918MHz and 2.45GHz. The latter is used most often and applied in domestic microwave ovens. The microwave power dissipation in a medium is given by the following equations.

$$p = 2\pi |E|^2 f\varepsilon'' = 2\pi |E|^2 f\varepsilon' \tan\delta \qquad (2.7)$$

$$\tan\delta = \varepsilon''/\varepsilon' \qquad (2.8)$$

where f is radiation frequency, ε' is the relative permittivity which is a measure of the ability of a molecule to be polarized under an electric field (E), ε" is the dielectric loss which represents the ability of a medium to convert dielectric energy to heat, and $tan\delta$ is the dielectric loss tangent or the energy dissipation factor which indicates the ability of a material to convert electromagnetic energy into heat energy at a given temperature and

frequency. The value of *tan δ* depends on the frequency of microwave, the temperature, and the physical state and composition of the mixture. It is obvious from the equations that ε" or *tan δ* is the most important parameter describing the ability of a medium to heat in microwave [58]. A medium with high tan *δ* or ε" is preferred for the reaction in microwaves. The value of ε', ε", and *tan δ* for a series of common solvents at room temperature are listed in **Table 2.1**. Ethylene glycol is one of the best solvents for the rapid synthesis of metallic nanostructures through microwave dielectric heating due to its high value of ε" compared to other solvents.

Table 2.1. Physical properties for common pure solvents at room temperature [59]

Solvent	B.p (°C)	ε'	ε"	tan δ
Dichloromethane	40	9.1	0.38	0.042
Tetrahydrofuran	66	7.6	0.36	0.047
Acetone	57	21	1.13	0.054
Ethyl acetate	77	6	0.35	0.059
Ethanol	78	24.3	4.86	0.2
Methanol	65	32.7	20.9	0.639
Dimethyl formamide	153	36.7	5.87	0.16
Methyl pyrrolidone	202	32	8.86	0.277
Ethylene glycol	198	38	44.46	1.17
Water	100	80	12.56	0.114

The rate of microwave dielectric heating depends on not only tan δ but also the size and quantity of the reaction mixture and on the heat capacity of the medium. Microwaves impinging on the volume of the mixture undergo a loss of their penetration depth into the mixture. The penetration depth (d) is related to tan δ given by the following equation [60].

$$d = \lambda_o \sqrt{\varepsilon'' / \varepsilon'} \text{ or } d = \frac{c\varepsilon^o}{2\pi f \varepsilon''} \quad (2.9)$$

where λ_o is the wavelength of the microwaves and ε^o the dielectric constant in free space.

As mentioned previously, a reaction medium or mixture should have a high $tan\delta$ for efficient absorption and consequently for rapid heating. *Tan* δ is proportional to the polarizability as well as the electrical conductivity of the reaction medium. Thus, the presence of carbon materials will be helpful to accelerate the rate of microwave dielectric heating. In addition, the strong absorbing properties of carbons reduce any possible the loss of microwave penetration into the medium when larger volume is used in the scale-up of this process.

2.4.2 Effects of Microwave Dielectric Heating

Effects of microwave dielectric heating can be divided into two kinds: thermal effects and non-thermal effects [61]. The former arise from the different temperature regime under microwave dielectric heating, the latter is caused by effects inherent to the microwaves.

2.4.2.1 Thermal Effects

1) Rapid Heating and Superheating

The factors which play an important role in microwave heating are superheating over boiling points of the medium in a large amount of ions, fast achievement of the reaction temperature, and efficient mixing and boundary effects.

Rapid microwave heating accelerates the reduction of metal salts and the nucleation of the metal cluster, which provides metallic nanoparticles with a narrow size distribution. The rate of acceleration can be further increased if microwave energy is absorbed by the reactant themselves. The uniformity of the temperature and lack of a thermal gradient is a direct result from the homogeneous microwave power dissipation through a medium and contributes to the uniform nucleation and growth conditions, leading to monodispersed metallic particles. The concerted effects of superheating and rapid and uniform heating make it possible to produce monodispersed small metallic particles with better crystallinity.

2) Hot spot and hot surface

If solids heated by microwave are present in the reaction, there are dramatic effects with respect to heating rate. Hot spots are created on the solid-liquid surfaces. Hot surface can be created on the surface of the metals or other solids by adsorption of organic materials with large polarizability. The formation of hot spots and hot surfaces accelerates the reduction of metal precursors and the nucleation of metal cluster, leading to monodispersed uniform nanostructured materials.

3) Pressure effect

The reaction yield carried out in a sealed reactor under a conventional heat was comparable to those carried out in a microwave oven. This result illustrates that the temperature effect due to the build up of pressure in the sealed reactor accounts for the effects observed during microwave heating [62].

2.4.2.2 None-thermal Effects

Non-thermal effects are ones which occur under the same temperature profiles of solvent between microwave heating and conventional heating during the reaction. There is a debate concerning if microwave irradiation of a reaction mixture induces microwave activation (non-thermal effect) or just thermal acceleration of the chemical reaction. This is a controversial issue and difficult to resolve [63].

2.4.3. Advantages of Microwave Process

The main advantages of microwave dielectric heating the synthesis of especially inorganic nanostructured materials can be summarized:

1) Microwave heating increase the kinetics of the reaction up to 1~2 orders of magnitude [64, 65].
2) Microwave heating induces uniform heating of the solution, leading to more homogeneous nucleation and a short crystallization time.
3) Microwave heating process is energy-effective due to initial rapid heating to reaction temperature [66].
4) Microwave heating creates localized hot spots at the reaction sites on the surface of the nanoparticles which enhances the reduction rate of metallic ions.
5) Microwave process is easy to control due to the absence of convection process and cost-effective.
6) Microwave process makes it possible to synthesize nanostructured materials in one-spot reaction.

7) Microwave heating process creates superheating of solvents over their boiling points which is beneficial to produce highly crystallized materials.
8) Microwave process can be adjusted to control morphologies of nanostructured materials by changing experimental factors such as the solvents, the reaction time and temperature, and the concentration of metal precursors and capping materials.

2.4.4 Microwave Process for Metal/Carbon Nanocomposites

There are many recent studies on carbon-supported noble metal or metal oxide nanoparticles synthesized by microwave-polyol process. Liu et al reported that Pt, Ru, and PtRu bimetallic nanoparticles uniformly dispersed on carbon black could be prepared by a microwave-assisted polyol process [67, 68]. The particle size of PtRu nanoparticles on carbon black was 2~6nm in diameter and they showed a higher and more durable electrocatalytic activity for methanol oxidation than a commercial catalyst. The authors concluded that the fast microwave heating accelerates the reduction of the metal precursor and the nucleation of small metal clusters, resulting in smaller particles with narrow size distribution on carbon black. It was also proposed that the surface functional groups such as carboxyl, hydroxyl, and carbonyl groups on the carbon interact with Pt and Ru ions and thus act as a nucleation precursor that finally reduced to produce PtRu nanoparticles on the carbon. The function of the carbon presence interrupting PtRu nanoparticle agglomeration was also emphasized.

Steigerwalt et al reported that PtRu nanoparticles were deposited on graphite nanofibers by using a single source molecular precursor of PtRu in microwave process [69]. They insisted that microwave heating process minimized metal diffusion on the

carbon supports and thus affords PtRu/graphite nanofiber containing 50wt. % total metal with average metal particle sizes of only 4-5nm.

Effect of pH on particle size and electrocatalytic activity for methanol oxidation was evaluated for Pt/CNT nanocomposites prepared by microwave process [70]. The mean size of Pt particles decreased with the increase of pH. Pd nanoparticles deposited on carbon black by applying microwave irradiation was also studied [71]. Depending on the Pd precursors, the size of Pd particles deposited on carbon black ranged from 8 to 10nm and from 10 to 75nm by 50s and 100s microwave irradiation, respectively. The carbon surface can be functionalized with heteroatoms such as oxygen, nitrogen and hydrogen which are sites suitable for heterogeneous nucleation of metal precursors. Carbons absorb microwave well, resulting in uniform hot surfaces and hot spots. The presence of carbon surface interrupts the growth of metal particles, preventing possible coagulation and flocculation of metal clusters. Hence, microwave dielectric heating can be employed to produce carbon-supported metal catalysts.

2.5. Ionic Liquid for the Synthesis of Metallic Particles

Ionic liquids are organic salts with low melting points and high polarity [72]. The ionic liquids are finding an increasing number of applications in catalysis [73], electrochemistry [74], polymer synthesis [75], and enzymatic reactions [76]. Another new intriguing application of ionic liquid is the synthesis of functional nanoparticles and other inorganic nanostructured materials [77]. Since ionic liquids have been used in the works for this thesis, their characteristics and synergistic effects expected when it is applied in microwave heating will be briefly described in this section.

2.5.1 Characteristics of Ionic Liquids

Ionic liquids (ILs) act as a solvent and stabilizer in the synthesis of very fine Ru and Ir metal nanoparticles [78]. The Ru and Ir system is very stable and shows high catalytic activity in catalytic hydrogenation. Thus a lot of advantages of ionic liquids for the synthesis of metallic nanoparticles can be considered.

1) ILs is classified as a kind of molten salts. While the melting points of common salts like NaCl are very high, ILs have low melting points. One important property of ILs is their low melting points due to low symmetry [79], week intermolecular interaction [80], an increasing size of anion [81], and a good distribution of charges in the cation [82]. Hence, without any special caution or pretreatment, ILs can be directly added to the polyol system and they are completely dissolved, resulting in a miscible and homogeneous ILs-polyols solution.

2) Since ILs have low surface tensions in spite of their high polarity, they can easily adsorb to other phase, which will weaken Ostwald ripening in the growth stage of metallic particle leading to the generation of very small particles. In addition, it is expected to accelerate the nucleation rate due to hot spot and hot surface effects created at the solid-liquid interface in microwave heating, resulting in the smaller particles. Low interfacial energy of ILs can be translated into stabilization of molecular or metal species.

3) ILs has high thermal stability. Some ILs is stable up to more than 400°C [83]. Hence, reactions to produce nanostructured materials can be conducted at high temperature beyond 100°C in non-pressurized reactors. Additionally,

owing to their thermal stability, ILs is not decomposed even at high temperature environment created in microwave-polyol heating process and thus has no detrimental effect on the final products.

4) High polarity of IL will increase the heating rate to desired reaction temperature in microwave process, leading to accelerate the nucleation rate of metal species and consequently produce smaller particles.

5) ILs have other unconventional and very rare properties which may be useful for the synthesis of functional materials and other inorganic materials: the ability of forming extended hydrogen-bonding and the properties as a supramolecular solvent [84]. Those features are the molecular basis of most molecular recognition and self-assembly process, which can be another application of IL-assisted microwave process.

2.5.2 Application of ILs for Metal/Carbon Nanocomposites

Metal nanoparticles should be stabilized against agglomeration into larger particles. The usual method is to use capping materials such as polymer, surfactants, or polyoxoanions for the stabilization of metal nanoparticles through electrostatic or steric repulsion. Two groups have reported the use of IL as a stabilizer and a polar solvent for wet chemical synthesis [85, 86]. Very recently, one group used a room temperature ionic liquid as a solvent for the impregnation preparation of PtRu/carbon black catalyst [87]. PtRu/carbon black catalyst synthesized with ionic liquids showed high electrocatalytic activity for methanol oxidation. The author insisted that IL can be recycled and synthetic procedure is simple compared to other impregnation methods.

In spite of advantageous features in ILs for microwave heating process, there is no report on the application of ILs to synthesize supported transition metal catalysts by using a microwave heating process. Thus, this will be an intriguing research topic.

2.6 Bibliography

1. E. Gaffet, M. Tachikart, O.El kedim, and R. Rahouadj, "Nanostructural materials formation by mechanical alloying: Morphologic analysis based on transmission and scanning electron microscopic observations", Mater. Charact., 36, p185-190, 1996.

2. K.J. Klabunde, Y.X. Li, B.J. Tan, "Solvated metal atom dispersed catalysts", Chem. Mater., 3, p30-39, 1991.

3. D.V. Goia, "Preparation of monodispersed metal particles", New J. Chem., p1203-1215, 1998.

4. E. Matijevic, "Uniform inorganic colloid dispersions. Achievements and challenges", Langmuir, 10, p8, 1994.

5. T. Sugimoto, "Preparation of monodispersed colloidal particles", Adv. Colloid Interface Sci., 28, p65-108, 1993.

6. J. H. Hodak, A. Henglein and G.V. Hartland, "Photophysics of Nanometer Sized Metal Particles: Electron-Phonon Coupling and Coherent Excitation of Breathing Vibrational Modes", J. Phys. Chem. B, 104, p9954-9965, 2000.

7. E. Matijevic, "Preparation and Properties of well defined finely dispersed metals", Faraday Discuss. Chem. Soc., 92, p229-239, 1992.

8. A. Henglein, ""Electronics of colloidal nanometer particles", Ber. Bunsenges, Phys. Chem., 99, p903-913, 1995.

9. H. Bonnemann and R.M. Richard, "Nanoscopic Metal Particles - Synthetic Methods and Potential Applications", Eur. J. Inorg. Chem., p2455-2480, 2001.

10. D.V. Goia, "Preparation and formation mechanisms of uniform metallic particles in homogeneous solutions", J. of Mater. Chem., 14, p451-458, 2004.

11. W.P. Hsu and L. Ronnquist and E. Matijevic, "Preparation and properties of monodispersed colloidal particles of lanthanide compounds. 2. Cerium(IV)", Langmuir, 4, p31-37, 1988.

12. M. Ocana, C.j. Serna and E. Matijevic, "Formation of "monodispersed" SnO_2 powders of various morphologies", Colloid Polym. Sci., 273, p681-686, 1995.

13. S.H. Lee, Y.S. Her and E. Matijevic, "Preparation and growth mechanism of uniform colloidal copper oxide by the controlled double-jet precipitation", J. Colloid Interface Sci., 186, p193-202, 1997.

14. A. Henglein, "Physicochemical properties of small metal particles in solution-microelectrode reactions, chemisorption, composite metal particles, and the atom-to-metal transition", J. Phys. Chem., 97, p5457-5471, 1993.

15. P.V. Kamat, "Interfacial charge-transfer processes in colloidal semiconductor systems", Prog. React. Kinet, 19, p277-316, 1994.

16. J.S. Bradly, J.M. Millar, E.W. Rill, "Surface chemistry on colloidal metals: a high-resolution NMR study of carbon monoxide adsorbed on metallic palladium crystallites in colloidal suspension", J. Am. Chem. Soc., 113, p4016-4017, 1991.

17. T. Teranishi and M. Miyake, "Size Control of Palladium Nanoparticles and Their Crystal Structures", Chem. Mater, 10, p594-600, 1998.

18. G. Frens, "Controlled nucleation for regulation of particle-size in monodisperse gold suspensions", Nature-Phys. Sci., 241, p20-22, 1973.

19. X. Zhai and E. Efrima, "Silver Colloids and Interfacial Colloids-Adsorption of Alizarin Yellow 2G and Its Effect on Colloidal Nucleation", Langmuir, 13, p420-425, 1997.

20. D.V. Leff, P.C. Ohara, J.R. Heath, and W. Gelbart, "Thermodynamic Control of Gold Nanocrystal Size: Experiment and Theory", J. Phys. Chem., 99, p7036-7041, 1995.

21. G. Braun and H. Bonnemann, "Enantioselective hydrogenations on platinum colloids", Angew. Chem. Int. Ed. Engl., 35, p1992-1995, 1996.

22. K. Meguro, M. Torizuka, and K. Esumi, "The preparation of colloidal precious metal particles using copolymers of vinyl alcohol-N-vinylpyrrolidone", Bull. Chem. Soc. Jpn., 61, p341-345, 1988.

23. M.B. Mohamed, Z.L. Wang, M.A. El-Sayed, "Temperature-Dependent Size-Controlled Nucleation and Growth of Gold Nanoclusters", J. Phys. Chem. A, 103, p10255-10259, 1999.

24. V. Privman, D.V. Goia and E. Matijevic, "Mechanism of formation of monodispersed colloids by aggregation of nanosize precursors", J. Colloid Interface Sci., 213, p36-45, 1999.

25. B.L. Cushing, V.L. Kolesnichenko, and C.J. O'Connor, "Recent Advances in the Liquid-Phase Syntheses of Inorganic Nanoparticles", Chem. Rev., 104, p3893-3946, 2004.

26. G. Madras and B.G. McCoy, "Ostwald ripening with size-dependent rates: Similarity and power-law solutions", J. Chem. Phys., 117, p8042-8047, 2002.

27. M. Tokuyama, K. Kawasaki, and Y. Enomoto, "Kinetic-equations for Ostwald ripening", Physica A, 134A, p323-328, 1986.

28. G. Oskam, Z. Hu, R.L. Penn, N. Pesika, and P.C. Searson, "Coarsening of metal oxide nanoparticles", Phys. Rev. E, 66, 011403, 66, 2002.

29. J.S. Bradley, in: "Clusters and Colloids", VCH, Weinheim, p469-473, 1994.

30. C. Ducamp-Sanguesa, R. Herrera-Urbian, M. Figlarz, "Synthesis and Characterization of find and monodisperse silver particles of uniform shape", J. Solid State Chem., 100, p272-280, 1992.

31. L.K. Kurihara, G.M. Chow, and P.E. Schoen, "Nanocrystalline metallic powders and films produced by the polyol method", Nanostruct. Mater., 5, p607-613, 1995.

32. E.A. Sales, B. Benhamida, V. Caizergues, J.P. Lagier, F. Fievert, F. Bozon-Verduraz, "Alumina-supported Pd, Ag and Pd-Ag catalysts: Preparation through the polyol process, characterization and reactivity in hexa-1,5-diene hydrogenation", Appl. Catalysis A, 172, p273-283, 1998.

33. G. Viau, F. Ravel, O. Acher, F. Fievert-Vincent, F. Fievert, "Preparation and microwave characterization of spherical and monodisperse $Co_{20}Ni_{80}$ particles", J. Appl. Phys., 76, p6570-6572, 1994.

34. D. Mercier, J.C.S. Levy, G. Viau, F. Fievert-Vincent, F. Fievert, P. Toneguzzo, O. Acher, "Magnetic resonance in spherical Co-Ni and Fe-Co-Ni particles", Phys. Rev. B, 62, p532-544, 2000.

35. S. Sun, C.B. Murray, D. Weller, L. Folks, and A. Moser, "Monodisperse FePt Nanoparticles and Ferromagnetic FePt Nanocrystal Superlattices", Science, 287, p1989-1992, 2000.

36. Y. Sun and Y. Xia, "Shape-Controlled Synthesis of Gold and Silver Nanoparticles", Science, 298, p2176-2179, 2002.

37. D.R. Lide (Ed.), "Handbook of Chemistry and Physics", vol. 84, CRC Press, Boca Raton, FL, 2003.

38. C. Feldmann, "Polyol-mediated synthesis of nanoscale functional materials", Adv. Funct. Mater., 13, p101-107, 2003.

39. C. Feldmann and H.O. Jungk, "Polyol-Mediated Preparation of Nanoscale Oxide Particles", Angew. Chem. Int. Ed., 40, p359-362, p2001.

40. F. Fievet, J.P. Lagier, M. Figlarz, "Homogeneous and heterogeneous nucleations in the polyol process for the preparation of micron and sub-micron size metal particles", Solid State Ionics, 32-33, p198-205, 1989.

41. J. Yang, T.C. Deivaraj, H.P. Too, and J.Y. Lee, "Acetate Stabilization of Metal Nanoparticles and Its Role in the Preparation of Metal Nanoparticles in Ethylene Glycol", Langmuir, 20, p4241-4245, 2004.

42. M. Figlarz, F. Fievet, and J.P. Lagier, in Powder Preparation/Rapid Quenching, Proc. Int. Meeting on Advanced Materials, Tokyo 1988, p125.

43. K. Tekaia-Ehlsissen, A. Delahaye-Vidal, G. Nowogrocki, and M. Figlarz, C.R. Acad. Sci., Paris 309-II, p349, 1989.

44. P. Nilsson, M. Larhed, and A. Hallberg, "Highly Regioselective, Sequential, and Multiple Palladium-Catalyzed Arylations of Vinyl Ethers Carrying a Coordinating Auxiliary: An Example of a Heck Triarylation Process", J. Am. Chem. Sci., 123, p8217-8225, 2001.

45. A. Diaz-Ortiz, P. Prieto, and E. Vazquez, "Heck reactions under microwave irradiation in solvent-free conditions", Synlett., 3, p269-270, 1997.

46. A. Lew, P.O. Krutzik, M.E. Hart, and A.R. Chamberlin, "Increasing rates of reaction: Microwave-assisted organic synthesis for combinatorial chemistry", J. Comb. Chem., 4, p95-105, 2002.

47. D. Villemin, M. Heroux, and V. Blot, "Silanol–molybdenum hexacarbonyl as a new efficient catalyst for metathesis of functionalised alkynes under microwave irradiation", Tetrahedron Lett., 42, p3701-3703, 2001.

48. W. Tu and H. Liu, "Rapid synthesis of nanoscale colloidal metal clusters by microwave irradiation", J. Mater. Chem., 10, p2207-2212, 2000.

49. R. He, X. Qian, J. Yin, Z. Zhu, "Preparation of polychrome silver nanoparticles in different solvents", J. Mater. Chem., 12, p3783-3786, 2002.

50. M. Tsuji, M. Hashimoto, Y. Nishizawa, and T. Tsuji, "Preparation of Gold Nanoplates by a Microwave-polyol Method", Chem. Lett., 32, p1114-1115, 2003.

51. Y. J. Zhu and X.L. Hu, "Microwave-polyol Preparation of Single-crystalline Gold Nanorods and Nanowires", Chem. Lett., 32, p1140-1141, 2003.

52. F. Liu, Y. Chang, F. Ko, and T. Chu, "Microwave rapid heating for the synthesis of gold nanorods", Mater. Lett., 58, 373-377, 2004.

53. R. Harpeness and A. Gedanken, "Microwave Synthesis of Core-Shell Gold/Palladium Bimetallic Nanoparticles", Langmuir, 20, 3431-3434, 2004.

54. I. Pastoriza-Santos and L. Liz-Marzan, "Formation of PVP-Protected Metal Nanoparticles in DMF", Langmuir, 18, 2888, 2002.

55. T. Yamamoto, Y. Wada, T. Sakata, H. Mori, M. Goto, S. Hibino, and S. Yanagida, "Microwave-assisted Preparation of Silver Nanoparticles", Chem. Lett., 33, p158-159, 2004.

56. M. Tsuji, M. Hashimoto, Y. Nishimzawa, M. Kubokawa, and T. Tsuji, "Microwave-assisted synthesis of metallic nanostructures in solution", Chem. Eur. J., 11, p440-452, 2005.

57. Y. Wang, J.W. Ren, K. deng, L.L. Gui, and Y.Q. Tang, "Preparation of Tractable Platinum, Rhodium, and Ruthenium Nanoclusters with Small Particle Size in Organic Media", Chem. Mater., 12, p1622-1627, 2000.

58. E.T. Thostension and T.W. Chou, "Microwave processing: fundamentals and applications", Composite: Part A, 30, p1055-1071, 1999.

59. H.M. Kingston and S.J. Haswell, Microwave-Enhanced Chemistry: Fundamentals, Sample Preparation, Application, American Chemical Society, Washington DC, 1997.

60. J. Mijovic and J. Wijaya, "Review of cure of polymers and composites by microwave-energy", Polymer Composites, 11, p184-191, 1990.

61. S.A. Galema, "Microwave chemistry", Chem. Soc. Rev., 26, p233-238, 1997.

62. R.N. Gedye, W. Rank and K.C. Westaway, "The rapid synthesis of organic-compounds in microwave-ovens. 2.", Can. J. Chem., 69, p706-711, 1991.

63. F. Chemat and E. Esveld, "Microwave super-heated boiling of organic liquids: Origin, effect and application", Chem. Eng. Technol., 24, p735-744, 2001.

64. S. Komarneni, R. Roy, and Q.H. Li, "Microwave-hydrothermal synthesis of ceramic powders", Mater. Res. Bull., 27, p1393-1405, 1992.

65. Girnus, K. Jancke, R. Vetter, J. Richter-Mendau, and J. Caro, "Large $AlPO_{4-5}$ crystals by microwave heating", Zeolites, p15, p33-39, 1995.

66. S. Komarneni, "Nanophase materials by hydrothermal, microwave-hydrothermal and microwave-solvothermal methods", Current Science, 85, p1730-1734, 2003.

67. Z. Liu, J.Y. Lee, W. Chen, M. Han and L.M. Gan, "Physical and Electrochemical Characterizations of Microwave-Assisted Polyol Preparation of Carbon-Supported PtRu Nanoparticles", Langmuir, 20, p181-187, 2004.

68. W. Chen, J. Zhao, J.Y. Lee, and Z. Liu, "Microwave Polyol Synthesis and Characterizations of Carbon-supported Pt and Ru Nanoparticles", Chem. Lett., 33, p474-475, 2004.

69. E.S. Steigerwalt, G.A. Deluga, and C.M. Lukehart, "Rapid preparation of Pt-Ru/graphitic carbon nanofiber nanocomposites as DMFC anode catalysts using microwave processing", J. of Nanosci. Nanotech., 3, p247-251, 2003.

70. X. Li, W.X. Chen, J. Zhao, W. Xing, and Z.D. Xu, "Microwave polyol synthesis of Pt/CNTs catalysts: Effects of pH on particle size and electrocatalytic activity for methanol electrooxidization", Carbon, 43, p2168-2178, 2005.

71. D.L. Boxall and C.M. Lukehart, "Rapid synthesis of Pt or Pd/Carbon nanocomposites using microwave irradiation", Chem. Mater., 13, p806-810, 2001.

72. K.R. Seddon, A. Stark, and M. Torres, "Influence of chloride, water, and organic solvents on the physical properties of ionic liquids", Pure Appl. Chem., 72, p2275-2287, 2000.

73. J. Dupont, R.F. de Suoza, P.A.Z. Suarez, "Ionic Liquid (Molten Salt) Phase Organometallic Catalysis", Chem. Rev., 102, p3667-3692, 2002.

74. J. Fuller, R.T. Carkin, and R.A. Osteryoung, "The room temperature ionic liquid 1-ethyl-3-methylimidazolium tetrafluoroborate: Electrochemical couples and physical properties", J. Electrochem. Soc., 144, p3881-3886, 1997.

75. Y.L. Zhao, J.M. Zhang, J. Jiang, C.F. Chen, F. Xi, "Atom transfer radical copolymerization of *n*-hexylmaleimide and styrene in an ionic liquid", J. Polym. Sci., Part A, 40, p3360-3366, 2002.

76. S.V. Dzyuba, R.A. Bartsch, "Recent Advances in Applications of Room-Temperature Ionic Liquid/Supercritical CO_2 Systems", Angew. Chem. Int. Ed., 42, p148-150, 2003.

77. Y. Jiang and Y.J. Zhu, "Microwave-Assisted Synthesis of Sulfide M_2S_3 (M = Bi, Sb) Nanorods Using an Ionic Liquid", J. Phys. Chem. B, 109, p4361-4364, 2005.

78. G.S. Fonseca, A.P. Umpierre, P.F.P. Fichtner, S.R. Teixera, J. Dupont, "The Use of Imidazolium Ionic Liquids for the Formation and Stabilization of Ir^0 and Rh^0 Nanoparticles: Efficient Catalysts for the Hydrogenation of Arenes", Chem.- Eur. J. 9, p3263-3269, 2003.

79. K.R. Seddon, "Room-temperature ionic liquids: Neoteric solvents for clean catalysis", Kinetics and Catalysis, 37, p693-697, 1996.

80. A. Elaiwi, P.B. Hitchcock, K.R. Seddon, N. Srinivasan, Y.M. Tan, T. Welton, and J.A. Zora, "Hydrogen-bonding in imidazolium salts and its implications for ambient-temperature halogenoaluminate ionic liquids", J. Chem. Soc. Dalton Trans., p3467-3472, 1995.

81. H. Stegemann, A. Rhode, A. Reiche, A. Schnittke, and H. Fullbier, "Room temperature molten polyiodides", Electrochim. Acta, 37, p379-383, 1992.

82. A.A. Fannin, D.A. Floreani, L.A. King, J.S. Landers, B.J. Piersma, D.J. Stech, R.L. Vaughn, J.S. Wilkes, and J.L. Willams, "Properties of 1,3-dialkylimidazolium chloride-aluminum chloride ionic liquids. 2. Phase transitions, densities, electrical conductivities, and viscosities", J. Phys. Chem., 88, p2614-2621, 1984.

83. P. Bonhote, A.P. Dias, N. Papageorgiou, K. Kalyanasundaram, and M. Gratzel, "Hydrophobic, Highly Conductive Ambient-Temperature Molten Salts", Inorg. Chem., 35, p1168-1178, 1996.

84. A. Mele, C.D. Tran, and S.H.D. Lacerda, "The Structure of a Room-Temperature Ionic Liquid with and without Trace Amounts of Water: The Role of C—H···O and C·····H···F Interactions in 1-*n*-Butyl-3-Methylimidazolium Tetrafluoroborate", Angew. Chem., Int. Ed., 42, p4364-4366, 2003.

85. H. Itoh, K. Naka, Y. Chujo, "Synthesis of Gold Nanoparticles Modified with Ionic Liquid Based on the Imidazolium Cation", J. Am. Chem. Soc., 126, p3026, 2004.

86. J. Dupont, G.S. Fonseca, A.P. Umpierre, P.F.P. Fichtner, and S.R. Teixeira, "Transition-Metal Nanoparticles in Imidazolium Ionic Liquids: Recycable Catalysts for Biphasic Hydrogenation Reactions", J. Am. Chem. Soc., 124, p4228-4229, 2002.

87. X. Xue, T. Lu, C. Liu, W. Xu, Y. Su, Y. Lv, and W. Xing, "Novel preparation method of Pt–Ru/C catalyst using imidazolium ionic liquid as solvent", Electrocimica Acta, 50, p3470-3478, 2005.

CHAPTER 3

CARBON SUPPORTED METAL CATALYSTS

3.1. Introduction

Catalysis is of vital importance to not only fine chemical industry but also fuel cell industry and hydrogen economy. Most chemical processes need a catalyst and electrochemically active catalysts are inevitable in fuel cell systems. Many techniques of producing hydrogen from renewable and sustainable resources are conducted only with the addition of a specific catalyst.

Solid supported catalysts are of special interest. A high activity of a catalyst calls for a large active surface area and high dispersion of the active phase. Small metallic particles meet these requirements. However, small particles tend to easily sinter at relatively low temperature. This problem is resolve by applying small particles onto the support surface. As a result of decorating the surface of the support with small metallic particles, they can be thermally stable and maintain a high specific surface are up to high temperature [1]. Supports allow for the fine dispersion and stabilization of metallic particles, making it possible for the reactant to access to a much larger number of catalytically active sites than in the corresponding bulk metals.

Catalytic activities of a supported catalyst depend on a number of factors: the size and shape of metallic particles and the specific surface area, pore size distribution, pore volume, density of supports. Mechanical and electrical properties of supports are also an important factor. Another critical factor which must be taken into account in most catalyzed reactions is the interaction between metallic particles and supports. Due to this interaction, the catalytic performance strongly depends on a complex contribution of the dispersion of the active phases and the changed electronic properties of the metal [2].

Hence, a survey of the literature was focused on supported catalysts, especially carbon-supported precious metal catalysts, for they are a key material in a fuel cell system, and can be applied for other next generation energy/power sources. In this section, the basic principles of catalyst synthesis including the surface chemistry of the carbon supports and interaction of the carbon surface with the metal precursor are reviewed. Synthetic routes for carbon-supported metal catalysts are also summarized, followed by catalyst design and recent trends of carbon-supported catalysts.

3.2 Basic Principles of Catalyst Synthesis

Support materials are selected on the basis of desirable characteristics such as inertness, stability, porosity, surface area, mechanical properties, and physical form [3]. Among a variety of possible supports, only three materials meet these characteristics, which are alumina, silica, and carbons. Carbons are more convenient than alumina and silica because of their resistance to acidic or basic media, stability at high temperatures, low cost compared to other supports, easy recovery of metals from spent catalyst by burning away the carbon support, and surface flexibility for tailoring catalyst properties to specific needs [4].

Properties of carbons which are of importance to catalyst preparation and application include composition, particle size, shape and distribution, surface area, functional groups, pore shape and size distribution, microstructure, oxidation and corrosion resistance, electrical conductivity and hydrophobicity [5]. Mineral composition and content are dependent on the raw material source. This will affect the hardness of the carbon, the surface area, the redox properties and the acid/base properties. Particle size, shape and

distribution can affect filterability and filtration rate as well as catalyst activity. Surface area, surface groupings, pore size distribution and pore shape affect catalyst preparation and catalyst activity. Oxidation and corrosion resistance, electrical conductivity and hydrophobicity are of great importance for fuel cell catalyst application.

The chemical inertness of carbons can sometimes be a disadvantage which makes it difficult to deposit metal particles. Thus, the surface chemistry of carbons needs to be changed in order to improve the interaction between metals and carbons [6].

3.2.1 Surface Chemistry

The carbon surface is inert but not as inert as expected. The carbon surface has active sites which consist of unsaturated valences at the edges and defects of graphene layers. Heteroatoms such as nitrogen, hydrogen and oxygen on the carbon surface are also active sites. Among them, oxygen groups are the most important groups influencing the synthesis of carbon-supported catalysts. Several oxygen groups on the carbon surface are shown in **Figure 3.1** [7]. The portion of oxygen groups can be increased by the treatment with oxidizing gas or liquids or decreased by heat treatment in inert atmosphere. The oxygen groups provide chemical reactivity toward the metal precursor. Physical interaction with the metal precursor is also possible due to the amphoteric character of carbon. However, the chemical accessibility of the metal precursor to the oxygen groups is more important in obtaining maximum dispersion of active sites and the catalytic activity of supported catalysts [8].

The oxygen groups on the carbon surface can be divided in acidic, neural and basic. Carboxyl, quinone, and lactone groups are acidic. Due to their negative charge, they

improve the interaction between the carbon surface and positively charged metal precursor. The metal precursor in aqueous solution can easily access the carbon [9, 10]. Phenol, carbonyls, and ethers are weekly acidic to neutral. These groups increase the interaction of the metal precursor or metal particles with the carbon, leading to reduce sintering of metallic particles [10].

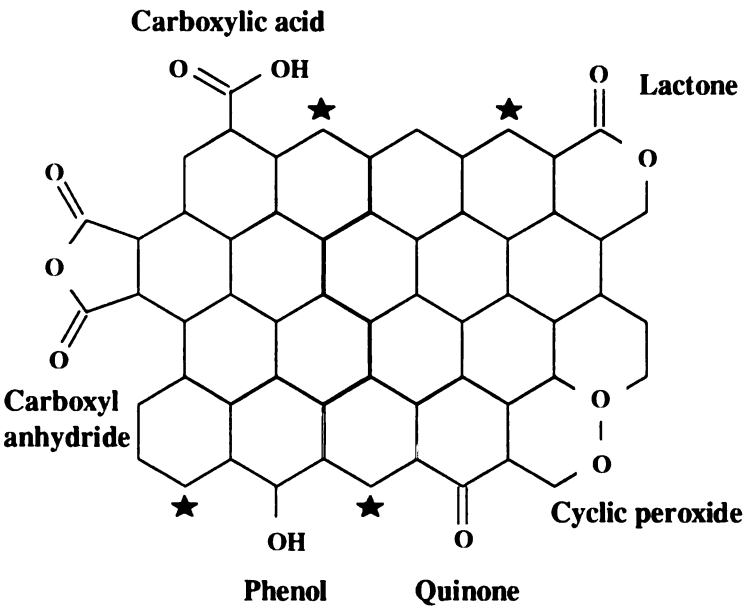

Figure 3.1.Surface groups containing oxygen and localized π sites (★) on a graphene layer.

Heat treatment of the carbon in inert atmosphere further graphitizes it, increasing crystalline order and crystallite size. The basicity of the carbon is also increased, which can not be explained by the creation of basic groups [11]. The basicity of carbon surface mostly originated from the delocalized π sites and the localized π sites. The former is on aromatic systems corresponding to the basal plane of the carbon and the latter is created in between two non-neighboring oxygen atoms mostly at the edge of the carbon. The delocalized π electrons have a great effect on the basicity of the carbon because the

surface area of the basal plane is much larger than that from the edge. Nitrogen can be introduced onto the carbon surface by treating the carbon with ammonia at high temperature [12]. It was found that the carbon with nitrogen increase the activity of the metallic particles [13]. Amide, imides, and lactams can be created and converted to pyridines in an inert atmosphere at higher temperature.

3.2.2 Surface – Precursor Interaction

The oxygen surface groups and π sites on a carbon surface play a very critical role in interactions between a carbon surface and a metal precursor and consequently in the interaction of metallic particles with the carbon support.

The π sites on the carbon support also act as anchoring sites for the metal particle. The basal plane of graphite with its planar structure along the c-axis contains a number of delocalized π electrons as shown in **Figure 3.2**. The strong interaction between a metal atom and the π sites on the xGnP is the reason that exfoliated graphite nanoplatelets (xGnP) are expected to be decorated by the metallic particles. The π sites on the carbon basal plane interact with water, followed by the electrostatic attraction with the metal ions as follows [14]:

$$C_\pi + 2H_2O \leftrightarrows C_\pi H_3O^+ + OH^- \qquad (3.1)$$

$$C_\pi H_3O^+ — MCl_6^{-2} \ (M = Pt, Pd...) \qquad (3.2)$$

C_π represents surface carbon with delocalized π electrons. As a result of this reaction, the dispersion of metallic particles and the interaction between metallic particles and the carbon are increased, leading to the increase in the resistance to sintering of the metallic

particles [15]. As the strength of the π sites on the support increases, the probability of smaller and well-dispersed metal particles on the carbon increases [16].

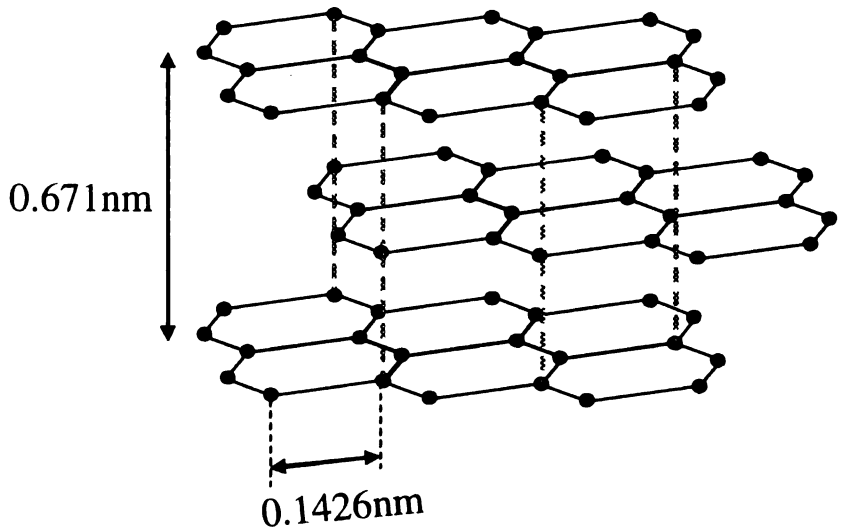

Figure 3.2. Three dimensional schematic of layered graphite structure (•: carbon atom).

The oxygen groups make the carbon surface more hydrophilic and thus the metal precursor in polar solution can easily access to the carbon as mentioned in the previous section. This means that the more oxygen groups are created on the carbon, the more metal ions interact with it. The oxygen groups act as anchoring centers for the metal ions. However, after the complete reduction of the metal precursor, the dispersion of metallic particles decreases as the oxygen content on the carbon surface increases [17]. After the metal-organic compound reduction, the oxygen groups have a detrimental effect on the interaction between the metallic particles and the carbon support. Sintering of the metallic particles easily takes place regardless of the high initial dispersion of the metal ions, resulting in larger particles with worse dispersion.

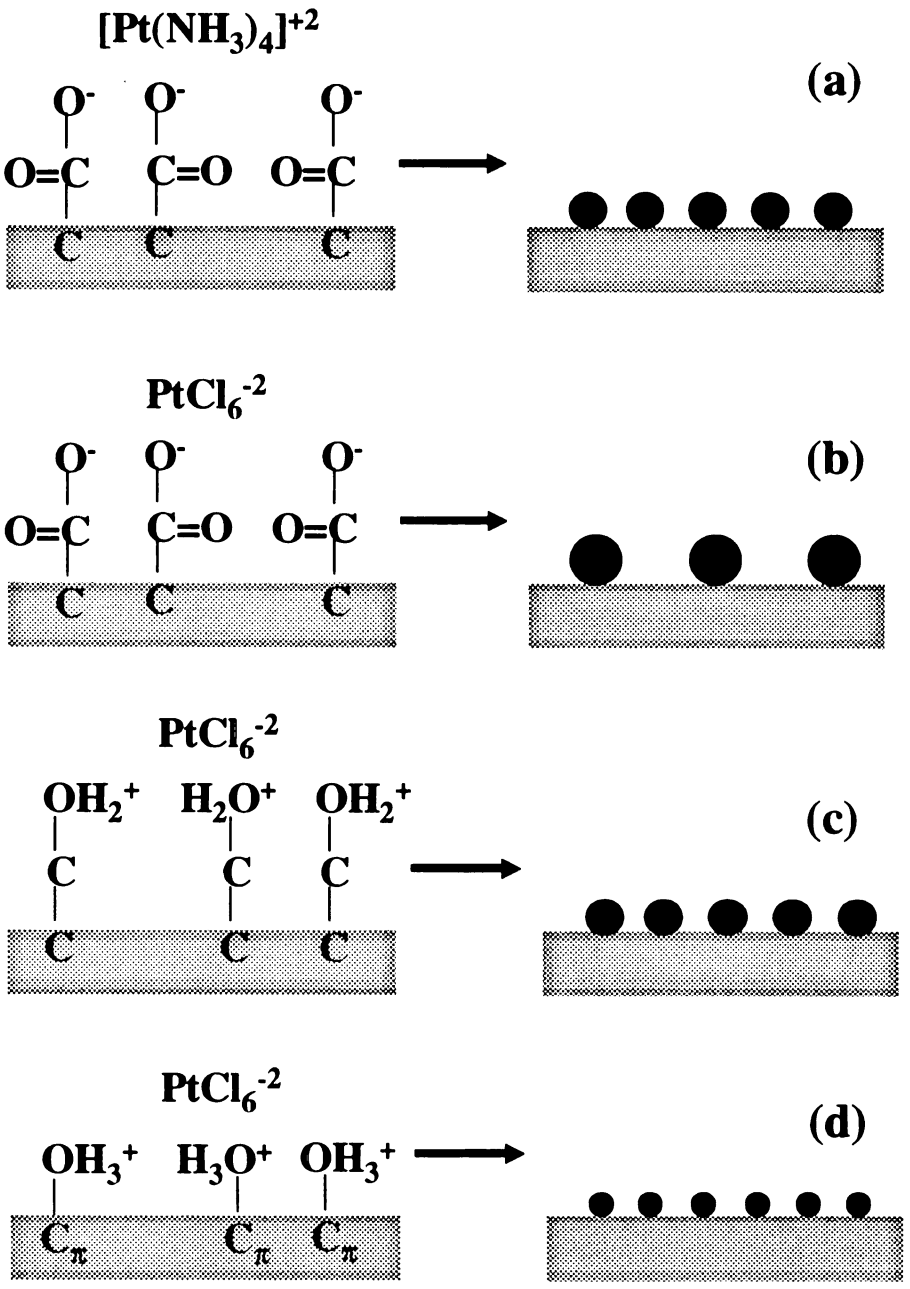

Figure 3.3 Schematic representing the common interactions between the active sites of a carbon surface and metal ions and their effect on particle size and distribution.

The possible interactions between the metal ions and the oxygen functional groups on the carbon and the formation of metal particles after the complete reduction reaction

carbon surface groups are illustrated with Pt precursors as an example in **Figure 3.3**. If the acidic oxygen groups are dominant on the carbon surface, the metal cations are preferred to the metal anions to produce fine and well-dispersed particles. In contrast, the metal anions are preferred in the case of the carbon support which is abundant with basic groups or delocalized π sites. Fine metal particles widely dispersed can be achieved by either increasing the π sites on the basal plane of the carbon to increase the electrostatic attraction with the metal anion or by oxidizing the carbon which will favor the electrostatic attraction with the metal cations.

3.3 Synthetic Routes of Carbon-Supported Catalysts

The preparation procedure of supported metal nanoparticles can also be divided into physical or chemical methods. High vacuum sputtering is a representative example of the former method. Although it is difficult to obtain the dispersion of metal particles with a narrow size distribution especially when high loading is needed and a uniform composition is required among different metal particles for supported bimetallic particles, this method is convenient for rapid screening of supported mixed metal catalysts compared to the chemical methods [18].

A number of examples for chemical methods have been applied for the synthesis of supported catalysts as listed in **Table 3.1**. Chemical changes of a metal precursor either in an ionic or a molecular state are initiated by reducing the metal precursor to metal atoms, which then grow to form the metal particles. The chemical synthesis of the metal particles from the metal precursor dissolved in an aqueous or organic liquid is usually affected by the introduction of a reducing agent. This wet chemical routes can be initiated

by physical mixing, microwave irradiation [19] or, radiolytic [20], sonochemical [21], or electrochemical [22, 23] methods.

Table 3.1 Examples of chemical method for synthesis of carbon-supported metal particles

Metals	Supports	Loading (%)	Size (nm)	Method	Precursor	Ref.
Pt	CNT[a]	10	2 ~ 5	Colloid	H_2PtCl_6	24
		12 ~13	2 ~ 4	Colloid	K_2PtCl_4	25
	CB[b]	20 ~ 60	2 ~ 3	Radiolytic	H_2PtCl_6	26
		40	2.9	Colloid	H_2PtCl_6	27
	SWNH[c]	20 ~ 40	2	Impregnation	H_2PtCl_6	28
PtRu	CNT		1.5 ~ 1.6	Impregnation	H_2PtCl_6, $RuCl_3$	29
	CB	40	4 ~ 20	Microemulsion	H_2PtCl_6, $RuCl_3$	30
	CB	10 ~ 90	3 ~ 15	Impregnation	$Na_6Pt(SO_3)_4$, $Na_6Pt(SO_3)_4$	31
	GNF[d]	50	4 ~ 5	Microwave	$(\eta\text{-}C_2H_4)ClPt(\mu\text{-}Cl_2)RuCl$	32
	GNF	42	7	Impregnation	$(\eta\text{-}C_2H_4)ClPt(\mu\text{-}Cl_2)RuCl$	33
	CNC[e]	60	2.3	Colloid	H_2PtCl_6, $RuCl_3$	34
PtSn	CB	20	3 ~ 4	Impregnation	Pt/C, tetrabutyltin	35
PtCr	CB	20	3 ~ 4.5	Impregnation	Na_2PtCl_6, $CrCl_3$	36
Pd	CNF[f]	2.5	4	Deposition-reduction	$Pd(NH_3)_4Cl_2$	37
	CB, Gr[g]			Deposition-reduction	K_2PdCl_4	38

[a]Carbon Nanotube, [b]Carbon Black (Vulcan XC-72R), [c]Single-Wall Carbon Nanohorn, [d]Graphite Nanofiber, [e]Carbon Nanocoil, [f]Carbon Nanofiber, [g]Graphite.

As explained in the previous chapter, the metal atoms collide to form a nucleus in the early stage of wet chemical processes. Nuclei that grow beyond a critical size are stable, but a mechanism is needed to control the growth of particles and to achieve a narrow size distribution. The addition of a support or a capping material prevents particle growth. Depending on the growth control mechanism and strategies, chemical methods to

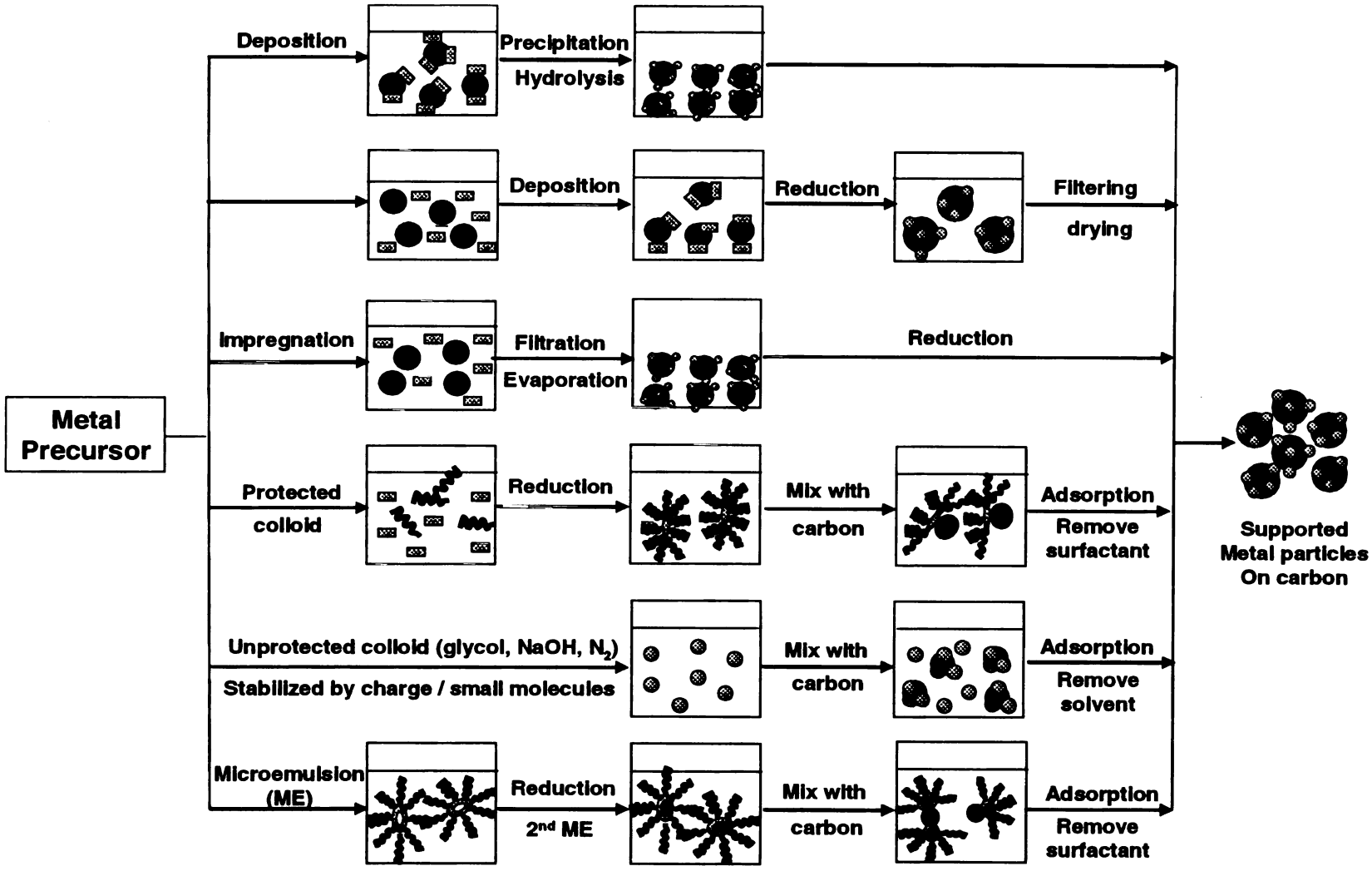

Figure 3.4. Simplified procedures for chemical routes to prepare supported metal particles (modified from [39])

synthesize supported metal catalysts can largely be divided into five categories such as deposition-precipitation, deposition-reduction, impregnation-drying, colloid method and microemulsion. Thus, the discussion on these five synthetic routes will be of use to understand distinct differences in the strategy of the growth control of metal particles supported especially on the carbon materials. **Figure 3.4** shows schematic procedure for those chemical routes.

3.3.1 Deposition-Precipitation

Carbon supports are pretreated with an oxidizing agent in order to introduce oxygen surface groups, followed by the induction of $M(OH)_2$ (M = Pd, Pt, Ru, ...) resulting from alkaline hydrolysis of a metal halide precursor and the reduction of the precipitated $M(OH)_2$ with an reducing agent [40]. Normally, the reduction by hydrogen results in higher metal dispersion in a range of 50 ~ 70 %.

3.3.2 Deposition-Reduction

Procedures of this method are very similar to those of deposition-precipitation method. They consist of 5 steps: 1) pretreatment of carbon supports with an oxidizing agent, 2) suspension of the treated carbons in distilled water, 3) addition of an aqueous solution of a metal precursor, 4) reduction of metal ions by adding a reducing agent into the system, and as a final step, 5) filtration of the suspension. The catalyst obtained is dried in an inert atmosphere at room temperature or an elevated temperature. In order to avoid sintering of metal particles, the catalyst must be heated slowly. This method is an appropriate method for carbon supports with wide pores due to the fast reduction reaction [41]. For carbons with smaller pores, the impregnation-drying method is preferred.

3.3.3 Impregnation Method

This method is simple and the most common. A dissolved metal precursor is absorbed into the pores of a carbon support and any liquid phase is removed by evaporation, followed by reduction to produce supported metal particles dispersed on a support. The reduction step can be chemical or electrochemical. Hydrazine, borohydride, formic acid and hydrogen are used as the common reducing agents. The pore size distribution and the morphology of the substrate play an important role in penetration of the precursor into the support and also providing the confinement for metal particle growth. Reaction time and kinetics and mass transfer of the reducing agent affect the nucleation and growth of the nanoparticles. In the case of the electrochemical reduction, the growth of the particle can be controlled by the amount of current. The major drawback of this method is the lack of size control of metal particles except for porous substrates with a narrow pore size distribution, e.g. in highly ordered mesoporous carbon [42].

3.3.4 Colloid Method

The metal precursor is chemically reduced to form metal nanoparticles in the presence of a protective agent like PVA, PVP, PPh_3, and NR_4^+. A narrow size distribution is achieved as the colloidal metal particles are stabilized either by steric hindrance or by electrostatic charges. Steric stabilization is provided by coating the metal core with organic molecules. On the other hand, protection from aggregating into larger particles is provided by the electrostatic repulsion of like charges in the case of adsorbed ions or charged colloids. Though a narrow size distribution of metal nanoparticles is obtained

from this method, the major drawback is the presence of the protecting agent hindering the catalytic activity of the nanoparticles.

An alternative route of preparing metal particles without the use of protecting agents was developed. This is achieved for certain metals by proper combination of precursor, solvents, reducing agent and electrolytes. The use of sodium hydroxide dissolved in ethylene glycol as a solvent as well as protecting agent is a representative example [43]. The glycol is removed by electro-oxidation during usage as an anode or by decomposition at 160°C. The size and dispersion of metal particles is controlled by the process parameters, e.g. pH and water concentration. This glycol colloidal process is appropriate for large-scale synthesis of metal nanoparticles.

3.3.5 Microemulsion

This method offers unique flexibility in the simultaneous control of size and composition of mixed metal nanoparticles. The microemulsion is uniformly dispersed in a continuous medium, which is immiscible with the precursor containing liquid phase. Normally, oil and water are a dispersed liquid phase and a continuous medium, respectively. The introduction of a reducing agent into the microemulsion is achieved by stirring. The chemical reaction is confined within a microemulsion which is a tiny drop of precursor containing liquid engulfed by surfactant molecules. Since chemical reaction takes place within the microemulsion, a narrow particle size distribution can be obtained. After the reduction step, nanoparticles are protected from agglomeration by the surfactant molecules. Similarly to the colloidal method where protecting agents are used, the nanoparticles should be adsorbed onto a porous support before the surfactant molecules

are removed. The size distribution of metal particles can be further controlled and improved by a two-component microemulsion method with the reducing agent confined in a separate emulsion [44, 45]. The final composition of the mixed metal nanoparticles can be easily controlled by the ratio of the metal precursor solutions. Nevertheless, the microemulsion method requires the use of costly surfactant molecules with extra washing steps and thus is not economical for a large scale synthesis.

3.4 Requirements of Carbon Support

The properties of carbon-supported catalysts are affected by those of carbon supports. The carbons with high surface area are necessary for a high dispersion of metal catalysts, excellent crystallinity, a pore structure suitable for maximum contact with reactants and release of byproducts and good interaction with metal particles are generally required. Other properties of carbon supports required especially for fuel cell application are surface inertness in a strongly oxidizing environment, good electrical conductivity to facilitate electron transport, and availability at low cost [46, 47].

High surface area and a well developed porosity are essential for accomplishing large metal dispersion, which usually, but not always, results in a high catalytic activity. However, there are many examples showing that neither dispersion nor catalytic activity is a function of the porosity and surface area of the carbon support. One of such examples is the result of Rodriguez-Reinoso et al. which showed that iron loading on the carbon support is a function of the metal precursor used, showing the access of the metal solution was related not just to the increasing porosity of the carbons, but also to the chemical character of its surface and its interaction with the different solutions [48]. On the other

hand, the surface area of carbon supports influences their corrosion rates in an oxidizing environment. Carbons with the higher surface area show higher corrosion rates [49]. Thus, although carbons with high surface area are good for high loading and dispersion of metal catalysts, they may have a detrimental effect on long-term stability of fuel cell system.

Surface inertness or corrosion resistance of carbon supports in an oxidizing environment means that carbon materials must be highly graphitized. Less graphitized carbons have a wider interlayer spacing and poorer alignment than graphitized ones. This less aligned carbons is more reactive to oxidation and corrodes from the inside outwards [49]. Thus, most carbon supports must be graphitized especially for fuel cell cathode to which oxygen or air is supplied.

Excellent electrical conductivity is a major requirement of carbon supports for fuel cell application. Although the graphitization of carbons can result in a decrease of their electrical conductivity, their variation is not wide [50]. Hence, if carbons have inherently high electrical conductivity, their electrical properties are not an important factor to be considered before any treatment to optimize carbon properties.

Well-adjusted carbon properties can contribute to improve the performance of fuel cell system through enhanced catalytic activity of carbon-supported catalysts. However, significant advances have been made in the performance of fuel cell catalysts by combining well characterized, corrosion resistant, graphitic carbon supports with platinum based metal or metal alloy electrocatalysts.

3.5 Catalyst Design – Metal location

The size of metal particles deposited on a support affects the performance of a heterogeneous catalyst. In general, increased metal dispersion and decreased metal particle size result in increased catalytic activity. The size of a reactant is also considered. If the reactant is bulky, the higher catalytic activity is obtained from the catalysts with the metals located on the external surfaces. The other important factor which has an effect on the catalytic performance of a supported catalyst is the location of metal particles on the support material [51]. This is related to the effect of pressure and temperature in reaction systems. If the metal is deposited within the pore structure (intermediate and interior locations), it will not all be accessible to reactants at low pressure and thus a surface-loaded catalyst is preferred. As the pressure increases, an increasing proportion of the metal will become accessible and thus exhibit a higher activity than the catalyst with metal deposited only on the external surface. Consequently, when operating a catalytic system free from mass transport limitations and catalyst poison, one would choose a catalyst with an exterior metal location at low pressure, an intermediate location at medium pressure and an interior location at high pressure. The effect of metal location on thermal sintering resistance must be considered for the reaction carried out at different temperature. At higher temperature, catalysts with an interior metal location have the greatest sintering resistance and show higher activity.

Catalysts can be designed with different metal locations for reactions which take place under different conditions of pressure and temperature. Exterior location of metal particles on carbon supports is preferred in fuel cell systems because they are operated at

low pressure and low temperature. xGnP may be an excellent carbon support for fuel cell applications because it generates the highest surface-loaded catalyst.

3.6 Examples of Catalysts Supported on New Carbon Nanostructures

Recently, new carbon forms such as graphite nanofibers (GNF) and carbon nanotubes (CNT), carbon nanohorn and carbon nanocoil have attracted a great deal of attention as catalyst supports in fuel cell electrodes to replace the classically used carbon black [52~56] because they are believed to be breakthrough materials for energy storage, electronics, and catalysis due to their exceptionally high adsorption, electronic, mechanical and thermal properties.

3.6.1 Graphite Nanofiber (GNF)-Supported Catalysts

GNF consists of extremely small graphite platelets perfectly arranged in various orientations with respect to the fiber axis, giving rise to assorted conformations. Depending on the morphology of the graphite layers, there are four types of GNF: 1) *herringbone* structure (H-GNF) where the graphite layers are stacked obliquely in respect to the growth axis, 2) a *platelet* GNF (P-GNF) where the layers are oriented perpendicular to the fiber axis, 3) a *spiral* GNF (S-GNF) where the graphite platelets in the helical nanofibers are oriented parallel to the fiber axis, and 4) finally a *ribbon-like* form (R-GNF) where the platelets are aligned parallel to the fiber axis [57, 58].

GNF-supported platinum or platinum/ruthenium catalysts have been synthesized by the impregnation method [59~61] and the combination of impregnation and microwave irradiation [62]. The results of their performance as anode catalysts of DMFC prove that,

as metal supports in fuel cell electrodes, GNF can replace the classically used carbon blacks. Catalysts consisting of 5wt. % platinum supported on P-GNF and R-GNF exhibited activities comparable to that displayed by about 25wt. % platinum on Vulcan carbon black. While P-GNF and R-GNF supports showed 400~500% improvement in the current yield compared to the Vulcan carbon support, H-GNF-supported Pt exhibited much less electrocatalytic activity toward methanol oxidation. The superior catalytic reactivity of GNF-supported Pt over Vulcan-supported Pt results from (1) increased electrical conductance of the GNF, (2) decreased impurities, (3) efficient mechanism for the removal of the adsorbents, and (4) interaction between the highly ordered GNF substrate and crystallographically oriented platinum particles.

The fuel cell performance of GNF-supported Pt-Ru catalysts was compared with SWNT- and MWNT-supported ones. The highest performance was achieved when Pt-Ru catalyst on narrow tubular H-GNF was used. An enhancement of up to ~64% relative to that recorded for an unsupported Pt-Ru colloid anode catalyst of similar surface area was reported. The samples having some degree of Ru metal phase separation from Pt-Ru alloy have given the highest electrocatalytic performances. Relatively small particle sizes were measured on all supports even at very high meal loading (40~60wt. %). Surprisingly, a low surface area was reported for SWNT ($109 m^2/g$) and especially MWNT ($8 m^2/g$) that could be related to the poor quality of the materials. No explanation for these different behaviors has been proposed. The use of microwave irradiation process in synthesizing makes it possible to develop larger-scale preparations of metal carbon nanocomposites without the expense of catalytic reactivity.

3.6.2 Carbon Nanotube (CNT)-Supported Catalysts

Many studies as to the synthesis of CNT-supported catalysts and their application in heterogeneous catalysis have been reported. Li and coworkers [63, 64] explored oxidized CNT as supports for platinum catalyst in order to solve the slow reaction rate of the cathode oxygen reduction reaction (ORR) in DMFC. They obtained Pt/CNT catalyst with a metal loading of 10 wt. % by chemically reducing chloroplatinic acid in ethylene glycol. The average diameter of Pt ranges from 2~4nm. The results show that CNT as supports for cathode catalyst in a direct methanol single cell produces better performance compared to XC-72 carbon black (CB). The increase in ORR activity of Pt/CNT over Pt/CB is attributed to (1) the unique structure and better electrical properties of CNT, (2) a small amount of organosulfur impurities of CNT, and (3) the specific interaction between Pt and CNT. Matsumoto et al [65] also investigated the cell performance with two electrodes comprising Pt/CNT catalyst fabricated by chemical reduction of K_2PtCl_4 in ethanol. The Pt content was estimated to be ~12wt. %. This 12wt. % Pt-deposited CNT electrode showed 10% higher voltages than a 29 wt. % Pt/CB and reduced the Pt usage by 60% in polymer electrolyte fuel cells with hydrogen and oxygen. The results indicate the importance of the high conductivity of supports for high performance with a low Pt load. High population of the triple-phase boundary (gas-electrolyte-electrode) of Pt/CNT catalyst is another contribution for higher efficiency over Pt/CB with multiple-phase boundary. Platinum nanoparticles 1~5nm in diameter were deposited onto MWNT by an electroless plating procedure [66]. The surface of MWNT was functionalized by HNO_3 and $K_2Cr_2O_7/H_2SO_4$ before the deposition. The electrode comprising this Pt/MWNT catalyst showed higher electrocatalytic activity for ORR in a single stack fuel cell test.

Template method was applied to prepare Pt/MWNT and Pt-Ru/MWNT catalyst which is tested as the anode [67]. The current density of methanol oxidation for a Pt supported on MWNT membrane electrode was found to be 20 times higher than that of a bulk platinum electrode. This material can also be used to electrocatalyze ORR. It is found that the electrochemical activity follows the order: Pt-WO_3/CNT > Pt-Ru/CNT > Pt-Ru/CB > Pt/CNT > Pt/CB > bulk platinum [68]. The higher electrochemical response of CNT based materials is attributed to the higher available electroactive surface area.

3.6.3 Other Carbon Nanomaterials-Supported Catalysts

Single-wall carbon nanohorns (SWNH) which are a new type of carbon materials having a horn-shaped sheath of single-wall graphitic sheets were used as a support material for Pt deposition to demonstrate the suitability of its application for the electrodes of Polymer electrolyte membrane fuel cell [69]. Pt oxide colloids were adsorbed on the SWNH surface and dried and reduced in H_2. Pt particle size was about 2nm which was less than half of that supported on the conventional CB. The current density for the SWNH cell was larger than that for the CB cell.

The electrocatalytic performance of 60wt. % PtRu alloy catalysts supported on newly synthesized carbon nanocoil (CNC) with excellent crystallinity and large surface area was reported [70, 71]. CNC composed of nanometer-thick graphitic fibers was synthesized by simple heat treatment of mixtures of a carbon precursor, silica, and a transition-metal salt. Resorcinol-formaldehyde sol and Co/Ni salt were used as a carbon precursor and a catalyst. A silica sol was added in order to obtain high surface area carbon. Depending on the quantity of metal salts, the synthesized CNS has high surface

area varying from 200 to 500 m^2/g. In addition, the CNT has well-defined porosity which favors the diffusion of fuel and the removal of the by-product CO_2 gas. CNC-supported PtRu catalyst showed excellent electrochemical stability over the potential range of the methanol oxidation process for DMFC and a capacitance over ten times higher than that of Vulcan XC-72R CB. The current density ($20mAcm^{-2}$) of the CNC-supported catalyst was four times higher than that ($5mAcm^{-2}$) of Vulcan CB. The maximum power density of the CNC-supported catalyst was 150% higher than the Vulcan CB. The remarkably enhanced performance of this catalyst is attributed to the high electrical conductivity, the high surface area, and the high crystallinity of CNC and the superior dispersion of the metal catalyst on CNC.

3.7 Summary

From chapter 1 to 3, the general background of low temperature fuel cells, especially PEMFC and DMFC, the current status of the technology and the important technological challenges in electrocatalyst for PEMFC and DMFC and basic features of the direct ethanol fuel cell (DEFC) and the direct formic acid fuel cell (DFAFC) as alternative fuel cells have been described. Brief review on the formation mechanism of metal, operational principle of the microwave heating, and the role of the polyol and ionic liquids have also provided to assist understanding the results of this dissertation works. So-far developed Synthetic routes for carbon-supported metal catalysts, the surface chemistry of carbons and its effect on the interaction between carbons and metal precursors, and catalyst design and recent trends of carbon-supported catalysts appropriate for fuel cell systems have also been included.

3.8 Research Objectives

The electrocatalysts are supported on carbon materials with high surface area, high mesoporous distribution, good electronic conductivity and graphitic character. Carbon black (CB) is the most widely used carbon support for the preparation of fuel cell catalysts because it meets those requirements well. However, highly active catalysts with novel carbon material as a support have been explored in order to enhance the methanol and hydrogen oxidation in the anode and the rate of ORR in the cathode. Carbon nanotube (CNT) and graphite nanofiber (GNF) have drawn much attention from both a fundamental and an applied perspective due to their good mechanical and unique electrical properties. As reviewed in chapter 3, CNT-supported Pt nanoparticle showed superior activity in ORR in a half-cell test and CNT consequently reduced Pt usage compared to CB-supported electrocatalysts. GNF is also considered to be a potential support, which has high activities for the electrochemical oxidation of methanol. Pt/GNF as an anode catalyst greatly increased the performance of the DMFC over Pt/CB or Pt-Ru colloid catalyst. These studies strongly suggest the possible application of GNF and CNT as novel supports in fuel cell electrodes.

However, although GNF and CNT satisfied the characteristics which are required to be an ideal support material for the electrocatalyst in a fuel cell, their main drawback is the cost of commercial production caused by harsh synthetic condition and low production yields. There are no available synthetic techniques that can produce CNT of reasonable purity and quality in large quantities. The market price of CNT is still too high (~$200/g) at present for realistic commercial application, even though CNT may be available to consumers for less than $100/pound in a few years. Another disadvantage is

in the manipulation of CNT. CNT is needed to be purified for the bulk applications because as-produced CNT contains a lot of undesirable metal contaminants (Fe, Co, Ni...). Again, the purified CNT should be oxidized in harsh acidic condition, which is inevitable for better dispersion in solvent. This surface oxidation of CNT may cause the loss of its original electronic properties which negatively affect the performance of the catalyst. Additionally, it is revealed that high loading of Pt is not achieved without the surface oxidation of CNT. Instead of its surface oxidation, CNT can be functionalized covalently and non-covalently to be dispersed in solvent but the loss of the conductivity of CNT is always accompanied. The case for GNF is not much different from that of CNT. Hence, CNT and GNF have many impediments to their wide spread commercialization because of these inherent problems.

Exfoliated graphite nanoplatelets (xGnP) produced by MSU proprietary method is a much more cost-effective alternative and in addition has superior properties such as excellent mechanical and electrical properties comparable to CNT and GNF. More importantly, xGnP possesses higher corrosion and oxidation resistance and higher crystallinity than CNT and GNF as will be described in chapter 5. Hence, it is worthy while to investigate xGnP as a support material for the electrodes of a fuel cell.

The overall goal of this research is to develop and understand a method for depositing metal nanoparticles on xGnP as a support for an electrocatalyst for a fuel cell system. This is of great importance because Pt-related catalysts mounted onto carbon supports are applied as heterogeneous catalysts and electrodes in fuel cell. Another reason is that the specific activity of the platinum catalyst in ORR in both PEMFC and DMFC is also highly related to the carbon support which functions to allow the reactant

to easily get to the electrocatalyst, show good corrosion resistance in the cathode under strongly oxidizing conditions, and have adequate water-handling capability at the cathode. This research will be accomplished by 1) understanding the fundamental physical/chemical mechanism controlling the dispersion and size of metal nanoparticles deposited on xGnP and 2) evaluating the performance and relating it to morphology of xGnP-supported pure Pt and/or bimetallic PtRu alloys which will be highly dispersed on the xGnP. The catalytic activity of xGnP-supported Pt-based electrocatalyst will also be compared to that of commercially available XC-72 Carbon black-supported Pt catalyst from E-TEK.

On the other hand, there are many studies underlining the difficulty of using conventional methods to prepare Pt catalysts with high metal loadings (> 30wt.%) and small particle sizes at the same time. Metal particle sizes for a catalyst with 10wt.% and 30wt. % Pt loading can be produced at 2.0nm and 3.2nm, respectively, but increase to 8.8nm for a 60wt. % Pt catalyst. Therefore, the synthesis of highly dispersed and highly loaded nanosized metal catalysts is a challenge. Hence, ionic liquids will be used in this microwave process in order to control the size of metal particles even at highly loaded and supported metal catalysts. High concentration of polar molecules in ionic liquid will be a good additive to accelerate the reduction rate of metal precursor, resulting in the synthesis of small and monodispersed metal particles.

3.9 Bibliography

1. L.A.M. Herans, and J.W. Geus, "Recent Advances in Basic and Applied Aspects of Industrial Catalysis", Stud. Surf. Sci. Catal., 113, 1997.

2. A. Yu, Stakheev, and L.M. Kustov, "Effects of the support on the morphology and electronic properties of supported metal clusters: modern concepts and progress in 1990s", Appl. Catal. A: Gen., 188, p3-35, 1999.

3. C.N. Satterfield, "Heterogenous Catalysis in Practice", McGraw-Hill, New York, 1980.

4. F. Rodriguez-Reinoso, "The role of carbon materials in heterogeneous catalysis", Carbon 36 (3), p159-175, 1998.

5. D.S. Cameron, S.J. Cooper, I.L. Dodgson, B. Harrison, and J.W. Jenkins, "Carbons as supports for precious metal catalysts", Catalysis Today, 7, p113-137, 1990.

6. F. Rodriguez-Reinoso, "The role of carbon materials in heterogeneous catalysis", Carbon, 36, p159-175, 1998.

7. G. Ertl, H. Knozinger, and J. Weitkamp (Eds.), "Preparation of Solid Catalysts", Wikey, Weinhein, 1999 (Chapter 3 and 4).

8. C.A. Leon y Leon, J.M. Solar, V. Calemma, and L.R. Radovic, "Evidence for the protonation of basal plane sites on carbon", Carbon, 30, p797-811, 1992.

9. C. Prado-Burguete, A. Linares-Solano, F. Rodriguez-Reinoso, C. Salinas-Martinez de Lecea, "The effect of oxygen surface groups of the support on platinum dispersion in Pt/carbon catalysts", J. Catal. 115, p98-106, 1989.

10. S.V. Gurevich, P.A. Simonov, A.S. Lisitsyn, V.A. Likholobov, E.M. Moroz, A.L. Chuvilin, and V.N. Kolomiichuk, "Influcence of carbon support pretreatment on properties of catalysts", React. Kinet. Catal. Lett., 41, p211-216, 1990.

11. H.P. Boehm, "Some aspects of the surface chemistry of carbon blacks and other carbons", Carbon, 32, p759-769, 1994.

12. H.P. Boehm, G. Mair, T. Stoehr, A.R. de Rincon, B. Tereczki, "Carbon as a catalyst in oxidation reactions and hydrogen halide elimination reaction", Fuel, 63, 1061, 1984.

13. F. Derbyshire, V.H.J. de Beer, G.M.K. Abotsi, A.W. Scaroni, J.M. Solar, and D.J. Skrovanek, "The influence of surface functionality on the activity of carbon supported catalysts", Appl. Catal., 27, p117-131, 1986.

14. F. Coloma, A. Sepulveda-Escribano, and F. Rodriguez-Reinoso, "Heat-Treated Carbon-Blacks as Supports for Platinum Catalysts", J. of Catalysis, 154, p299, 1995.

15. S.S. Barton, M.J.B. Evans, E. Halliop, J.A.F. MacDonald, "Acidic and basic sites on the surface of porous carbon", Carbon, 35, p1361-1366, 1997.

16. T.J. Fabish and D.E. Schleifer, "Surface chemistry and the carbon black work function", Carbon, 22, p19-38, 1984.

17. F. Coloma, A. Sepulveda-Escribano, J.L.G. Fierro and F. Rodriguez-Reinoso, "Preparation of Platinum Supported on Pregraphitized Carbon Blacks", Langmuir, 10, p750-755, 1994.

18. J. H. Hodak, A. Henglein and G.V. Hartland, "Photophysics of Nanometer Sized Metal Particles: Electron-Phonon Coupling and Coherent Excitation of Breathing Vibrational Modes", J. Phys. Chem. B, 104, p9954-9965, 2000.

19. T. Fujimoto, S. Terauchi, H. Umehara, I. Kojima, and W. Henderson, "Sonochemical Preparation of Single-Dispersion Metal Nanoparticles from Metal Salts", Chem. Mater., 13, p1057-1060, 2001.

20. M.T. Reet and W. Helbig, "Size-Selective Synthesis of Nanostructured Transition Metal Clusters", J. Am. Chem. Soc., 116, p7401-7402, 1994

21. I. Lee, K.Y. Chan and D.L. Philips, "Growth of electrodeposited platinum nanocrystals studied by atomic force microscopy", Appl. Surf. Sci., 136, p321-330, 1998.

22. F. Fievet, J.P. Lagier, and M. Figlarz, "Preparing monodisperse metal powders in micrometer and submicrometer sizes by the polyol process", MRS Bull., 24, p29, 1989.

23. S.H. Joo, S.J. Choi, I. Oh, J. Kwak, Z. Liu, O. Terassaki, and R. Ryoo, "Ordered nanoporous arrays of carbon supporting high dispersions of platinum nanoparticles", Nature, 412, p169-172, 2001.

24. W. Li, C. Liang, W. Zhou, J. Qiu, Z. Zhou, G. Sun, and Q. Xin, "Preparation and Characterization of Multiwalled Carbon Nanotube-Supported Platinum for Cathode Catalysts of Direct Methanol Fuel Cells", J. Phys. Chem. B, 107, p6292-6299, 2003.

25. T. Matsumoto, T. Komatsu, K. Arai, T. Yamazaki, M. Kijima, H. Shimizu, Y. Takasawa, and J. Nakamura, "Reduction of Pt usage in fuel cell electrocatalysts with carbon nanotube electrodes", Chem. Commun., p840-841, 2004.

26. B.L. Gratiet, H. Remita, G. Picq, and M.O. Delcourt, "CO-Stabilized Supported Pt Catalysts for Fuel Cells: Radiolytic Synthesis", J. Catal., 164, p36-43, 1996.

27. Z. Zhou, S. Wang, W. Zhou, G. Wang, L. Jiang, W. Li, S. Song, J. Liu, G. Sun, and Q. Xin, "Novel synthesis of highly active Pt/C cathode electrocatalyst for direct methanol fuel cell", Chem. Commun., 394-395, 2003.

28. T. Yoshitake, Y. Shimakawa, S. Kuroshima, H. Kimura, T. Ichihashi, Y. Kubo, D. Kasuya, K. Takahashi, F. Kokai, M. Yudasaka, and S. Iijima, "Preparation of fine platinum catalyst supported on single-wall carbon nanohorns for fuel cell application", Physica B, 323, p124-126, 2002.

29. G. Che, B.B. Lakshmi, E.R. Fisher, and C.R. Martin, "Carbon nanotubule membranes for electrochemical energy storage and production", Nature, 393, p346-349, 1998.

30. Z. Liu, J. Lee, M. Han, W. Chen, and L. Gan, "Synthesis and characterization of PtRu/C catalysts from microemulsions and emulsions", J. Mater. Chem., 12, p2453-2458, 2002.

31. K.F. Friedrich, K.P. Geyzers, A.J. Dickinson, and U. Stimming, "Fundamental aspects in electrocatalysis: from the reactivity of single-crystals to fuel cell electrocatalysts", J. Electroanal. Chem., 524, p261-272, 2003.

32. E.S. Steigerwalt, G.A. Deluga and C.M. Lukehart, "Rapid preparation of Pt-Ru/graphitic carbon nanofiber nanocomposites as DMFC anode catalysts using microwave processing", J. of Nanosci. & Nanotech., 3, p 247, 2003.

33. E.S. Steigerwalt, G.A. Deluga, D.E. Cliffel and C.M. Lukehart, "A Pt-Ru/Graphitic Carbon Nanofiber Nanocomposite Exhibiting High Relative Performance as a Direct-Methanol Fuel Cell Anode Catalysts", J. Phys. Chem. B, 105, p8097-8101, 2001.

34. K. Park, Y. Sung, S. Han, Y. Yun, and T. Hyeon, "Origin of the Enchanced Catalytic Activity of Carbon Nanocoil-supported PtRu alloy electrocatalyst", J. Phys. Chem. B, 108, p939, 944, 2004.

35. E.M. Crabb, R. Marshall, and D. Thompsett, "Carbon monoxide electro-oxidation properties of carbon-supported PtSn catalysts prepared using surface organometallic chemistry", J. Electrochem. Soc., 147, p4440-4447, 2000.

36. H. Yang, N. Alonso-Vante, J. Leger, and C. Lamy, "Tailoring, Structure, and Activity of Carbon-Supported Nanosized Pt-Cr Alloy Electrocatalysts for Oxygen Reduction in Pure and Methanol-Containing Electrolytes", J. Phys. Chem. B, 108, 1938-1947, 2004.

37. M.S. Hoogenraad, R.A.G.M.M. van Leeuwarden, G.J.B. van Breda Vriesman, A. Broersma, A.J. van Dillen, and J.W. Geus, Stud. Surf. Sci., Catal., 91, p263, 1995.

38. G. Farkas, L. Hegedus, A. Tunger, T. Mathe, J.L. Figueiredo, and M. Freitas, "Effect of carbon support properties on enantioselective hydrogenation of isophorone over palladium catalysts modified with (-)-dihydroapovincaminic acid ethyl ester", J. Mol. Catal. A: Chem., 153, p215-219, 2000.

39. K.Y. Chan, J. Ding, J. Ren, S. Cheng and K.Y. Tsang, "Supported mixed metal nanoparticles as electrocatalysts in low temperature fuel cells", J. Mater. Chem., 14, p505-516, 2004.

40. H. Jin, S.E. Park, J.M. Lee, and S.K. Ryu, "The shape-selectivity of activated carbon fibers as a palladium catalyst support", Carbon, 34, p429-431, 1996.

41. G.R. Heal, and L.L. Mkayula, "The preparation of palladium metal catalysts supported on carbon part II: Deposition of palladium and metal area measurements", Carbon, 26, p815-823, 1988.

42. S.H. Joo, S.J. Choi, I. Oh, J. Kwak, Z. Liu, O. Terassaki, and R. Ryoo, "Ordered nanoporous arrays of carbon supporting high dispersions of platinum nanoparticles", Nature, 412, p169-172, 2001.

43. Y. Wang, J. Ren, K. Deng, L. Gui and Y. Tang, "Preparation of Tractable Platinum, Rhodium, and Ruthenium Nanoclusters with Small Particle Size in Organic Media", Chem. Mater., 12, p1622-1627, 2000.

44. M.H. Lee, C.Y. Tai and C.H. Lu, "Synthesis of spherical zirconia by precipitation between two water/oil emulsions", J. Eur. Ceram. Soc., 19, p2593-2603, 1999.

45. A.S. Bommarius. J.F. Holzarth, D.I.C. Wang and T.A. Hatton, "Coalescence and solubilizate exchange in a cationic four-component reversed micellar system", J. Phys. Chem., 94, p7232-7239, 1990.

46. D.S. Cameron, S.J. Cooper, I.L. Dodgson, S. Harrison and J.W. Jenkins, "Carbons as supports for precious metal catalysts", Catalysis Today, 7, p113-137, 1990.

47. K.W. Park, Y.E. Sung, S. Han, Y. Yun, and T. Hyeon, "Origin of the Enhanced Catalytic Activity of Carbon Nanocoil-Supported PtRu Alloy Electrocatalysts", J. Phys. Chem. B, 108, p939-944, 2004.

48. F. Rodriguez-Reinoso, C. Salinas-Martinez de Lecea, A. Sepulveda-Escribano, and J. D. Lopez-Gonzalez, "Effect of support porosity in the preparation and catalytic activity for CO hydrogenation of carbon-supported Fe catalysts", Catal. Today, 7, p287, 1990.

49. K. Kinoshita and J.A.S. Bett, "Electrochemical oxidation of carbon black in concentrated phosphoric acid at 135°C", Carbon, 11, p237-247, 1973.

50. A. Espinola, P.M. Miguel, M.R. Salles, and A.R. Pinto, "Electrical properties of carbons-resistance of powder materials", Carbon, 24, p337, 1986.

51. J.C. Long, R.W. Soffel, L.L. Winter, E.L. Piper, J.T. Meers, and E.M. Dannenburg, Kirk-Othmer, "Enecyclopedia of Chemical Technology", vol. 4, p556-596, 1978.

52. W. Li, C. Liang, J. Qiu, W. Zhu, H. Han, Z. Wei, G. Sun, and Q. Xin, "Homogeneous and controllable Pt particles deposited on multi-wall carbon nanotubes as cathode catalyst for direct methanol fuel cells", Carbon 42, p436-439, 2004.

53. Z. Liu, X. Lin, J.Y. Lee, W. Zhang, M. Han, L.M. Gan, "Preparation and Characterization of Platinum-Based Electrocatalysts on Multiwalled Carbon Nanotubes for Proton Exchange Membrane Fuel Cells", Langmuir, 18, p4054-4060, 2002.

54. G. Che, B.B. Lakshmi, C.R. Martin, E. R. Fisher, "Metal-Nanocluster-Filled Carbon Nanotubes: Catalytic Properties and Possible Applications in Electrochemical Energy Storage and Production", Langmuir, 15, p750-758, 1999.

55. T. Yoshitake, Y. Shimakawa, S. Kuroshima, H. Kimura, T. Ichihashi, Y. Kubo, D. Kasuya, K. Takahashi, F. Kokai, M. Yudasaka, and S. Iijima, "Preparation of fine platinum catalyst supported on single-wall carbon nanohorns for fuel cell application", Physica B, 323, p124-126, 2002.

56. K. Park, Y. Sung, S. Han, Y. Yun, and T. Hyeon, "Origin of the Enhanced Catalytic Activity of Carbon Nanocoil-Supported PtRu Alloy Electrocatalysts", J. Phys. Chem. B, 108, p939-944, 2004.

57. C. Park and R.T.K. Baker, "Catalytic Behavior of Graphite Nanofiber Supported Nickel Particles. 2. The Influence of the Nanofiber Structure", J. of Phys. Chem., 102, p5168-5177, 1998.

58. C.A. Bessel, K. Laubernds, N.M. Rodriguez and R.T.K. Baker, "Graphite Nanofibers as an Electrode for Fuel Cell Applications", J. Phys. Chem. B, 105, p1115-1118, 2001.

59. E.S. Steigerwalt, G.A. Deluga, D.E. Cliffel and C.M. Lukehart, "A Pt-Ru/Graphitic Carbon Nanofiber Nanocomposite Exhibiting High Relative Performance as a Direct-Methanol Fuel Cell Anode Catalyst", J. Phys. Chem. B, 105, p8097-8101, 2001.

60. E.S. Steigerwalt, G.A. Deluga and C.M. Lukehart, "Pt-Ru/Carbon Fiber Nanocomposites: Synthesis, Characterization, and Performance as Anode Catalysts of Direct Methanol Fuel Cells. A Search for Exceptional Performance", J. Phys. Chem. B, 106, p760-766, 2002.

61. E.S. Steigerwalt, G.A. Deluga and C.M. Lukehart, "Rapid preparation of Pt-Ru/graphitic carbon nanofiber nanocomposites as DMFC anode catalysts using microwave processing", J. of Nanosci. & Nanotech., 3, p 247-251, 2003.

62. W. Li, C. Liang, J. Qiu, W. Zhou, H. Han, Z. Wei, G. Sun, and Q. Xin, "Homogeneous and controllable Pt particles deposited on multi-wall carbon nanotubes as cathode catalyst for direct methanol fuel cells", Carbon 42, p436, 2004.

63. W. Li, C. Liang, J. Qiu, W. Zhou, H. J. Qiu, Z. Zhou, G. Sun, and Q. Xin, "Preparation and Characterization of Multiwalled Carbon Nanotube-Supported Platinum for Cathode Catalysts of Direct Methanol Fuel Cells", J. Phys. Chem. B, 107, p6292-6299, 2003.

64. T. Matsumoto, T. Komatsu, K. Arai, T. Yamazaki, M. Kijima, H. Shimizu, Y. Takasawa, and J. Nakamura, "Reduction of Pt usage in fuel cell electrocatalysts with carbon nanotube electrodes", Chem. Commun., p840-841, 2004.

65. Z. Liu, X. Lin, J.Y. Lee, W. Zhang, M. Han, and L.M. Gan, "Preparation and Characterization of Platinum-Based Electrocatalysts on Multiwalled Carbon Nanotubes for Proton Exchange Membrane Fuel Cells", Langmuir, 18, p4054-4060, 2002.

66. G. Che, B.B. Lakshmi, C.R. Martin, and E.R. Fisher, "Metal-Nanocluster-Filled Carbon Nanotubes: Catalytic Properties and Possible Applications in Electrochemical Energy Storage and Production", Langmuir, 15, p750-758, 1999.

67. B. Rajesh, K.R. Thampi, J.M. Bonard, N.X. Xanthospoulos, H.J. Mathieu, and B. Viswanathan, "Pt-WO3 supported on carbon nanotubes as possible anodes for direct methanol fuel cells", Fuel, 81, p2177-2190. 2002.

68. M.S. Whittingham, A.J. Jacobson, editors, "Intercalation Chemistry", New York & London: Academic Press; 1982.

69. T. Yoshitake, Y. Shimakawa, S. Kuroshima, H. Kimura, T. Ichihashi, Y. Kubo, D. Kasuya, K. Takahashi, F. Kokai, M. Yudasaka, and S. Iijima, "Preparation of fine platinum catalyst supported on single-wall carbon nanohorns for fuel cell application", Physica B, 323, p124, 2002.

70. K. Park, Y. Sung, S. Han, Y. Yun, and T. Hyeon, "Origin of the Enhanced Catalytic Activity of Carbon Nanocoil-Supported PtRu Alloy Electrocatalysts", J. Phys. Chem. B, 108, p939-944, 2004.

71. T. Hyeon, S. Han, Y. Sung, K. Park, and Y. Kim, "High-Performance Direct Methanol Fuel Cell Electrodes using Solid-Phase-Synthesized Carbon Nanocoils", Angew. Chem. Int. Ed., 42, p4352-4356, 2003.

CHAPTER 4

THE SYNTHESIS OF UNSUPPORTED AND SUPPORTED NOBLE METAL NANOPARTICLES VIA MICROWAVE PROCESS IN THE PRESENCE OF ROOM TEMPERATURE IONIC LIQUIDS (RTIL)

4.1 Introduction

The synthesis of nanoscale metal colloids or clusters has been the object of much research in modern nanotechnology due to their great impact on new technological applications [1, 2]. Nanoscale particles possess unique optical, thermal, electronic, magnetic properties and chemical reactivity which comes from their quantum size effect which is not observed in the bulk [3~8]. Most of their unique physical and chemical properties strongly depend on the size and shape of the metal nanoparticles [9]. Therefore, an effective synthetic method is required to obtain uniform small metal powders with a controlled size and a narrow size distribution. Examples of advanced techniques to produce such nanoparticles are sol-gel processes, microemulsion methods, hydrothermal/solvothermal processes, electrochemical reduction, sonochemical routes, and microwave-assisted processes, all of which involve the reduction of the corresponding metal ions [10-16].

There are two important points to be considered in the synthesis of metal nanoparticles. One is to control particle size, particle size distribution, and shape of particle at the growth stage of metal nanoparticles. The other is to achieve the stabilization of the metal nanoparticles in solutions. Generally, the control of particle size and the particle stabilization are achieved by using capping materials such as polymers, surfactants, coordinating ligands and changing their content in solution [17-19]. The reduction rate of the metal ions is another way of controlling the size of metal particle [20]. This chapter is devoted to reporting a process to synthesizing fine precious metal nanoparticles by a new and simple strategy of reducing metal ions in a liquid polyol

under microwave irradiation in the presence of ionic liquids and illustrating how effective this process can control particle size and uniform size distribution.

Nanocomposites consisting of either metals or metal oxides supported on carbons or metals dispersed on metal oxides can be advantageous for applications in automobiles [21, 22], batteries [23-26], supercapacitors [27-30], fuel cells [31-33], hydrogen storage and production [34, 35], as well as for sensors[36]. Platinum-based metal nanoparticles are especially crucial components for low temperature fuel cells in which they are the most active catalysts for the oxidation of fuels supplied and the oxygen reduction reaction at their anode and cathode, respectively. However, the biggest obstacle to commercialize these fuel cells is the cost of precious metals and thus considerable efforts are expended to reduce the amount of the precious metals and obtain their maximum performance at the same time. The reduction of precious metal catalysts can be accomplished by enhancing the utilization of the metal catalyst on both the anode and cathode [37, 38], which is possible by introducing a high degree of dispersion of fine platinum-based catalysts onto carbon supports having a high surface area and conductivity.

Carbon supports play an important role in the properties of supported metal particles. They have a great effect on not only metal particle size and its dispersion but also electrocatalytic activity due to metal-support interactions, mass transport and electronic conductivity of the catalyst layer, and the stability of the metal particles [39, 40]. Many different novel carbons such as graphite nanofibers [41, 42], carbon nanocoils [43, 44], carbon nanotube [45, 46], mesocarbon microbeads [47], and carbon nanohorns [48] have been studied and compared as supports for precious metal catalyst. However, there is no known report in which carbon will be the best support for the maximum fuel cell

performance. This is because of the multiple influences of carbon supports with various physical properties, different size of metal particles and their degree of dispersion, as well as different extent of alloying bimetallic catalysts.

In this chapter, a simple approach is introduced to synthesize different metal catalysts supported on various carbons with an almost consistent particle size and dispersion and similar degree of alloying in bi- or multi-metallic catalysts. This makes it possible to investigate systematically the effect of carbon supports and compare their fuel cell performances directly.

4.2 Experimental Details

4.2.1 Materials

A reagent grade of ethylene glycol (EG, bp = 197.3°C) was purchased from J.T. Baker and used as a reducing agent for unsupported and carbon-supported platinum-based metal catalysts. Chloroplatinic acid hexahydrate ($H_2PtCl_6 \cdot 6H_2O$), ruthenium chloride hydrate ($RuCl_3 \cdot xH_2O$), palladium nitrate hydrate ($Pd(NO_3)_2 \cdot xH_2O$) were purchased from Aldrich and used as metal precursors. Room temperature ionic liquids used in this work are 1-butyl-3-methylimidazolium acetate ($bmimCH_3CO_2$), 1-butyl-3-methylimidazolium methyl sulfate ($bmimCH_3SO_4$), 1-butyl-3-methylimidazolium thiocyanate (bmimSCN), and 1-butyl-3-methylimidazolium hexafluorophosphate ($bmimPF_6$) and their chemical structures are shown in **Figure 4.1**. All of them were obtained from Aldrich and used as received. Multi-walled carbon nanotubes (MWNT), carbon black (CB, Vulcan XC-72R), and graphite nanofiber (GNF) were purchased from Aldrich, Cabot Co., and Nanomirae Inc., respectively and used as carbon supports.

Purified single wall carbon nanotube (SWNT) from Southwest and exfoliated graphite nanoplatelets (xGnP) made in-house were also investigated. Two commercial metal oxides (TiO_2 and CeO_2) from Aldrich were investigated as non-carbon supports.

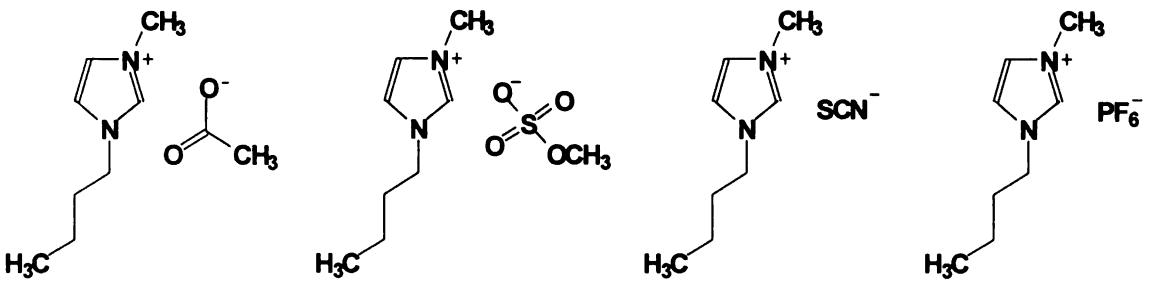

(a) (b) (c) (d)

Figure 4.1 Chemical structures of room temperature ionic liquids for the synthesis of catalysts (a: bmimCH_3CO_2, b: bmimCH_3SO_4, c: bmimSCN, d: bmimPF_6).

4.2.2 Preparation of Unsupported and Supported Metal Particles

The typical experimental procedures for producing unsupported metal particles are described as follows: First, a predetermined amount of a metal precursor was dissolved in 2g of EG in a 10mL beaker. Second, a controlled quantity of a RTIL were mixed with 18g of EG in a separate beaker and then combined in one beaker. The mixture was mechanically stirred for 30min, placed in a microwave oven (National, 2.45GHz, 1300W), and then heated for 50s. The resulting suspension was centrifuged and washed with acetone. The solid product was stored in a re-dispersed state in acetone.

Pt particles supported on various carbon supports and metal oxides consist of the following steps: In one beaker, carbons or metal oxides were ultrasonically dispersed in 18mL of EG for 30 min followed by cooling to room temperature under mechanical stirring. In another 10 ml beaker, a specific quantity of the Pt precursor was added to 2 ml

EG and completely dissolved. Contents in those beakers were mechanically mixed in a 100mL beaker for another 30 min, transferred into the microwave oven and irradiated for a total of 55 ~ 60 seconds to effect the precursor reduction. After cooling to ambient temperature, the resulting suspension was centrifuged and the residual slurry was washed with acetone several times and dried in a vacuum oven at 393K overnight. The weight ratio of Pt and support was controlled according to the targeted metal loading on supports. The catalysts obtained are called as the Pt/C-N. C can represent XC-72R, MWNT, SWNT, or GNF.

For Pt/C nanocomposites synthesized in the presence of the RTIL, the controlled amount of RTIL was added and dissolved in 18mL ethylene glycol prior to the dispersion of carbons. The molar ratios of RTIL to Pt precursor were seat at 1, 2.5, 5, 10, 20, and 50. Other steps are the same as for Pt/C-N catalysts. The Pt/C nanocomposites synthesized with the addition of, bmimPF_6, bmimCH_3CO_2, bmimCH_3SO_4, and bmimSCN are denoted as Pt/C-bmimPF_6, Pt/C- bmimCH_3CO_2, bmimCH_3SO_4, and Pt/C- bmimSCN, respectively. For example, Pt/MWNT- bmimPF_6 represents the MWNT-supported Pt particles synthesized by microwave irradiation in the presence of bmimPF_6.

4.2.3 Characterization Methods

The Pt colloidal formation process was investigated by UV-vis spectra with a Perkin Elmer Lamda 900 spectrometer in the range of 220~700nm with 1cm path length quartz cuvettes. The Pt precursor of 1.0×10^{-6} M was completely dissolved in ethylene glycol before the measurement. Pt particles dispersed on various carbons and metal oxides were characterized by recording their X-ray diffraction (XRD) patterns on a Regaku Rotaflex

200B X-ray diffractometer using Cu-Kα radiation with a curved graphite monochromator in order to identify the phases present in the catalyst and to evaluate the particle size of the dispersed metal crystallites. The 2θ region between 10^{o} and 100^{o} was explored at 45keV and 100 mV at a scan rate of 5^{o}/min. The average metal particle size was calculated using the Scherrer equation according to the XRD broadening Pt (220) reflections which was re-scanned at a rate of 1^{o}/min. The transmission electron microscopy (TEM) investigation was carried out with JEOL 100CX operating at a voltage of 100keV to determine the morphology of the dispersed Pt particles and the determination of the mean Pt particle size. Specimens were prepared by ultrasonically re-dispersing the sample powders in acetone for 15 min, applying the power suspension onto lacey carbon coated Cu grids and drying it in air. X-ray photoelectron spectroscopy (XPS) results of carbon supported Pt catalysts were obtained from a Physical Electronics PHI 5400 ESCA system and used to determine the presence of the oxide phases and the interaction between metal and supports. A non-monochomatic Mg source (with a $K_{\alpha 1,2}$ wavelength at 1253.6eV) was used with a take-off angle of 45degrees. Data was collected by a multi-channel detector with a Omni VI lens assembly. The instrument was operated with a pass energy of 93.90eV for survey scans and 29.35 eV for regional scans. The regional XPS of Pt (4f) was de-convoluted to recognize different oxidation states of Pt on carbons. Semi quantitative atomic concentrations were calculated using predetermined sensitivity factors. XPS samples were prepared by applying the catalyst powders directly to double-sided copper tape on a stainless steel stub.

4.3 Results and Discussions

4.3.1 Formation of Pt Nanoparticles

4.3.1.1 Pt formation in the absence of RTIL

The formation process of Pt nanoparticles in ethylene glycol (EG) by microwave (MW) heating in the absence of RTIL was investigated by UV-vis spectroscopy and the results were plotted in **Figure 4.2**. The ethylene glycol solution containing $H_2PtCl_6 \cdot 6H_2O$ before microwave reduction was pale yellow and showed a peak at 266nm in its UV-vis spectrum due to the ligand-to-metal charge transfer transition of the $[PtCl_6]^{-2}$ ions [49]. As the reaction time under MW heating increased, the peak at 266nm in the UV-vis spectrum decreased and disappeared after 20s reduction in the MW, suggesting that all

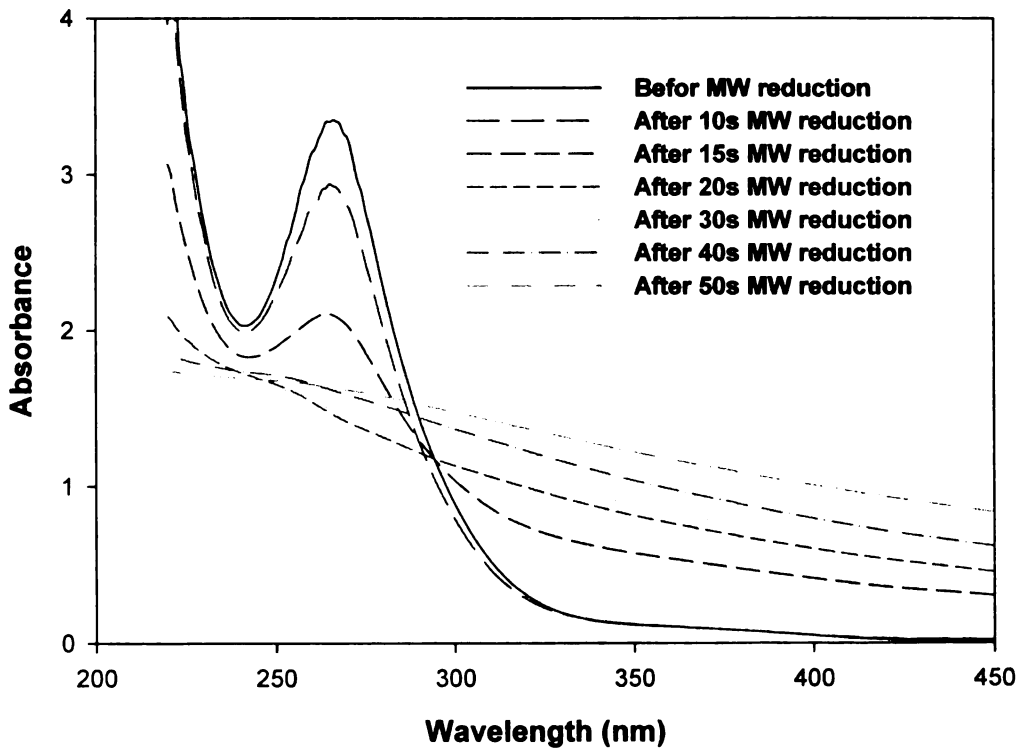

Figure 4.2. UV-vis absorption spectral change of $H_2PtCl_6 \cdot 6H_2O$-ethylene glycol solution in the absence of RTIL before and after microwave reduction.

$[PtCl_6]^{-2}$ ions were reduced to P^o. The color of the solution turned from pale yellow to dark brown. The adsorption from the ultraviolet to the visible region increased, which indicates that the band structure of Pt nanoparticles was formed [50]. This broadening tail peak appeared after 20s reduction in the MW and increased with increasing irradiation time as a result of particle growth or agglomeration. No further change was found after 50s MW reduction, suggesting the completion of Pt nanoparticles formation and growth.

4.3.1.2 Pt formation in the presence of RTILs

The high polarity of solvents is one of the most important properties to be considered in microwave chemistry. RTIL is good microwave absorbent due to large positive organic cations with a high polarizability and appropriate anions, leading to very high heating rate and further reduction in reaction time in microwave irradiation. Therefore, RTIL possesses some advantages in synthesizing inorganic nanomaterials such as tellurium nanowire, gold nanosheet and metal sulfides by microwave dielectric heating [51~53]. However, the application of RTIL for microwave chemistry to produce nanostructures has not been blossomed in spite of such advantages. Reduction experiments utilizing microwave irradiation in the presence of RTIL have been conducted and results on the reduction of $H_2PtCl_6 \cdot 6H_2O$ in EG by microwave irradiation to determine the influence of RTIL such as bmim CH_3SO_4, bmimPF_6, and bmimCH_3CO_2 on formation of Pt nanoparticles are reported.

Reduction in the presence of bmimCH_3CO_2. In the first set of experiments, the influence of bmimCH_3O_2 on Pt formation from $H_2PtCl_6 \cdot 6H_2O$-EG solution was

investigated. A constant amount of Pt precursor of 1.54×10^{-4} M was used. The effect of MW reduction time was studied with a fixed composition of $bmimCH_3O_2$/ $H_2PtCl_6 \cdot 6H_2O$ = 20 in molar ratio. The results are shown in **Figure 4.3**. When $bmimCH_3O_2$ was introduced into EG containing Pt salt, the peak intensity at 267nm corresponding to $[PtCl_6]^{-2}$ ions in the UV-vis spectrum decreased slightly with 5s MW irradiation but completely disappeared after 10s MW reduction as clearly seen in **Figure 4.3**. The broadening tail peak in the visible region indicating the formation of Pt nanoparticles was almost uniform in spite of increasing MW irradiation, suggesting that Pt nanoparticle formation and growth can be completed within 10s in the presence of $bmimCH_3O_2$. It can be concluded in this set of experiments that the reduction reaction in the presence of $bmimCH_3O_2$ is at least twice as fast as that in the absence of RTIL and the growth and agglomeration of Pt particles is restricted by the presence of $bmimCH_3CO_2$, which may result in the formation of smaller Pt nanoparticles in RTIL-assisted microwave process.

The mechanism of the protecting agent can be measured by UV-vis spectroscopy. If $bmimCH_3CO_2$ acts as a protecting agent, the peak at 267nm shifts to higher wavelength due to the expansion of the ligand field splitting of Pt5d orbital as a result of the coordination of N and/or O atoms of $bmimCH_3CO_2$ to Pt^{4+}[54]. No peak shift was found in this work after the addition of $bmimCH_3CO_2$, indicating that $bmimCH_3CO_2$ does not act as a protecting material. However, TEM images of Pt nanoparticles synthesized in the presence of $bmimCH_3CO_2$ indicates that it has a great effect on preventing Pt nanoparticles from agglomerating with each other. The details on this will be discussed in the next section.

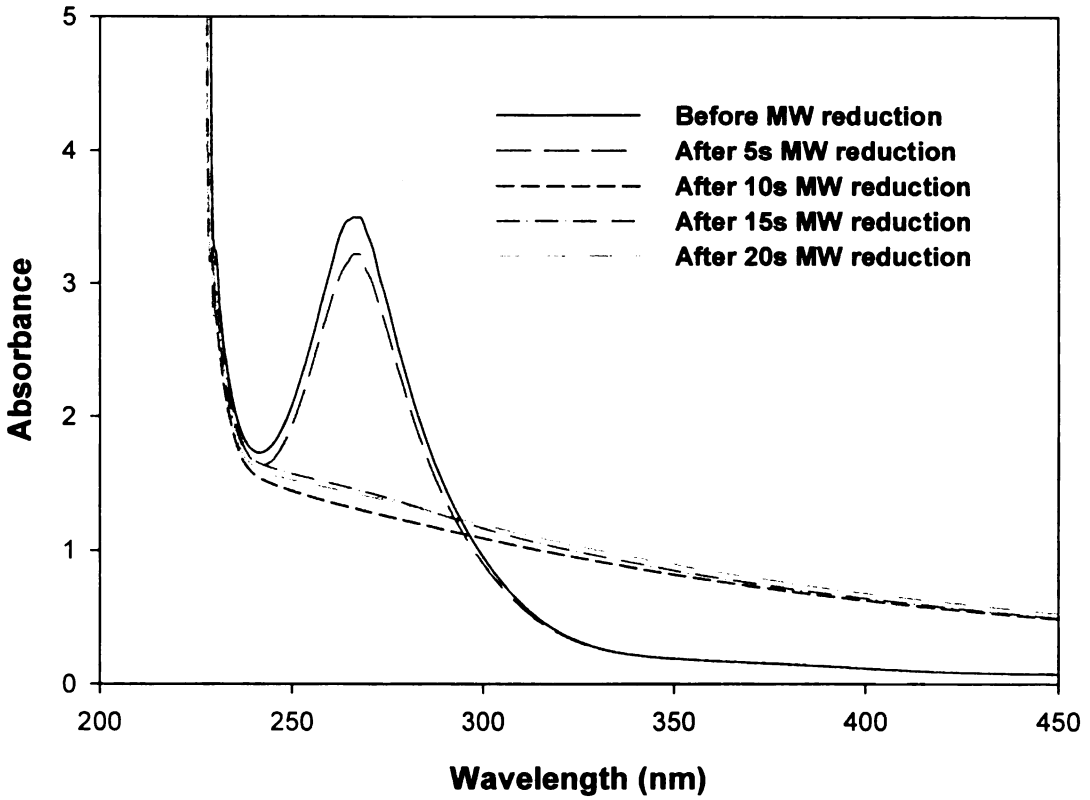

Figure 4.3. Typical UV-vis absorption spectral change of $H_2PtCl_6 \cdot 6H_2O$-ethylene glycol solution containing bmimCH_3CO_2 before and after microwave reduction.

The effect of bmimCH_3O_2 content on the process of Pt particle formation was also monitored through UV-visible spectrometry. The concentration of bmimCH_3O_2 was varied so that the molar ratio of bmimCH_3O_2 to Pt precursor (1.54×10^{-4} M) was either1, 5, 10, or 20. **Figure 4.4** was plotted with UV-vis adsorption spectra obtained after 10s MW reduction, which provided clear difference on the reduction rate. The Figure clearly showed that the peak at 267nm quickly decreased with increasing the content of bmimCH_3O_2. When the molar ratio of bmimCH_3O_2/Pt > 10, the peak at 267nm completely disappeared even after 10s MW irradiation. The adsorption spectral patterns above bmimCH_3O_2/ $H_2PtCl_6 \cdot 6H_2O$ = 20 were not affected in spite of the further increase

of bmimCH_3O_2 concentration, suggesting that no further addition of bmimCH_3O_2 to Pt precursor-EG solution is needed to increase the reduction rate of Pt ions at the present condition of MW irradiation.

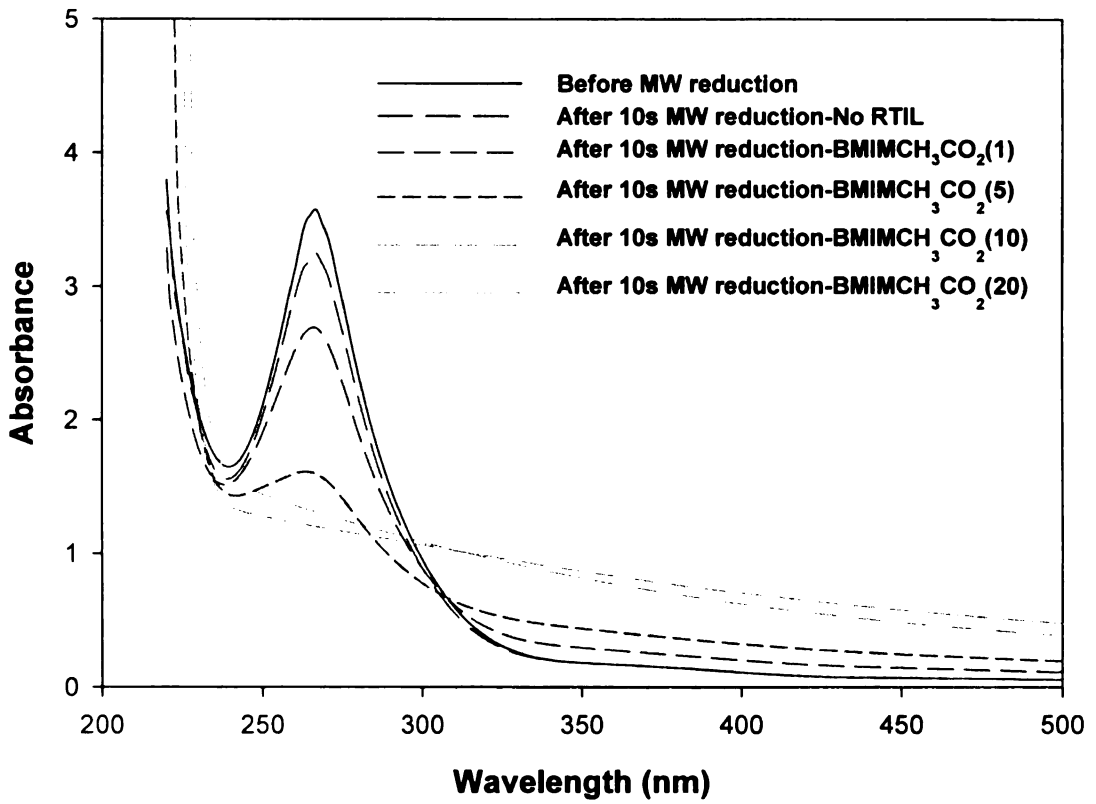

Figure 4.4. UV-vis absorption spectral change of $H_2PtCl_6 \cdot 6H_2O$-ethylene glycol solution containing different amount of bmimCH_3CO_2 before and after microwave reduction.

Reduction in the presence of bmimCH_3SO_4 and bmimPF_6. The influence of other two RTIL, bmimCH_3SO_4 and bmimPF_6, on the formation of Pt particles was investigated at a fixed composition of the RTIL/ $H_2PtCl_6 \cdot 6H_2O$ = 20 in molar ratio. The concentration of both RTIL was determined on the basis of previous results obtained by bmimCH_3CO_2. As shown in **Figure 4.5** obtained in the presence of bmimCH_3SO_4, the peak corresponding

to Pt ions drastically decreased after 10s MW irradiation and Pt nanoparticles completely form after 20s MW irradiation, suggesting that the reduction reaction of Pt ions and the formation of Pt can be completed in 20s through MW heating. The similar behavior was obtained in the presence of $bmimPF_6$ (not shown in here).

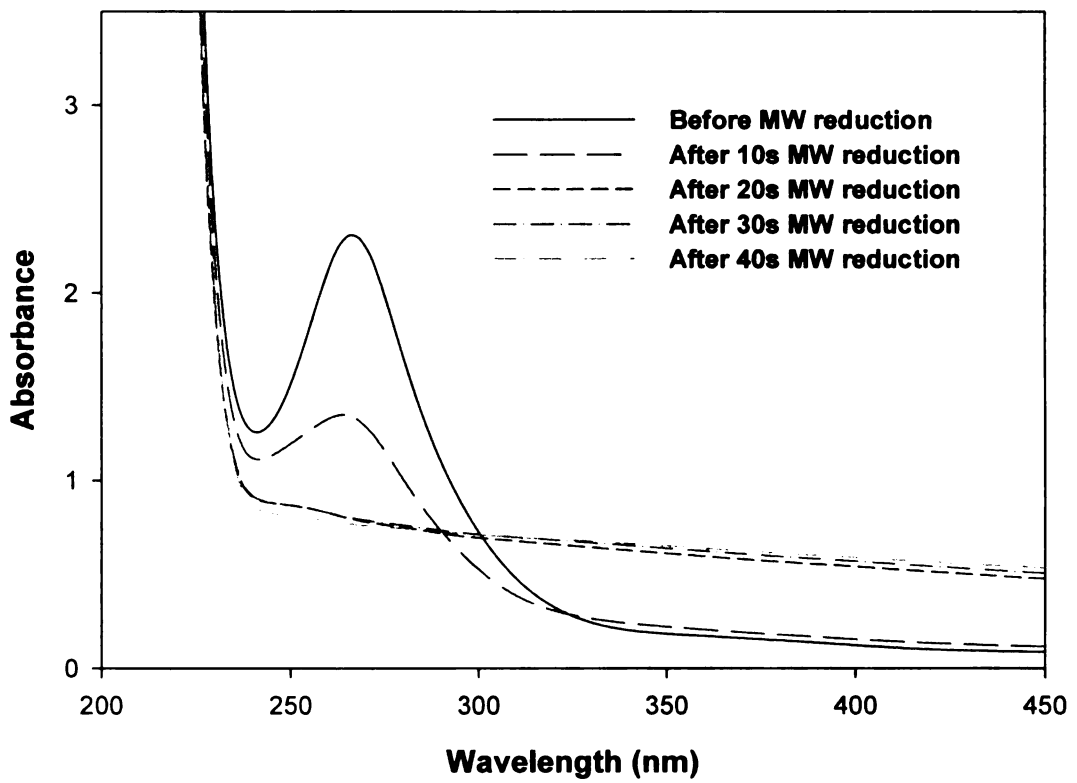

Figure 4.5. Typical UV-vis absorption spectral change of $H_2PtCl_6 \cdot 6H_2O$-EG solution in the presence of $bmimCH_3SO_4$ in MW irradiation.

The reduction rate of $[PtCl_6]^{-2}$ in the presence of $bmimCH_3CO_2$, $bmimPF_6$, and $bmimCH_3SO_4$ were compared in **Figure 4.6**. The molar ratio between RTIL and Pt salt was 20. The resulting data were recorded after 10s MW irradiation. As clearly seen in the Figure, the peak height of Pt ions rapidly decreased in the following order; $bmimCH_3CO_2$

> $bmimPF_6$ > $bmimCH_3SO_4$. This order may have resulted from the different polarity of RTIL because the reaction has been conducted in the microwave oven. All of the RTIL

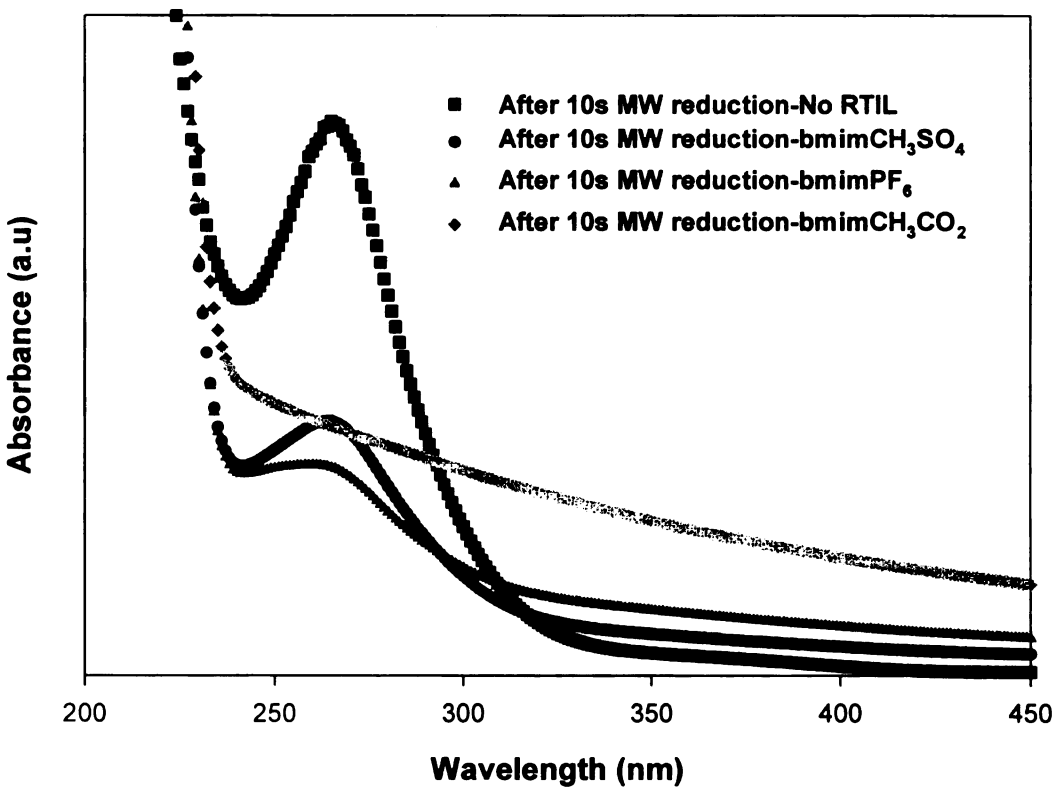

Figure 4.6. Comparison of UV-vis absorption spectra obtained in the presence of three RTILs such as $bmimCH_3SO_4$, $bmimPF_6$, and $bmimCH_3CO_2$ after 10s MW reduction.

have the same cation, 1-butyl-3-methylimidazolium but different anions. Thus, only a difference in the polarity originates from anion groups such as CH_3CO_2, CH_3SO_4, and PF_6. CH_3CO_2 is expected to have the highest polarity due to unsymmetrical arrangement by oxygen atoms among them. Hence, the decrease of the peak intensity was most dramatic in the presence of $bmimCH_3CO_2$. Meanwhile, since both CH_3SO_4 and PF_6 have fairly symmetrical molecular geometry, it is hard to tell which one has higher polarity. It

has been reported that for the $bmim^+$ ionic liquid, the polarity correlates with anion size and large anion results in a decrease of the polarity [55, 56]. Based on this report, PF_6 seems to have slightly higher polarity than CH_3SO_4 because the former has a smaller size compared to the latter. Therefore, the introduction of bmimPF6 resulted in faster reduction than $bmimCH_3SO_4$. Overall the decreasing order of the reduction rate seems reasonable. It is also expected based on the results in **Figure 4.6** that the size of Pt nanoparticles may be in the following order of $bmimCH_3SO_4$ > $bmimPF_6$ > $bmimCH_3CO_2$ because the faster reduction produce smaller particles, which is supported in section 4.3.2.

Reduction in the presence of bmimSCN.

Another set of UV-vis measurements has been conducted to monitor the formation process for bmimSCN/Pt = 20 in ethylene glycol via microwave irradiation. As shown in **Figure 4.7**, UV-vis spectra of mixed solutions of Pt precursor with bmimSCN were totally different from those obtained for the Pt solutions with three RTIL studied previously. The mixed solution of Pt precursor and bmimSCN initially showed significant absorbance enhancement of the Pt ion peak at about 280nm. Within 10s, the peak became broader and a shoulder formed at about 370nm which seems to correspond to another type of Pt ions [57]. After 20s, the peak completed to shift to a higher wavelength at 300nm proving the coordination of bmimSCN to Pt ions, which in turn provides the stabilizing action of bmimSCN to Pt metal clusters. As MW irradiation proceeded, the peak intensity at 300nm decreased and disappeared completely, indicating the formation and the growth of Pt clusters and the completion of Pt growth.

The ability of bmimSCN to reduce Pt ions in ethylene glycol without MW irradiation was also studied. The mixed solution of $H_2PtCl_6 \cdot 6H_2O$-EG-bmimSCN was stored in a vial at room temperature for a day and then UV-vis measurements for the solution were conducted. Surprisingly, the peak at 280nm corresponding to Pt ions disappeared completely and only a broader shoulder was found after 1 day without MW irradiation as shown in **Figure 4.8**. This phenomenon was not found with other RTIL used in this work. The result suggests that bmimSCN itself can act as a weak reducing agent. Consequently, bmimSCN acts as a strong protecting agent as well as a reducing agent, which is expected to have a synergic effect on the reduction of Pt size.

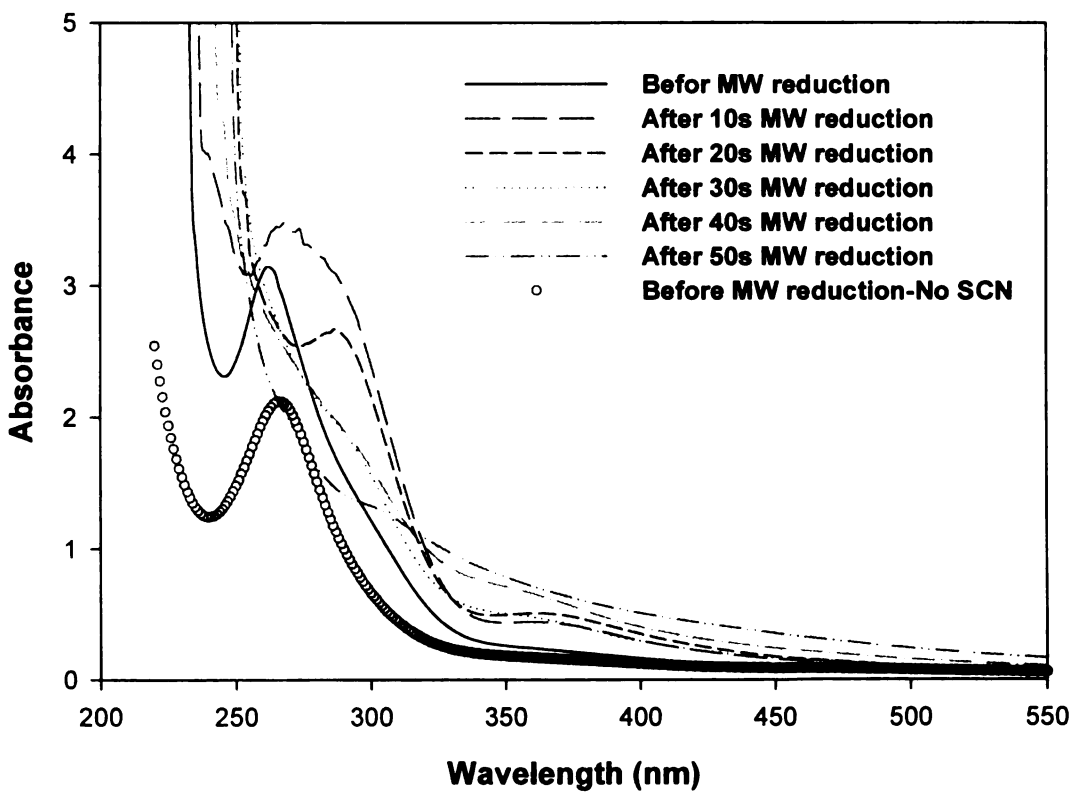

Figure 4.7. UV-vis absorption spectral change of $H_2PtCl_6 \cdot 6H_2O$-EG solution containing of bmimSCN(20) before and after microwave reduction.

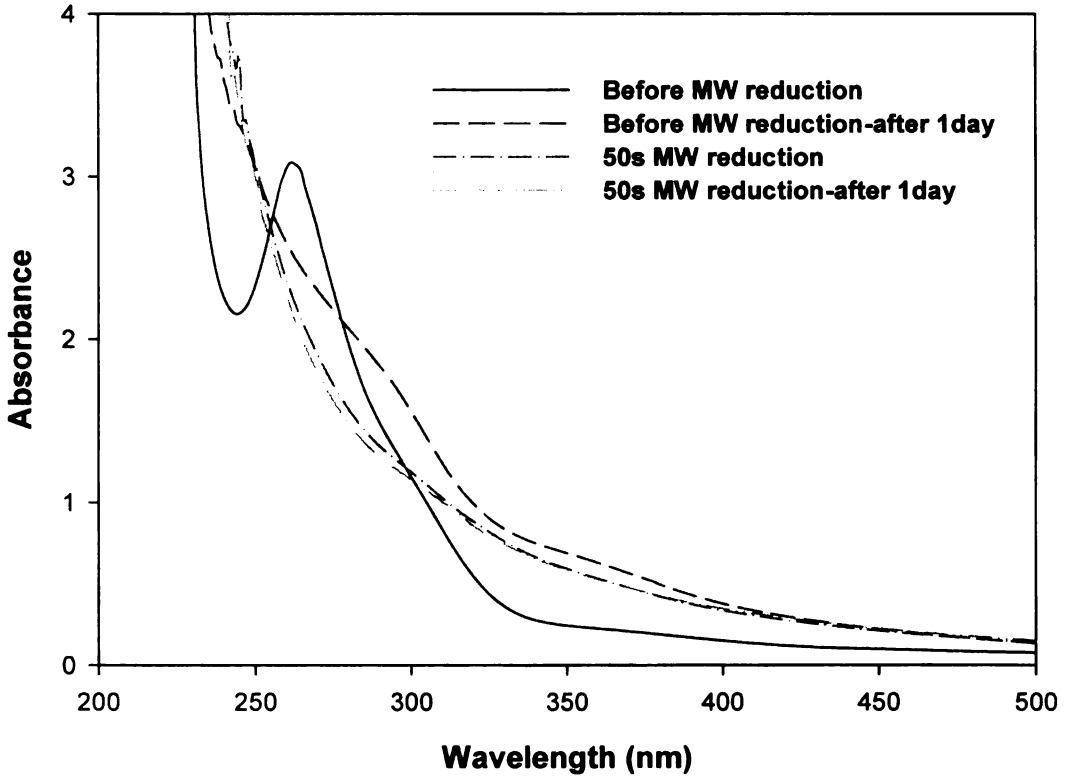

Figure 4.8. UV-vis absorption spectral change showing the ability of bmimSCN reducing Pt ions.

4.3.2 Unsupported Metal Nanoparticles

Three samples of unsupported Pt nanoparticles were synthesized in the absence and the presence of bmimPF_6 and bmimCH_3CO_2 by MW irradiation in ethylene glycol in order to know if there is the ability of RTIL as a stabilizing agent. **Figure 4.9** show TEM micrographs of Pt nanoparticles and corresponding Pt size distribution histograms of the samples. The size and the size distribution of the metal particles was obtained by measuring the size of 150 ~ 200 randomly selected particles in TEM images.

Pt particles reduced by MW irradiation in ethylene glycol without the addition of the RTIL were easily precipitated. It was observed as in **Figure 4.9 (a)** that, most of the Pt

nanoparticles were agglomerated and connected to form a network, resulting from the absence of capping materials which terminate particle growth and prevent Ostwald ripening (also referred to as *coarsening*) of the metal particles. The corresponding histogram revealed that the average particle size was 6.22 ± 0.87 nm and it size distribution was rather wide. Unlike Pt particles prepared without the RTIL, no immediate precipitation of Pt nanoparticles synthesized in the presence of bmimPF_6 occurred but some precipitated Pt particles were found 2 day later. They seemed to exist in the form of agglomeration as in Pt-N but actually were well separated individually and 3-dimensionally as in **Figure 4.9 (b)** with the mean size of 2.05 ± 0.27nm. On the other hand, there was no precipitation of Pt particles prepared with the addition of bmimCH_3CO_2 even after long storage for days, demonstrating high stability of the Pt particles. TEM image of the Pt metals in **Figure 4.9 (c)** shows a remarkably uniform and high dispersion of Pt metals on a copper grid. Pt particles have the average diameter of 1.62 nm ± 0.27 with a much narrower particle size distribution compared with Pt particles obtained in the absence of RTIL. Similar results were obtained from other RTIL used in this work.

It is generally agreed now that the size of metal nanoparticles depends on the reduction rate of the metal sources [58]. The faster the reduction rate, the smaller the metal particles are generated. It has also been proved in UV-vis measurements that the reduction rate of the Pt precursor increases with the addition of RTIL and is proportional to RTIL content. Therefore, the formation of much smaller Pt particles in the presence of RTIL results from the further accelerated fast heating due to the high polarity of RTIL under microwave irradiation. Additionally, the homogenous MW heating reduces the

temperature and concentration gradients in the ethylene glycol and thus provides a uniform environment for the nucleation and growth of metal particles, as well as to produce a narrow distribution of metal particles. Another important factor for the formation of the smaller unprotected Pt particles in the presence of RTIL is its low interface tension. RTIL is easily adsorbed onto the surface of metal particles which reduces the tendency to undergo Ostwald ripening [59]. As a result, very small particles are generated.

Although there was no obvious evidence from UV-vis spectrometry investigation, how can the high stabilized Pt nanoparticles prepared in the presence of bmimPF_6 and bmimCH_3CO_2 be explained? The plausible answer may be the fact that the intrinsic high charge and the steric bulk of RTILs can create an electrostatic and steric colloid-type stabilization of transition-metal nanoparticles, which was proved by the Dupont group [60, 61]. When the metal-nanoparticles have been stabilized or capped by ionic liquids, it will be quite meaningful to define them as metal-doped or metal-containing ionic liquids which have potential for many chemical reactions [62, 63]. It is worth noting that RTILs can stabilize and facilitate the formation of small Pt particle with a narrow size distribution from the simple Pt precursor via MW reduction.

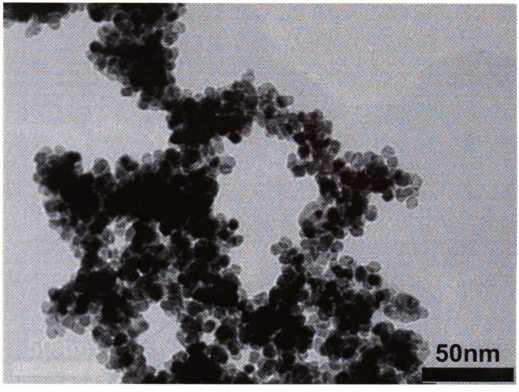

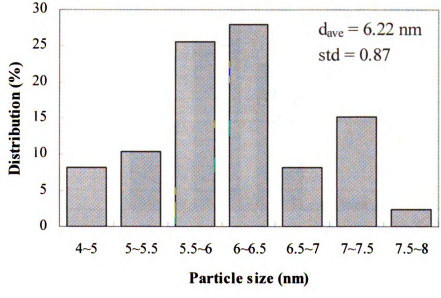

(a)

Figure 4.9. TEM analyses of Pt nanoparticles in the absence (a) and the presence of (b) bmimPF_6 and (c) bmimCH_3CO_2.

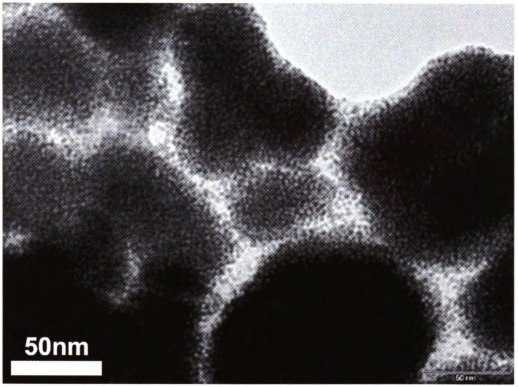

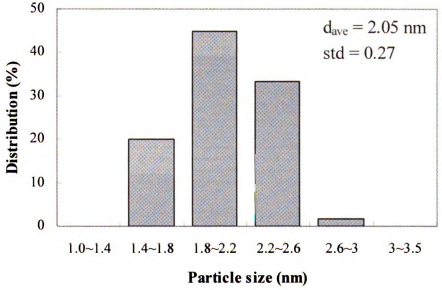

(b)

Figure 4.9. Continued

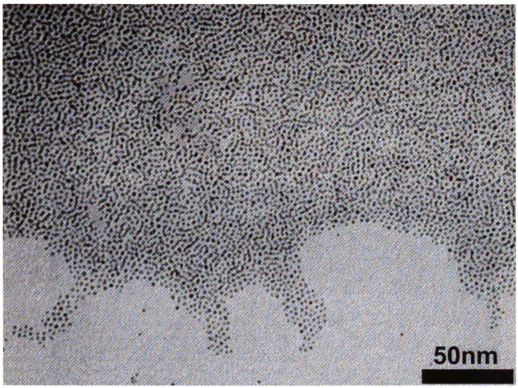

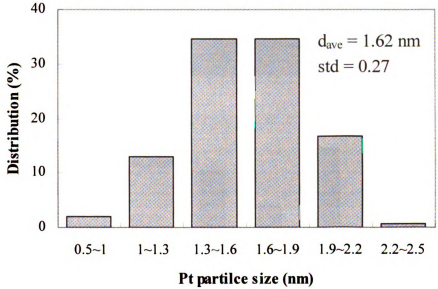

(c)

Figure 4.9. Continued

TEM analysis of Ru nanoparticles synthesized with the addition of $bmimCH_3CO_2$ via microwave irradiation is shown in **Figure 4.10**. Like Pt nanoparticles produced at the same reaction condition, Ru particles were separated and stabilized by the RTIL. The mean size of the particles was 1.08nm and the size distribution was very narrow.

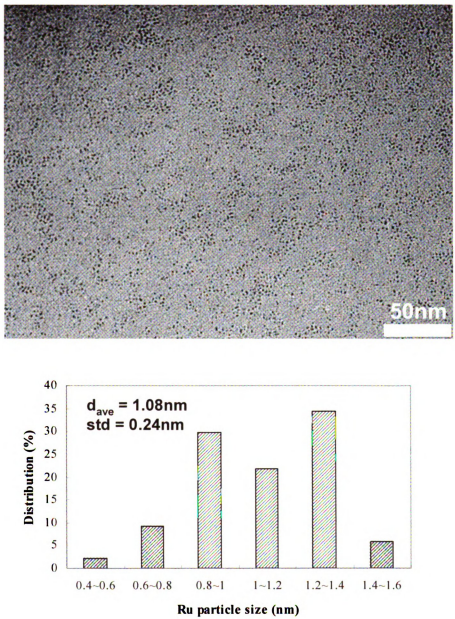

Figure 4.10. TEM analysis of Ru nanoparticles with the addition of $bmimCH_3CO_2$.

Pd nanoparticles were also prepared with the addition of bmimSCN and seen in **Figure 4.11**. The extremely small size of Pd particles (1nm in diameter) existed in a similar form as Pt particles synthesized with bmimPF_6.

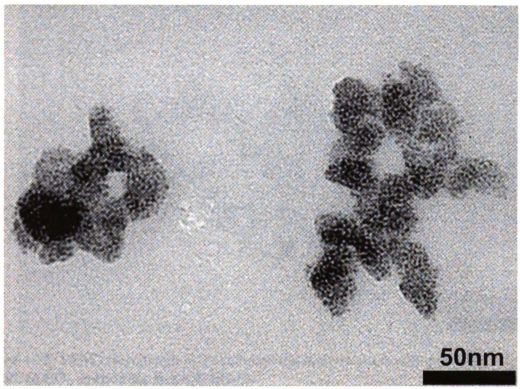

Figure 4.11. TEM image of Pd nanoparticles with the addition of bmimSCN.

The Pt precursor was reduced only in bmimCH_3CO_2 by MW heating process at the same condition for the synthesis unsupported Pt metals to investigate the ability of RTIL reducing the Pt precursor. After 30 second in a microwave, light gray powders corresponding to irregular Pt networks as in **Figure 4.12** were precipitated, suggesting that bmimCH_3CO_2 itself can also reduce the Pt precursor to Pt nanoparticles via microwave heating. High polarizability of RTIL due to large positive ions makes it a very good medium for absorbing microwave radiation [64]. Hence the use of RTIL for the

synthesis of inorganic nanostructures may lead to interesting research such as for the large-scale production of gold nanosheets in bmimPF_6 by microwave reduction [65].

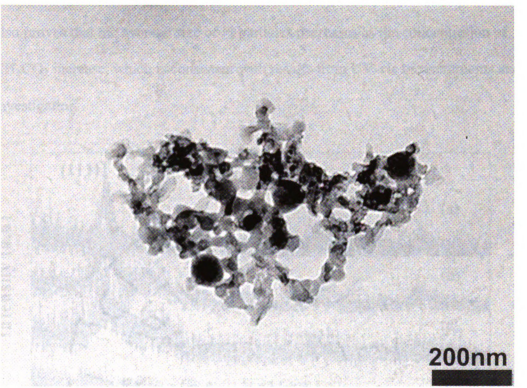

Figure 4.12. TEM micrograph of Pt reduced via microwave heating of 1mL bmimCH_3CO_2 containing $H_2PtCl_6 \cdot 6H_2O$.

The crystalline structure of unsupported platinum nanoparticles was obtained by using powder X-ray diffraction (XRD). **Figure 4.13** shows the XRD patterns of the platinum nanoparticles prepared in the presence of various amount of bmimCH_3CO_2. The four clear peaks, namely (111), (200), (220), and (311), identified by Miller indices were shown in the sample (**Figure 4.13 a**) synthesized without the addition of bmimCH_3CO_2. The peaks were consistent with face centered cubic (fcc) crystalline for Pt. The four characteristic peaks became broader as the content of the RTIL increased (**Figure 4.13 b and c**). When the molar ratio between bmimCH_3CO_2 and Pt precursor became over 20

(**Figure 4.13d**), the diffraction peaks disappeared. The peak broadening in the XRD pattern indicates the formation of Pt particles in the nanometer scale [66] and validates the efficiency of the present experimental technique to produce nanosized metal particles. XRD also proves that the average size of Pt particles decreases as the concentration of $bmimCH_3CO_2$ increase, which is consistent with results from UV-vis measurements and TEM investigation.

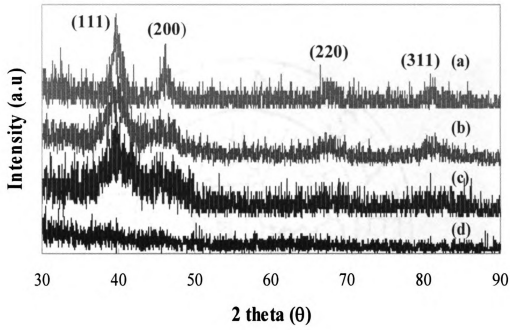

Figure 4.13. X-ray diffraction patterns of Pt nanoparticles synthesized in EG at (a) $bmimCH_3CO_2$/Pt precursor = 0, (b) 2.5, (c) 5, and (d) 20.

4.3.3 Carbon Supported Pt Catalysts

4.3.3.1 Multiwalled carbon nanotube (MWNT)-supported Pt particles

Pt nanoparticle supported MWNT were synthesized via microwave-polyol process in the presence of all of the RTIL used in this work. The molar ratio of RTIL to Pt precursor was fixed at 50. Their TEM images are shown in **Figure 4.14**. The largest Pt was

produced in the absence of any RTIL and the smallest Pt in the presence of bmimSCN. The size of Pt particles is in the decreasing order of Pt-N > Pt-bmimCH_3SO_4 > Pt-bmimPF_6 > Pt-bmimCH_3CO_2 > Pt-bmimSCN as expected from the results of UV-vis measurement in which the reduction rate was in the increasing order of Pt-N < Pt-bmimCH_3SO_4 < Pt-bmimPF_6 < Pt-bmimCH_3CO_2. The smallest Pt with the addition of bmimSCN is resulted from the synergic effect of bmimSCN as a good microwave absorbent, strong protecting agent as well as weak reducing agent.

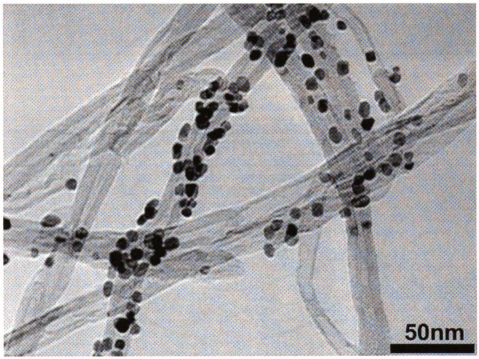

(a)

Figure 4.14. TEM images of (a) Pt/MWNT-N and (b) Pt/MWNT- bmimCH_3SO_4, (c) Pt/MWNT-bmimPF_6, (c) Pt/MWNT- bmimCH_3CO_2, and (e) Pt/MWNT-bmimSCN.

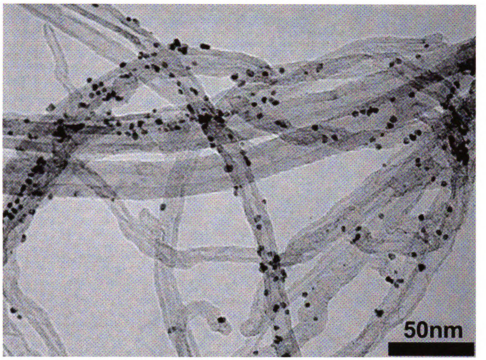

(b)

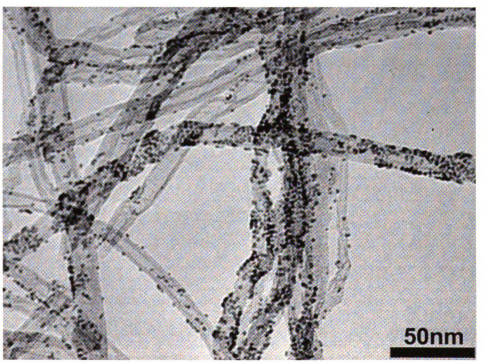

(c)

Figure 4.14. Continued.

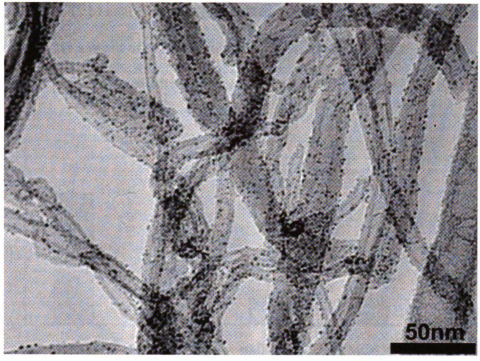

(d)

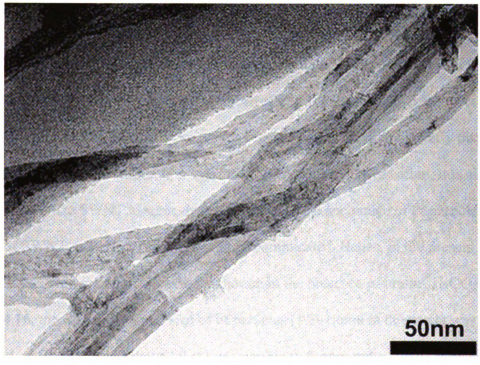

(e)

Figure 4.14. Continued.

The result of TEM analysis for Pt particles dispersed on the surface MWNT is shown in **Figure 4.15**. As a result of the introduction of RTIL, the average size and standard deviation of Pt particles drastically decreased, indicating the improved size distribution.

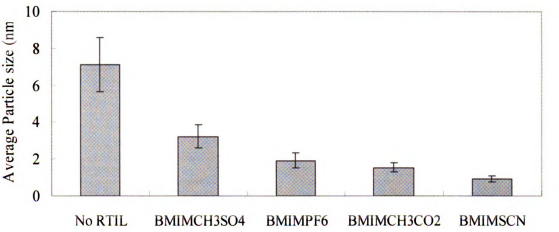

Figure 4.15. Average size of Pt nanoparticles supported on MWNT synthesized in the presence of different RTILs.

A few reports on the deposition of Pt nanoparticles on SWNT [67~69] was found very recently. However, the size and dispersion of Pt particles seemed to have yet to reach at the satisfactory level in those papers because they were not uniformly dispersed on SWNT and their size distribution was quite broad. Before Pt deposition, it is also required to oxidize SWNT to some degree to improve the anchorage of Pt particle on the surface of SWNT, which makes the procedure complicated. Hence, in the present work, Pt/SWNT has been prepared via MW irradiation in the presence of bmimCH_3CO_2. As in **Figure 4.16**, the extremely small size of Pt particles (1.3~1.6nm in diameter) was highly dispersed on SWNT. It is believed that it is possible to further reduction of their size with the addition of bmimSCN.

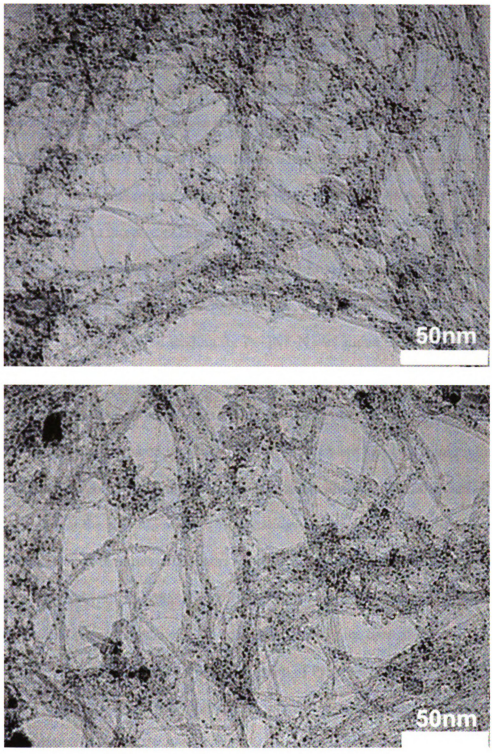

Figure 4.16 TEM images of Pt particles dispersed on SWNT synthesized in the presence of bmimCH_3CO_2.

4.3.2.1 Graphite nanofiber (GNF)-supported Pt nanocomposites

TEM morphologies of Pt/GNF-N, Pt/GNF-bmimPF_6, and Pt/GNF- bmimCH_3CO_2 nanocomposites with 20wt. % metal loading and the effect of RTIL on the mean size of Pt phase corresponding to each sample are shown in **Figure 4.17**. It has been known that there are difficulties in depositing Pt onto carbon nanofibers or graphite nanofibers via colloidal and conventional routes. Hence, multistep deposition/decomposition of Pt precursor is applied to increase Pt metal loading on them [70, 71]. The problem continued even in microwave process as in **Figure 4.17a**. It was found that only approximately 10 wt.% of Pt was deposited onto GNF in final product, even though Pt precursor corresponding to 20wt. % metal loading for Pt/GNF-N was added to the starting mixture. The above fact confirms that Pt can not be efficiently supported on GNF even using conventional microwave-polyol process. However, it was obvious from **Figure 4.17b** and **4.17c** that the samples prepared in the presence of RTILs were highly covered with smaller Pt particles compared to those synthesized in the absence of RTIL. Therefore, it is clearly seen that the addition of RTIL in microwave-polyol process for the preparation of GNF-supported Pt particles contributes not only to increase Pt loading deposited onto GNF but also to generate the smaller Pt particles with narrow the size distribution. It is worth noting that the agglomerates of Pt are rarely found in the case of Pt/GNF-bmimCH_3CO_2. The effect of RTIL on the reduction of Pt size for GNF-supported catalysts is clearly shown in **Figure 4.17d**. The average sizes of Pt particles in Pt/GNF-N, Pt/GNF-bmimPF_6, and Pt/GNF-bmimCH_3CO_2 catalysts are 3.3 ± 1.1nm, 2.46 ± 0.7nm, and 1.53 ± 0.4nm, respectively.

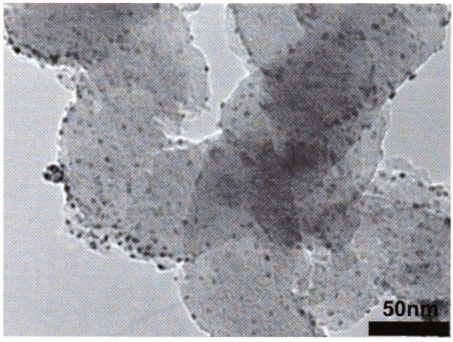

(a)

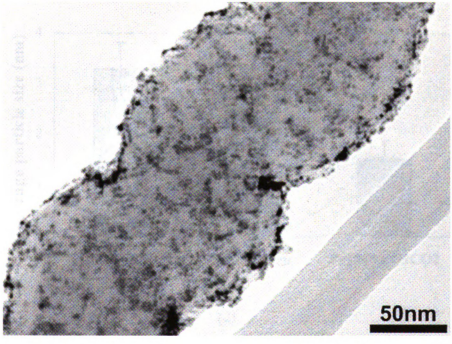

(b)

Figure 4.17. TEM morphologies of spiral graphite nanofiber (GNF)-supported Pt (20wt.%) nanocomposites by microwave heating process (a) in the absence of RTIL and in the presence of (b) bmimPF_6 and (c) bmimCH_3CO_2 and (d) the mean size of Pt particles obtained from TEM analysis for all the samples.

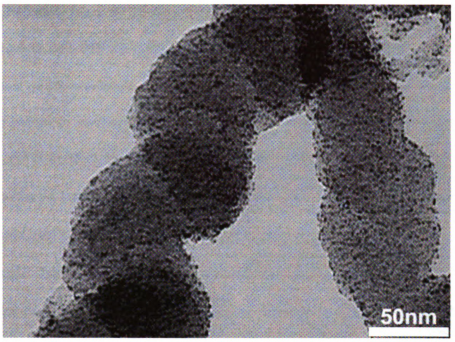

(c)

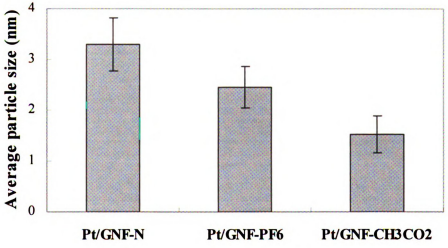

(d)

Figure 4.17. Continued.

4.3.2.3 Carbon black (CB)-supported Pt Nanocomposites

Figure 4.18 and **4.19** show TEM analysis of Pt particles supported on XC-72R carbon black which was fabricated by microwave dielectric heating in the presence and absence of $bmimPF_6$ and $bmimCH_3CO_2$. Nanosized Pt particles were quite uniformly dispersed on CB in all of the samples. However, the mean particle size of Pt in Pt/CB-N nanocomposite was about 3.38 ± 1.01 nm, while the size of Pt in Pt/CB-$bmimPF_6$ and Pt/CB-$bmimCH_3CO_2$ were 1.75 ± 0.74 nm and 1.28 ± 0.24nm, respectively. In addition, the Pt particle distribution of Pt/CB-N was much broader than that of Pt/CB-$bmimPF_6$ and Pt/CB-$bmimCH_3CO_2$. The results explain the addition of RTIL in synthesizing CB-supported Pt catalyst is very effective to reduce the Pt size and improve Pt dispersion on the surface of CB as in the Pt dispersed on MWNT and GNF, which is expected to enhance the electrocatalytic activity for fuel cell applications.

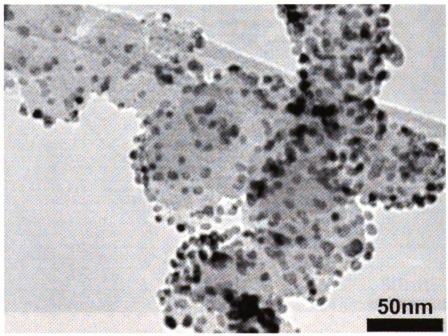

(a)

Figure 4.18. TEM morphologies of (a) Pt/XC-72R-N, (b) Pt/XC-72R-$bmimPF_6$ and (c) Pt/XC-72R-$bmimCH_3CO_2$ composites.

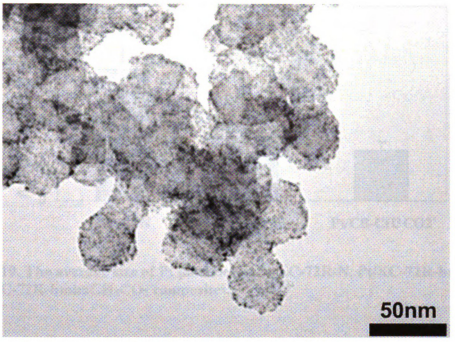

(b)

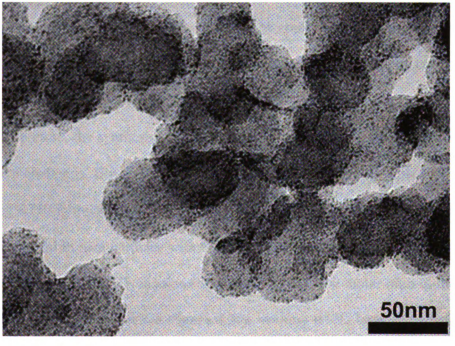

(c)

Figure 4.18. Continued.

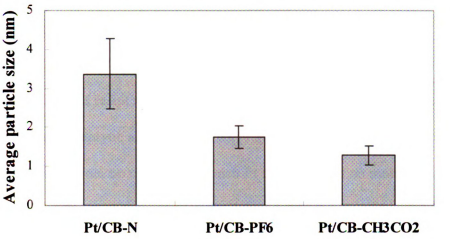

Figure 4.19. The average size of Pt particles in Pt/XC-72R-N, Pt/XC-72R-bmimPF_6 and Pt/XC-72R-bmimCH_3CO_2 composites.

4.3.2.4 Highly loaded Pt/carbon nanocomposites

It is difficult to achieve the synthesis of Pt catalysts with high metal loadings (> 30wt.%) and small particle sizes at the same time by applying conventional methods [72-74]. Metal particle size for a catalyst with 10wt.% and 30wt. % Pt loading can be produced at 2.0nm and 3.2nm, respectively, but increase to 8.8nm for a 60wt. % Pt catalysts. Therefore, the synthesis of highly dispersed and highly loaded nanosized metal catalysts is a challenge. However, the problem can be resolved by a simple method of introducing RTIL in microwave process. **Figure 4.20** shows TEM images various carbons-supported Pt nanoparticles with 60wt. % metal loading which were produced without or with bmimCH_3CO_2 in microwave heat process. The molar ratio of the RTIL to the Pt salt was set at 50. As seen in **Figure 4.20a**, without RTIL, large Pt particles over 9nm in average size were highly agglomerated and the coarsening of the particles by Ostwald ripening was clearly shown. The corresponding size histogram (not shown here) showed very broad distribution. However, when Pt dispersed on the carbons was

synthesized in the present of RTIL, the mean size of Pt particles decreased strikingly below 2.0nm with a narrow size distribution and they were very well dispersed on the carbons (**Figure 4. 20 b and c**). Agglomerates of Pt particles were rarely found in spite of high loading metals. This result suggests a simple and effective way of tuning active surface area of Pt and catalytic activity of carbon supported Pt catalyst by controlling the particle size and dispersion, no matter how much Pt is loaded and no matter what kinds of carbon support is used.

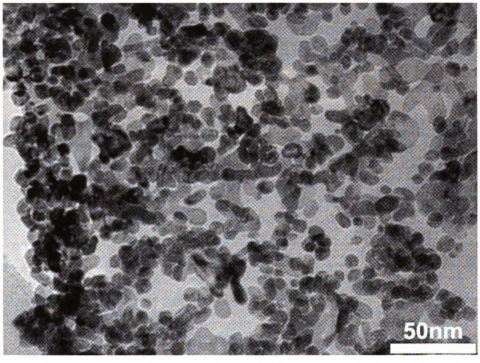

(a)

Figure 4.20. TEM images of Pt nanoparticles highly loaded on (a) Pt/xGnP-N, (b) Pt/Vulcan XC-72R-bmimCH_3CO_2 and (c) Pt/MWNT-bmimCH_3CO_2.

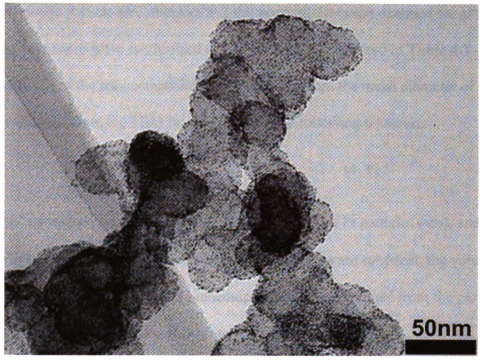

(b)

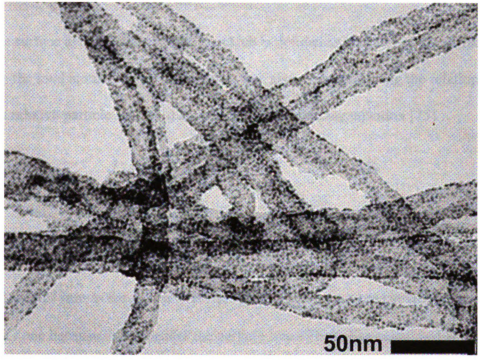

(c)

Figure 4.20. Continued.

The average particle size diameter and the standard deviation obtained for all of the Pt/carbon nanocomposites synthesized in this work are summarized in **Table 4.1**. The surface area (S) of the nanocomposites was calculated from the mean diameter of the particles obtained from the TEM images by using the following equation:

$$S = \frac{6000}{\rho d} \qquad (4.1)$$

where S is the surface area (m^2/g), d is the mean diameter of Pt particles (nm), and ρ is the density of Pt ($21.4 g/cm^3$). Assuming that all Pt particles are spherical, the volume-surface mean diameter (d_{vs}) of each nanocomposte could be obtained from the particle size distribution according to the following equation:

$$d_{vs} = \frac{\sum n d_i^3}{\sum n d_i^{2.19}} \qquad (4.2)$$

Then the surface average dispersion (D), which is defined as the ratio of the surface atoms to the total atoms within the particles, was also calculated using the relationship between relative particle size (d_{rel}) according to the following equation [75].

$$d_{rel} = \frac{d_{vs}}{d_{at}} \qquad (4.3)$$

$$D = \frac{2.64}{(d_{rel})^{0.81}} \qquad (4.4)$$

where $d_{at} \cong 0.278$nm as the atomic diameter of Pt. These equations provide more accurate than other one because they consider the particle size effects. The calculated D values for all nanocomposites are also included in the **Table 4.1**.

Table 4.1 Information of Pt particles on various carbon supports synthesized via RTIL assisted MW heating process

samples	Pt content (wt. %)	d (nm)	S (m^2/g)	D (%)
Pt/MWNT-N	20	7.10 ± 1.47	39.47	18.22
Pt/MWNT-bmimPF_6	20	1.92 ± 0.40	145.80	51.72
Pt/MWNT-bmimCH_3CO_2	20	1.55 ± 0.25	181.03	63.08
Pt/MWNT-bmimCH_3CO_2	60	1.65 ± 0.26	169.72	59.94
Pt/MWNT-bmimCH_3SO_4	20	3.23 ± 0.63	86.80	34.27
Pt/MWNT-bmimSCN	20	0.93 ± 0.17	301.48	94.20
Pt/CB-N	20	5.56 ± 0.90	50.36	22.45
Pt/CB- bmimPF_6	20	1.75 ± 0.29	160.18	56.88
Pt/CB- bmimCH_3CO_2	20	1.28 ± 0.24	218.98	76.08
Pt/CB- bmimCH_3CO_2	60	1.57 ± 0.32	181.03	61.44
Pt/GNF-N	20	3.29 ± 0.53	85.22	34.33
Pt/GNF- bmimPF_6	20	2.46 ± 0.41	113.97	43.33
Pt/GNF- bmimCH_3CO_2	20	1.52 ± 0.36	184.46	61.05
Pt/xGnP-N	20	3.74 ± 0.64	74.93	30.94
Pt/xGnP-N	60	8.25 ± 1.59	33.97	18.32
Pt/xGnP-bmimPF_6	20	1.95 ± 0.37	144.05	51.51
Pt/xGnP-bmimCH_3CO_2	20	1.68 ± 0.30	166.81	56.17
Pt/xGnP-bmimCH_3CO_2	60	1.58 ± 0.33	175.15	59.89

It can be seen from the Table that Pt/C nanocomposites prepared via MW irraidiation in the presence of RTIL generally exhibit surface area and dispersion of Pt particles than Pt/C prepared in the absence of RTIL. Especially, the surface area and dispersion of Pt particles in Pt/C-bmimSCN are extremely high over 300m3/g and 90%, respectively, so

that bmimSCN may provide the chance to synthesize the excellent catalysts with high catalytic activity. Therefore, the present preparation method developed in this work seems to be a great way to obtain the supported nanosized noble metal nanoparticles with a narrow size distribution and thus a great dispersion on the supports.

4.3.3 Metal Oxide Supported Pt Catalysts

Nanocomposites composed of noble metal nanoparticles and metal oxides such as TiO_2, CeO_2, ZrO_2, etc, have attracted much attention because they possess extraordinary catalytic, optical and electronic properties [76, 77]. Such nanocomposites are of great importance as catalysts for next generation power/energy conversion devices. Pt/TiO_2 nanocomposite is most attractive among various combinations because it is a key material in biomass conversion, solar energy conversion, photocatalytic cells, and photochatalytic water splitting [78]. Their catalytic properties are influenced by interaction between metal and support and the size of metal phase. Hence, it is challengeable to develop new method of manipulating the size and dispersion of metal particles by which metal-support interactions is affected. Pt nanoparticles dispersed on TiO_2 nanopowders fabricated via MW process in the presence of $bmimCH_3CO_2$ were compared to those in the absence of it in Figure 4.21. Pt/TiO_2-$bmimCH_3CO_2$ nanocomposite consisted of much smaller particles with narrow size distribution and better dispersion than Pt/TiO_2-N. Similar results were obtained with CeO_2 and Al_2O_3nanopowders as shown in **Figure 4.21 (c) ~ (f)**. Therefore, MW process assisted with RTIL can also be an effective way to produce supported noble metal particles on various metal oxides.

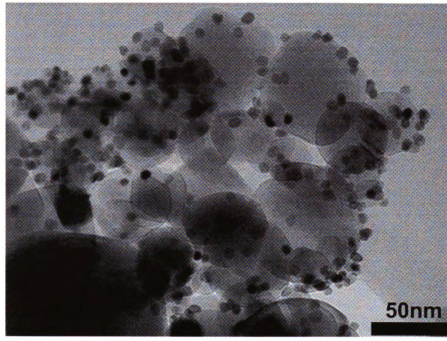

(a)

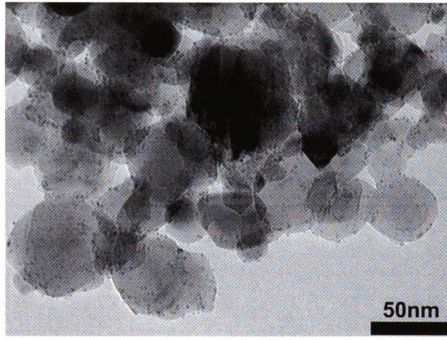

(b)

Figure 4.21. TEM images of Pt particles in (a) Pt/TiO_2–N, (b) Pt/TiO2-$bmimCH_3CO_2$, (c) Pt/CeO_2-N, (d) Pt/CeO2-$bmimCH_3CO_2$, (e) Pt/Al_2O_3-N, and (f) Pt/Al_2O_3-$bmimCH_3CO_2$.

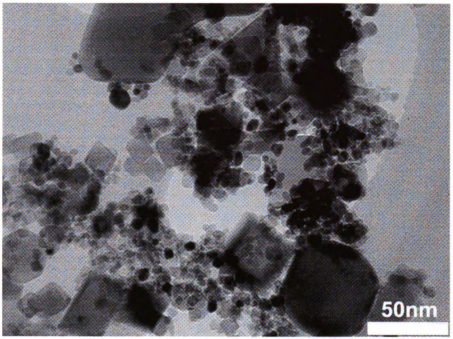

(c)

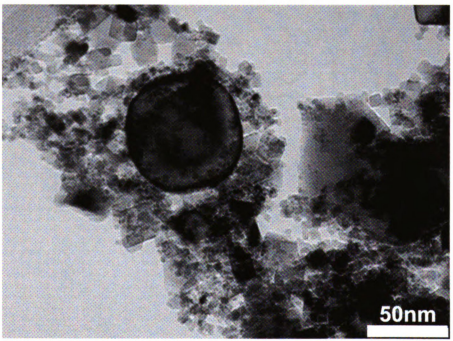

(d)

Figure 4.21. Continued.

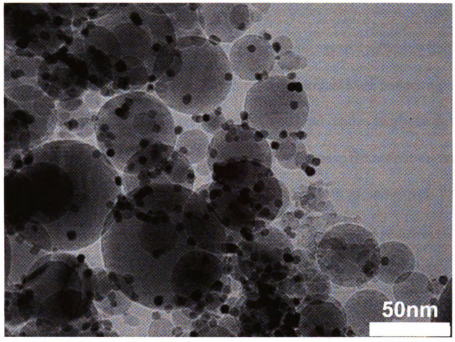

(e)

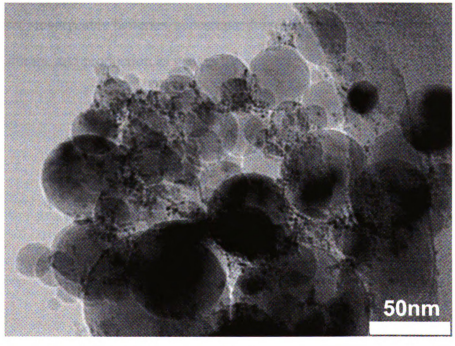

(f)

Figure 4.21. Continued.

4.4 Conclusion

A simple and effective RTIL-assisted microwave process to synthesize uniform small metal powders with a narrow size distribution and to fabricate nanocomposites consisting of metals dispersed either on carbons or on metal oxides has been developed. It has demonstrated that RTIL can act as a promoter to increase the reduction rate of metal salt, a protecting material to prevent metal particles from growing and agglomerating each other, and a reducing agent to reduce metal ions to metal particles in microwave heating process. It has also shown that metal particles can be highly dispersed on various carbon and metal oxides with the help of RTIL. Depending on the combination of metal particles and support materials, such novel method is expected to have promising applications in a wide variety of fields including industrial catalysts, automobiles, rechargeable batteries, supercapacitors, low temperature fuel cells, hydrogen storage and production as well as for sensors.

4.5 Bibliography

1. J. Le Bars, U. specht, J.S. Bradley, and D. Blackmond, "A Catalytic Probe of the Surface of Colloidal Palladium Particles Using Heck Coupling Reactions", Langmuir, 15, p7621-7625, 1999.

2. G. Schmid, "Large clusters and colloids. Metals in the embryonic state", Chem. Rev., 92, p1709-1727, 1992.

3. M.C. Daniel and D. Astrue, "Gold nanoparticles: Assembly, supramolecular chemistry, quantum-size-related properties, and applications toward biology, catalysis, and nanotechnology", Chem. Rev., 104, p293-346, 2004.

4. V.L. Colvin, M.C. Schlamp, and A.P. Alivisatos, "Light emitting diodes made from cadmium selenide nanocrystals and a semiconducting polymer", Nature, 370, p354-357, 1994.

5. R. Elghanian, J. Storhoff, R. Mucic, R. Letsinger, and C. Mirkin, "Selective colorimetric detection of polynucleotides based on the distance-dependent optical properties of gold nanoparticles", Science, 277, p1078-1081, 1997.

6. S. Chen, R. Ingram, M. Hostetler, J. Pietron, R. Murray, T. Schaaff, J. Khoury, M. Alvarez, and R. Whetten, "Gold nanoelectrodes of varied size: Transition to molecule-like charging", Science, 280, p2098-2101, 1998.

7. H. Bonnemann and R.M. Richards, "Nanoscopic metal particles - Synthetic methods and potential applications", Eur. J. Inorg. Chem., 10, p2455, 2001.

8. T. Yonezawa, S. Onoue, and N. Kimizuka, "Preparation of Highly Positively Charged Silver Nanoballs and Their Stability", Langmuir, 16, p5218, 2000.

9. I.S. Armadi, Z.L. Wang, T.C. Green, A. Henglein, M.A. El-Sayed, "Shape-controlled synthesis of colloidal platinum nanoparticles", Science, 272, p1924, 1996.

10. L.L. Hench and J.K. West, "The sol-gel process", Chem. Rev., 90, p33-72, 1990.

11. R. Zana, "Microemulsions", Heterog. Chem. Rev., 1, 145-157, 1994.

12. G. Demazeau, "Solvothermal processes: a route to the stabilization of new materials", J. Mater. Chem., 9, p15-18, 1999.

13. U.K. Gautam, M. Ghosh, M. Rajamathi, and R. Seshardri, "Solvothermal routes to capped oxide and chalcogenide nanoparticles", Pure Appl. Chem., 74, p1643-1649, 2002.

14. M.T. Reetz and W. Helbig, "Size-Selective Synthesis of Nanostructured Transition Metal Clusters", J. Am. Chem. Soc., 116, p7401, 1994.

15. K.S. Suslick, "Sonochemistry"Science, 247, p1439-1445, 1990.

16. F. Fievet, J.P. Lagier, M. Figlarz, "Homogeneous and heterogeneous nucleations in the polyol process for the preparation of micron and sub-micron size metal particles", Solid State Ionics, 32-33, p198-205, 1989.

17. L Motte, F. Billoudet, E. Lacaze, J. Douin, and M.P. Pileni, "Self-Organization into 2D and 3D Superlattices of Nanosized Particles Differing by Their Size", J. Phys. Chem. B, 101, p138, 1997.

18. D.V. Leff, P.C. Ohara, J.R. Heath, and W.M. Gelbart, "Thermodynamic Control of Gold Nanocrystal Size: Experiment and Theory", J. Phys. Chem., 99, p7036, 1995.

19. J.H. Fendler and F.C. Meldrum, "The colloid-chemical approach to nanostructured materials", Adv. Mater., 7, p607-632, 1995.

20. T. Teranishi, I. Kiyokawa, and M. Miyake, "Synthesis of monodisperse gold nanoparticles using linear polymers as protective agents", Adv. Mater., 10, p596, 1988.

21. H.S. Gandhi, G.W. Graham, and R.W. McCabe, "Automotive exhaust catalysis", J. Catal., 216, p433-442, 2003.

22. M. Fernandez-Garcia, A. Martinez-Arias, L.N. Salamanca, J.M. Cornado, J.A. Anderson, J.C. Conesa, and J. Soria, "Influence of ceria on Pd activity for the CO+O-2 reaction", J. Catal, 187, p474-485, 1999.

23. X. Zhang, S. Huang, G. Wu, S. Lu, and Z. Cai, "Tin oxide-graphite composite for lithium storage material in lithium-ion batteries", Rare Metals, 22, p226-229, 2003.

24. J. Xie and V.K. Varadan, "Synthesis and characterization of high surface area tin oxide/functionalized carbon nanotubes composite as anode materials", Mater. Chem. and Phy., 91, p274-280, 2005.

25. Y. Shan and L. Gao, "Multiwalled carbon nanotubes/Co3O4 nanocomposites and its electrochemical performance in lithium storage", Chemistry Letters, 33, p1560-1561, 2004.

26. H. Huang, E.M. Kelder and J. Schoonman, "Graphite-metal oxide composites as anode for Li-ion batteries", J. Power Sources, 97-98, p114-117, 2001.

27. Y. Wang and X. Zhang, "Preparation and electrochemical capacitance of RuO2/TiO2 nanotubes composites", Electrochim. Acta, 49, p1957-1962, 2004.

28. G. Arabale, D. Wagh, M. Kulkarni, I.S. Mulla, S.P. Vernekar, K. Vijayamohanan, and A.M. Rao, "Enhanced supercapacitance of multiwalled carbon nanotubes functionalized with ruthenium oxide", Chem. Phys. Lett., 376, p207-213, p2003.

29. X. Qin, S. Durbach, and G.T. Wu, "Electrochemical characterization on RuO2 center dot xH(2)O/carbon nanotubes composite electrodes for high energy density supercapacitors", Carbon, 42, p451-453, 2004,

30. C. Wang and C. Hu, Mater. Chem. and Phys., 83, p289-297, 2004.

31. R. Parsons and T. Vandernoot, J. Electroanal. Chem., 257, p9, 1998.

32. E. Antolini, "Formation of carbon-supported PtM alloys for low temperature fuel cells: a review", Mater. Chem. Phys., 78, p563-573, 2003.

33. C. Rice, S. Ha, R.I. Masel, A. Wieckowski, "Catalysts for direct formic acid fuel cells", J. Power Sources, 115, p229-235, 2003.

34. R. Zacharia, K.Y. Kim, A.K.M. Fazle kibria, and K.S. Nahm, "Enhancement of hydrogen storage capacity of carbon nanotubes via spill-over from vanadium and palladium nanoparticles", Chem. Phys. Lett., 412, p369-375, 2005.

35. H.S. Kim, H. Lee, K.S. Han, J.H. Kim, M.S. Song, M.S. Park, J.Y. Lee and J.K. Kang, "Hydrogen Storage in Ni Nanoparticle-Dispersed Multiwalled Carbon Nanotubes", J. Phys. Chem. B, 109, p8983-8986, 2005.

36. M. Yang, Y. Yang, Y. Liu, G. Shen, and R. Yu, Biosensors and Bioelectronics, 21, p1125-1131, 2006.

37. F. Gloaguen, J.M. Leger, and C. Lamy, "Electrocatalytic oxidation of methanol on platinum nanoparticles electrodeposited onto porous carbon substrates", J. Appl. Electrochem., 27, p1052-1060, 1997.

38. R. Dillon, S. Srinivasan, A.S. Arico, and V. Antonucci, "International activities in DMFC R&D: status of technologies and potential applications", J. Power Sources, 127, p112-126, 2004.

39. Y. Takasu, T. Kawaguchi, W. Sugimoto, Y. Murakami, Electrochim. Acta, 48, p169, 2001.

40. A.S. Arico, L. Pino, P.L. Antonucci, and N. Giordano, "The role of Pt loadind, thermal treatment and exposure to air on the acid-base behavior of a Pt-carbon black catalyst", Carbon, 28, p599-609, 1990.

41. C.A. Bessel, K. Laubernds, N.M. Rodriguez, and R.T.K. Baker, "Graphite Nanofibers as an Electrode for Fuel Cell Applications", J. Phys. Chem. B, 105, p1115-1118, 2001.

42. E.S. Steigerwalt, G.A. Delunga, and C.M. Lukehart, "Pt-Ru/Carbon Fiber Nanocomposites: Synthesis, Characterization, and Performance as Anode Catalysts of Direct Methanol Fuel Cells. A Search for Exceptional Performance", J. Phys. Chem. B, 106, p760-766, 2002.

43. T. Hyeon, S. Han, Y.E. Sung, K.W. Park, and Y.W. Kim, "High-performance direct methanol fuel cell electrodes using solid-phase-synthesized carbon nanocoils", Angew. Chem. Int. Ed., 42, p4352-4356, 2003.

44. K.W. park, Y.E. Sung, S. Han, Y. Yun, and T. Hyeon, "Origin of the Enhanced Catalytic Activity of Carbon Nanocoil-Supported PtRu Alloy Electrocatalysts", J. Phys. Chem. B, 108, p939-944, 2004.

45. W.Z. Li, C.H. Liang, J.S. Qiu, G.Q. Sun, and Q. Xin, "Carbon nanotubes as support for cathode catalyst of a direct methanol fuel cell", Carbon, 40, p791-794, 2002.

46. G. Girishkumar, T.D. Hall, K. Vinodgopal, and P.V. Kamat, "Single Wall Carbon Nanotube Supports for Portable Direct Methanol Fuel Cells", J. Phys. Chem. B, 110, p107-114, 2006.

47. Y.C. Liu, X.P. Qiu, Y.Q. Huang, W.T. Zhu, "Methanol electro-oxidation on mesocarbon microbead supported Pt catalysts", Carbon, 40, p2375-2380, 2002.

48. T. Yoshitake, Y. Shimakawa, S. Kuroshima, H. Kimura, T. Ichihashi, and Y. Kubo, "Preparation of fine platinum catalyst supported on single-wall carbon nanohorns for fuel cell application", Phys. B. Condens Mater., 323, p124-126, 2002.

49. S.Y. Zhao, S.H. Chen, S.Y. Wang, D.G. Li, and H.Y. Ma, "Preparation, Phase Transfer, and Self-Assembled Monolayers of Cubic Pt Nanoparticles" Langmuir, 18, p3315-3318, 2002.

50. D.G. Dff, P.P. Edwards, B.F.G. Johnson, "Formation of a Polymer-Protected Platinum Sol: A New Understanding of the Parameters Controlling Morphology", J. Phys. Chem, 99, p15934-15944, 1995.

51. Z. Li, Z. Liu, J. Zhang, B. Han, J. Du, Y. Gao, and T. Jiang, "Synthesis of Single-Crystal Gold Nanosheets of Large Size in Ionic Liquids", J. Phys. Chem. B, 109, p14445-14448, 2005.

52. Y. Zhu, W. Wang, R. Qi, and X. Hu, "Microwave-assisted synthesis of single-crystalline tellurium nanorods and nanowires in ionic liquids", Angew. Chem. Int. Ed, 43, p1410-1414, 2004.

53. Y. Jiang and Y. Zhu, "Microwave-Assisted Synthesis of Sulfide M_2S_3 (M = Bi, Sb) Nanorods Using an Ionic Liquid", J. Phys. Chem. B, 109, p4361-4364, 2005.

54. T. Teranishi, M. Hosoe, T. Tanaka, and M. Miyake, "Size Control of Monodispersed Pt Nanoparticles and Their 2D Organization by Electrophoretic Deposition", J. Phys. Chem. B, 103, p3818-3827, 1999.

55. C. Chiappe and D. Pieraccini, "Ionic liquids: solvent properties and organic reactivity", J. Phys. Org. Chem., 18, p275-297, 2005.

56. A.J. Charmichael and K.R. Seddon, "Polarity study of some 1-alkyl-3-methylimidazolium ambient-temperature ionic liquids with the solvatochromic dye, Nile Red", J. Phys. Org. Chem., 13, p591-595, 2000.

57. N. Toshima, K. Nakata, and H. Kitoh, "Giant platinum clusters with organic ligands: preparation and catalysis", Inorg. Chim. Acta, p149-153, 1997.

58. Z. Liu, J.Y. Lee, W. Chen, M. Han, and L.M. Gan, "Physical and Electrochemical Characterizations of Microwave-Assisted Polyol Preparation of Carbon-Supported PtRu Nanoparticles", Langmuir, 20, p181-187, 2004.

59. M. Antonietti, D. Kuang, B. Smarsly, and Y. Zhou, "Ionic liquids for the convenient synthesis of functional nanoparticles and other inorganic nanostructures", Angew. Chem. Int. Ed. 43, p4988-4992, 2004.

60. G.S. Fonseca, A.P. Umpierre, P.F.P. Fichtner, S.R. Teixeira, and J. Dupont, "The use of imidazolium ionic liquids for the formation and stabilization of Ir-0 and Rh-0 nanoparticles: Efficient catalysts for the hydrogenation of arenes", Chem. Eur. J., 9, p3263-3269, 2003.

61. C.W. Scheeren, G. Machado, J. Dupont, P.F.P. Fichtner, and S.R. Texeira, "Nanoscale Pt(0) Particles Prepared in Imidazolium Room Temperature Ionic Liquids: Synthesis from an Organometallic Precursor, Characterization, and Catalytic Properties in Hydrogenation Reactions", Inorg. Chem., 42, p4738~4742, 2003.

62. J. Huang, T. Jiang, B. Han, H. Gao, Y. Chang, G. Zhao, and W. Wu, "Hydrogenation of olefins using ligand-stabilized palladium nanoparticles in an ionic liquid", Chem. Commum., p1654-1655, 2003.

63. R. Tatumi, and H. Fujihara, "Remarkably stable gold nanoparticles functionalized with a zwitterionic liquid based on imidazolium sulfonate in a high concentration of aqueous electrolyte and ionic liquid", Chem. Commum., p83-85, 2005.

64. N.E. Leadbeater and H.M. Torenius, "A Study of the Ionic Liquid Mediated Microwave Heating of Organic Solvents", J. Org. Chem., 67, p3145-3148, 2002.

65. Z. Li, Z. Liu, J. Zhang, B. Han, J. Du, Y. Gao, and T. Jiang, "Synthesis of Single-Crystal Gold Nanosheets of Large Size in Ionic Liquids", J. Phys. Chem. B, 109, p14445-14448, 2005.

66. V. Radmilovic, H.A. Gasteiger, and P.N. Ross, "Structure and chemical composition of a supported PtRu electrocatalyst for methanol oxidation", J. Catal., 154, p98-106, 1995.

67. V. Lordi, N. Yao, and J. Wei, "Method for Supporting Platinum on Single-Walled Carbon Nanotubes for a Selective Hydrogenation Catalyst", Chem. Mater., 13, p733-737, 2001.

68. A. Kongkanand, S. Kuwabata, G. Girishkumar, and P. Kamat, "Single-Wall Carbon Nanotubes Supported Platinum Nanoparticles with Improved Electrocatalytic Activity for Oxygen Reduction Reaction", Langmuir, 22, p2392-2396, 2006.

69. G. Girishkumar, T.D. Hall, K. Vinodgopal, and P. Kamat, "Single Wall Carbon Nanotube Supports for Portable Direct Methanol Fuel Cells", J. Phys. Chem. B, 110, p107-114, 2006.

70. E.S. Steigerwalt, G.A. Deluga, D.E. Cliffel, and C.M. Lukehart, "A Pt-Ru/Graphitic Carbon Nanofiber Nanocomposite Exhibiting High Relative Performance as a Direct-Methanol Fuel Cell Anode Catalyst", J. Phys. Chem. B, 105, p8097-8101, 2001.

71. R.T.K. Baker, N. Rodriguez, A. Mastalir, U. Wild, R. Schlogl, A. Wootsch, and Z. Paal, "Platinum/Graphite Nanofiber Catalysts of Various Structure: Characterization and Catalytic Properties", J. Phys. Chem. B, 108, p14348-14355, 2004.

72. M. Watanabe and K. Sakairi, "Electrode for polymer electrolyte electrochemical cell and process of preparing same", US Patent, 5728485, 1998.

73. P. Stonehart, "Platinum alloy catalyst", US Patent, 5593934, 1997.

74. A. Gamez, D. Richard, P. Gallezot, F. Gloaguen, R. Faure, R. Durand, "Oxygen reduction on well-defined platinum nanoparticles inside recast ionomer", Electrochim. Acta, 41, p307, 1996.

75. A. Borodzinski and M. Bonarowska, "Relation between Crystallite Size and Dispersion on Supported Metal Catalysts", Langmuir, 13, p5613, 1997.

76. X. Wang, J.C. Yu, H.Y. Yip, L. Wu, P.K. Wong, and S.Y. Lai, "A mesoporous Pt/TiO2 nanoarchitecture with catalytic and photocatalytic functions", Chem. Eur. J., 11, p2997-3004, 2005.

77. H. Nakajima, T. Mori, and M. Watanabe, "Influence of platinum loading on photoluminescence of TiO2 powder", J. of Appl. Phys., 96, p925-927, 2004.

78. A. Galinska and J. Walendziewski, "Photocatalytic water splitting over Pt-TiO2 in the presence of sacrificial reagents", Energy & Fuels, 19, p1143-1147, 2005.

CHAPTER 5

THE EVALUATION OF EXFOLIATED GRAPHITE NANOPLATELETS (xGnP) AS A SUPPORT FOR Pt CATALYSTS IN DIRECT METHANOL FUEL CELL

5.1 Introduction

Fuel cells have attracted attention because they can provide an alternative way to reduce the dependence on fossil fuels. Direct methanol fuel cell (DMFC) seems to be the most promising among the various types of fuel cells. It is expected to be used in portable power sources and transportation in the near future [1~3]. However, DMFC has critical shortcomings which include methanol crossover from anode to cathode, slow kinetics at both anode and cathode, and the cost of the precious metal catalysts [4~6]. One strategy for last two problems is to achieve maximum utilization of the precious metal catalysts which is possible by dispersing small metal particles on support materials without any agglomeration. Platinum-based nanoparticles supported on conductive supports with high surface area are currently and widely used as electrocatalysts in DMFC [7~11].

The catalytic activity of supported Pt catalysts is determined by many factors such as the size and size distribution of Pt particles, their shape, and the crystallographic orientation of Pt [12, 13]. This implies that the catalytic performance of supported Pt particles depends on the synthetic route used to produce them. It is difficult to achieve a high degree of dispersion of nanosized platinum particle with narrow size distribution on the surface of supports through a conventional synthetic method. Therefore, it is still desirable to develop an alternative simple and effective technique to manipulate Pt particle shape, size, and distribution. The ideal method should be applicable to all kinds of supports without any pretreatment and should produce consistent catalytic activity in spite of large scale synthesis.

The catalytic activity of supported Pt particles is also related to the nature of the supports [14]. Carbons are ideal for supporting nanosized Pt particles because they are

the only material having all of the essential properties such as high electrical conductivity, high surface area, excellent crystallinity, good corrosion resistance, appropriate pore structure, surface properties conducive to water-handling capability, and low cost. Those properties are critical requirements which a good support should have. Carbon black, especially XC-72 carbon, has been widely studied as a support but it has been shown that the presence of micropores and sulfuric acid groups on XC-72 carbon black lead to a poor utilization and aggregation of Pt particles, respectively [15, 16]. Hence, a variety of novel carbon nanostructures such as single wall carbon nanotube (SWNT) and multiwall carbon nanotube MWNT), graphite nanofiber (GNF), carbon nanohorn (CNH), carbon nanocoil (CNC) have been investigated and have shown promising results [17~23]. Among them, SWNT and MWNT appear to be the most promising due to their excellent thermal, mechanical and electrical properties [24, 25]. As an additionally advantage of both MWNT and SWNT, Pt particles dispersed on the external walls of them are highly effective since it is easier to make contact with the reactant gas or liquid than those in the pores of other carbons.

Exfoliated graphite nanoplatelets (xGnP) have been produced in MSU by expanding the graphite layers from graphite intercalation compounds via a specific thermal shock and downsizing the expanded layers through ultrasonication and/or milling process. xGnP meets the key properties required as an excellent carbon support. It has high surface area, excellent corrosion resistance and superior mechanical and electrical properties [26, 27]. xGnP is a much more cost-effective than SWNT and MWNT. In addition, if Pt nanoparticles are well dispersed on the surface of xGnP, they can make easy contact with the reactant as CNT and thus utilization of the catalyst is expected to

increase. In spit of such great benefits, the potential application of xGnP as a carbon support has not been fully investigated.

In this chapter, the superior properties of xGnP to other carbons are manifested and a simple technique to prepare xGnP supported Pt nanoparticles is reported. The method is related to the reduction of Pt precursor in ethylene glycol solution in the presence of room temperature ionic liquid (RTIL) and xGnP via microwave irradiation. The influence of preparation conditions such as water and RTIL content were investigated. XRD, XPS, and TEM characterizations were carried out to determine the particle size and distribution. Cyclic voltammetry measurements for xGnP supported Pt catalysts were performed to evaluate their catalytic activity. The results were compared with those of a commercially available Pt catalysts deposited on XC-72R carbon black from E-TEK.

5.2 Experimental Details

5.2.1 Materials

Chloroplatinic acid hexahydrate ($H_2PtCl_6 \cdot 6H_2O$) was purchased from Aldrich and used as a Pt precursor. Ethylene glycol (EG, bp = 197.3°C), diethylene glycol (DEG, bp = 245°C), and triethylene glycol (TEG, bp = 285°C) from J.T. Baker were used as agents to reduce the Pt precursor. Two different RTILs, 1-butyl-3-methylimidazolium hexafluorophosphate ($bmimPF_6$) and 1-butyl-3-methylimidazolium acetate ($bmimCH_3CO_2$), were used in this work. Their chemical structures are shown in Figure 4.1 of chapter 4. $bmimPF_6$ is denoted as **RTIL-1** and $bmimCH_3CO_2$ as **RTIL-2** in this chapter for convenience. Both of them were purchased Aldrich and used as received. xGnP produced in MSU was used as a carbon support. **Figure 5.1** shows typical

dimension of xGnP which has average thickness of 12nm and average diameter of 1μm. MWNT, carbon black (CB, Vulcan XC-72R), and GNF were purchased from Aldrich, Cabot Co., and Nanomirae Inc., respectively and used for comparison. Purified SWNT from Southwest was also used for that purpose.

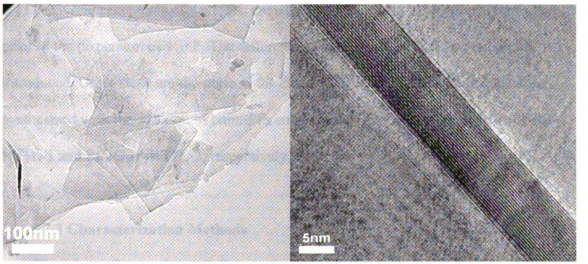

Figure 5.1 Typical TEM pictures of xGnP.

5.2.2 Preparation of xGnP Supported Catalysts

Typical procedures to fabricate Pt/xGnP catalysts with 20wt. % Pt loading in the absence of RTIL consist of the following steps: In a glass beaker, xGnP is ultrasonically dispersed in 18mL EG for 30 min and the EG solution containing xGnP is cooled down to room temperature under mechanical stirring. In another 10 ml beaker, a specific quantity of the Pt precursor is added to 2 ml EG and completely dissolved. Contents in those beakers are mechanically mixed in a 100mL beaker for another 30 min, transferred into a commercial microwave oven (National, 2.45GHz, 1300W), and irradiated under air for a total of 50seconds to reduce the Pt precursor. After cooling down to ambient

temperature, the resulting suspension was centrifuged and the residual slurry was washed with acetone several times and dried in a vacuum oven at 373K overnight. The weight ratio of Pt and xGnP was controlled according to the targeted metal loading on the support. The catalysts obtained in this way are called as the **Pt/xGnP-N**.

For Pt (20wt. %)/xGnP catalysts synthesized in the presence of the **RTIL-1** and **RTIL-2**, various contents of the RTIL are added and dissolved in 18mL ethylene glycol prior to the dispersion of xGnP. The different molar ratios of RTIL/Pt precursor are introduced. Other steps are the same as for Pt/xGnP-N catalyst. The Pt/xGnP catalysts synthesized with the addition of bmimPF_6 and bmimCH_3CO_2 are denoted as **Pt/xGnP-RTIL-1** and **Pt/xGnP-RTIL-2**, respectively.

5.2.3 Characterization Methods

Pt catalysts dispersed on xGnP were characterized by recording their X-ray diffraction (XRD) patterns on a Regaku Rotaflex 200B X-ray diffractometer using Cu-K_α radiation with a curved graphite monochromator in order to identify the phases present in the catalyst and to evaluate the lattice parameter and the particle size of the Pt crystallites dispersed on xGnP. The 2θ region between 10° and 100° was scanned at 45 keV and 100 mV at a scan rate of 5°/min. The average metal particle size was calculated using Scheller equation according to the XRD broadening Pt (220) reflections which was scanned at a rate of 1°/min again. Transmission electron microscopy (TEM) investigation was carried out with JEOL 100CX and JEOL 2200FS operating at a voltage of 100keV and 200keV for the morphology of the dispersed Pt electrocatalysts and the determination of the average size of Pt particles. Specimens were prepared by ultrasonically re-dispersing the

sample powders in acetone for 15 min, applying the power suspension onto lacey carbon coated Cu grids and drying them in air at ambient temperature. Thermo-gravimetric Analysis (TGA 2950, TA instrument) was performed to compare the thermal-oxidative stability of various carbons, evaluate the degradation of xGnP supported Pt catalysts and determine the Pt loading. Samples weighing 3~4mg were tested over temperatures ranging from room temperature to 800°C (for supported Pt catalysts) or 1000°C (carbons) at 20°C/min under flowing air. X-ray photoelectron spectroscopy (XPS) results of Pt/xGnP catalysts were obtained from a Physical Electronics PHI 5400 ESCA system and used to invesitage the presence of the oxide phases and the interaction between Pt and xGnP. The regional XPS of Pt (4f) was de-convoluted to recognize different metallic and oxidation states of Pt on the xGnP.

Electrochemical investigation was performed by cyclic voltammetry (CV) using a potentiostat (Gamry, FAS2 Femtostat). A conventional three-electrode cell equipped with a platinum wire counter electrode, an Ag/AgCl reference electrode, and glassy carbon working electrode was used. The glassy carbon electrode with 3mm diameter was polished to a mirror finish with a 0.05 μm alumina suspension before each experiment. The catalyst ink was prepared by ultrasonically dispersing 5mg of Pt/xGnP catalysts in 0.8ml of alcohol containing 0.1ml of 0.1wt % Nafion solution for 20 min. Then 20 μL of the catalyst ink was micropipetted on the top surface of the glassy carbon electrode. Finally, the electrode was dried at 40°C to yield a Pt loading of about 0.3142mg/cm^2. The CV experiments were performed in 1M H_2SO_4 solution in the absence and the presence of 2M CH_3OH at the scan rate of 50mV/s. All the solutions were prepared by using ultrapure water. N_2 gas was purged for 15 min before starting the experiment. The

chronoamperometry tests were also performed in 2M CH_3OH/1M H_2SO_4 at 0.45V for the period of 3000s to study the catalyst stability.

5.3 Results and Discussions

5.3.1 Comparisons of Various Carbon Supports

Supported electrocatalysts used in the fuel cells have to meet severe performance requirements of long-term stability over 40,000 hours. Oxygen is supplied on the cathode side for oxygen reduction reaction (ORR) and water generated in ORR has to be rapidly removed from the electrode. This environment has the potential for unwanted surface oxidation of carbon supports on the cathode in PEMFC and DMFC. Support corrosion may occur due to the presence of oxygen, which is responsible for the performance loss of PEMFC and DMFC. Therefore, the carbon support inevitably influences the catalytic activity of carbon supported catalysts in ORR at the cathode in PEMFC and DMFC [14]. Good corrosion resistance or oxidation resistance is one of important characteristics that an ideal support should possess for applications in PEMFC and/or DMFC under strong oxidizing conditions. Kinetic stabilization of the support towards corrosion can be accomplished by increasing the graphitization of the carbon supports which in turn facilitate the easy water removal by hydrophobization of the carbon surface.

Figure 5.2 shows the thermo-oxidation stability of various carbon supports measured in an air environment by TGA. Three carbons such as MWNT, XC-72R and xGnP started to decompose above 600°C, while SWNT and GNF were completely decomposed before reaching at 600°C. Thus, MWNT, XC-72R, and xGnP appear to be more appropriate supports than SWNT and GNF on the basis of long-term stability in the oxidizing or

corrosive environment in fuel cell systems. xGnP showed the highest oxidation resistance among all of the support candidates. This is an expected result because the graphite has the highest degree of graphitization among all of the carbons, which is proven from XRD data. Interestingly, the XC-72R CB which is the most widely used in fuel cell showed higher onset temperature for decomposition than either GNF or SWNT, which may suggests a heat treatment of the CB to increase its graphitization.

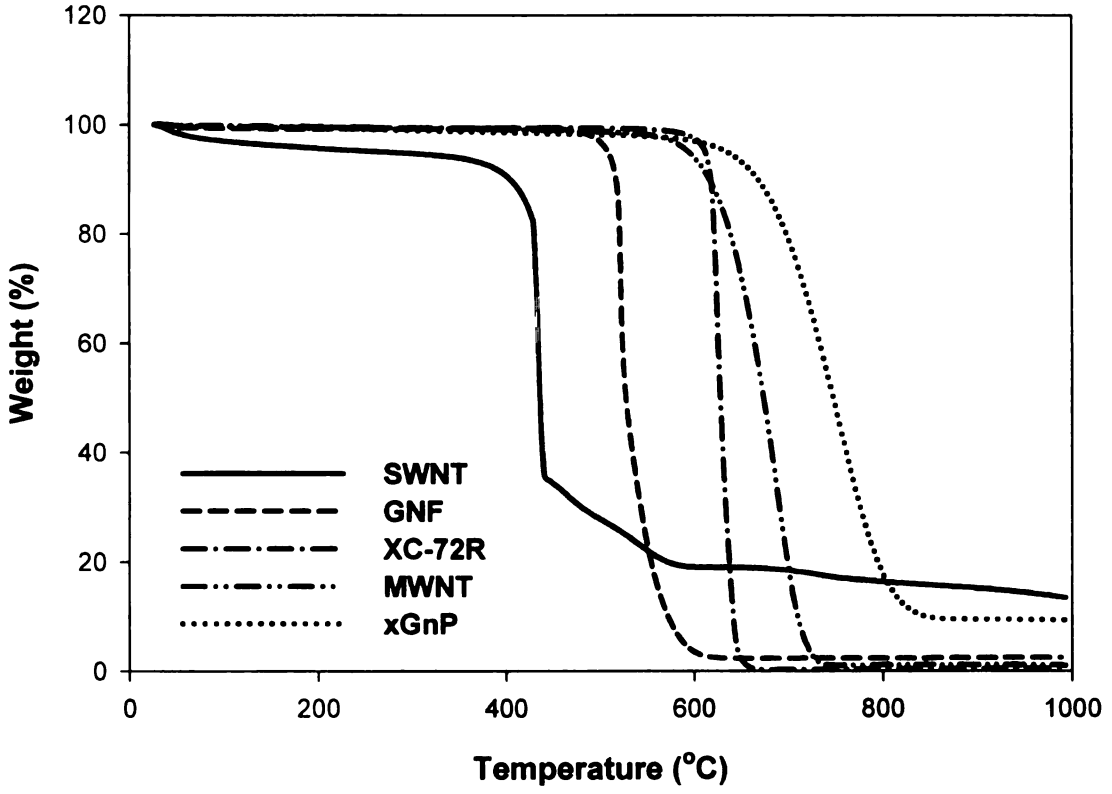

Figure 5.2. Thermo-oxidative stability of various carbon supports in an air environment.

Since the Pt particles loaded on carbons can act as a catalyst for chemical combustion of the carbon support which causes a decrease of fuel cell performance, it is interesting to compare combustion resistance of each carbon loaded with Pt particles.

Hence, XC-72R CB was selected because it is most widely used in fuel cell at present. The combustion stability of xGnP and XC-72R CB loaded with 20wt. % Pt particles is compared in **Figure 5.3**. When both catalysts were exposed to air at elevated temperature, XC-72R lost its weight more rapidly at about 230°C lower temperature than the bare CB. However, the decomposition temperature of xGnP loaded with Pt particles shifted 100oC lower temperature compared to bare xGnP. This result indicates that xGnP support for Pt particles possesses much better stability in oxidizing environment of fuel cells than the commercial one.

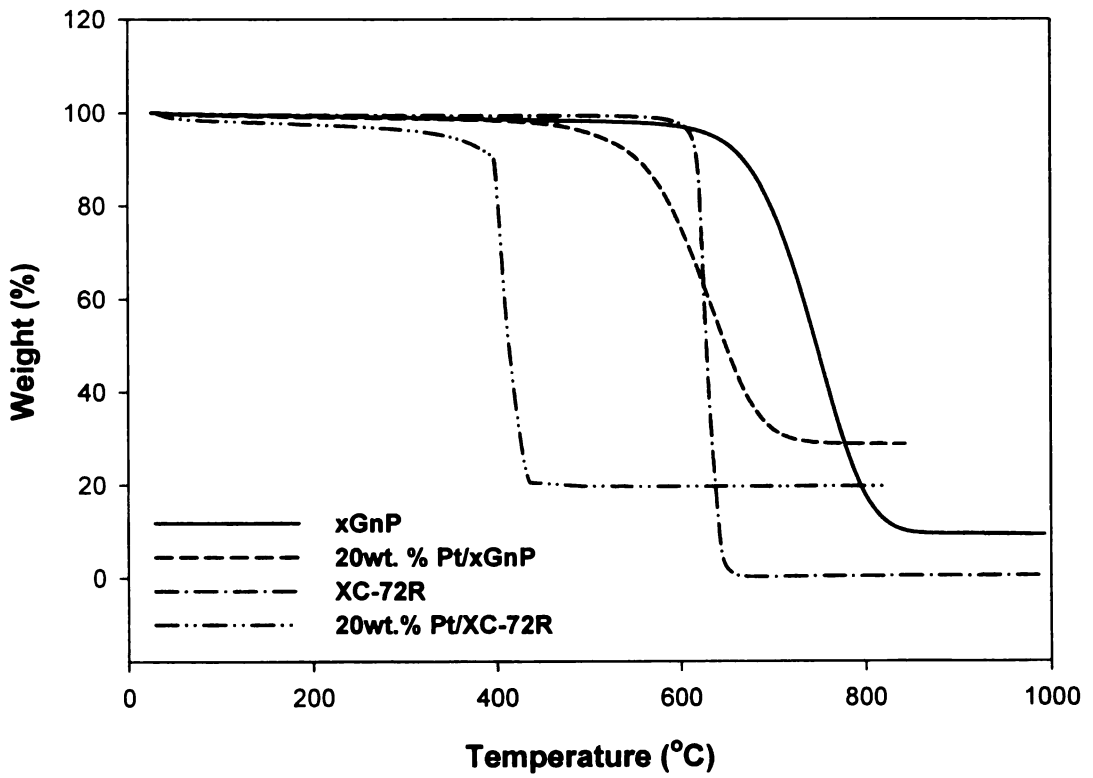

Figure 5.3. Comparison of TGA curves for xGnP and XC-72R with and without 20wt. % Pt particle. Scan rate 25°C/min.

The degree of crystallinity of carbons can be compared from X-ray diffraction analysis. **Figure 5.4** shows X-ray diffraction patterns measured on all the carbon supports used in the present work. There is a common major peak at between $2\theta = 24\sim 26^{\circ}$ corresponding to (002) plane for all carbons and some of carbons have minor peaks at about $2\theta = 44^{\circ}$ and/or 55°. SWNT shows the lowest graphitization with a (002) plane d spacing of 3.49 Å among all carbons, while xGnP has the highest graphitization with a d-spacing of 3.37Å. It is found on the basis of peak height at (002) plane that the degree of crystallinity is in the order of xGnP > GNF > CB > MWNT > SWNT. This provides reason why xGnP showed the best thermo-oxidative stability among all of the carbons.

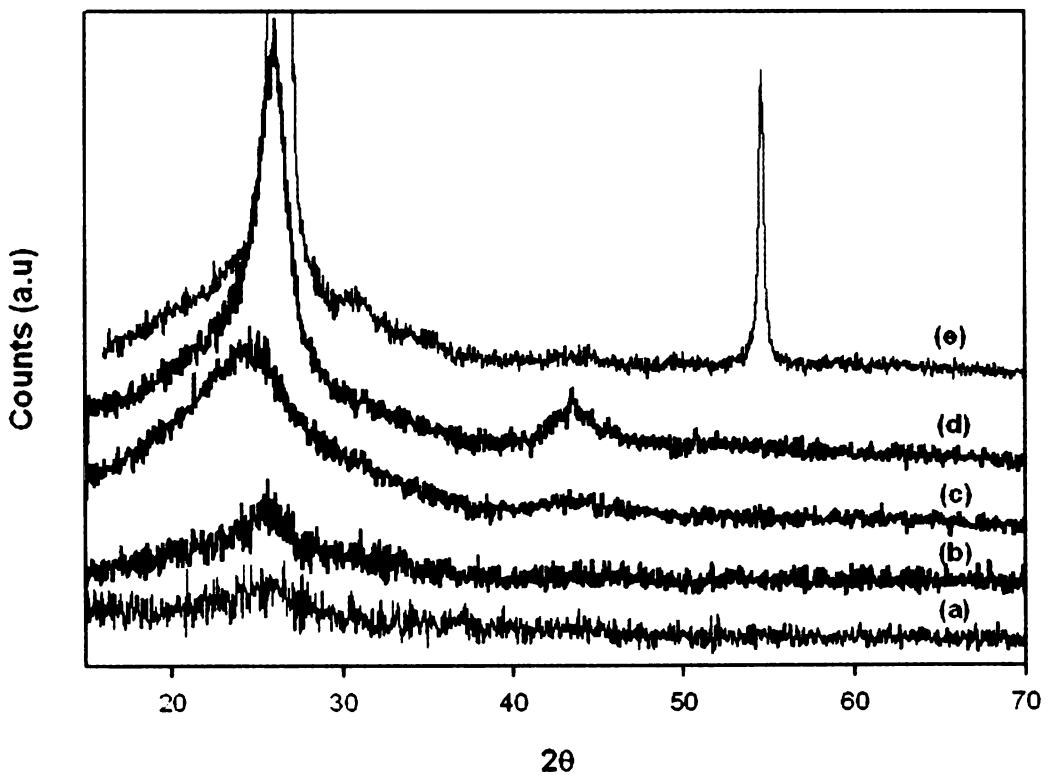

Figure 5.4. X-ray diffraction patterns of various carbon supports (a: SWNT, b: MWNT, c: CB, d: GNF, and e: xGnP) used in the present work.

The crystallite size of individual carbon materials perpendicular to the basal plane can be calculated from the (002) peak according to Debye-Scherrer formula as shown below:

$$D = \frac{0.9\lambda_{K\alpha}}{B(2\theta)\cos\theta_{\max}} \qquad (5.1)$$

where D is the crystallite size, $\lambda_{K\alpha}$ is the X-ray wavelength (0.154138nm), θ_{max} is the maximum angle of the (002) peak, and $B(2\theta_{max})$ is the full width half maximum peak (FWHM) in radian. The results calculated are listed in **Table 5.1**. xGnP has the smallest d-spacing and the largest crystallite which also explain why xGnP showed the highest oxidation and combustion resistance. Consequently, it is proved from TGA and XRD data that xGnP can be an excellent carbon support with good corrosion resistance.

Table 5.1. Characteristics of carbon supports calculated from their XRD pattern

Carbons	θ_{max} (°)	d-spacing	FWHM	$B(2\theta_{max})$	D (nm)
SWNT	25.20	0.349	6.06	0.1058	1.31
MWNT	25.45	0.350	4.69	0.0819	1.74
CB	24.50	0.363	6.90	0.1204	1.18
GNF	26.02	0.342	2.20	0.0384	3.71
xGnP	26.45	0.337	0.24	0.0042	34.02

5.3.2 XRD analysis of Pt/xGnP

Figure 5.5 shows the X-ray diffraction patterns measured on microwave synthesized **Pt/xGnP-N** and **Pt/xGnP-RTIL-2** with the addition of various molar ratio of RTIL-2/Pt. The peaks at about $2\theta = 26.48^{\circ}$ (002) and 54.6° (004) are attributed to the graphite

structure (002) and (004) of xGnP, respectively. For Pt particles, XRD pattern display diffraction characteristic of a face-centered cubic (fcc) crystal structure with major peaks at $2\theta = 39.74^{o}$ (111), 46.32^{o} (200), 67.6^{o} (220), and 81.62^{o} (311). The diffraction peak at $2\theta = 39.74^{o}$ for Pt (111) corresponds well to the d-spacing = 0.227nm at Pt (111) plane. While the sharp reflections are found when low molar ratio of RTIL-2/Pt are introduced, the four characteristic peaks become broader at RTIL-2/Pt = 10 and disappear at RTIL-2/Pt =50. This large extent of peak broadening suggests the formation of very small Pt nanoparticles and their good dispersion [28]. XRD intimates that the average size of Pt particles decreases as the concentration of the RTIL-2 increase and visible evidences are in section 5.3.3.3.

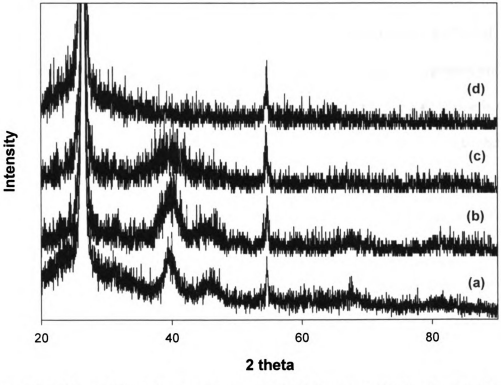

Figure 5.5. X-ray diffraction patterns of Pt/xGnP prepared (a) without RTIL-2 and with the addition of (b) RTIL-2/Pt = 2.5, (c) 10, and (d) 50.

5.3.3 TEM analysis of Pt/xGnP

5.3.3.1. Effect of water

There are two experimental factors to produce metal nanoparticles with different average size dispersed on carbon supports in microwave heating process of EG containing metal precursor. One is to control pH value of EG solution. It has been reported that Pt particles became smaller and more uniformly dispersed on the surface of CNT when the synthesis pH increased [29]. The other is the ratio of EG to distilled (DI) water. This is probably another key factor in controlling the particle size and distribution of Pt on carbon supports in the synthesis of metal particle via microwave heating process, even though it has not been reported. Li et al. reported that, in conventional EG method, smaller and more homogeneous Pt particles are obtained by increasing the concentration of EG or decreasing water content [30]. The mean size of Pt particles was 2.0 nm when no water was added and increased to 4.5 nm when the water content was 70 vol. % in EG. Wang et al. also reported a polyalcohol route for the preparation unsupported noble-metal (Pt, Ru, Rh, etc) nanoclusters, in which they found that the metal particle size is very sensitive to the water content of the solvent [31]. The size of Pt particles was about 1.1nm without the addition of water and about 2.4 nm with the water content of 9 vol. %.

TEM analysis of Pt/xGnP catalysts prepared via microwave irradiation by controlling DI water content in EG solution clearly showed the effect of water content on the size and dispersion of Pt particles supported on xGnP as in **Figure 5.6** and **5.7**. **Figure 5.6a** is a representative TEM image at a low magnification, showing that the whole surface of a single xGnP was very well covered with Pt nanoparticles. As seen in **Figure 5.6 b, c, d** and **Figure 5.7**, the average size of Pt decreased from about 3.8nm to

about 2.6nm as the content of DI water increased from 0 to 50 vol. % in EG solution. This result was contrary to the reports mentioned above. This may result from the different mechanism in synthesizing Pt particles deposited on xGnP. Li et al. and Wang et al. prepared Pt particles through conventional heating method of EG-metal salt solution, which is different from microwave process for this work. It is known that the size of the metal particles is determined by the reduction rate of the metal precursor. The fast heating by microwave irradiation accelerates the reduction of metal precursor and the nucleation of the metal clusters. Hence, the introduction of a high dielectric solvent, DI water (ε = 80.1 at 298K), into a relatively low dielectric EG (ε = 41 at 298K) will help the fast heating which contributed to the formation of small Pt particles by microwave dielectric heating. However, it is worth noting that the presence of a large quantity of water hinders the dispersion of Pt particles on xGnP because DI water has low chemical affinity to the basal plane of xGnP which is highly hydrophobic.

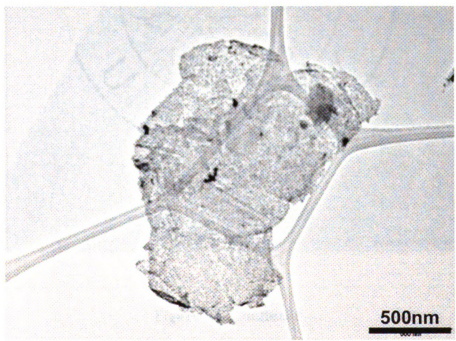

(a)

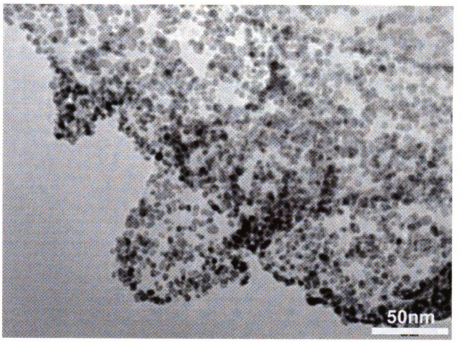

(b)

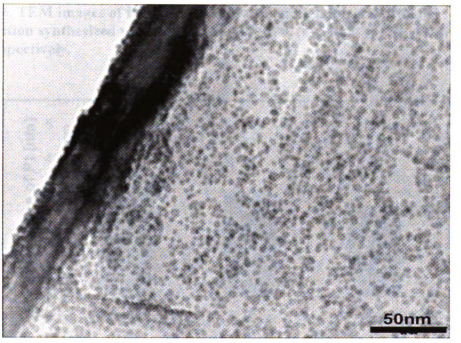

(c)

Figure 5.6. Continued.

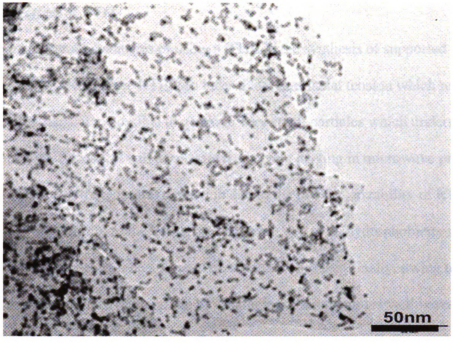

(d)

Figure 5.6. TEM images of Pt/xGnP (a) at low magnification and at high magnification synthesized with the addition of (b) 0, (c) 5, and (d) 50 vol. % DI water, respectively.

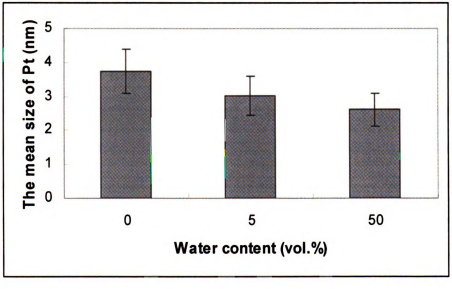

Figure 5.7. The effect of water content in EG on Pt particle size determined in TEM.

5.3.3.2. Effect of RTIL

There are several advantages of using a RTIL in the synthesis of supported metal nanoparticles [32]. First, since RTIL produces a low interfacial tension which results in high nucleation rates, it is possible to generate very small particles which undergo weak Ostwald ripening. Second, it will accelerate the solvent heating in microwave process enough to ensure a sufficient rate of reaction due to the high polarizability of RTIL. Third, RTIL has a strong affinity to the basal plane of xGnP due to its hydrophobicity and thus most of RTIL molecules will be adsorbed on the xGnP surface. Finally, owing to the high thermal stability of RTIL, reactions can be conducted at temperatures well beyond 100°C safely. All of these advantages synergistically accrue to generate well dispersed small Pt particles on the surface of xGnP. **Figure 5.8** and **5.9** show the result s of TEM analysis of **Pt/xGnP-N**, **Pt/xGnP-RTIL-1**, and **Pt/xGnP-RTIL-2**. Compared to Pt particles of 3.74nm in average size obtained in the absence of RTIL (figure 5.8a and 5.9), the mean size of Pt reduced to about 2.0nm when RTIL-1 is introduced to EG (figure 5.8b and 5.9) and further decreased to about 1.68nm when RTIL-2 was added (figure 5.8c and 5.9). The size distribution of Pt particles also was improved by the introduction of RTIL-1 and RTIL-2. As proven by data from UV-vis spectroscopy in chapter 4, RTIL-2 increased the reduction rate of the Pt precursor more rapidly than RTIL-1. Therefore, the smaller Pt particles on the surface of xGnP generated by the addition of RTIL-2 are in good agreement with the result in previous chapter. Consequently, as a result of the presence of RTIL, it is possible to achieve the very high heating rate by microwave, which results in the increase of reduction rate of the metal precursor and thus producing smaller Pt

particles well dispersed on xGnP. RTIL also act as a capping materials of preventing the Pt particles from experiencing Ostwald ripening

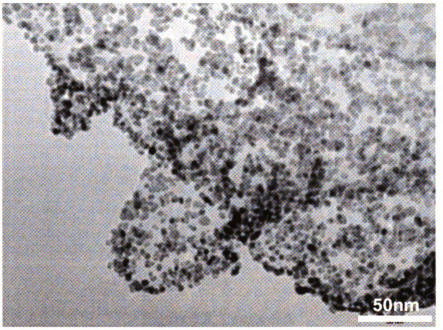

(a)

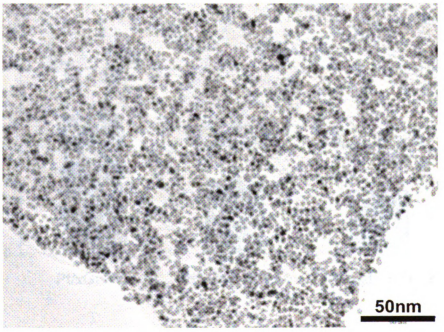

(b)

Figure 5.8. TEM images of (a) Pt/xGnP-N, (b) Pt/xGnP-RTIL-1, and (c) Pt/xGnP-RTIL-2.

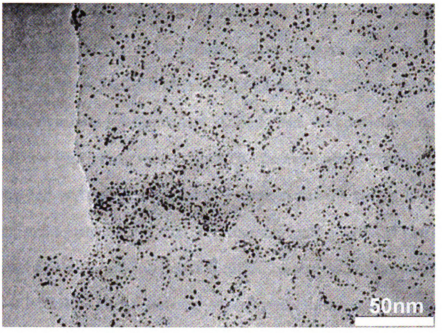

(c)

Figure 5.8. Continued.

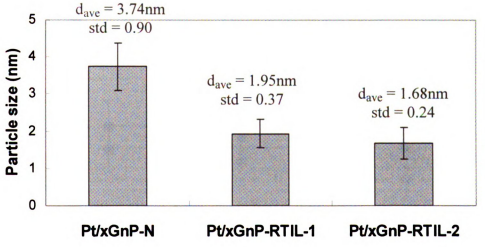

Figure 5.9. The average particle size and size distribution of Pt particles in (a) Pt/xGnP-N, (b) Pt/xGnP-RTIL-1, and (c) Pt/xGnP-RTIL-2.

5.3.3.3. Effect of RTIL content

The effect of RTIL content on the particle size and distribution of Pt particles was investigated. As shown in **Figure 5.10**. Addition of both RTIL results in the reduced size of Pt particles with narrow size distribution. While 3.74nm of Pt particles with large standard deviation were formed without any RTIL, the mean size of Pt particles was reduced below 3nm and their size distribution became narrower when the RTIL corresponding to the molar ratio of RTIL/Pt precursor =1 was added. The size of Pt particles further decreased with increase of the RTIL content but asymptotically approach 1.5nm beyond RTIL/Pt = 10 in molar ratio. Therefore, the RTIL content beyond RTIL/Pt = 10 does not seem to have a great effect on further size reduction of Pt particles on xGnP.

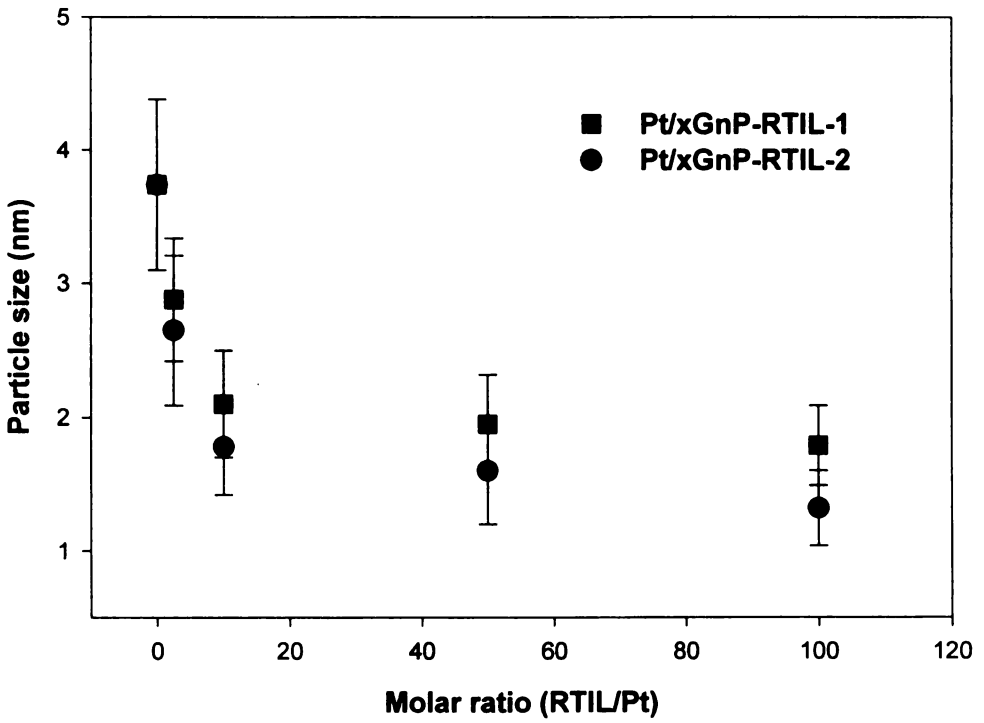

Figure 5.10. Effect of RTIL content on the size of Pt particles supported on xGnP.

5.3.3.3. Effect of reducing agents

The size of the Pt on xGnP synthesized by the present method is dependent on the nature of the reducing agents. Employing DEG or TEG as reducing agents, the change of Pt size was studied and the results are shown in **Figure 5.11**. When Pt/xGnP was prepared in DEG or TEG by microwave heating process without the addition of RTIL-2, the larger Pt particles with irregular shapes were formed on xGnP compared to those in EG (**Figure 5.11a, b** and **Figure 5.8a**) and they were agglomerated. However, the particle size was drastically reduced below 2nm and monodispersed on the xGnP surface when Pt/xGnP catalysts were fabricated in the presence of the RTIL-2. No significant effect of reducing agent on Pt particle size was found in this case.

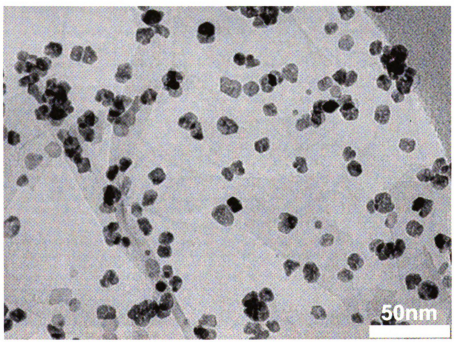

(a)

Figure 5.11. TEM images of Pt/xGnP-N synthesized in (a) DEG and (b) TEG, respectively and Pt/xGnP-RTIL-2 prepared in (c) DEG and (d) TEG, respectively.

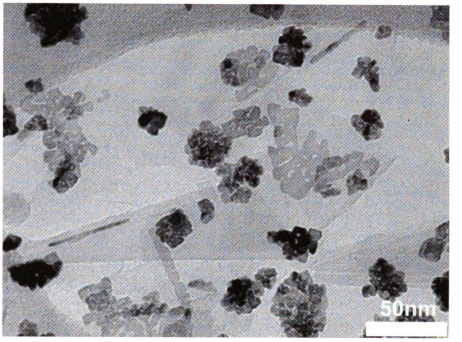

(b)

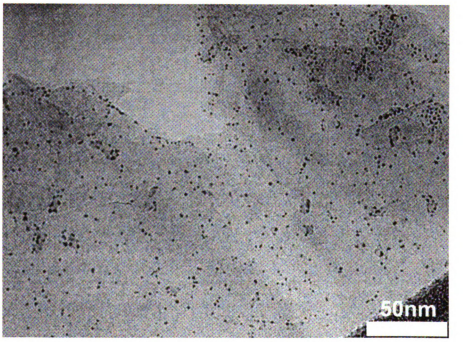

(c)

Figure 5.11. Continued.

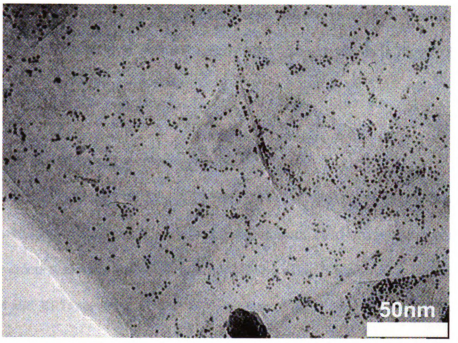

(d)

Figure 5.11. Continued.

Generally, the metal size is influenced by the reduction temperature and reduction rate. The increase of reduction temperature accelerates the reduction rate of the metal precursors, resulting in smaller metal particles with a narrow size distribution. The boiling points of all the reducing agent in the present work are in the order of TEG > DEG > EG. Hence, if Pt/xGnP nanocomposites were prepared through reflux at high temperature, the particle size should be in the order of increasing boiling point. However, since the most important factor dominating the particle size in the microwave heating process is the reduction rate which is determined by the MW-adsorbing properties of the reducing solvents, dielectric constant of each solvent must be considered. Dielectric constant of all the solvents here is in the following order; EG > DEG > TEG [33] which is reverse to the order of boiling point but will be the order of fast reduction rate in

microwave process. Therefore, it is expected that the particles size decreases in the order of TEG > DEG > EG which is well consistent with TEM analysis as in **Figure 5.8** and **5.11**.

5.3.3.4. Comparison of morphological data

In **Table 5.2**, the averages sizes of Pt particles in Pt/xGnP catalysts prepared at different molar ratio of RTIL/Pt precursor measured from TEM images were compared with those calculated from the XRD peak at (220) by using Equation (1). The results from TEM and XRD agreed well. The surface areas of those catalysts are calculated from the mean diameter of the particles obtained from the TEM images by using the following equation:

$$S = \frac{6000}{\rho d} \qquad (5.2)$$

where S is the surface area (m^2/g), d is the mean diameter of Pt particles (nm), and ρ is the density of Pt ($21.4 g/cm^3$). Among all the catalysts, the surface area is found to be increased with increasing molar ratio of RTIL/Pt. Dispersion (D) of the metal particles is an important parameter used to calculate the activity of the catalyst per surface metal atom. D is defined as the mean fraction of the total metal atoms exposed at the surface. D of Pt particles deposited on xGnP roughly calculated from d = 1.08/D (nm) with TEM results [34] were also listed in **Table 5.2**. The data showed that RTIL-2 is more effective in reducing Pt size and thus increasing Pt dispersion on xGnP than RTIL-1. It is also interesting that the surface area and dispersion of Pt particles in the highly loaded catalyst with 60wt. % of Pt synthesized in the presence of RTIL-2 were 5 and 3 times higher than those in the catalyst prepared without RTIL.

Table 5.2 Comparison of morphological data of XC-72R and xGnP supported Pt (20wt. %) catalysts prepared at different molar ratio of RTIL/Pt

samples	RTIL/Pt in molar ratio	d from TEM (nm)	d from XRD (nm)	S (m^2/g)	D (%)
Pt/XC-72R	-	2.23 ± 0.55	2.54	125.73	48.43
Pt/xGnP-N	0	3.74 ± 0.64	3.94	74.97	30.94
	0[a]	8.25 ± 1.59	6.65	33.97	18.32
Pt/xGnP-RTIL-1	2.5	2.88 ± 0.46	3.01	97.35	37.50
	5	2.54 ± 0.41	2.56	110.38	42.52
	10	2.10 ± 0.40	2.43	133.51	51.43
	50	1.95 ± 0.37	2.09	144.05	55.38
Pt/xGnP-RTIL-2	2.5	2.64 ± 0.41	2.81	106.20	40.91
	5	2.01 ± 0.39	2.28	139.49	53.73
	10	1.78 ± 0.37	2.05	157.51	60.67
	50	1.68 ± 0.30	1.99	166.81	64.29
	50[b]	1.58 ± 0.33	1.83	175.15	68.35

[a.b]The catalysts loaded with 60wt. % Pt.

5.3.4 XPS analysis of Pt/xGnP

Pt/xGnP catalysts prepared without and with the addition of RTIL-2 were analyzed by XPS to determine the oxidative state of Pt particles as well as the interaction between Pt and xGnP. **Figure 5.12** shows the Pt 4f signal in Pt/xGnP-N consisting of three pairs of doublets. The two strong energy band at 71.66 and 74.99 eV are due to Pt particles in metallic state, while two weak energy bands observed at 73.09 and 76.42 can be assigned to Pt^{+2} and Pt^{+4} in oxidation state. XPS study explains the electron donation by Pt to a carbon support [34]. The Pt $4f_{7/2}$ peak for the Pt/xGnP catalyst shifted to higher values by 0.56eV with respect to 71.1eV for Pt metal in the literature [36, 37], indicating the strong Pt-xGnP support interaction through electron transfer from Pt to the surface of xGnP. This shift can be interpreted as a small particle effect as reported earlier in [38, 39]: particles in the 1~2 nm range have not yet attained the normal bulk band structure, so the

binding energy for the particles shifts to higher values. On the other hand, it is worth noting as in **Figure 5.13** that the XPS spectrum did not show the peak at 198eV corresponding to the presence of Cl^-, indicating the perfect reduction of Pt precursors. This is a significant advantage because of the necessity of Cl-free electrode preparation in order to avoid the catalytic loss or degradation of Pt/xGnP catalysts.

Deconvolution of the XPS spectrum was carried out for other RTIL-2 /Pt precursor molar ratio = 2.5, 5, 10, and 50 catalysts. The percentage of Pt particles in metallic and oxidative state was calculated and listed in **Table 5.3**. The results for unsupported Pt blacks synthesized in the absence and the presence of RTIL-2 and a commercial Pt/XC-72R from E-TEK Inc. were also included for comparison. While **Pt/xGnP-N** and the E-TEK catalyst showed similar content of metallic Pt particles, higher percentages of metallic Pt were present in **Pt/xGnP-RTIL-2**. However, the content of metallic Pt species decreased with increase of RTIL-2 content. It is not clearly known if the partial oxidation of Pt takes place in the middles of synthetic steps of supported catalysts and/or if the reduction reaction of the Pt precursor is incomplete. Pt oxidation can occur when the supported Pt is exposed to air because oxygen can easily be chemisorbed on the surface of the Pt clusters. The presence of Pt oxides may be responsible for the detection of oxygen-containing species found on the oxygen groups of xGnP support. The content reduction of Pt species in oxidation is possibly due to the lower susceptibility of oxidation of Pt nanoparticles which are adsorbed by RTIL-2. However, the decrease of metallic Pt at high molar catalysts may result from the increase of RTIL-2 on Pt particles.

The electronic interaction between Pt and xGnP can be recognized by the shift of metallic Pt peak location for Pt/xGnP with respect to unsupported Pt [40, 41]. As listed in

Table 5.3, the metallic Pt peaks for xGnP-supported RTIL-2 /Pt precursor molar ratio = 0, 2.5, 5, and 50 catalysts shifted to higher values by 0.28, 1.16, 0.87, and 1.68eV with respect to corresponding unsupported Pt blacks. This result can be interpreted as related to the presence of Pt-xGnP electronic effect. The Pt-xGnP interaction is through electron transfer from Pt to the surface of xGnP. In the absence of mechanical interlocking, the adhesion arises from molecular, electrostatic, chemical surface forces acting across the interface of two solids [42]. The shift of Pt peaks for Pt/xGnP-RTIL-2 samples is bigger than the commercial Pt/XC-72R, indicating that the interaction between Pt-xGnP is stronger than that between Pt-XC-72R carbon black. The small size effect is excluded here because the Pt size for supported samples is similar to that for corresponding unsupported particles.

Table 5.3 Peak location of Pt4f and content of different Pt species determined from Pt/xGnP-N and Pt/xGnP-RTIL-2 samples

Samples	RTIL/Pt in molar ratio	Metallic Pt (peak locations, eV)	Pt oxide (peak locations, eV)
Pt	0	64.57 % (71.38, 74.72)	35.43 % (72.52, 75.96)
Pt-RTIL-2	2.5	65.80% (70.67, 74.03)	34.20% (71.60, 74.03)
	5	71.13% (71.09, 74.39)	28.87% (72.17, 74.39)
	50	73.64% (70.54, 73.87)	26.36% (71.67, 75.50)
Pt/XC-72R	—	65.55 % (71.78, 75.10)	34.45 % (73.35, 76.91)
Pt/xGnP-N	—	65.45 % (71.66, 74.99)	34.55 % (73.09, 76.42)
Pt/xGnP-RTIL-2	2.5	82.68 % (71.83, 75.16)	17.32 % (73.40, 76.73)
	5	73.81 % (71.96, 75.29)	26.19 % (73.45, 76.78)
	10	72.42 % (72.17, 75.50)	27.58 % (73.40, 76.73)
	50	67.80 % (72.12, 75.45)	32.20 % (73.60, 76.93)

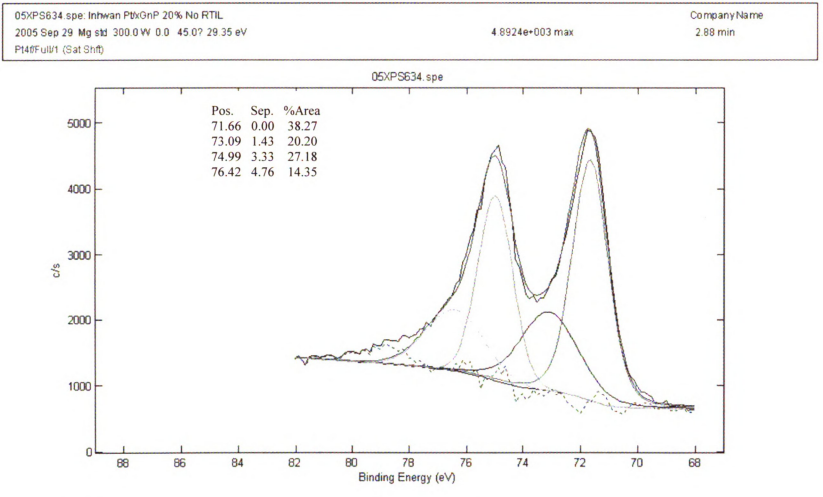

Figure 5.12. XPS core level spectra for the Pt 4f regions of a Pt catalyst of 3.7nm mean particle size supported on xGnP.

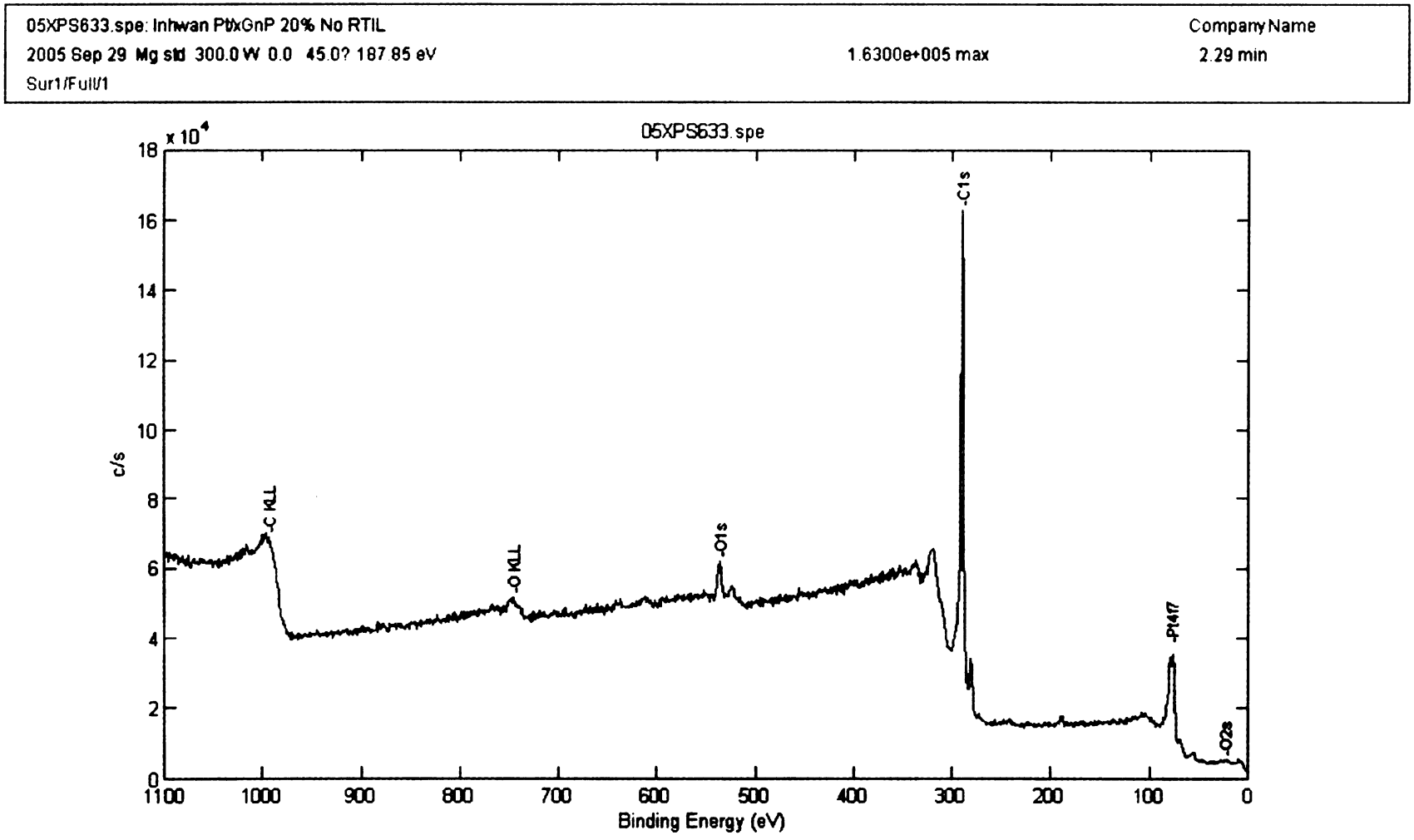

Figure 5.13. XPS core level spectra for the Pt 4f regions of a Pt catalyst of 3.7nm mean particle size supported on xGnP.

5.3.5 Electro-oxidation of Methanol

The electrochemical performance of Pt/xGnP catalysts synthesized in the absence and the presence of RTIL-1 and RTIL-2 was studied for methanol oxidation in 1M H_2SO_4 + 2M CH_3OH solution at 50mV/s scan rate at the room temperature. A commercial Pt /XC-72R catalyst from E-TEK was also tested for comparison. All of the catalysts have approximately 20wt. % of Pt particles. Figure 5.14 shows the results of cyclic voltammetry measurement for Pt/xGnP and Pt/XC-72R catalysts. The methanol oxidation is represented by the peak in the current at around 0.8 V in the forward scan, while the other oxidation peak at around 0.57 V in the reverse scan is associated with the removal of the residual carbon species formed in the forward scan [43, 44]. The magnitude of the peak current in the forward scan is directly proportional to the amount of methanol oxidized at the anode in DMFC. As clearly shown in Figure 5.14, all of the Pt/xGnP catalysts showed higher oxidation current than Pt/XC-72R, indicating that the former is more active for methanol oxidation than the latter. Especially, the oxidation current obtained from **Pt/xGnP-RTIL-2** catalysts increased almost twice as high as Pt/XC-72R. This enhancement of the catalytic activity for methanol oxidation may be attributed to the improved utilization of Pt phase on the surface of xGnP. This better Pt dispersion and utilization on the Pt/xGnP catalysts are due to the higher accessible surface area provided by the surface of xGnP. Pt particles on XC-72R can be trapped in its pores where the reactant can not access to or Nafion can not form a three phase boundary but there are no such Pt regions on xGnP. This difference explains the efficiency of Pt/xGnP catalysts over the commercial catalyst. The stronger interaction between Pt particles and xGnP

may be another possible reason of explaining the better catalytic performance of **Pt/xGnP-RTIL-2**, which was proved by data from XPS spectra of Pt 4f.

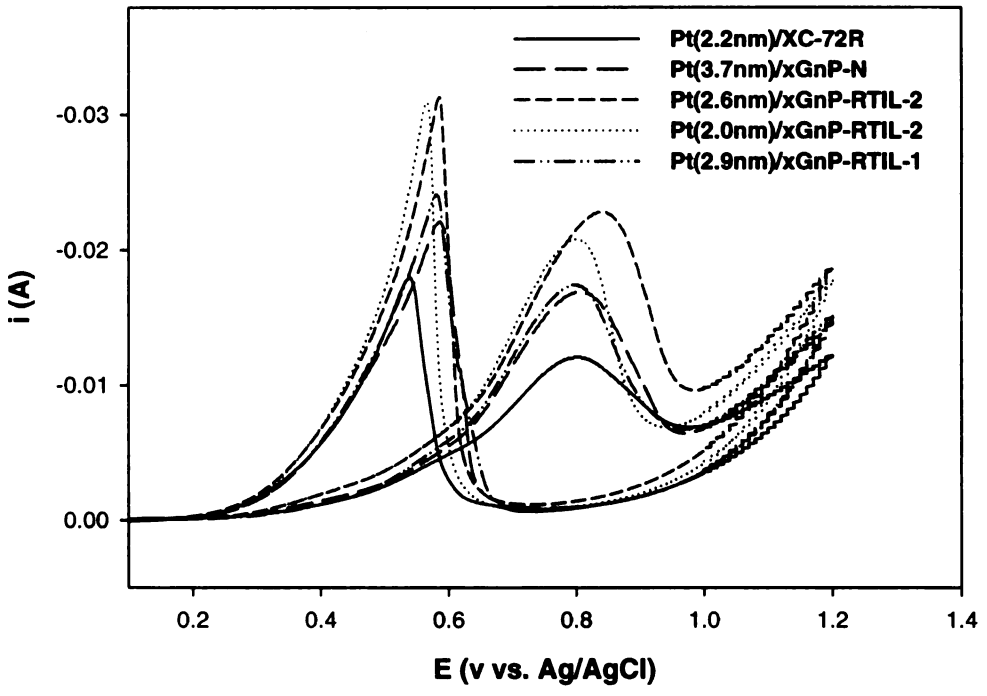

Figure 5.14. Comparison of catalytic activity for methanol oxidation on Pt/XC-72R, Pt/xGnP-N, and Pt/xGnP- RTIL-1, Pt/xGnP- RTIL-2 catalysts.

The difference between peak potentials for the forward and backward scan indicates the tolerance of the catalysts toward CO [45]. The lower value means the better CO-tolerance. The peak potential differences for **Pt/XC-72R**, **Pt/xGnP-N**, **Pt/xGnP-RTIL-1**, and two different **Pt/xGnP-RTIL-2** catalysts with 2.6 and 2.0nm of Pt particles were 268, 232, 253, 225, 253, and 239mV, respectively. Even though all of the Pt/xGnP catalysts had lower potential difference, it seems hard to insist the better CO-tolerance of the Pt/xGnP than the commercial Pt/XC-72R catalyst but they seemed to have similar CO-tolerant properties.

Table 5.4 Mass activity of Pt particles for Pt/xGnP catalyst prepared via microwave irradiation at the various molar ratios of RTIL/Pt

Samples	Pt size (nm)	Pt loading (wt.%)[a]	Mass of Pt (mg)	Mass activity at peak in forward (mA/mg Pt)	Mass activity at peak in reverse (mA/mg Pt)
Pt/XC-72R	2.23	19.79	0.0218	577.98	828.44
Pt/xGnP-N	3.74	19.75	0.0217	788.01	1025.81
Pt/xGnP-RTIL-1	2.88	19.57	0.0215	840.47	1135.81
Pt/xGnP-RTIL-2	2.64	19.36	0.0213	1090.14	1485.92
Pt/xGnP-RTIL-2	2.01	18.90	0.0208	999.04	1487.02

[a] Measured from TGA in air environment at 25°C/min ramp rate.

Mass activity (the current/quantity of the catalyst), which is the way to express the catalytic activity of Pt particles dispersed on carbon supports, is particularly important because the cost of electrodes in fuel cells depends on the amount of Pt-based catalysts. If the catalysts have high mass activity, it is possible to reduce the loading of precious Pt metal. Mass activities of Pt/xGnP catalysts calculated at peaks in the forward and the reverse scan were compared with those of the Pt/XC-72R catalyst in Table 5.4. All of the Pt/xGnP catalyst showed better activity than Pt/XC-72R and two different **Pt/xGnP-RTIL-2** samples with 2.64 and 2.01nm of Pt especially provided much higher mass activity than Pt/XC-72R with 2.23nm Pt. They showed an 80% increase in mass activity compared to Pt/XC-72R, resulting from much better utilization of the Pt particles on xGnP. It was reported that 3nm Pt-based particles exhibited higher mass catalytic activity for methanol oxidation and oxidation reduction [46, 47]. However, that report does not agree with the present result. According to the result of mass activity, a more critical

factor influencing catalytic activity of support Pt catalysts seems to be the utilization of Pt particles rather than the Pt size. The structure of xGnP which allows the active phase to make an easy contact with reactant and the proton conductive materials simultaneously also contributes to the increase in the utilization of Pt phase in Pt/xGnP catalysts.

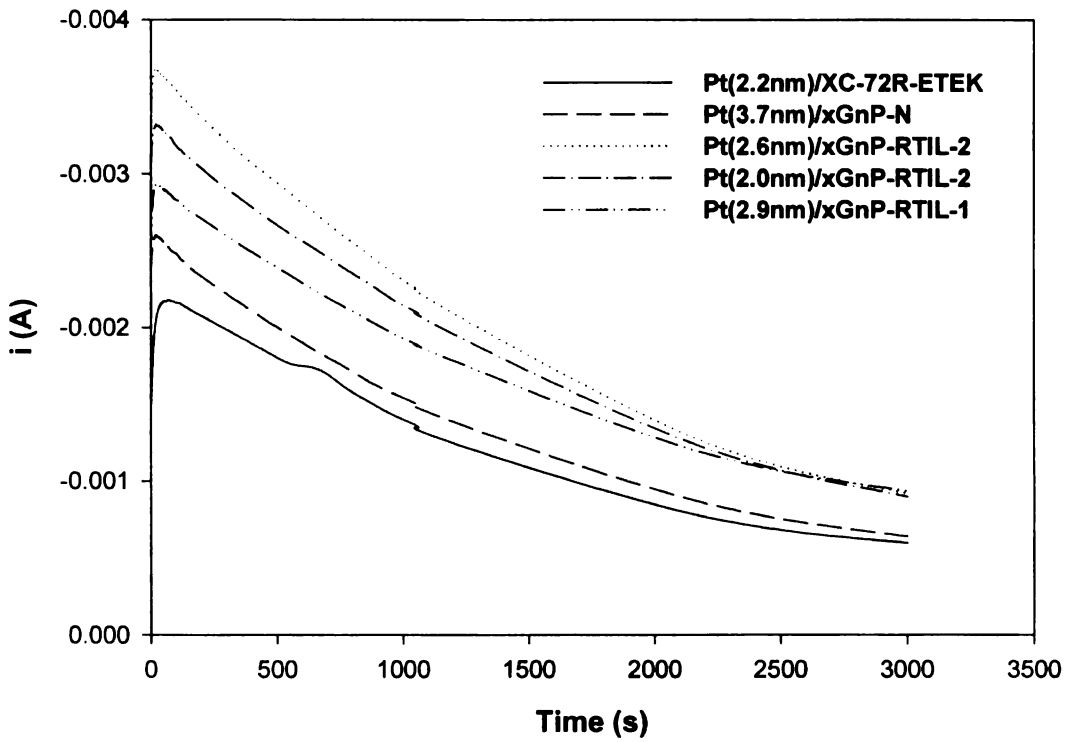

Figure 5.15. Chronoamperometry curves for methanol oxidation at 0.45V on Pt/XC-72R, Pt/xGnP-N, and Pt/xGnP- RTIL-1, Pt/xGnP- RTIL-2 catalysts.

The catalytic stability is another important evaluation of carbon supported Pt catalysts for methanol oxidation. The current-time curves at 0.45V are shown in Figure 5.15. The initial methanol oxidation currents for Pt/xGnP catalysts were higher than that of Pt/XC-72R and their order of the initial currents was in good agreement with the results of CV measurements. The currents for all the catalysts gradually decayed with time, which is caused by the adsorption of intermediate species on the surface of Pt

particles during the methanol oxidation reaction [48]. The current values for Pt/xGnP catalysts synthesized in the present of RTIL-1 and RTIL-2 were always higher than that of Pt/XC-72R for the period of the measurement, although initial relatively fast drop in the first 500s. This suggests the better long-term stability of **Pt/xGnP-RTIL** catalysts.

5.4. Conclusion

The purpose of this work is to evaluate xGnP as a support for the catalytic oxidation of methanol in DMFC. xGnP has suitable properties such as good electronic conductivity, high corrosion resistance, high surface area, high mechanical properties, high accessible area for the reactant, as well as low resistance between the interface of electrolytes and xGnP. The thermo-oxidative stability and combustion resistance of xGnP have been studied with TGA and compared with other novel carbon nanostructures. TGA results proved that xGnP has the highest stability among other carbon candidates for fuel cell application. The 20wt. % Pt/xGnP catalysts have been prepared in the presence of various molar ratios of RTIL to chloroplatinic acid hexahydrate in EG, DEG, and TEG as reducing agents via microwave technique. TEM and XRD results reveal that, regardless of Pt loading level, highly-dispersed Pt nanoparticles below 3nm with a narrow size distribution were synthesized on the xGnP by introducing RTIL to the solution and the size of Pt nanoparticles were tuned by changing the molar ratio of RTIL/xGnP. Pt/xGnP catalysts exhibit higher catalytic activity than the commercial Pt/XC-72R catalysts due to higher dispersion and utilization of the Pt particles as well as stronger Pt-support interaction. All the results presented in this chapter indicate the use of xGnP as a support with a great potential not only for DMFC but also for other low temperature fuel cells.

5.5. Bibliography

1. S. Wasmus and A. Kuver, "Methanol oxidation and direct methanol fuel cells: a selective review", J. Electroanal. Chem., 461(1-2), p14-31, 1999.

2. K. Scott, W.M. Taama, and P. Argyropoulos, "Engineering aspects of the direct methanol fuel cell system", J. Power Sources, 79, p43-59, 1999.

3. C.K. Dyer, "Fuel cells for portable applications", J. Power Sources, 106(1-2), p31-34, 2002.

4. B.D. McNicol, D.A.J. Rand, and K.R. Williams, "Direct methanol–air fuel cells for road transportation", J. Power Sources, 83(1-2), p15-31, 1999.

5. V. Gogel, T. Frey, Z. yongsheng, K.F. Friedrich, L. Jorissen, and J. Garche, "Performance and methanol permeation of direct methanol fuel cells: dependence on operating conditions and on electrode structure", J. Power Sources, 127(1-2), p172-180, 2004.

6. R. Dillon, S. Srinivasan, A.S. Arico, and V. Antonucci, "International activities in DMFC R&D: status of technologies and potential applications", J. Power Sources, 127(1-2), p112-126, 2004.

7. A.K. Shukla, M. Neergat, B. Arthasarathi, V. Jayaraman, M.S. Hedge, "An XPS study on binary and ternary alloys of transition metals with platinized carbon and its bearing upon oxygen electroreduction in direct methanol fuel cells", J. Electroanal. Chem., 504(1), p111-119, 2001.

8. A. Lima, C. Coutanceav, J.M.. Leger, and C. Lamy, "Investigation of Ternary Catalysts for Methanol Electrooxidation", J. Appl. Electrochem., 31(4), p379-386, 2001.

9. M. Hogarth, and T. Ralph, "Catalysis for Low Temperature Fuel Cells", Platinum Met. Rev., 46, p146, 2002.

10. T. Kawaguchi, W. Sugimoto, Y. Murakami and Y. Takasu, "Temperature dependence of the oxidation of carbon monoxide on carbon supported Pt, Ru, and PtRu", Electrochem. Commun., 6(5), p480-483, 2004.

11. A.S. Arico, V. Baglio, E. Modica, A. Di Blasi, and V. Antonucci, "Performance of DMFC anodes with ultra-low Pt loading", Electrochem. Commun., 6(2), p164-169, 2004.

12. I.S. Armadi, Z.L. Wang, T.C. Green, A. Henglein, and M.A. El-Sayed, "Shape-Controlled Synthesis of Colloidal Platinum Nanoparticles", Science, 272(5270), p1924-1925, 1996.

13. W.Z. Li, S.Q. Song, W.J. Zhou, G.Q. Sun, Q. Xin, C. Poulianitis, and P. Tsiakaras, "Direct methanol fuel cells: The influence of methanol on the reduction of oxygen over Pt/C catalysts with different particle sizes", Ionics, 11(1-2), p112-119, 2005.

14. P.J. Britto, K.S.V. Santhanam, R. Rubio, J.A.A. Alonso, and P.M. Ajayan, "Improved Charge Transfer at Carbon Nanotube Electrodes", Adv. Mater., 11(2), p154, 1999.

15. H. Shi, "Activated Carbons and Double Layer Capacitance", Electrochim. Acta, 41(10), p1633-1639, 1996.

16. S.C. Roy, P.A. Christiensen, A. Hamnett, K.M. Thomas, and V. Trapp, "Direct Methanol Fuel Cell Cathodes with Sulfur and Nitrogen-Based Carbon Functionality", J. Electrochem. Soc., 143(10), p3073-3079, 1996.

17. G. Girishkumar, K. Vinodgopal, and P.V. Kamar, "Carbon Nanostructures in Portable Fuel Cells: Single-Walled Carbon Nanotube Electrodes for Methanol Oxidation and Oxygen Reduction", J. Phys. Chem. B, 108(52), p19960-19966, 2004.

18. W. Li, C. Liang, W. Zhou, J. Qiu, Z.H. Zhou, G. Sun, and Q. Xin, "Preparation and Characterization of Multiwalled Carbon Nanotube-Supported Platinum for Cathode Catalysts of Direct Methanol Fuel Cells", J. Phys. Chem. B, 107(26), p6292, 2003.

19. K.W. Park, Y.E. Sung, S. Han, Y. Yun, and T. Hyeon, "Origin of the Enhanced Catalytic Activity of Carbon Nanocoil-Supported PtRu Alloy Electrocatalysts", J. Phys. Chem. B, 108(3), p939-944, 2004.

20. C.A. Bessel, K. Laubernds, N.M. Rodriguez, R.T.K. Baker, "Graphite Nanofibers as an Electrode for Fuel Cell Applications", J. Phys. Chem. B, 105(6), p1115, 2001.

21. T. Yoshitake, Y. Shimakawa, S. Kuroshima, H. Kimura, T. Ichihashi, Y. Kubo, D. Kasuya, K. Takahashi, F. Kokai, M. Yudasaka, and S. Iijima, Physica B-Condensed Matter., 323 (1-4), p124-126, 2002.

22. G. Wu, Y.S. Chen, and B.Q. Xu, "Remarkable support effect of SWNTs in Pt catalyst for methanol electro oxidation", Electrochem. Commun., 7(12), p1237-1243, 2005.

23. E.S. Steigerwalt, G.A. Deluga, C.M. Lukehart, "Pt-Ru/Carbon Fiber Nanocomposites: Synthesis, Characterization, and Performance as Anode Catalysts of Direct Methanol Fuel Cells. A Search for Exceptional Performance", J. Phys. Chem. B, 106(4), p760-766, 2002.

24. R.H. Baughman, A.A. Zakhidov, and W.A. Heer, "Carbon Nanotubes--the Route Toward Application", Science, 297(5582), p787-792, 2002.

25. K.M. Lee, L.C. Li, and L.M. Dai, "Asymmetric End-Functionalization of Multi-Walled Carbon Nanotubes", J. Am. Chem. Soc., 127(12), p4122-4123, 2005.

26. A. Peigney, C. Laurent, E. Flahaut, R.R. Basca, and A. Rousset, "Specific surface area of carbon nanotubes and bundles of carbon nanotubes", Carbon, 39(4), p507-514, 2001.

27. L.S. Schadler, S.C. Giannaris, and P.M. Ajayan, "Load Transfer in Carbon Nanotube Epoxy Composites", Appl. Phys. Lett., 73(26), p3842-3844. 1998.

28. V. Radmilovic, H.A. Gasteiger, and P.N. Ross, "Structure and Chemical Composition of a Supported Pt-Ru Electrocatalyst for Methanol Oxidation", J. Catal., 154(1), p98-106, 1995.

29. X. Li, W. Chen, J. Zhao, W. Xing, and Z. Xu, "Microwave polyol synthesis of Pt/CNTs catalysts: Effects of pH on particle size and electrocatalytic activity for methanol electrooxidization", Carbon, 43(10), p2168-2174, 2005.

30. W. Li, C. Liang, W. Zhou, J. Qiu, Z. Zhou, G. sun, and Q. Xin, "Preparation and Characterization of Multiwalled Carbon Nanotube-Supported Platinum for Cathode Catalysts of Direct Methanol Fuel Cells", J. Phys. Chem. B, 107(26), p6292, 2003.

31. Y. Wang, J.W. Ren, K. deng, L.L. Gui, and Y.Q. Tang, "Preparation of Tractable Platinum, Rhodium, and Ruthenium Nanoclusters with Small Particle Size in Organic Media", Chem. Mater., 12(6), 1622-1627, 2000.

32. M. Antonietti, D. Kuang, B. Smarsly, and Y. Zhou, "Ionic Liquids for the Convenient Synthesis of Functional Nanoparticles and Other Inorganic Nanostructures", Angew. Chem. Int. Ed. 43(38), p4988-4992, 2004.

33. R.J. Sengwa, K. Kaur, and R. Chandhary, "Dielectric properties of low molecular weight poly(ethylene glycol)s", Polymer International, 49(6), p599-608, 2000.

34. J.E. Benson and J. Boudart, "Hydrogen-oxygen titration method for the measurement of supported platinum surface areas", J. Catal., 4(6), p704-710, 1965.

35. J. Escard, C. Leclerc, and J.P. Contour, "The state of supported irdium in a hydrazine decomposition catalyst", J. Catal, 29(1), p31-39, 1973.

36. E. Antoline, L. Giorgi, F. Cardellini, and E. Passalacqua, "Physical and morphological characteristics and electrochemical behaviour in PEM fuel cells of PtRu/C catalysts", J. Solid State Electrochem., 5(2), p131-140, 2001.

37. A.K. Shukla, M.K. Ravikumar, A. Roy, S.R. Barman, D.D. Sarma, A.S. Arico, V. Antonucci, L. Pino, and N. Giordano, "Electro-oxidation of Methanol in Sulfuric Acid Electrolyte on Plantinized-Carbon Electrodes with Several Functional-Group Characteristics", J. Electrochem. Soc., 141(6), p1517-1521, 1994.

38. M.G. Mason, "Electronic Structure of Supported Small Metal Clusters", Phys. Rev. B, 27(2), p748-762, 1983.

39. W. Eberhadt, P. Fayet, D.M. Cox, Z. Fu, A. Kaldor, R. Sherwood and D. Sondericker, "Photoemission from Mass-selected Monodispersed Pt Clusters", Phys. Rev. Lett., 64(7), p780, 1990.

40. E. Antolini, "Formation, microstructural characteristics and stability of carbon supported platinum catalysts for low temperature fuel cells", J. Mater. Sci., 38, p2995-3005, 2003.

41. E. Antolini, L. Giorgi, F. Cardellini, and E. Passalacqua, "Physical and morphological characteristics and electrochemical behaviour in PEM fuel cells of PtRu/C catalysts", J. Solid State Eelectrochem., 5, p131-140, 2001.

42. K.L. Mittal, "Adhesion aspects of metallization of organic polymer surfaces", J. Vac. Sci. Technol., 13, p19-25, 1976.

43. T. Yajima, H. Uchida, and M. Watanabe, "In-Situ ATR-FTIR Spectroscopic Study of Electro-oxidation of Methanol and Adsorbed CO at Pt-Ru Alloy", J. Phys. Chem. B, 108(8), p2654-2659, 2004.

44. C. Lamy, J.M. Leger, and S. Srinivasan, "Direct Methanol Fuel Cells: From a 20th Century Electrochemist's Dream to a 21st Century Emerging Technology", Mod. Aspects. Electrochem., 34, p73, 2001.

45. B. Rajesh, K.R. Thampi, J.M. Bonard, N. Xanthopoulos, H.J. Mathieu, and B. Viswanathan, "Carbon Nanotubes Generated from Template Carbonization of Polyphenyl Acetylene as the Support for Electrooxidation of Methanol", J. Phys. Chem. B, 107(12), p2701-2708, 2003.

46. K. Kinoshita, "Particle Size Effects for Oxygen Reduction on Highly Dispersed Platinum in Acid Electrolytes", J. Electrochem. Soc., 137(3), p845-848, 1990.

47. Y. Takasu, H. Itaya, T. Iwazaki, R. Miyoshi, T. Ohmuna, and W. Susmoto, "Size effects of ultrafine Pt–Ru particles on the electrocatalytic oxidation of methanol", Chem. Commun., (4), p341-342, 2001.

48. J. Jiang, and A. Kucemak, "Electrooxidation of small organic molecules on mesoporous precious metal catalysts: II: CO and methanol on platinum–ruthenium alloy", J. Electroanal. Chem., 543(2), p187-199, 2003.

CHAPTER 6

PtRu NANOPARTICLE FORMATION BY RTIL-ASSISTED MICROWAVE PROCESS AND EVALUATION OF PtRu/xGnP ELECTROCATALYSTS FOR DIRECT METHANOL FUEL CELL (DMFC)

6.1 Introduction

Fuel cells have many benefits such as elimination of air pollutions, less noise pollution, high electrical efficiencies, good reliability, and possibility of remote and unattended operation [1-3]. They are able to meet requirements as potent and lightweight power and energy sources for a variety of applications. The best choice of fuels for fuel cells is pure hydrogen but it has inherent problems which include hydrogen production and storage, hydrogen distribution, and safety. Liquids fuels such as methanol, ethanol, ethylene glycol and formic acid are considered as alternatives for pure hydrogen. They can be produced in a large quantity and additionally, they are easy to be stored and distributed. Methanol has been most widely studied among them.

DMFC has a critical problem resulting in low overall performance. The problem is caused by the sluggish methanol oxidation at the anode and the high overpotential for oxygen reduction reaction at cathode resulting from methanol crossover [4]. Pt is the only metal catalyst showing a significant activity for methanol oxidation but Pt alone is not sufficient due to CO-poisoning. There is a need to achieve facile oxidation of CO chemisorbed on the surface of Pt at the anode. A first popular approach is to produce Pt alloys with different metals to form the surface oxide in the potential range for methanol oxidation. A second method is to introduce surface adatoms on the surface of Pt [5, 6]. A third type is to deposit Pt or PtRu onto a metal oxide such as CeO_2 or WO_3 [7, 8].

It is also required to develop methanol tolerant cathode catalysts for oxygen reduction reaction for commercialization of DMFC. Three classes of catalysts have been investigated for this purpose. A first one is to use the macrocyclic derivatives of a wide range of transition metal compounds [9]. A second class is related to Chevrel-type

compounds of the composition of $Mo_{6-x}M_xX_8$ (X=S, Se, Te) or transition metal cluster catalysts such as $M_{1-x}Mo_xSeO_z$, which are based on transition metal and non-metallic counter ions [10-12]. A third is unsupported noble metal catalysts as nanoparticle, binary alloys, single or polycrystalline surfaces and supported noble metal catalysts. Among them, PtRu and PtSn alloys as methanol oxidation catalysts are particularly effective in the high and the low potential region, respectively [13, 14] and Pt-based alloys with transitional metals with carbon have been extensively investigated for methanol tolerant oxygen reduction catalysts [15, 16].

Pt and Pt-based alloys, especially PtRu, are the best materials for oxygen reduction and methanol oxidation at the cathode and anode in DMFC, respectively [17]. However, there have been demands to reduce amounts of Pt because the high cost and low availability of Pt is one of obstacles against practical implementation of DMFC. One way is to employ electrically conductive and high surface are carbons for Pt dispersion, resulting in fine Pt nanoparticles supported on carbons with a high catalytically active surface area. Catalytic properties of Pt particles are strongly influenced by carbon materials. They affect the size and size distribution of metal particles, the extent of alloying in multimetallic catalysts, the stability and the utilization degree of supported metal particle [18-19]. Catalytic activity of Pt-based catalysts is also affected by the fabrication techniques [20]. There are many different methods to synthesize carbon supported catalysts for DMFC, which includes impregnation, colloids, sol-gel, electrodeposition, thermal decomposition, microwave irradiation, and supercritical processes. It is desirable to develop a low cost, easy, rapid and consistent fabrication method which guarantees highly active catalyst.

xGnP supported PtRu catalysts synthesized in a similar way as described in chapter 5 were investigated and the results presented in this chapter. The influence of xGnP as a new support on the dispersion and the performance of PtRu catalyst was investigated and compared with a commercial carbon black supported catalyst.

6.2 Experimental Details

6.2.1 Materials

A reagent grade of ethylene glycol (EG, bp = 197.3°C) from J.T. Baker was used as reducing agent for xGnP supported PtRu catalysts. Chloroplatinic acid hexahydrate ($H_2PtCl_6 \cdot 6H_2O$) and ruthenium chloride hydrate ($RuCl_3 \cdot xH_2O$) from Aldrich were used as Pt and Ru precursors, respectively. RTIL used in this work are 1-butyl-3-methylimidazolium hexafluorophosphate ($bmimPF_6$) and 1-butyl-3-methylimidazolium acetate ($bmimCH_3CO_2$) and their chemical structures are shown in **Figure 4.1** of chapter 4. $bmimPF_6$ is denoted as **RTIL-1** and $bmimCH_3CO_2$ as **RTIL-2** in this work. Both were purchased from Aldrich and used as received. xGnP with 12nm of thickness and 1μm of diameter made in MSU was used as a carbon support. The morphology of xGnP can be seen in **Figure 5.1** of chapter 5.

6.2.2 Preparation of Unsupported and Supported Catalysts

The typical experimental procedures for unsupported bimetallic PtRu particles are described as follows. In two separate 10 ml beakers, a specific quantity of Pt and Ru precursors was dissolved in 2mL EG, respectively. In another 100mL beaker, **RTIL-1** or **RTIL-2** was mixed with 16g of EG solution vigorously to which two EG solutions of Pt

and Ru precursor was added and stirred vigorously for 30min. The mixture was transferred into a microwave oven (National, 2.45GHz, 1300W), and irradiated for 50seconds for the reduction of Pt and Ru precursors at the same time. The resulting suspension was centrifuged and washed with acetone several times. The PtRu particles was re-dispersed in acetone and stored in a vial.

For PtRu(30 and 40wt. %) /xGnP catalysts synthesized in the presence of RTIL, various weight ratios of EG to RTIL were added and dissolved in 18mL ethylene glycol prior, followed by the addition and the ultrasonic dispersion of xGnP. Other steps are similar to PtRu nanoparticles in the presence of RTIL. The PtRu/xGnP catalysts synthesized with the addition of bmimPF_6 and bmimCH_3CO_2 are denoted as **PtRu/xGnP-RTIL-1(*X*)** and **PtRu/xGnP-RTIL-2(X),** respectively, in which *X* represents the weight ratio of EG to RTIL. *PtRu/xGnP-N* represents PtRu bimetallic particles deposited on xGnP, which was prepared in the absence of RTIL.

6.2.3 Characterization Methods

PtRu catalyst samples dispersed on xGnP were characterized by recording their X-ray diffraction (XRD) patterns on a Regaku Rotaflex 200B X-ray diffractometer using Cu-Kα radiation with a curved graphite monochromator in order to identify the phases present in the catalyst and to evaluate the particle size of the PtRu particles. The 2θ region between 10° and 100° was explored at 45 keV and 100 mV at a scan rate of 5°/min. The average metal particle size was calculated using Scheller equation according to the XRD broadening PtRu (220) reflections which was scanned at a rate of 1°/min again. Transmission electron microscopy (TEM) investigation was carried out with JEOL

100CX and JEOL 2200FS operating at a voltage of 100keV and 200keV for the morphology of the dispersed PtRu electrocatalyst and the determination of the mean size of PtRu particles. Specimens were prepared by ultrasonically re-dispersing the sample powders in acetone for 15 min, applying the power suspension onto lacey carbon coated Cu grids and drying them in air. The particle size and distribution of the metal particles was obtained by measuring the size of 150 ~ 200 randomly selected particles in TEM images. Thermo-gravimetric Analysis (TGA 2950, TA instrument) was performed to measure real loading of PtRu bimetallic particles deposited on xGnP. Samples weighing 3~4mg were tested over temperatures ranging from room temperature to 1000°C at 25°C/min under flowing air.

Electrochemical investigation was performed by cyclic voltammetry (CV) using a potentiostat (Gamry, FAS2 Femtostat). A conventional three-electrode cell equipped with a platinum wire counter electrode, an Ag/AgCl reference electrode, and glassy carbon working electrode was used. The glassy carbon electrode with 3mm diameter was polished to a mirror finish with a 0.05 μm alumina suspension before each experiment. The catalyst ink was prepared by ultrasonically dispersing 5mg of 30wt. % PtRu/xGnP catalyst, 0.8ml of ethanol and 0.1ml of 0.1wt % Nafion solution. Then 20 μL of the catalyst ink was micropipetted out on the top surface of the glassy carbon electrode to yield a Pt loading of about 0.3142mg/cm^2. The CV experiments were performed in 1M H_2SO_4 solution in the absence and the presence of 2M CH_3OH at the scan rate of 50mV/s. All the solutions were prepared by using ultrapure water. N_2 gas was purged for 15 min before starting the experiment. The chronoamperometry tests were performed in 2M CH_3OH/1M H_2SO_4 at 0.40V for the period of 2500s.

6.3 Results and Discussion

6.3.1 Unsupported PtRu catalysts

Distinct differences in the morphologies and particle sizes of unsupported PtRu nanoparticles synthesized in ethylene glycol via microwave heating process with and without the addition of RTIL-2 are shown in **Figure 6.1**. While PtRu-N sample prepared without RTIL-2 showed large particle-aggregated morphology and PtRu particles held together by an irregular network as in **Figure 6.1 (a)**, PtRu particles fabricated with the addition of RTIL-2 appeared to have the same particle-aggregated morphology as PtRu-N but they were much smaller due to rapid reduction rate by RTIL-2 and very well separated individually and 3-dimensionally due to the stabilization effect by RTIL-2. The average particle size in PtRu-RTIL-2 was about 1.5nm with very small standard deviation.

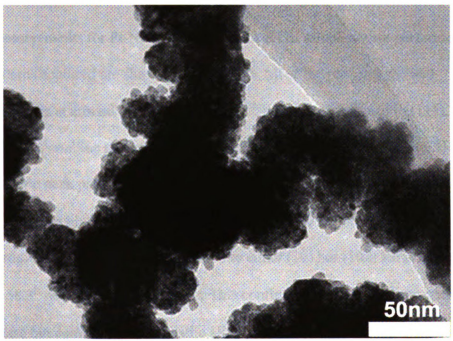

(a)

Figure 6.1. TEM microscophs of (a) PtRu-N and (b) PtRu-RTIL-2 (400).

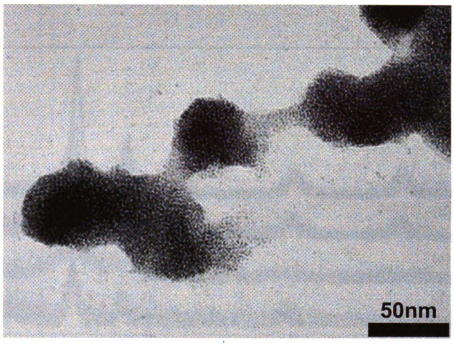

(b)

Figure 6.1. Continued.

XRD measurements for Pt-N, PtRu-N and PtRu-RTIL samples were performed and the XRD patterns acquired are shown in **Figure 6.2**. All of the particles showed characteristic peaks at around 40^{o}, 46^{o}, 68^{o}, and 82^{o}, which are attributed to (111), (200), (220), and (311) crystalline plane of Pt with face-centered cubic (fcc) structure. However, the most dramatic peak pattern was obtained from PtRu-RTIL2(400) particles which have (111) and (200) reflections merged together and (220) and (311) peaks broadened due to the small particle size. No visible peaks related to either (101) or (102) Ru reflection at $2\theta = 44$ and 58.3^{o} were found in the Figure. This confirms that Ru is not segregated in a separated phase but comprised in bimetallic alloy particles.

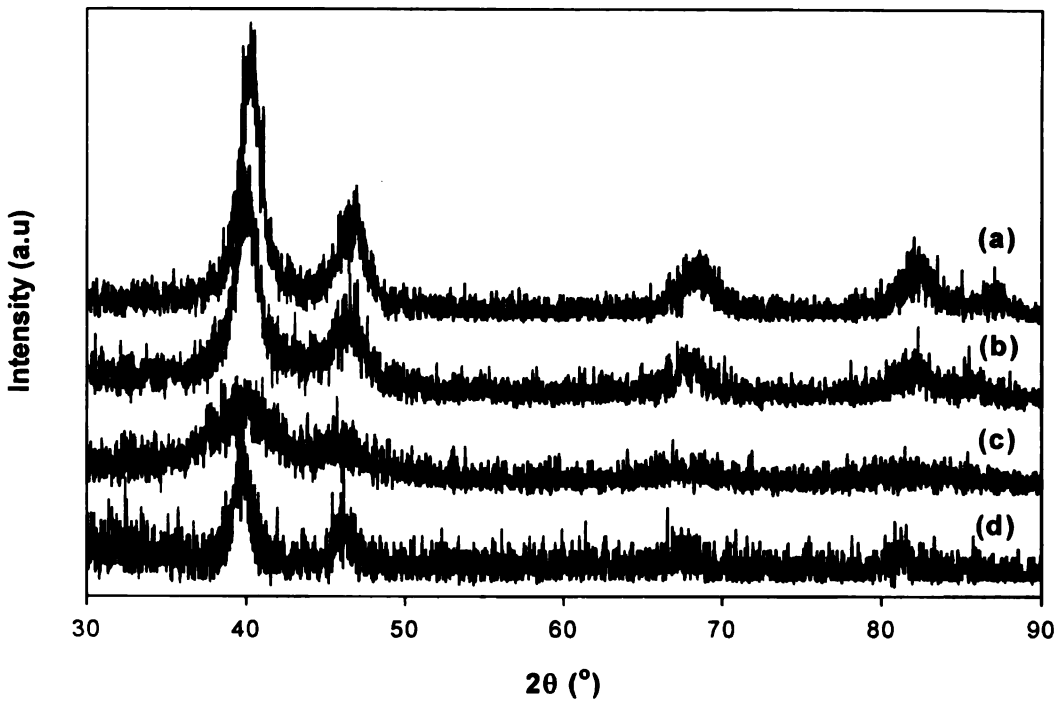

Figure 6.2. XRD patterns of (a) PtRu-N, (b) PtRu-RTIL2(800), (c) PtRu-RTIL2(400) and (d) Pt-N.

The 2θ change of the (220) peaks for Pt-N, PtRu-N and PtRu-RTIL particles is shown in **Figure 6.3**. The (220) peak for PtRu particles prepared with and without the addition of RTIl-2 clearly shifted towards the higher degree compared to Pt peak. The higher angle shift of the peak represents the formation of PtRu particles homogeneously alloyed with Pt and Ru atoms and the existence of Pt-Ru interaction. On the other hand, PtRu-N sample showed the highest shift and the shift degree seemed to decrease as the content of RTIL-2 increased. The large extent of the peak broadening was also observed as a result of the very small particle size with the increase of RTIL-2 content. All these features intimate that the lattice parameters and the composition of Pt and Ru atoms in PtRu bimetallic particles are distinct from each sample.

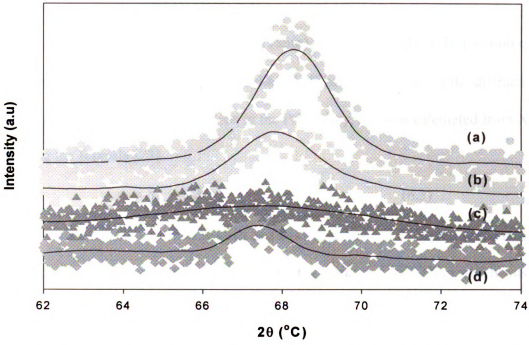

Figure 6.3. The change of (220) peaks of (a) PtRu-N, (b) PtRu-RTIL2(800), (c) PtRu-RTIL2(400) and (d) Pt-N.

Pt and Ru form an alloy with Ru atoms replacing Pt atoms in a Pt fcc structure when Ru atomic fractions is below 0.62 [21]. Above 0.62, Pt atoms replace Ru atoms in a Ru hcp structure. The composition of Pt and Ru atoms in the PtRu alloy particles can be determined by the information obtained by the shift of Pt reflections. After fitting with a Gaussian distribution, the (220) peak was used to calculate the lattice parameter, the average particle size and the composition of PtRu alloy particles.

The lattice parameter of the PtRu crystal was calculated from θ_{max} according to Vegard's law [22]:

$$a = \frac{\sqrt{2}\lambda_{K\alpha 1}}{\sin\theta_{\max}} \qquad (6.1)$$

The diameter (D) of PtRu particles was calculated according to the Scherrer's formula:

$$D = \frac{0.9\lambda_{K\alpha 1}}{B(2\theta)\cos\theta_{\max}} \qquad (6.2)$$

where $\lambda_{K\alpha 1}$ is the X-ray wavelength (0.154138nm), θ_{max} is the angle at the position of the peak maximum and $B(2\theta_{max})$ is the full width at half-height (FWHM) of the diffraction peaks in radian. The Ru atomic fraction in the PtRu alloy, X_{Ru} was calculated from XRD data using the formula [23].

$$a = a_0 - kX_{Ru} \qquad (6.3)$$

where a_0 is the lattice constant of pure Pt and k is a constant = 0.0124nm.. In the case of unsupported pure Pt, a_0 = 0.3923nm [24] but in this work, a_0 = 0.3927nm which was calculated from XRD measurement. The a, D, and X_{Ru} values deduced from XRD data are listed in Table 6.1. First of all, the particle sizes calculated from XRD measurement were in good agreement with those obtained by TEM analysis. The lattice constant of all PtRu particles was smaller than that of Pt particles. The decreased lattice parameters in the presence of Ru confirm that PtRu particles are not a physical mixture of Pt and Ru but a solid solution of two metals. The lattice parameter increased with increasing RTIL-2 content. Ru fraction in PtRu alloys showed the reversed trend. It has been reported that Ru % in PtRu alloys is independent of the particle size but strongly depends on the preparation method of the metal particle, metal loading and the form of the particles (bulk or nanoparticles, with or without supports, etc [25, 26]. Therefore, the difference of Ru % in the alloys in this work appears to result from different reduction rate due to the presence of RTIL-2.

Table 6.1. The data from XRD and TEM for the different PtRu and Pt particles

Samples	$2\theta_{max}$	a (nm)	FWHM	D_{dia} from XRD (nm)	D_{dia} from TEM (nm)	X_{Ru}
Pt-N	67.45	0.3927	1.75	5.463	6.22	–
PtRu-N	68.28	0.3885	2.26	4.251	–	0.34
PtRu-RTIL2(800)	67.86	0.3906	2.53	3.767	3.92	0.17
PtRu-RTIL2(400)	67.80	0.3909	5.24	1.828	1.47	0.15

6.3.2 Supported PtRu

The morphologies and particle size distribution of xGnP supported PtRu nanoparticles synthesized via microwave irradiation with and without the addition of RTIL-1 and RTIL-2 are shown in **Figure 6.4**. The loading of PtRu paritlces was 40wt. %. For **PtRu/xGnP-N**, the PtRu particles had an average size of around 5nm and partially agglomerated compared to PtRu-N. The particles showed poor distribution on the surface of xGnP. For **PtRu/xGnP-RTIL-1** and **PtRu/xGnP-RTIL-2** samples, the size of PtRu particles drastically decreased to 2.33 and 1.57nm in average, respectively. The particles were highly dispersed over the xGnP without agglomeration compared to those of PtRu/xGnP-N. This result confirms again that the use of RTIL in microwave process leads to the formation of smaller PtRu bimetallic nanoparticles with a much more uniform size distribution.

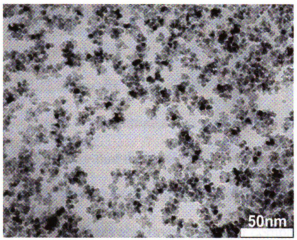

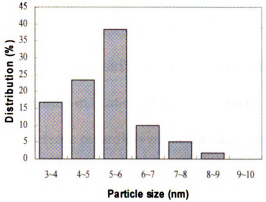

(a)

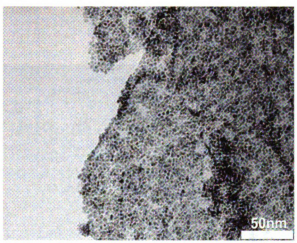

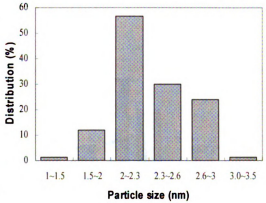

(b)

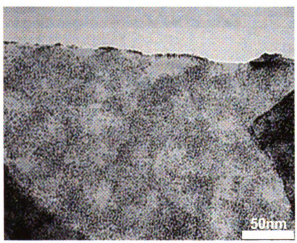

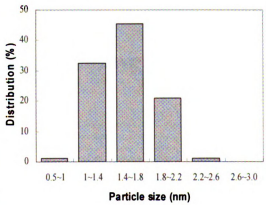

(c)

Figure 6.4. TEM analyses of PtRu/xGnP-N, PtRu/xGnP-RTIL-1, and PtRu/xGnP-RTIL-2 catalysts with 40wt. % metal loading (from top to bottom).

Figure 6.5 shows the effect of RTIL-2 on the dispersion and size of PtRu catalysts supported on xGnP with 30wt. % metal loading. It was clearly seen that, as the content of RTIL-2 increased, much smaller particles with narrower size distribution formed and the dispersion of the particles was greatly improved with little indication of agglomeration. It is noteworthy that the particle size of PtRu did not increase regardless of increasing metal loading, which can be compared from the **Figure 6.3** and **6.4 (c)**. A commercial PtRu/CB from E-TEK was also investigated for comparison (**Figure 6.5 d**). An average diameter of the particles of around 1.90nm was obtained but some of them were agglomerated.

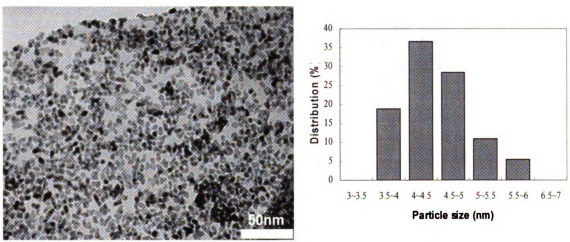

(a)

Figure 6.5. TEM analyses of (a) PtRu/xGnP-N, (b) PtRu/xGnP-RTIL2(800), (c) PtRu-RTIL2(400), and a commercial PtRu/CB catalysts.

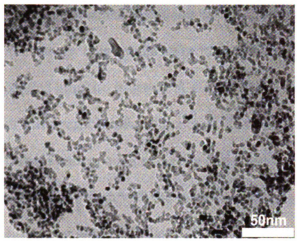

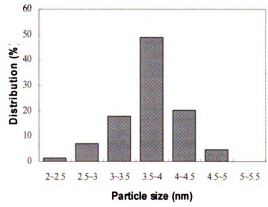

(b)

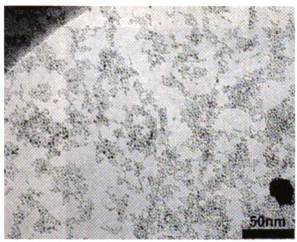

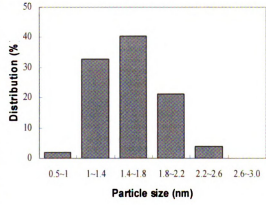

(c)

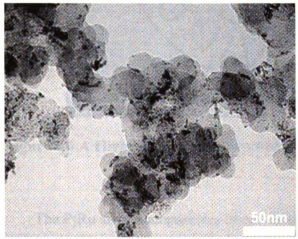

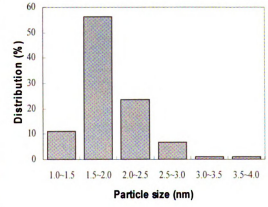

(d)

Figure 6.5. Continued.

Nanosized PtRu particles on xGnP were characterized by high resolution electron microscopy (**Figure 6.6**). The "A" area on the TEM image is corresponding to the layered graphite structure of xGnP of which the interplanar spacing looks bigger than that of PtRu particle although unclear. The image shows a well-crystallized PtRu structure. Fringes corresponding to PtRu lattice structure in a polyhedral shape at the edge of xGnP were clearly seen with the interplanar spacing of about 0.39nm which is in good agreement with XRD data.

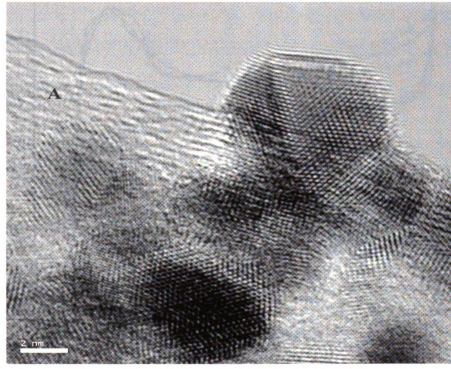

Figure 6.6 A High resolution TEM image of PtRu/xGnP-N catalyst (scale bar: 2nm).

The PtRu alloy nanoparticles dispersed on xGnP were characterized by cyclic voltammetry (CV) in electrolytes of 1M H_2SO_4 as shown in Figure 6.7. The potential was scanned between -0.25 and 1.20V at the rate of 50mV/s. The peaks in hydrogen

adsorption and desorption region from 0 to 0.33V corresponding to the reductive adsorption of protons in the cathodic scan and the subsequent oxidation of the hydrogen adatoms in the anodic scan were clearly shown for all of the samples. The hydrogen region seemed to be slightly more defined for the **PtRu/xGnP-RTI-L2** catalysts than PtRu/CB-ETEK, suggesting that **PtRu/xGnP-RTIL-2** catalysts may have the higher degree of alloying.

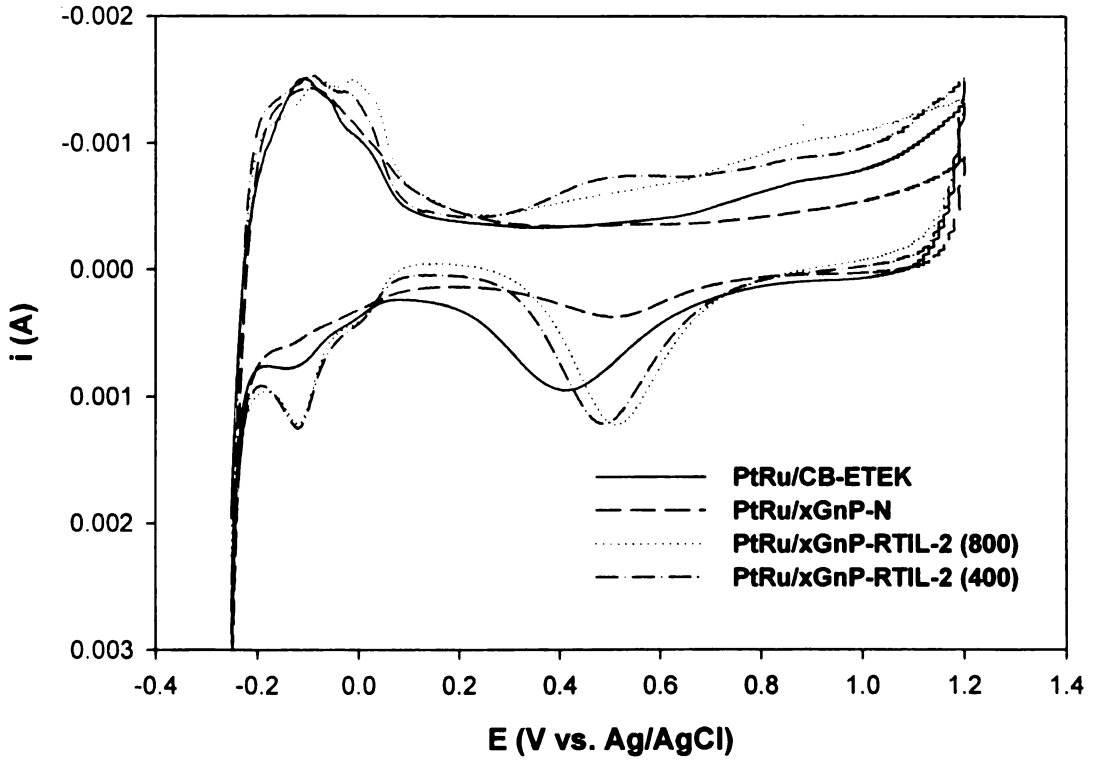

Figure 6.7. Cyclic voltammograms recorded at 50mV/s of PtRu/xGnP catalysts via microwave process and a commercial PtRu/CB-ETEK.

The electrochemical active surface area (EAS) for PtRu/xGnP catalysts and the PtRu/CB catalyst can be estimated from the integrated charge in the hydrogen electrosorption region of the cyclic voltammogram according to the following formula [27]:

$$EAS = \frac{Q_H}{[PtRu]} \qquad (6.4)$$

where *EAS* has unit of $m^2/g\ PtRu$, [PtRu] represents the PtRu loading in the electrode and $Q_H = 0.21\ mC/cm^2$. The calculated results listed in Table 6.2. The value of integrated charge was obtained by using software called 'Echem Analyst' which was provided by Gamry. The active surface area of all PtRu/xGnP catalysts followed the order of PtRu/xGnP-N < PtRu/CB-ETEK < PtRu/xGnP-RTIL2(800) < PtRu/xGnP-RTIL2(400). Even PtRu/xGnP-RTIL2(800) (3.72nm) which have the larger average size than PtRu/CB-ETEK (1.90nm) showed higher active surface area, suggesting better utilization of PtRu particles on xGnP than on CB. The highest active surface area was obtained from PtRu/xGnP-RTIL2(400) which has the smallest particle size.

Table 6.2. Electrochemically active surface area of PtRu particles for PtRu/xGnP synthesized via microwave process and a commercial PtRu/CB catalyst

Samples	Q_H	S_{EL} (cm^2)	Catalyst loading (mg)	EAS (m^2/g)
PtRu/CB-ETEK	2.977	14.18	0.03602	39.36
PtRu/xGnP-N	2.087	9.94	0.03277	30.32
PtRu/xGnP-RTIL2(800)	3.720	17.71	0.02869	61.75
PtRu/xGnP-RTIL2(400)	4.098	19.51	0.02482	78.62

Figure 6.8 shows the results of cyclic voltammetry carried out to evaluate the activities of PtRu/xGnP catalysts for methanol electrooxidation at room temperature against a commercial PtRu/CB from E-TEK. The peak at around 0.8V during the forward scan (from 0 to 1.2V) corresponds to methanol oxidation and another peak at about 0.5V during reverse scan (from 1.2 to 0V) represents the removal of the removal of the residual

carbon species formed in the forward scan [28, 29]. The peak current due to methanol oxidation for PtRu/xGnP-N, PtRu/xGnP-RTIL2 (800), PtRu/xGnP-RTIL2(400), and the E-TEK sample were 8.77, 13.23, 16.96, and 9.14 mA, respectively. Therefore, the catalyst activities were in the following order; PtRu/xGnP-N < PtRu/CB-ETEK < PtRu/xGnP-RTIL2(800) < PtRu/xGnP-RTIL2(400). This result is consistent with EAS data obtained from hydrogen electrosorption but dose not match with the well-known fact that PtRu particles with around 3.0nm exhibits most high catalytic activity for methanol oxidation [30]. Thus, this discrepancy may mainly result from the different degree of dispersion and utilization of PtRu particles in between PtRu/xGnP and PtRu/CB catalysts.

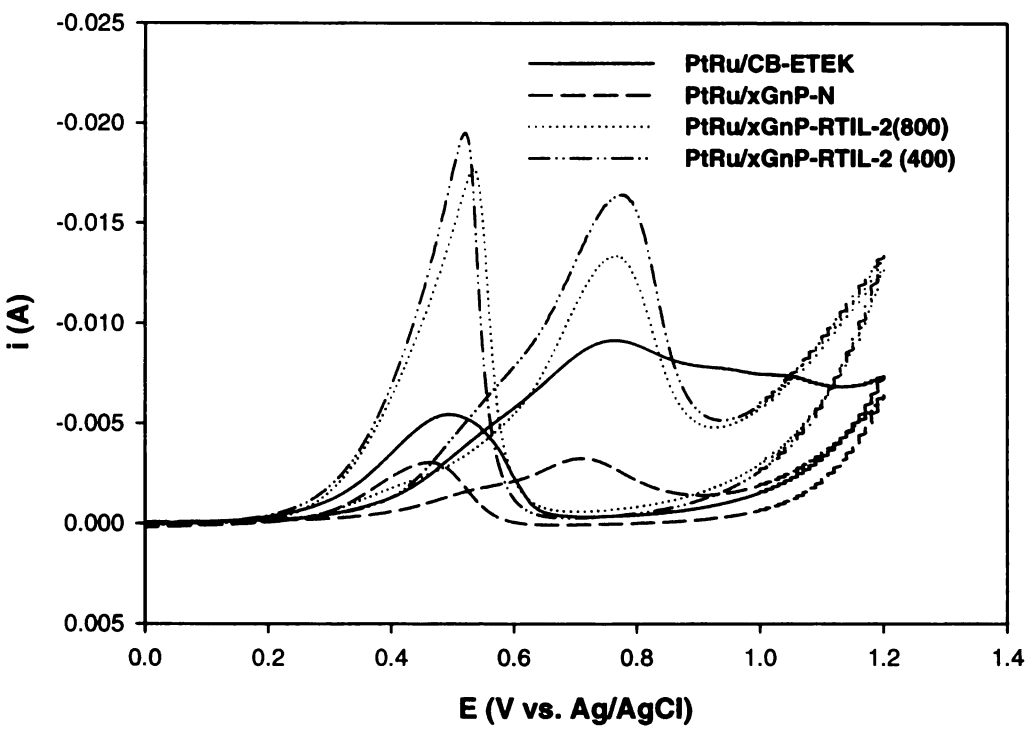

Figure 6.8. Cyclic voltammograms of the methanol oxidation in 1M H_2SO_4 + 2M CH_3OH at 50mV/S for PtRu/xGnP catalysts and a commercial PtRu/CB-ETEK.

Chronoamperometric curves were measured at 0.4V for three PtRu/xGnP and PtRu/CB-ETEK electrodes. As shown in **Figure 6.9**, the initial methanol oxidation currents for all of the catalysts were in good agreement with the result of CV measurements and ESA calculation. However, the decay in the methanol oxidation currents for each catalyst with time was different. While PtRu/CB-ETEK lost 87% of initial current after 2500s, PtRu/xGnP-RTIL2 (400) and PtRu/xGnP-RTIL2 (800) were less pronounced with 73% loss, which indicate their long-term stability compared to the commercial PtRu bimetallic catalysts. PtRu/xGnP-N showed the highest current loss of 94% among all the catalysts measured.

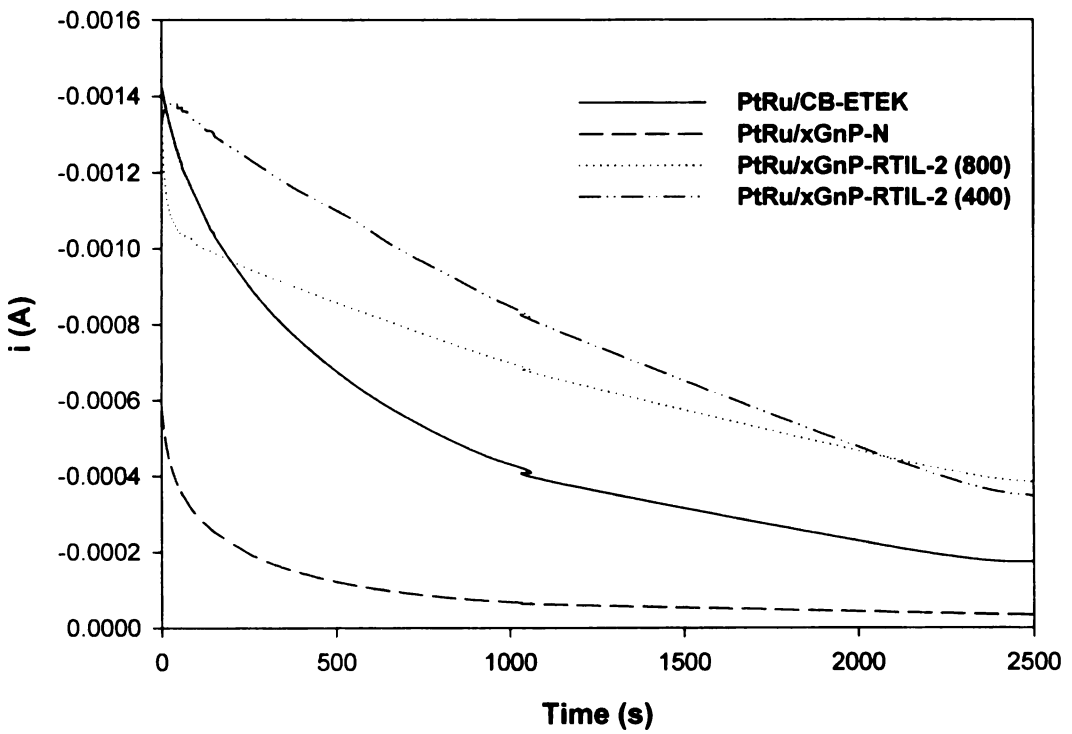

Figure 6.9 Chronoamperometry curves for methanol oxidation at 0.40V on PtRu/CB-ETEK and three PtRu/xGnP catalysts.

6.4. Conclusion

xGnP supported or unsupported PtRu bimetallic nanoparticles have been synthesized via microwave dielectric heating method in the presence of RTIL. It was proved from TEM investigation that the introduction of RTIL during reduction reaction of Pt and Ru precursors in microwave process results in the smaller particles with a narrow size distribution for unsupported samples and high dispersion of the particles on the surface of xGnP in the case of supported samples. The methanol oxidation of PtRu bimetallic particles dispersed on xGnP was evaluated using electrochemical measurement and compared with a commercial PtRu/CB catalyst. PtRu/xGnP catalysts prepared in the presence of RTIL displayed the higher active surface area than the commercial catalyst, which seems to come from improved utilization of the PtRu particles on xGnP. Hence, the enhanced catalytic activity for methanol oxidation was obtained from PtRu/xGnP-RTIL catalysts. All the results presented in this chapter give credence for synthetic method to control the size, distribution, and dispersion of Pt-based metal particles and for the use of xGnP as a support with a great potential for DMFC.

6.5 Bibliography

1. K.V. Kordesch and G.R. Simander, "Environmental Impact of Fuel Cell Technology", Chem. Rev., 95(1), p191-207, 1995.

2. V. Plzak and B. Rohland, Advanced Electrochemical Hydrogen Technologies, in Modern Aspects of Electrochemistry No. 26, Plenum Press, New York, p105, 1994.

3. L. Blomen and M.N. Mugerwa, "Fuel Cell Systems", Plenum, New York, 1993.

4. X.M. Ren, E.T. Springer, T.A. Zawodzinski, and S. Gottsfield, "Methanol Transport through Nation Membranes. Electro-osmotic Drag Effects on Potential Step Measurements", J. Electrochem. Soc, 147(2), p466-474, 2000.

5. Dianxue Cao and Steven H. Bergens, "A nonelectrochemical reductive deposition of ruthenium adatoms onto nanoparticle platinum: anode catalysts for a series of direct methanol fuel cells", Electrochimica Acta, 48(27), p4021-4031, 2003.

6. Dianxue Cao and Steven H. Bergens, "An organometallic deposition of ruthenium adatoms on platinum that self poisons at a specific surface composition: A direct methanol fuel cell using a platinum–ruthenium adatom anode catalyst", J. of Electroanal. Chem., 533(1-2), p91-100, 2002.

7. C. Roth, M. Goetz, and H. Fuess, "Synthesis and characterization of carbon-supported Pt–Ru–WO*x* catalysts by spectroscopic and diffraction methods", J. Appl. Electrochem., 31(7), p793-798, 2001.

8. A.K. Shukla, M.K. Ravikumar, A.S. Arico, G. Candiano, V. Antonucci, N. Giordano, and A. Hamnett, "Methanol electrooxidation on carbon-supported Pt-WO_{3-x} electrodes in sulphuric acid electrolyte", J. Appl. Electrochem., 25(6), p528-532, 1995.

9. R. Jasinski, "Cobalt Phthalocyanine as a Fuel Cell Cathode", J.Electrochem. Soc., 112(5), p526, 1965.

10. N. Alanso-Vante, P. Bogdanoff, and H. Tributsch, "On the Origin of the Selectivity of Oxygen Reduction of Ruthenium-Containing Electrocatalysts in Methanol-Containing Electrolyte", J. Catal., 190(2), p240-246, 2000.

11. O. Solorza, K. Ellmer, M. Giersig, and N. Alonso-Vante, "Novel low-temperature synthesis of semiconducting transition metal chalcogenide electrocatalyst for

multielectron charge transfer: molecular oxygen reduction", Electrochim. Acta, 39(11-12), p1647-1653, 1994.

12. H. Tributsch, M. Bron, M. Hilgendorff, H. Schulenburg, I. Dorbandt, V. Eyert, P. Bogdanoff, and S. Fiechter, "Methanol-resistant cathodic oxygen reduction catalysts for methanol fuel cells", J. Appl. Electrochem., 31(7), p739-748, 2001.

13. A.S. Arico, H. Kim, V. Antonucci, A.K. Shukla, M.K. Ravikumar, and N. Giordano, "Methanol oxidation on carbon-supported Pt---Sn electrodes in silicotungstic acid", Electrochim. Acta, 39(5), p691-700, 1994.

14. M. Watanabe, Makoto Uchida and Satoshi Motoo, "Preparation of highly dispersed Pt + Ru alloy clusters and the activity for the electrooxidation of methanol", J. Electroanal. Chem., 229(1-2), p395-406, 1987.

15. N.M. Markovic, T.J. Schmidt, and V. Stamenkovic, and P.N. Ross, "Oxygen Reduction Reaction on Pt and Pt Bimetallic Surfaces: A Selective Review", Fuel Cells, 1(2), p105-116, 2001.

16. T. Toda, H. Igarashi, and H. Uchida, M. Watanabe, "Enhancement of the Electroreduction of Oxygen on Pt Alloys with Fe, Ni, and Co", J. Electrochem. Soc., 146(10), 3750-3756, 1999.

17. S. Wasmus and A. Kuver, "Methanol oxidation and direct methanol fuel cells: a selective review", J. Electroanal. Chem., 461(1), p14-31, 1999.

18. Y. Takasu, T. Kawaguchi, W. Sugimoto, and Y. Murakami, "Effects of the surface area of carbon support on the characteristics of highly-dispersed Pt---Ru particles as catalysts for methanol oxidation", Electrochim. Acta, 48(25-26), p3861-3868, 2003.

19. V. Rao, P.A. Simonov, E.R. Savinova, G.V. Plaksin, S.V. Cherepanova, G.N. Kryukova, and U. Stimming, J. of Power Sources, "The influence of carbon support porosity on the activity of PtRu/Sibunit anode catalysts for methanol oxidation", 145(2), p178-187, 2005.

20. Y. Takasu and Y. Murakami, "Design of oxide electrodes with large surface area", Electrochim. Acta, 45(25-26), p4135-4141, 2000.

21. E. Antolini and F. Cardellini, "Formation of carbon supported PtRu alloys: an XRD analysis", J. Alloy. Comp., 315(1), p118-122, 2001.

22. D. Chu and S. Gilman, "Methanol Electro-oxidation on Unsupported Pt-Ru Alloys at Different Temperatures", J. Electrochem. Soc., 143(5), p1685-1690, 1996.

23. E. Antolini, L. Giorgi, F. Cardellini, and E. Passalacqua, "Physical and morphological characteristics and electrochemical behaviour in PEM fuel cells of PtRu/C catalysts", J. Solid State Electrochem., 5(2), p131-140, 2001.

24. E. Antolini, F. Cardellini, L. Giorgi, and E. Passalacqua, "Effect of Me (Pt+Ru) content in Me/C catalysts on PtRu alloy formation: An XRD analysis", J. Mater. Sci. Lett., 19(23), p2099-2103, 2000.

25. E. Antolini, "Formation of carbon-supported PtM alloys for low temperature fuel cells: a review", Mater. Chem. And Phys., 78(3), p563-573, 2003.

26. Q. Lu, B. Yang, L. Zhuang, and J. Lu, "Anodic Activation of PtRu/C Catalysts for Methanol Oxidation", J. Phys. Chem. B, 109(5), p1715-1722, 2005.

27. Z.L. Liu, J.Y. Lee, M. Han, W.X. Chen, and L.M. Gan, "Synthesis and characterization of PtRu/C catalysts from microemulsions and emulsions", J. Mater. Chem., 12(8), p2453-2458, 2002.

28. R. Mancharan and J.B. Goodenough, "Methanol oxidation in acid on ordered NiTi", J. Mater. Chem., 2(8), p875, 1992.

29. X. Zhang, and K.Y. Chan, "Water-in-Oil Microemulsion Synthesis of Platinum-Ruthenium Nanoparticles, Their Characterization and Electrocatalytic Properties", Chem. Mater., 15(2), p451-459, 2003.

30. Y. Takasu, H. Itaya, T. Iwazaki, R. Miyoshi, and T. Ohnuma, W. Susimoto, and Y. Murakami, "Size effects of ultrafine Pt–Ru particles on the electrocatalytic oxidation of methanol", Chem. Commun., p341-342, 2001.

CHAPTER 7

DETAILS ON MECHANISM FOR NANOPARTICLE FORMATION IN SOLVENT AND IN THE PRESENCE OF SUPPORTS

7.1. Formation of Nanoparticles in Solution

The formation of metal nanoparticles in solution by a wet chemical route involves two distinct dynamic processes: the nucleation of primary clusters of atoms in saturated solution and the aggregation of the primary clusters into secondary or final particles [1~5]. The primary cluster of atoms forms through successive stages consisting of reduction of the metal salt, generation of the metal atom, embryos, nuclei formation, and diffusional growth of the nuclei. The secondary particles form as a result of an irreversible aggregation between new metal atoms with the primary cluster. The secondary particle can further grow to larger particles and be coarsened by Ostwald ripening due to the increased solubility of small particles with decreasing particle size. The sequence describing the formation of metal particles can be found in section 2.2.1 of chapter 2. In this section, the thermodynamic or dynamic growth mechanism for the general formation of metal nanoparticles is presented followed by a hypothesis for the formation mechanism of metal particles in the presence of RTIL.

7.1.1 Nucleation

The nucleus forms according to the following scheme:

$$mX_1 = X_m$$

$$X_m + X_1 = X_{m+1}$$

$$X_{(n-1)} + X_1 \leftrightarrows X_n$$

X_1 represents a metal atom and X_n an embryo which can be generated or disappeared by the reversible association/dissociation process. The metal atoms are referred to as solutes

which act as monomers for the primary-particle nucleation. In classical nucleation theory, the free energy of the n-solute embryos can be expressed by [6, 7]:

$$\Delta G = -\frac{4}{3}\pi R^3 \Delta F + 4\pi R^2 \gamma \qquad (7.1)$$

$$\Delta F = \rho kT \ln(c/c_o) \qquad (7.2)$$

where R is the radius of nucleus, ΔF is the bulk free energy difference per volume between solutes and nuclei, γ is the surface tension at the solute-liquid solvent interface, c is the solute concentration, c_o is the equilibrium saturation concentration, ρ is the density of solutes, k is Boltzmann's constant, and T is the temperature. The first term of right hand side in the Equation (1) is the volume term which favors the formation of the nuclei. The second term is the surface energy term which works against the formation of the nuclei. At large R, the volume term plays an important role in creating nuclei but at small R, the surface energy term will be more important.

As soon as a solution is supersaturated with metal atoms, nucleation begins with the association of metal atoms to form nuclei. There is the critical size of a nucleus, R_c, which is derived from the maximum value of ΔG in the derivative of ΔG with respect to R.

$$R_c = \frac{2\gamma}{\Delta F} = \frac{2\gamma}{\rho kT \ln(c/c_o)} \qquad (7.3)$$

The energy barrier to nucleation is equal to

$$\Delta G_c = \frac{16\pi\gamma^3}{3\Delta F} = \frac{16\pi\gamma^3}{3\rho kT \ln(c/c_o)} \qquad (7.4)$$

Thus, the nucleation rate given by activation over the free energy can be expressed as

$$J = J_o \exp\left(-\Delta G_c / kT\right) \tag{7.5}$$

From classical theory, it can be understood that the increased concentration of the solute will decrease the critical nucleus size and nucleation energy barrier and increase the nucleation rate, while the high surface energy of solutes will increase the critical size of nucleus and decrease the nucleation rate. Thus, in order to create monodispersed small metal particles, fast supersaturation of metal atoms in solution and low surface energy of metal atoms are required.

7.1.2 Growth

Primary particles dispersed in a solution present a very high degree of freedom for rotation and translation motions. Thus the particles experience a high collision rate at a high velocity due to the Brownian motion. The collision frequency for a single primary particle can be described by

$$z = \frac{\sqrt{2}\pi D^2 \nu N}{V} \tag{7.6}$$

$$\nu = \sqrt{\frac{3kT}{m}} \tag{7.7}$$

where D is the particle diameter, N is the total number of particles which can be empirically calculated [8], V is the total volume occupied by the system, ν is the mean velocity of the dispersed particles, and m is the mass of a particle. As an example, the mass of a spherical Pt primary particle with a radius of 0.5nm and a density of 21.45g/cm^3 is 1.1×10^{-20}g. The Pt particle presents a mean velocity of about 42m/s which is a very high value. N is approximately 2.45×10^{18} at Pt concentration of 0.0025M and

thus the collision frequency at 473K is estimated to be of about 2×10^7 collisions/s for each particle. This value is significant even if the calculation is approximate. Thus, the coagulation mechanism based on the effective collision of primary particles can be used to explain the particle growth and aggregation [9, 10]. The oriented attachment mechanism which is a simplified coagulation mechanism provides a good prediction of the behavior of particle growth [11~13]. However, deviation in the fitting of the equation due to the Ostwald ripening mechanism is observed [14]. Hence, the particle growth can be described by an equation by combining the oriented mechanism dominant in the initial stage and the Ostwald ripening mechanism which is prevalent later,

$$r^3 - r_{eq}^3 = \frac{8\gamma V_m^2 c_\infty}{54a\pi\eta N} \bullet t \qquad (7.8)$$

where C_∞ is the bulk solubility, V_m is the molar volume, and a is the radius of the solvated ion, N is Avogadro's number, r is the mean radius of secondary particles, r_{eq} is the equivalent radius at a time t, γ is the surface energy, and η is the viscosity of a liquid solution. This equation may provide a reasonable explanation on the growth of Pt particles synthesized in this work. As in nucleation stage, low surface energy of primary particles is preferred.

7.1.3 Formation of Metal Nanoparticles in the Absence of RTIL

Figure 7.1 shows the schematic process of synthesizing platinum nanoparticles in ethylene glycol via microwave heating in the absence of RTIL as an example. A metal precursor is solvated in a solvent which is a reducing agent and then the solution is supersaturated with metal atoms which result from the fast reduction of the solvated

metal ions by the microwave heating and composition of the organo-metallic precursor. The metal atoms spontaneously collide with each other or with metal ions, resulting in the formation of embryos. The embryos eventually reach a critical size to form the nuclei. The nuclei rapidly grow to unstable primary particles by further association with the remaining metal atoms. Secondary particles form through the process of growth, aggregation and Ostwald ripening (or coarsening). The formed secondary particles may agglomerate and grow in size due to the absence of capping agents to terminate further particle growth and reduce particle coarsening. Hence, when RTIL is not present, large and highly agglomerated metal particles are synthesized as shown in TEM image (Figure 4.9a) of chapter 4.

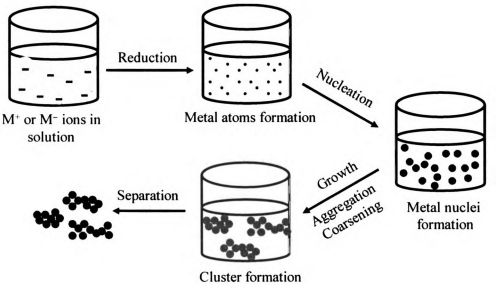

Figure 7.1 The simplified process for uniform particle formation synthesized via microwave process in the absence of RTIL.

7.1.4 Formation of Metal Nanoparticles in the Presence of RTIL

In the case when RTIL is added to the solution, the number of the nuclei and their size are particularly dependent on the surface energy of the nuclei and reaction

temperature since the addition of RTIL results in the significant change of those two experimental parameters. **Figure 7.2 (a)** shows how metal nanoparticles are synthesized in the presence of RTILs, especially bmimPF_6, bmimCH_3SO_4, and bmimCH_3CO_2. As shown by the results of UV-vis spectroscopy in chapter 4, those three RTILs are not coordinated with the solvated metal ions but the RTILs promote the reduction reaction due to a high heating rate resulted from the high polarizability of the RTIL in the microwave environment. The solution becomes supersaturated with metal atoms more quickly than in the absence of RTIL. Since the RTILs have low surface energy in spite of their high polarity, they easily adsorb onto the surface of atoms or embryos. As a result, the metal atoms or embryos have a low surface energy, which will reduce nucleation energy barrier and nuclei size based on Equation (4) and (5). As a result, many more primary particles with low surface energy are formed compared with the case of the absence of RTIL. The growth and the coarsening of the secondary particles are affected by the surface energy of the primary particles. On the basis of the Equation (8), it can be understood that low surface energy of the primary particles leads to the generation of the smaller secondary particles. In turn, the low surface energy of the secondary particles weakens Ostwald ripening in the particle growth stage, resulting in the production of very small metal particles. In addition, low interfacial energy of the RTILs can be translated into stabilization of molecular or metal species.

Figure 7.2 (b) shows the formation process of metal nanoparticles synthesized in the presence of bmimSCN. Unlike other RTILs used in this work, bmimSCN coordinates with the solvated metal ions, which has been shown by the shift of UV-vis adsorption spectrum in chapter 4. It is also shown in the same chapter that bmimSCN has the ability

to reecue metal ions. Hence, bmimSCN seems to participate actively in the formation of metal particles. As drawn in the Figure, the process of reduction, nucleation, particle growth and aggregation occurs almost simultaneously in a very short time in the presence of bmimSCN. The effect of low surface energy of bmimSCN on nucleation, particle growth and aggregation stage can be explained in a similar way as described for bmimPF_6, bmimCH_3SO_4, and bmimCH_3CO_2. Consequently, the role of bmimSCN with its low surface energy functions as a strong protecting agent as well as a reducing agent for the formation of the smallest metal particles among various RTILs.

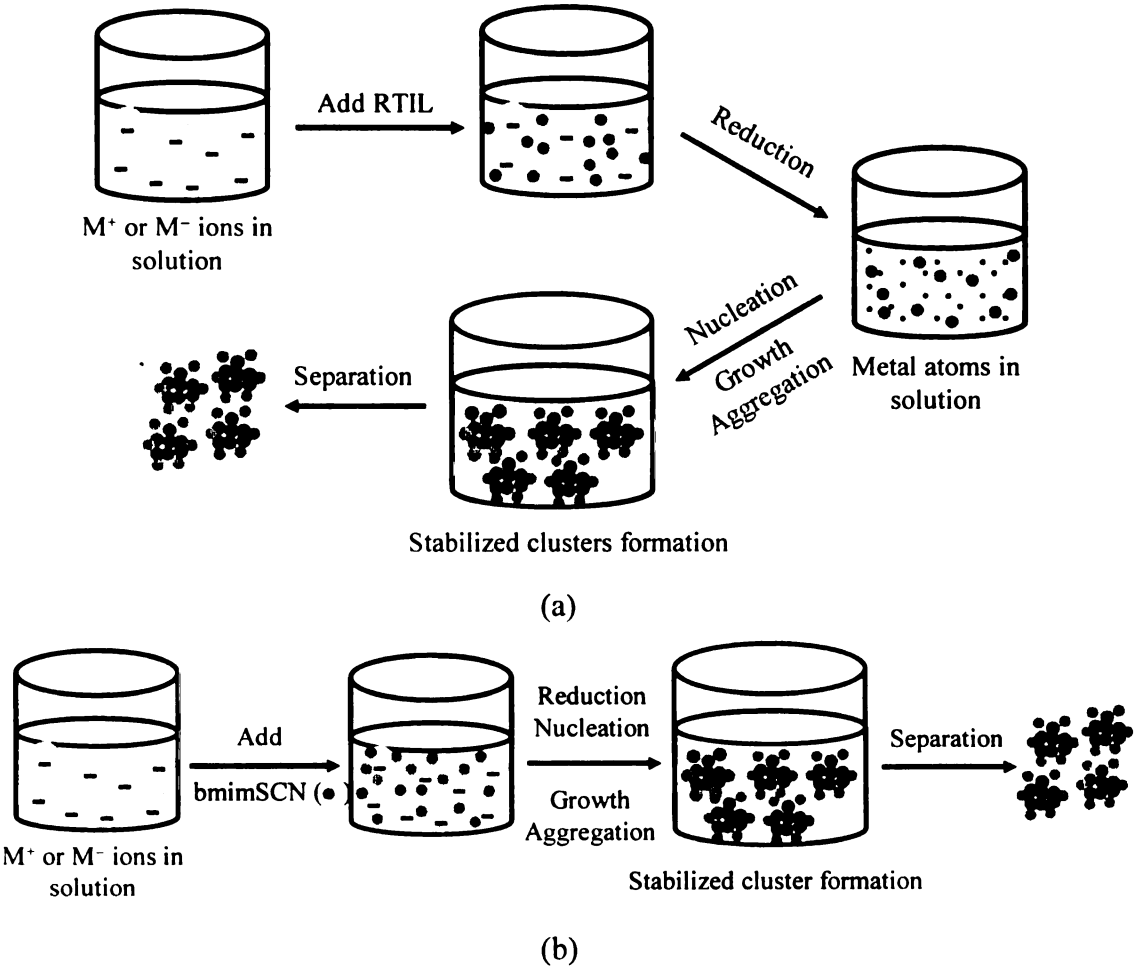

Figure 7.2 The simplified process for uniform particle formation synthesized via microwave process (a) in the presence of bmimPF_6, bmimCH_3SO_4, and bmimCH_3CO_2 and (b) bmimSCN.

7.2 Deposition of Nanoparticles on xGnP

Metal nanoparticles have been deposited on the surface of various carbons and metal oxide supports. Hence, in this section, some details on interaction between metal particles-supports and the formation and growth of metal particles on xGnP, which were not covered in previous chapter, will be described.

7.2.1 xGnP Surface-Metal Precursor Interaction

Among various heteroatoms, oxygen-containing groups greatly influence an acid/base character of the xGnP surface. Several oxygen groups on a graphene layer are shown in **Figure 7.3**. Surface oxides such as carbonyl, carboxyl, phenolic hydroxyl, lactone, and quinine groups are representative of the acidic groups. The basic groups are associated with ethers but the basicity of xGnP surface originates mostly from the π sites on a graphene layer. There are two sites of π electrons on the surface ox xGnP: the delocalized π sites and the localized π sites. The former are on aromatic systems corresponding to the basal plane of xGnP. The latter are created in between two non-neighboring oxygen atoms mostly at the edge of xGnP. The delocalized effect of π electrons has a great effect on the basicity of xGnP because the surface area of the basal plane is much larger than that from the edge.

The oxygen surface groups and π sites on xGnP surface play a very critical role in interactions between xGnP and a metal precursor and consequently in the interaction of the metal particles with the xGnP support. The xGnP basal plane with its planar structure along the c-axis contains a number of delocalized π electrons as shown in Figure 7.3. The

electrostatic interaction of the π sites-metal ions is also presented in Figure 7.4 in which C_π represents the delocalized π electrons and Pt anion is taken as an example metal ion.

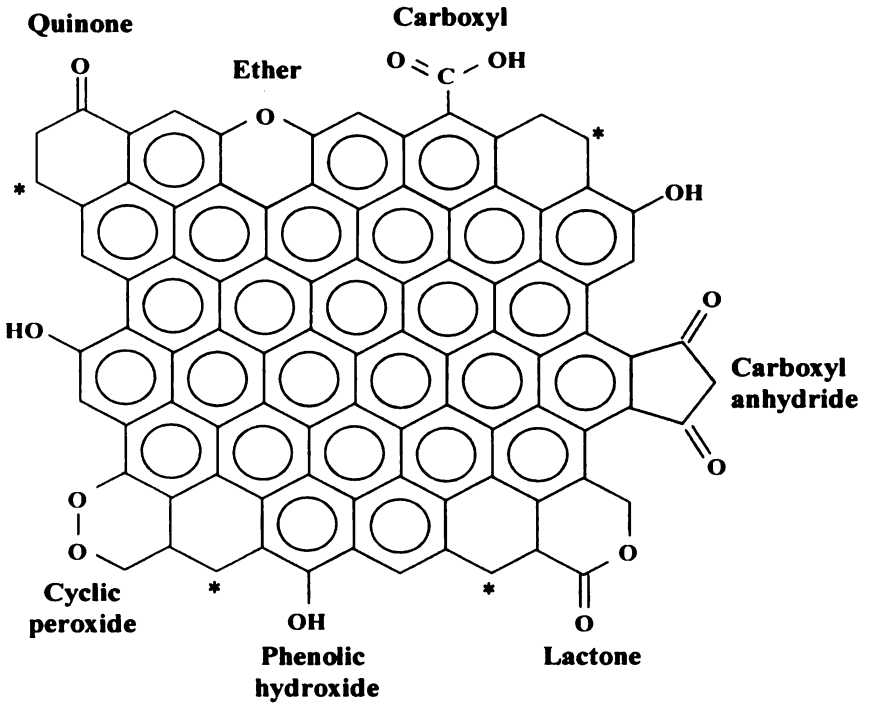

Figure 7.3. Schematic representation of oxygen-containing groups and localized π sites (★) on a graphene layer.

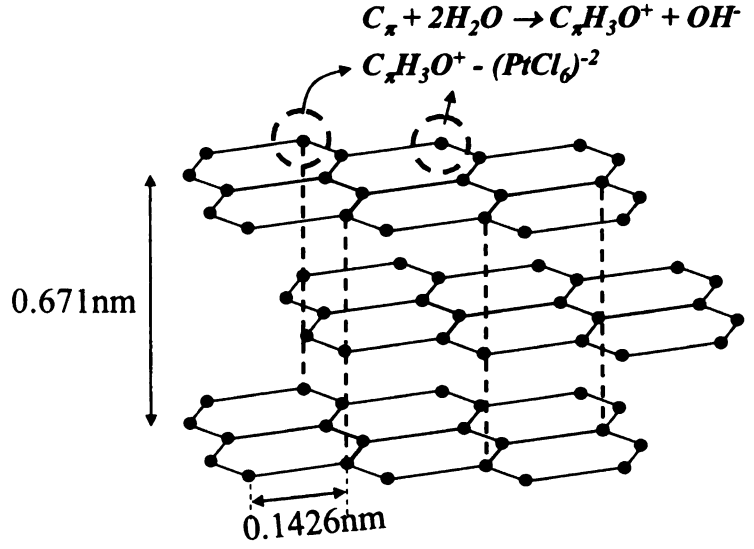

Figure 7.4. Three dimensional schematic of layered graphite structure (•: carbon atom) and schematic interaction between the delocalized π sites and Pt precursor as an example.

The increase of the basic C_π sites on the basal plane of xGnP will maximize the electrostatic attraction with the metal anion ($C_\pi - PtCl_6^{-2}$) and minimize the electrostatic repulsion ($COO^- - PtCl_6^{-2}$), resulting in increasing the dispersion of metal particles. The strong interaction between the solvated metal ions and the π sites on xGnP is responsible for metal particles depositing at high density on the surface of xGnP. Metal particles anchored on the π sites of xGnP are more resistant to metal sintering than those on oxygen groups, indicating the strong adhesion of metal particles on xGnP [15]. The oxygen groups are mostly located at the edges of xGnP. Thus, the metal particles at the edge of xGnP result from the interaction of the oxygen groups-metal ions in polar solvents. However, after the reduction of metal ions, the oxygen groups have a detrimental effect on the interaction between the metal particles and xGnP because sintering of the metal particles on oxygen groups easily takes place regardless of the high initial dispersion of the metal ions.

The possible interactions between the metal ions-the π sites on the xGnP basal plane and the metal ions-the oxygen groups at the xGnP edge and the formation of metal particles on xGnP after the complete reduction are again illustrated with Pt precursors in **Figure 7.5**. Fine and well-dispersed metal particles forms on the basal plane of xGnP as a result of strong attraction of the metal ions-π sites, while relatively large particles are deposited at the xGnP edge site due to less stable oxygen groups at an elevated temperature and the weak interaction of the metal ions-acidic oxygen groups.

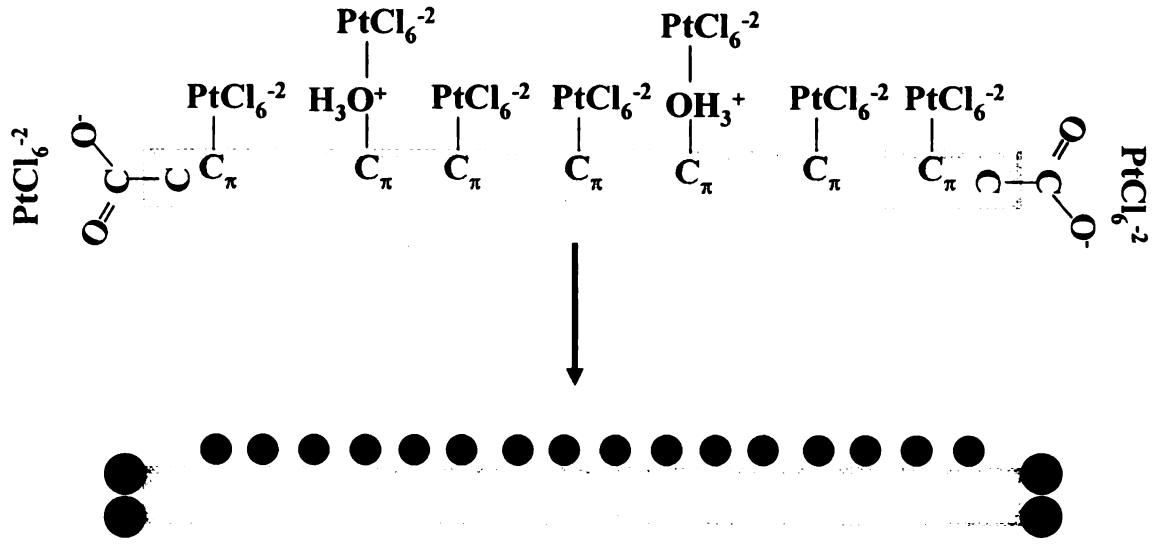

Figure 7.5 Schematic representing the common interactions between the metal ions and the active sites of xGnP and final metal particle size and distribution after the reduction.

7.2.2 Metal Oxide-Metal Precursor Interaction

Surfaces of most metal oxides have hydroxyl groups or become hydroxylated on contacting with water molecules. The hydroxyl groups can be acidic, neutral, or basic according to the pH of the surrounding solution. If the pH is below the isoelectric point (IEP) which is the value when the net surface charge is zero, the metal oxide surface becomes positively charged due to protonation. If the pH value of the solutions is above IEP, the surface of metal oxide particles becomes negatively charged due to deprotonation. Thus, the metal oxides adsorb metal anions like $PtCl_6^{-2}$ in solutions with pH values below IEP and metal cations like $Pt(NH_4)_2^{+2}$ at pH values above IEP, which is schematically represented in **Figure 7.6**. IEP values of some important metal oxides as catalyst supports are listed in **Table 7.1**.

Table 7.1 Iso-electric point values of some metal oxides [16, 17]

Metal oxides	IEP	Adsorption
WO_3	0.5	cations
SiO_2	1.0~2.0	
MnO_2	4.0~4.5	Cations or anions
SnO_2	5.5	
TiO_2	6	
γ-FeO_3	6.7	
ZrO_2	6.7	
CeO_2	6.8	
Al_2O_3	7.0~9.0	
ZnO	8.7~9.7	Anions
Y_2O_3	9	
La_2O_3	10.5	
MgO	12~13	

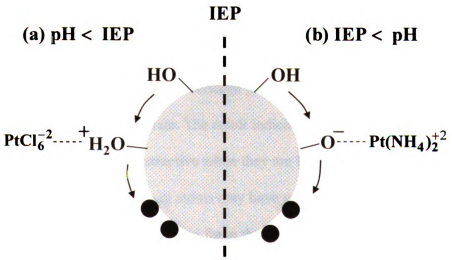

Figure 7.6 Schematic representing the metal precursor-metal oxide interaction at different pH condition and the formation of metal particle size.

7.2.3 Pt-Pt and Pt-Graphite Interactions

The Lennard-Jones (LJ) potential and the Sutton-Chen (SC) potential can be used to describe the interaction of platinum atoms as an example [18~21]. Although SC model is normally used for a molecular dynamic study for atomic interaction, the LJ model is more convenient than SC model when the substrate is present and thus involved in metal atom interaction. The general form of LJ potential and force is given by

$$U_{LJ} = 4\varepsilon\left[\left(\frac{\sigma}{r_{ij}}\right)^{12} - \left(\frac{\sigma}{r_{ij}}\right)^{6}\right] \tag{7.9}$$

$$F_{LJ} = \frac{4\varepsilon}{r_{ij}}\left[12\left(\frac{\sigma}{r_{ij}}\right)^{12} - 6\left(\frac{\sigma}{r_{ij}}\right)^{6}\right] \tag{7.10}$$

where ε is an energy parameter, σ is a lattice parameter, and r_{ij} is the distance between atoms i and j. The first term in Equation (9) and (10) represents the repulsion between atomic cores and the second term represents the bonding energy between atoms due to the surrounding electrons. ε=*0.694eV* and σ=*0.29471* can be used for platinum-platinum interaction [22] and ε=*0.0409eV* and σ=*0.2936* for platinum-graphite interaction [23]. **Figure 7.7** shows the force interaction between platinum atoms and also between platinum atom and graphite substrate. The result indicates that platinum-platinum and platinum-graphite are the most attractive when they are located at about 0.37nm. It is also expected from the plot that platinum atoms may have good mobility on the surface of xGnP due to their much higher attraction force than platinum-xGnP.

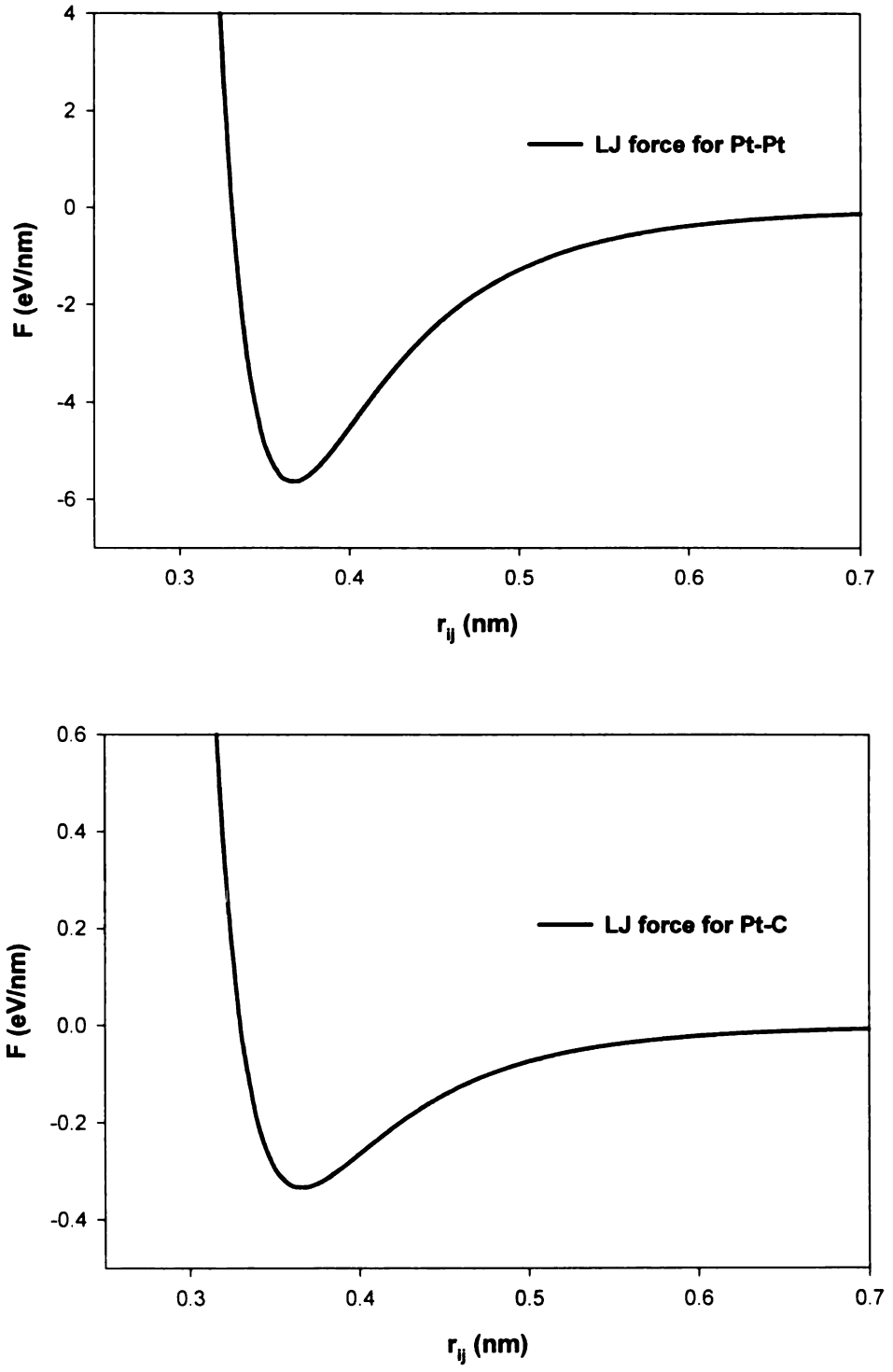

Figure 7.7 Force interaction in platinum-platinum (top) and platinum-graphite (bottom) obtained by Lennard-Jones formuation.

7.2.4 Particle Growth of Metal Particles on xGnP

Cluster growth of metal atoms or very small particles deposited on the basal plane of xGnP can be simplified as in **Figure 7.8**. Individual metal nanoparticles deposited on xGnP undergo Brownian motion with diffusion coefficient ($D = d^2/4\tau$, d is the diameter of metal and τ is the diffusion time) to form small metal islands composed of only two atoms or particles (**Figure 7.8 a and b**). The small metal islands grow by incorporation of diffusing atoms (or nanoparticle or another small metal island) (**Figure 7.8 c and d**). Finally, a 3-dimensional island is formed by the total coalescence (**Figure 7.8 f**). The shape of metal nanoparticles or 3D metal island can be half spheres or even flatter shape due to their interactions with xGnP.

What is the mechanism for 2D and 3D growth of metal islands? One of the answers on this question can be partially explained by the expected good mobility of Pt particles on xGnP due to their higher attractive force. Molecular dynamic study provides an additional important answer [24]. The metal particles can be locked on the surface of xGnP when xGnP and metal particle lattice parameters are compatible. However, slight deviations from this match result in a huge increase of the diffusivity of metal particles, suggesting the significant dependence of the diffusion coefficient on the lattice parameter mismatch of xGnP and metal nanoparticles [25]. When the mismatch is large, the particles undergo Brownian-like diffusion with no influence of the substrate. If the mismatch is small, the particles diffuse by hopping-like motion, jumping from site to site on the lattice defined by the substrate. The diffusion decreases as the number of atoms in metal nanoparticles increases and finally stop at the critical number of atoms.

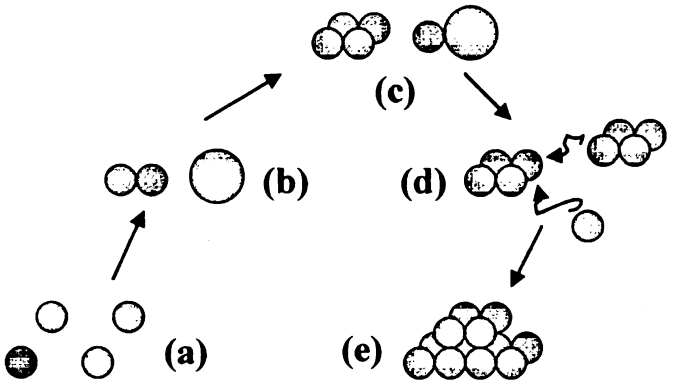

Figure 7.8. Main successive processes representing the formation of metal nanoparticles on the basal plane of xGnP.

7.2.5 Metal Particle Deposition on xGnP in the Presence of RTIL

The size and dispersion of metal particles on xGnP relies on when bmimCH_3CO_2, as an example of RTIL is added. **Figure 7.9** briefly shows the schematic of RTIL location in a solution containing platinum ions and TEM morphologies of the samples prepared by changing the sequence of bmimCH3CO2 addition to the solution. When bmimCH_3CO_2 is introduced in xGnP/ethylene glycol solutions before to the addition of a metal precursor (**Sequence-A, Figure 7.9 a**), bmimCH_3CO_2 adsorbs onto the surface of xGnP and thus metal ions interact weakly with xGnP through the adsorbed layer of bmimCH_3CO_2. Hence, there is a possibility of the formation of some metal atoms and particles separate from the xGnP surface, which may lead to the deposition of a small quantity of metal nanoparticles on xGnP. If bmimCH_3CO_2 is added in xGnP/ethylene glycol solutions after the addition of the metal precursor (**Sequence-B, Figure 7.9 c**), metal ions directly interact with the π sites on xGnP basal plane and some oxygen groups at the xGnP edge area. bmimCH_3CO_2 may adsorb on the surface of metal ions or the xGnP surface unoccupied by metal ions. Therefore, more metal atoms or particles form on the surface

of xGnP. TEM results shown in Figure 7.9 (b) and (d) support such assumptions well. The sample prepared from **Sequence-B** has more particles on xGnP than that from **Sequence-A** at no expense of particle size.

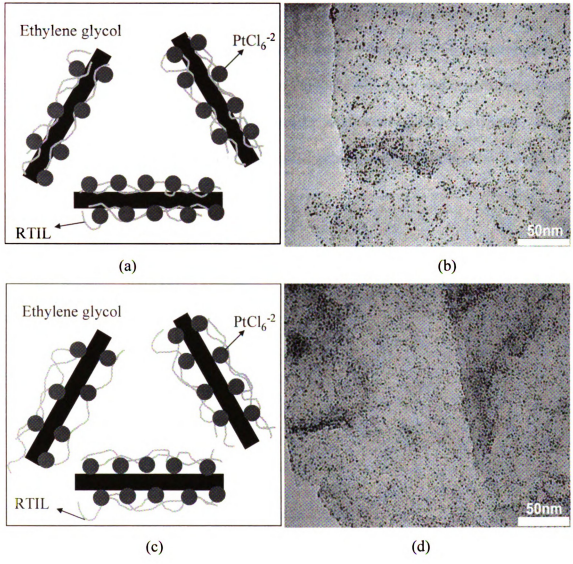

Figure 7.9. Suggested RTIL locations and TEM morphology of Pt/xGnP-bmimCH_3CO_2 sample when RTIL is added (a, b) before and (c, d) after Pt precursor.

FTIR data obtained from Pt/xGnP-bmimCH_3CO_2 nancomposites also support that the assumptions mentioned above are reasonable. As seen in the plots of **Figure 7.10**, the sample for **Sequence-B** has the same peak features as xGnP indicating there is no specific interaction between bmimCH_3CO_2 and xGnP and thus bmimCH_3CO_2 can be removed with easy after mild-washing with acetone. Meanwhile, in the case of **Sequence-A**, the sample shows peaks similar to those of bmimCH_3CO_2, suggesting that bmimCH_3CO_2 molecules mostly adsorb onto the surface of xGnP and considerable traces of bmimCH_3CO_2 still remains on xGnP even after mild washing. In this sequence, too much RTIL may be detrimental to achieve the targeted metal loading because it prevents metal ions from interacting with xGnP.

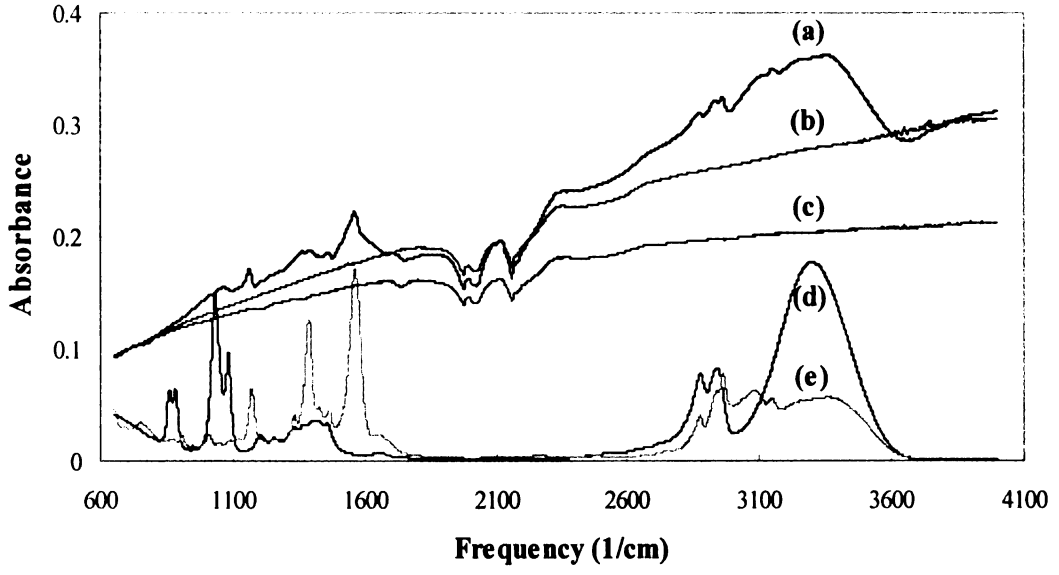

Figure 7.10 FTIR of (a) Pt/xGnP-bmimCH_3CO_2 (the addition of bmimCH_3CO_2 prior to Pt precursor), (b) xGnP, (c) Pt/xGnP-bmimCH_3CO_2 (the addition of Pt precursor prior to bmimCH_3CO_2) (d) ethylene glycol, and (e) bmimCH_3CO_2.

7.3 Summary

Nucleation and growth of metal particles in solvent without xGnP has been explained with classical nucleation theory and collision theory. The difference in the formation of metal particles in solvent in the absence and the presence of RTIL was explained with a simplified hypothesis. The principle of metal precursor-xGnP and metal precursor-metal oxide interactions was explained when xGnP or metal oxide is present in the synthesis of metal nanoparticles. It was found from calculation of the Lennard-Jones force that the interaction between platinum atoms is much stronger than that between platinum and xGnP, suggesting high mobility of platinum atoms on the surface xGnP. The effect of the sequence of the addition of RTIL and the metal precursor on the size and dispersion of metal particles was explained, and was supported by TEM and UV-vis spectroscopy data.

7.4. Bibliography

1. V.K. LaMer, "Nucleation in Phase Transitions", Ind. Eng. Chem., 44, p1270-1277, 1950.

2. V.K. LaMer and R.H. Dinegar, "Theory, Production and Mechanism of Formation of Monodispersed Hydrosols", J. Am. Chem. Soc., 72, p4847-4854, 1950.

3. S. Libert, V. Gorshkov, V. Privman, D. Goia, and E. Matijevic, "Formation of monodispersed cadmium sulfide particles by aggregation of nanosize precursors", Adv. Colloid Interface Sci., 100-102, p169-183, 2003.

4. J. Park, V. Privman, E. Matijevic, "Model of Formation of Monodispersed Colloids", J. Phys. Chem. B, 105, 11630, 2001.

5. M.A. Watzky and R.G. Finke, "Transition Metal Nanocluster Formation Kinetic and Mechanistic Studies. A New Mechanism When Hydrogen Is the Reductant: Slow, Continuous Nucleation and Fast Autocatalytic Surface Growth", J. Am. Chem. Soc., 119, p10382-10400, 1997.

6. D.W. Oxtoby, "Nucleation of First Order Phase Transitions", Acc. Chem. Res., 31, p91-97, 1998.

7. H. Furedi-Milhofer, "Spontaneous precipitation from electrolyte solutions", Pure Appl. Chem., 53, p2041-2055, 1981.

8. C. Ribeiro, E.J.H. Lee, T.R. Giraldi, E. Longo, J.A. Varela, and E.R. Leite, "Study of Synthesis Variables in the Nanocrystal Growth Behavior of Tin Oxide Processed by Controlled Hydrolysis", J. Phys. Chem. B, 108, p15612-15617, 2004.

9. G.H. Weiss, "Overview of theoretical models for reaction rates", J. Stat. Phys., 42, p3-36, 1986.

10. D. Mozyrsky and V. Privman, "Diffusional growth of colloids", J. Chem. Phys., 110, p9254-9258, 1999.

11. C. Ribeiro, E.J.H. Lee, E. Longo, and E.R. Leite, "A kinetic model to describe nanocrystal growth by the oriented attachment mechanisum", ChemPhysChem, 6, p690-696, 2005.

12. F. Huang, H.Z. Zhang, and J.F. Banfield, "Two-Stage Crystal-Growth Kinetics Observed during Hydrothermal Coarsening of Nanocrystalline ZnS", Nano Lett., 3, p373-378, 2003.

13. E.J.H. Lee, C. Ribeiro, E. Longo, and E.R. Leite, "Oriented Attachment: An Effective Mechanism in the Formation of Anisotropic Nanocrystals", J. Phys. Chem. B, 109, p20842-20846, 2005.

14. X.G. Peng, J. Wickham, and A.P. Alivisatos, "Kinetics of II-VI and III-V Colloidal Semiconductor Nanocrystal Growth: "Focusing" of Size Distributions", J. Am. Chem. Soc., 120, p5343-5344, 1998.

15. S.S. Barton, M.J.B. Evans, E. Halliop, J.A.F. MacDonald, "Acidic and basic sites on the surface of porous carbon", Carbon, 35, p1361, 1997.

16. M.L. Toebes, J.A. van Dillen, and K.P. de Jong, "Synthesis of supported palladium catalysts", J. Mole. Catal. A: Chem., 173, p75-98, 2001.

17. J.P. Brunelle, "Preparation of catalysts by metallic complex adsorption on metal oxides", Pure Appl. Chem, 50, p1211-1229, 1978.

18. S.P. Huang and P.B. Balbuena, "Pt nanoclusters on graphite substrates: a molecular dynamics study", Mole. Phys., 100, p2165-2174.

19. P. Deltour, J.L. Barrat, and P. Jensen, "Fast diffusion of a Lennard-Jones cluster on a crystalline surface", Phys. Rev. Lett., 78, p4597-4600, 1997.

20. E.J. Lamas, and P.B. Balbuena, "Adsorbate effects on structure and shape of supported nanoclusters: a molecular dynamic study", J. Phys. Chem. B, 107, p11682-11689, 2003.

21. A.P. Sutton and J. Chen, "Long-range finnis Sinclair potentials", Philos. Mag. Lett., 61, p139-146, 1990.

22. P.M. Agrawal, B.M. Rice, and D.L. Thompson, "Predicting trends in rate parameters for self-diffusion on FCC metal surfaces", Surface Science, 515, p21-35, 2002.

23. S.R. Calvo and P.B. Balbuena, "Molecular dynamics studies of phonon spectra in mono- and bimetallic nanoclusters", Surface Science, 581, p213-224, 2005.

24. H. Reiss, "Rotation and Translation of Islands in the Growth of Heteroepitaxial Films", J. Appl. Phys., 39, p5045, 1968.

25. J. Hautmann and M.L. Klein, "Microscopic wetting phenomena", Phys. Rev. Lett., 67, p1763-1766, 1991.

CHAPTER 8

CONCLUSIONS

AND

RECOMMENDED WORK

An intriguing research theme in modern nanotechnology is to synthesize nanoscaled metal colloids or clusters because they have great impact on the development of new technological applications. They possess unique optical, thermal, electronic, magnetic properties and chemical reactivity, which comes from their quantum size effect and is not observed in their bulky status. Most of their unique physical and chemical properties strongly depend on the size and shape of the metal nanoparticles. Therefore, an alternative and effective synthetic method is required to obtain uniform small metal nanoparticles with a controlled size and a narrow size distribution. On the other hand, xGnP is an interesting carbon with excellent mechanical, thermal and electrical features but much cost-effective compared to other carbon nanostructures. Hence, nanocomposites composed of xGnP and metal particles hold promises for their application in industrial catalysts, automobiles, batteries, supercapacitors, fuel cells, hydrogen storage and production as well as sensor. The objectives of this research were:

- Develop new synthetic technique to produce nanosized metals in a simple, effective and economic way.
- Extend the technique in order to produce various metal nanoparticles uniformly dispersed on the surface of carbon materials.
- Understand the formation mechanism of metal particles synthesized via the new technique.
- Fabricate xGnP-supported metal catalysts having possible application as electrocatalysts for fuel cell.
- Evaluate xGnP as a promising support to replace a commercial carbon

The accomplishments from the present work can be summarized as follows:

1) A simple and effective microwave heating process assisted with RTIL (MPR) to synthesize noble metal nanoparticles with a narrow size distribution has been developed. The average size of Pt, Ru, and Pd blacks was < 3nm and they are almost monodispersed. It has been confirmed that RTIL plays triple roles in synthesizing nanoscale metal particles, that is, a promoter to increase the reduction rate of metal salt, a protecting agent to prevent metal particles from growing and agglomerating each other, and a reductant to convert metal ions to metal particles in microwave heating process. Such triple roles of RTIL are responsible for the production of extremely small and well-stabilized individual metal particles.

2) It was tested if MPR could be applied to produce carbonaceous materials- or metal oxides-supported noble metal nanoparticles free from agglomeration. It was proved that MPR make it possible to disperse metal phase on any kind of carbon surface. MPR seemed effective of the deposition of metal particles on metal oxides, too.

3) Corrosion resistance and graphitization of exfoliated graphite nanoplatelets (xGnP) has been studied. It turned out that xGnP possesses the greatest corrosion and oxidation resistance in acidic environment and the highest degree of graphitization among various carbon materials. Combined with its excellent electrical conductivity, good mechanical strength and less impurity, this results support the potential of xGnP as a good substrate for metal catalysts.

4) xGnP-supported platinum catalysts was synthesized by MPR and their catalytic activity for methanol electro-oxidation was evaluated. Such catalysts showed much higher catalytic activity compared to a commercial platinum catalyst on the surface of carbon black. A main reason of excellent activity of the xGnP-supported catalyst stems from the geometric feature of xGnP which makes the reactant easily access to the surface of the active phases, leading to improve the utilization of platinum particles. This result proves the potential of xGnP as a support to replace the current carbon black.

5) xGnP-supported or unsupported PtRu bimetallic nanoparticles have also been synthesized via MPR. It was proved that MPR is facile to produce smaller PtRu bimetallic alloy particles with a narrow size distribution for unsupported samples and high dispersion of the particles on the surface of xGnP. The methanol oxidation of PtRu bimetallic particles dispersed on xGnP was evaluated and they displayed the higher active surface area and the higher activity than a commercial PtRu catalyst deposited onto carbon black surface, which is attributed to the improved utilization of the PtRu particles on xGnP surface.

The following works are recommended to extend the accomplishments from the present work for the next generation energy and power devices:

1) Hydrogen Production: The challenge is to find inexpensive and efficient routes to generate hydrogen in sufficient quantities from non-fossil natural resources. Hydrogen generated from water splitting process using solar energy is the most promising candidate as a renewable and environmentally safe energy carrier for

the future. Solar hydrogen technologies using solar energy for hydrogen production mainly consist of photoelectrochemical cell and photocatalytic water-gas shift reaction. Both technologies are relatively simple but the raw material for the former is only water and the latter needs scavenger reagent. The development of both solar hydrogen technologies depends on special materials serving as photosensitive photoelectordes in photoelectrochemical cell and as heterocatalysts in photoassisted water-gas shift. Among many candidate materials for photo-electrode and photocatalyst, TiO_{2-x} has unique properties that make it the most promising. Deposition of transition metals on TiO_{2-x} has a great impact on the catalytic activity of catalysts which depend on the method applied to synthesize them. Hence, it is worth investigating the effect of TiO_2-supported transition metal catalysts synthesized by the present process for the photocatalytic hydrogen generation.

2) Hydrogen Storage: The development of safe, reliable, cost-effective, and practical ways of storing hydrogen is the bottleneck of the breakthrough for the success of hydrogen economy and fuel-cell technologies. Hydrogen uptake of carbon materials by hydrogen spillover mechanism has recently attracted much attention to achieve the target department of energy set. To facilitate hydrogen spillover on carbon materials, metallic nanoparticles should be deposited on the surface of carbons. Thus, the investigation of hydrogen storage for metal-decorated carbon materials, especially xGnP, must be an intriguing research theme.

3) Lithium Batteries: In lithium batteries, the anode materials are more important than the cathode materials because the cycling behavior of the anode determines the cell life completely. There are two categories in anode materials: one is lithium alloy and metal oxides and the other is carbon materials. The former has higher theoretical capacity and better cycleability than carbon materials. However, large first cycle capacity loss and a large specific volume change during Li insertion and extraction reactions are major problems. Carbon materials have been used either as the anode itself or as a conductive enhancer for the active materials mainly due to their high electrical conductivity and good corrosion resistance in many electrolytes. Among various carbon materials, graphite is the most attractive due to its low cost, high specific capacity, and desirable charge-discharge curves. However, poor high rate performance due to the limited electrochemical reaction at the interface between graphite and electrolyte because of Li^+ migration taking place only at the edge plane of graphite limits their use. The graphite coated with metal thin film or deposited with metal or metal oxide nanoparticles can be a solution to enhance charge-discharge performance, coulombic efficiency, and cycling life at the same time. Hence, the surface and interface modification of the graphite with metal or metal oxide nanoparticles will be technical challenges to improve their electrochemical reaction.

4) Supercapacitors: Supercapacitors can be divided into two types on the basis of the charge storage mechanism: the double-layer capacitors and the redox

capacitors. The former stores charges within the interfacial double-layer of high specific area electrode in an aqueous or an organic electrolyte. This is called the electrical or electrochemical double-layer capacitor (EDLC). Activated carbons with very high surface area of 1000~2000m^2/g have been widely used for the electrodes. In the latter, Faradaic redox reactions take place at the electrode surface consisting of electroactive materials, as in a battery. This is called as pseudocapacitor which has been developed with transition metal oxide and conducting polymer. Since pseudocapacitor has a higher specific capacitance than EDLC, the former type is more attractive. The electrode materials of pseudocapacitors are electroactive materials with redox state and structure such as transition-metal oxides (oxides of Ru, Co, Ir, Ni, Mg, In, Sn, Fe, etc). Due to high specific capacitance and high chemical stability, iridium and ruthenium oxides are widely sued. However, the high cost of ruthenium and iridium precursors has limited their practical usage. Hence, there have been efforts to reduce the cost of materials. To do so, the recent research has focused on developing of ruthenium oxides/carbon composites. Carbon nanotube, carbon black, activated carbon, and mesoporous carbon have been studied but there is no report with xGnP which is expected to enhance utilization of ruthenium oxide and other active metal oxides, resulting in improved capacitance. Hence, metal oxide/carbons, especially metal oxides/xGnP nanocomposites fabricated by the present method may be a good research subject for this application.

5) Sensors: Sensors are devices converting subtle change of physical and chemical quantities into an electrical signal. Sensors continue to impact everyday life with a variety of applications such for biomedical, automotive, food, agriculture industry, and even security. Especially, sensors based on carbon nanotubes have the great potential of revolutionizing the sensor industry due to their exceptionally excellent properties. The decoration of carbon nanotubes with nanosized metal oxides or quantum dots is most interesting research theme for next generation sensor development. Hence, the present work may be applied for the deposition of such materials on carbon nanotube surface, which will be of importance for creating new types of sensors.